An Anatomically-based Computational Study of Cardiac Mechanics and Myocardial Infarction

By Carey Stevens
c.stevens@auckland.ac.nz

Supervised by
Professor Peter Hunter
p.hunter@auckland.ac.nz

A thesis submitted in partial fulfilment of the
requirements for the degree of Doctor of Philosophy

THE UNIVERSITY OF AUCKLAND
NEW ZEALAND

Department of Engineering Science
School of Engineering
The University of Auckland
New Zealand

2002

Abstract

An anatomically based computational model of the cardiac ventricles was developed. The model is based upon the pig ventricles, as the pig is now the principal large animal used experimentally. The model includes concise mathematical descriptions of the left and right ventricular walls and the basal skeleton geometries in rectangular cartesian coordinates. The non-homogeneous fibre and sheet microstructure is also incorporated. The finite element method for finite deformation elasticity was used to simulate the cardiac cycle and to investigate the global and regional mechanics. The deformation response showed good agreement with reported observations. For the physiological loading conditions chosen an ejection fraction of 48% was predicted with an apex-base shortening of approximately 4%. The large ejection fraction was achieved through an apex-base twist of 22.8 degrees and wall thickening of 33%. Predictions of the distributions of stress and strain in the ventricular myocardium are presented.

A finite element model was used to interpret the results from a published experimental study of myocardial infarction. A nonlinear optimisation problem was solved to determine the parameters for a published proposal for an exponential constitutive law for infarcted myocardium. The suitability of the "pole-zero" constitutive law for myocardium to model infarcted myocardium was also investigated. The pole-zero formulation, which incorporates structural details of the myocardium, yielded strain distributions more similar to those measured experimentally. The effect of infarction upon the regional and global mechanics of the new porcine ventricular model was then examined.

In order to accurately and efficiently represent the ventricular anatomy and the large spatial variations in the material properties and solution fields associated with myocardial infarction, several new techniques were developed. The hanging node method for high order cubic Hermite finite elements was developed to enable the use of localised mesh refinement. Mapping constraints, to enforce C^0-continuity between high order

elements with inconsistent parametric coordinates, were implemented to allow irregular mesh topology. Texture map evaluations were used to provide a method of prescribing the spatially varying constitutive parameters independent of mesh resolution . The new techniques and models have provided initial insights into the behaviour of infarcted myocardium, and a framework has been developed that can now be used for future studies of both physiologically normal and infarcted porcine hearts.

Acknowledgements

There are many people to thank for the work presented in this thesis. Without the collective knowledge and expertise offered to me by many talented researchers both in New Zealand and abroad, I simply could not have completed this body of work.

In particular, Dr Ian LeGrice for his expertise who, along with his group at the School of Medicine, performed the experimental work and provided the data upon which the porcine ventricular model was developed.

Dr Jeffrey Holmes now in the Cardiac Biomechanics Group at the University of Columbia who kindly provided the infarct remodelling data from his PhD thesis in collaboration with Dr. James Covell and Dr. Andrew McCulloch at the University of San Diego. The infarction modelling study presented here was very much a collaborative effort with Dr Holmes contributing significantly to discussions and analysis of results.

I would like to thank Drs. Marytn Nash and Chris Bradley who patiently answered my questions day and night and taught me the ropes of CMISS programming. The CMGUI team of Dr David Bullivant, Dr Richard Christie and Shane Blackett who provide and support the visualisation tools.

A big thanks to my friends and colleagues who make the Bioengineering Institute such an interesting and fun place to work. Many great people have been part of the research group over the years, but a I would like to specially mention a few of those that have shared the social side with me and provided countless hours of distraction; David Nickerson, Martin Buist, Leo Cheng, Richard Boyes, Ben Wright, Autumn Cuellar, Duane Malcolm, Merryn Tawhai, Karl Tomlinson, Alan Garny and Warren Hedley.

I am extremely grateful to my supervisor Professor Peter Hunter for his enthusiasm, patience and assistance. Peter was always approachable, helpful and encouraging which went a long way towards keeping me motivated. He has also contributed enormously

to the field of bioengineering, and continuously shares the benefits to seek the best for every one in the Bioengineering Research Group. As a result I have been fortunate to have visited several research groups and attended conferences abroad during this thesis.

I would also like to thank my family for always supporting whatever I have decided to do. Finally, to Deanna, my loving wife, who has always patiently supported me. Thanks again for all your encouragement and distraction.

Contents

List of Figures

List of Tables

Glossary of Symbols

$\{Y_j\}$	Global rectangular cartesian coordinate system
$\{\mathbf{i}_j\}$, $\{\mathbf{e}_j\}$, $\left\{\mathbf{g}_j^{(x)}\right\}$	Base vectors for the rectangular cartesian coordinate system
B_0, B	Undeformed and deformed configurations, respectively
$\mathbf{x}$, $\{x_i\}$	Rectangular cartesian coordinates of a point in B
$\mathbf{X}$, $\{X_M\}$	Material coordinates of the point $\mathbf{x}$ in B_0
$\mathbf{F}$, $\{F_M^i\}$	Deformation gradient tensor
$\mathbf{R}$, $\{R_L^i\}$	Orthogonal rotation tensor
$\mathbf{U}$, $\left\{U_M^L\right\}$	Right stretch tensor
$\mathbf{C}$, $\{C_{MN}\}$	Right Cauchy-Green or Green deformation tensor
$\{\lambda_i\}$	Principal extension ratios (eigenvalues of $\mathbf{U}$)
I_1, I_2, I_3	Principal invariants of $\mathbf{C}$
$\mathbf{E}$, $\{E_{MN}\}$	Lagrangian or Green strain tensor
$E_{(MN)}$	Physical Green strain components
Σ, $\{\sigma^{ij}\}$	Cauchy stress tensor
$\sigma^{(ij)}$	Physical Cauchy stress components
$\mathbf{S}$, $\left\{s^{Mj}\right\}$	First Piola-Kirchhoff stress tensor
$\mathbf{T}$, $\left\{T^{MN}\right\}$	Second Piola-Kirchhoff stress tensor
J	Jacobian for coordinate transformations
ρ, ρ_0	Material densities for deformed and undeformed configurations, respectively
$\mathbf{t}$, $\{t^i\}$	Internal stress or traction vector
$\mathbf{b}$, $\{b^i\}$	External body force vector
$\mathbf{v}$, $\{v^i\}$	Velocity vector
$\mathbf{f}$, $\{f^i\}$	Acceleration vector
$\hat{\mathbf{n}}$, $\{\hat{n}_i\}$	Unit normal vector to a given surface

$\delta\mathbf{v}$, $\{\delta v_i\}$	Virtual displacement vector
$\mathbf{s}$, $\{s^i\}$	External stress vector
W,$\overline{W}$	Strain energy function
δ^{MN}, δ^M_N, δ_{MN}	Kronecker delta (1 for $M = N$; 0 otherwise)
p	Hydrostatic pressure (scalar) field
c_1, c_2	Mooney-Rivlin constitutive paramters
$p_{(appl)}$	Applied surface pressure (physical stress)
$\mathbf{r}$	Position vector of a point $p\,(\mathbf{x})$ in B
$\mathbf{R}$	Position vector the same material point $P\,(\mathbf{X})$ in B_0
$\mathbf{u}$	Displacement vector ($\mathbf{u} = \mathbf{r} - \mathbf{R}$)
$\left\{\theta^k\right\}$	Spatial curvilinear reference coordinates
$\left\{\mathbf{g}_i^{(\theta)}\right\}$, $\left\{\mathbf{g}^i_{(\theta)}\right\}$	Covariant and contravariant base vectors for the θ_k-reference coordinate system
$\left\{g_{ij}^{(\theta)}\right\}$, $\left\{g^{ij}_{(\theta)}\right\}$	Covariant and contravariant metric tensors for the θ_k-reference coordinate system
$\{\nu_\alpha\}$	Microstructural material coordinates with respect to anatomically relevant axes
$\left\{\mathbf{A}_\alpha^{(\nu)}\right\}$, $\left\{\mathbf{A}^\alpha_{(\nu)}\right\}$	Covariant and contravariant base vectors for undeformed ν_α-material coordinates
$\left\{\mathbf{a}_\alpha^{(\nu)}\right\}$, $\left\{\mathbf{a}^\alpha_{(\nu)}\right\}$	Covariant and contravariant base vectors for deformed ν_α-material coordinates
$\left\{A_{\alpha\beta}^{(\nu)}\right\}$, $\left\{A^{\alpha\beta}_{(\nu)}\right\}$	Covariant and contravariant metric tensors for undeformed ν_α-material coordinates
$\left\{a_{\alpha\beta}^{(\nu)}\right\}$, $\left\{a^{\alpha\beta}_{(\nu)}\right\}$	Covariant and contravariant metric tensors for deformed ν_α-material coordinates
$u\vert_\alpha$	Covariant derivative of u with respect to the ν_α-material coordinate
$\Gamma^i_{j\alpha}$	Christoffel symbol of the second kind
$\{\xi_M\}$	Finite element material coordinates $0 \leq \xi_M \leq 1$
$\left\{\mathbf{G}_M^{(\xi)}\right\}$, $\left\{\mathbf{G}^M_{(\xi)}\right\}$	Covariant and contravariant base vectors for undeformed ξ_M-material coordinates
$\left\{\mathbf{g}_M^{(\xi)}\right\}$, $\left\{\mathbf{g}^M_{(\xi)}\right\}$	Covariant and contravariant base vectors for deformed ξ_M-material coordinates

$\left\{G^{(\xi)}_{MN}\right\}, \left\{G^{MN}_{(\xi)}\right\}$	Covariant and contravariant metric tensors for undeformed ξ_M-material coordinates
$\left\{g^{(\xi)}_{MN}\right\}, \left\{g^{MN}_{(\xi)}\right\}$	Covariant and contravariant metric tensors for deformed ξ_M-material coordinates
Ψ_i	Lagrange basis function
Ψ^i_n	Hermite basis function
$\left(\frac{\mathrm{d}s_i}{\mathrm{d}\xi_i}\right)_n$	Scale factor between the arc-length, s_i, and the finite element coordinate, ξ_i, at element node n (no sum on i)
H	Harmonic mean
$\xi^{(i)}$, w_i	Gaussian quadrature points and weights, respectively
δv^n_i	Virtual nodal displacements
Ψ^p_n	Hydrostatic pressure interpolation functions
p^e_n	Element parameters for the hydrostatic pressure field
$\mathbf{J}\left(\mathbf{x}\right)$	Jacobian of derivatives of residuals with respect to the solution variables
α, β, γ	Fibre, imbrication and sheet angles, respectively
a_{11}, a_{22}, a_{33}	Limiting strains or poles for axial modes of deformation
a_{12}, a_{13}, a_{23}	Limiting strains or poles for shear modes of deformation
$k_{\alpha\beta}$	Linear weighting coefficients for terms of the pole-zero strain energy function
$b_{\alpha\beta}$	Curvature parameters for terms of the pole-zero strain energy function
$\mathbf{F_g}$, $\{F_{g_{NM}}\}$	Growth tensor used to define the residually stressed state
λ^0_f, λ^0_s, λ^0_n	Initial extension ratios for the fibre, sheet and sheet-normal axes, respectively
T	Active tension developed by myocardial fibres
$\left[\mathrm{Ca}^{2+}\right]_i$	Intracellular calcium concentration
T_0	Actively developed isometric tension
T_{ref}	Isometric tension at resting length and saturating $\left[\mathrm{Ca}^{2+}\right]_i$
β	Slope of the λ-T_0 relation, normalised by the resting isometric tension $(T_0\vert_{\lambda=1})$
c_{50}	$\left[\mathrm{Ca}^{2+}\right]_i$ at which T_0 is 50% of its maximum
h	Hill coefficient for the sigmoidal dose-response relation
$\left[\mathrm{Ca}^{2+}\right]_{max}$	$\left[\mathrm{Ca}^{2+}\right]_i$ at which activation is maximal
$[\mathrm{Ca}_{actn}]$	activation parameter to determine $\left[\mathrm{Ca}^{2+}\right]_i$

E_{ff}, E_{cc}, E_{rr}	fibre, cross-fibre and radial axial Green strains, respectively
E_{fc}, E_{fr}, E_{cr}	Fibre/cross-fibre, fibre/radial and cross-fibre/radial shear Green strains respectively
C_i	fibre, cross-fibre and radial axial Green strains, respectively

Notation

- This thesis uses the Einstein summation convention, where repeated indices implies summation over the individual components. For example a vector dot product, in N dimensions, may be written:

$$a_i b_i = \mathbf{a} \cdot \mathbf{b} = \sum_{i=1}^{N} a_i b_i$$

  If an index is in parenthesis then summation is not implied. For example:

$$a_i b_{(i)} = \begin{cases} a_1 b_1 & \text{if } i = 1 \\ a_2 b_2 & \text{if } i = 2 \end{cases}$$

- Mathematical variables represented by bold lowercase letters generally refer to vector quantities, while bold uppercase letters refer to tensor quantities, except where noted.

- In general, this thesis uses lowercase indices when dealing with coordinates in the deformed state and uppercase for coordinates in the undeformed reference state. Moreover, Roman letters generally refer to spatial coordinates, while Greek characters refer to material coordinates.

Chapter 1

Introduction

The heart is a complex four chambered organ whose role is to pump blood throughout the body. In a typical person's life of 75 years their heart will beat over 3 billion times, pumping over 200 million litres of blood to supply the body's nutrient needs. Heart failure is the leading cause of non-accidental death in the industrially developed world and by 2010 the same will be true in developing countries (American Heart Association 2002).

Although vast resources have been dedicated to heart research for many years, our knowledge of normal cardiac function is far from complete. The quantity and complexity of data being acquired both clinically and in research laboratory environments is increasing as instruments become more sophisticated. Computer models are becoming necessary to filter, present and interpret the data. But more importantly computer models can be also be used to simulate cardiac behaviour and predict quantities that cannot be measured, such as mechanical stress in the beating muscle.

The heart continuously remodels itself in order to meet the demands upon it. The mechanical loading and deformation behaviour of an unhealthy heart varies from that of a normal heart. The remodelling responses vary depending upon the loads and are not well understood. One of the most common heart problems is *myocardial infarction* (described in detail below). The onset of myocardial infarction starts a remodelling response that changes the mechanical properties of the heart wall. The response is often not successful. The mechanical rupture of myocardial infarcts is the leading cause of in-hospital cardiac related deaths in the United States. Knowledge of the remodelling

response is essential to diagnosis and prescription of the optimal treatment.

In this thesis a new porcine heart model is developed along with tools to investigate the mechanical behaviour of infarcted myocardium and its effect on ventricular function.

The ventricular models developed and presented in this thesis build upon a solid and extensive foundation of mathematical principles and computational techniques contributed to by many researchers in the Auckland Bioengineering Research Group. The following two chapters, 2 and 3, present those techniques. Chapter 4 provides a review of the cardiac models developed to date and is the starting point for the modelling work completed in this thesis. A new model of the porcine ventricles is developed in Chapter 5 followed by its use to simulate the cardiac cycle in Chapter 6. Finally, Chapter 7 develops the techniques for investigating the effect of myocardial infarction upon ventricular mechanics and applies them to the new porcine ventricular model.

Appendix D includes an article accepted for publication that stems from the work completed for this thesis.

This chapter provides an overview of cardiac anatomy and function along with a description of myocardial infarction.

1.1 Cardiac Anatomy and Function

1.1.1 Gross Structure

Figure 1.1 shows the anatomy of the four heart chambers of a human heart. The two large lower chambers are the *left ventricle* (LV) and *right ventricle* (RV). The two smaller upper chambers are the *left atrium* (LA) and *right atrium* (RA). The thin-walled atria act as low pressure blood reservoirs for the ventricles which are the predominant pumping mechanisms.

The atria are connected to their respective ventricle via the *atrioventricular valves* which ensure blood flows from the atria into the ventricles and not the reverse. The left atrial valve is called the *mitral valve* and is composed of two leaflets (bicuspid). The valve from the right atrium, the *tricuspid valve*, has three leaflets. The outflow tracts to the great arteries are connected to the ventricles via the other two *semilunar valves.* The

left ventricle pumps blood up the aorta though the *aortic valve* which prevents it returning. Similarly the right ventricle pumps blood out the pulmonary artery though the one way *pulmonary valve*. Although the semilunar and atrioventricular valves perform similar functions, their mechanisms are quite different. The free edges of the atrioventricular valve cusps are connected by fibrous attachments (*chordae tendineae*) to finger like projections of muscle from the heart wall called *papillary muscles*. The aortic and pulmonary valve cusps have thick tendinous fibres along their free edges.

Heart muscle tissue is called *myocardium.* Atrial and ventricular myocardium is separated by the *basal skeleton* (also known as *cardiac skeleton*, *base* or *basal ring*). The basal skeleton is a fibrous framework formed by the rings of the four valves and surrounding connective tissue.

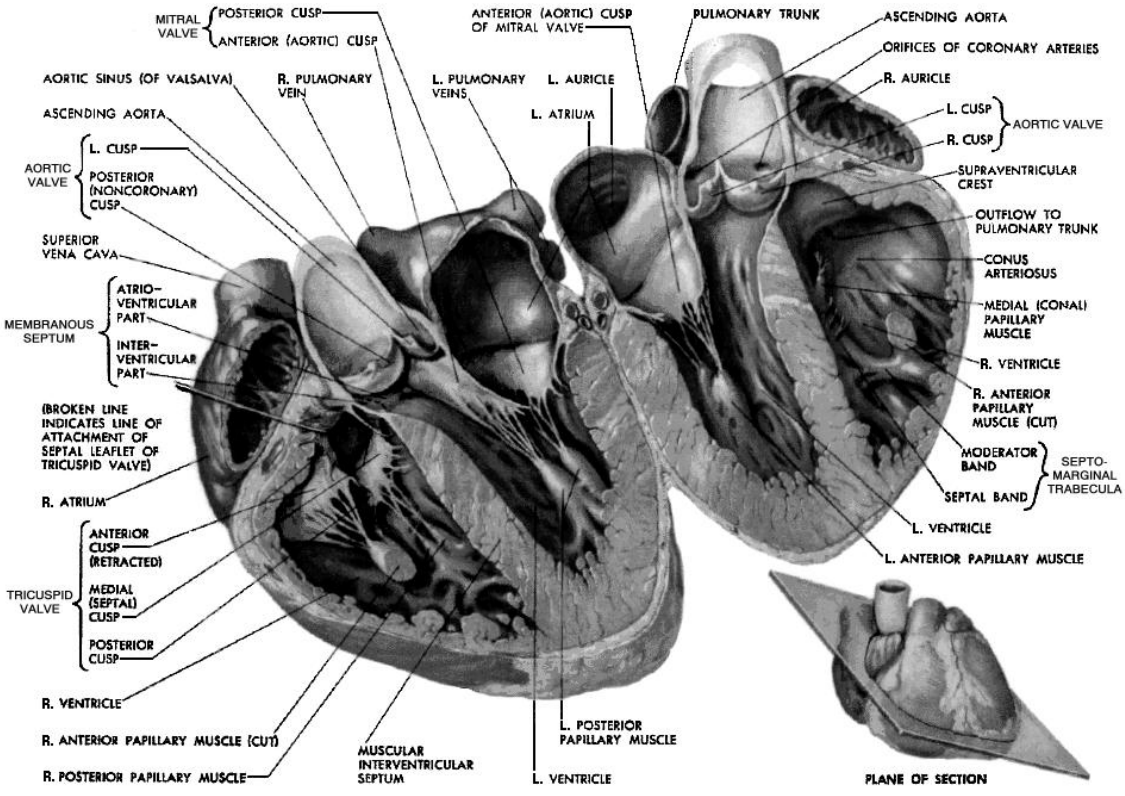

FIGURE 1.1: A cross-section of the heart taken though the four major chambers. Reproduced from Netter (1997).

1.1.2 Microstructure

The myocardium is largely comprised of a framework of connective tissue and cells, the surrounding extracellular space is fluid-filled. Cardiac muscle cells, called *myocytes*, are typically cylindrical with lengths between 80 to 100 μm and diameters ranging from 10 to 20 μm. At the turn of the century the heart was viewed as an assembly of discrete fibre bundles originating at the base and spiraling towards the apex (MacCallum 1900, Mall 1911). This qualitative description was generally accepted until Hort (1957) and Streeter & Bassett (1966) made the first quantitative measurements of the fibre angle throughout the heart wall. They found a smooth transmural variation of myocyte orientation, which led to the predominant view that the myocardium is a single muscle mass that is more appropriately described as a continuum than as discrete muscle bundles. Subsequently, more detailed studies (Streeter, Spotnitz, Patel, Ross & Sonnenblick 1969, Armour & Randall 1970) have confirmed this view for multiple spieces, including human hearts (Fox & Hutchins 1972, Greenbaum, Ho, Gibson, Becker & Anderson 1981). However, none of these studies sampled at more than eight sites on a single heart, nor did they refer the muscle fibre architecture to the ventricular geometry, so the data only provided a limited and essentially qualitative description of the ventricular fibre orientation.

The most thorough quantitative study to date of myocardial microstructure is that of LeGrice (1992), who progressively removed fine layers of myocardium from a mounted intact canine heart preparation. Muscle fibre orientation was measured together with the absolute coordinates at a large number of sites through successive layers. LeGrice also developed a method of drying thin transmural segments that exposed a transmural laminar organisation of the cardiac myocytes. These techniques are described in further detail in Sections 5.1.1 and 5.1.2 where they were used again to acquire data for this thesis. More recently the use of scanning electron microscopy (SEM) to image ventricular specimens has shown myocardial *sheets* are formed by layers of myocytes tightly coupled by endomysial collagen and about 4 cells thick; see Figure 1.2 (LeGrice, Smaill, Chai, Edgar, Gavin & Hunter 1995). The sheets are separated by cleavage planes and coupled via an extensive *perimysial* extracellular connective tissue network. There is also branching between layers with muscle bridges one to two cells thick. On the basis of these and other observations the conceptual model of myocardial architecture shown in Figure 1.3 has been developed.

Biaxial tension tests on thin sections of ventricular myocardium (Smaill & Hunter 1991)

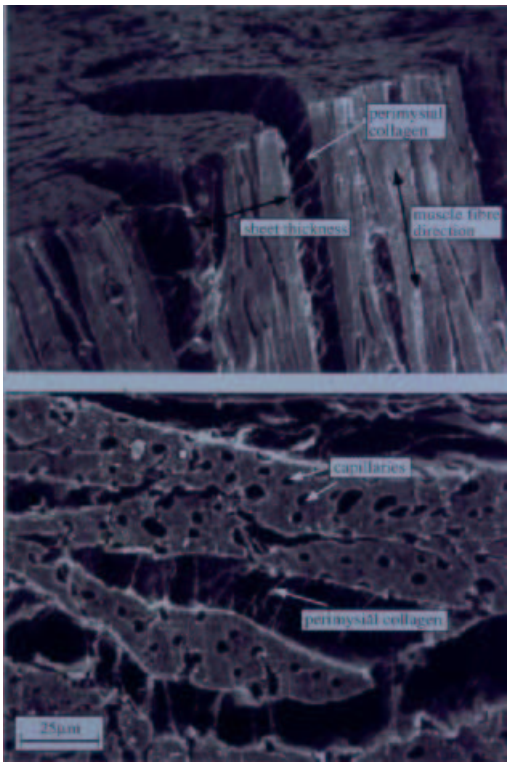

FIGURE 1.2: Top: SEM of ventricular myocardium sectioned parallel to the epicardial surface. Bottom: SEM of ventricular myocardium sectioned transverse to the myocyte axis. Capillaries and perimysial collagen can also be seen.

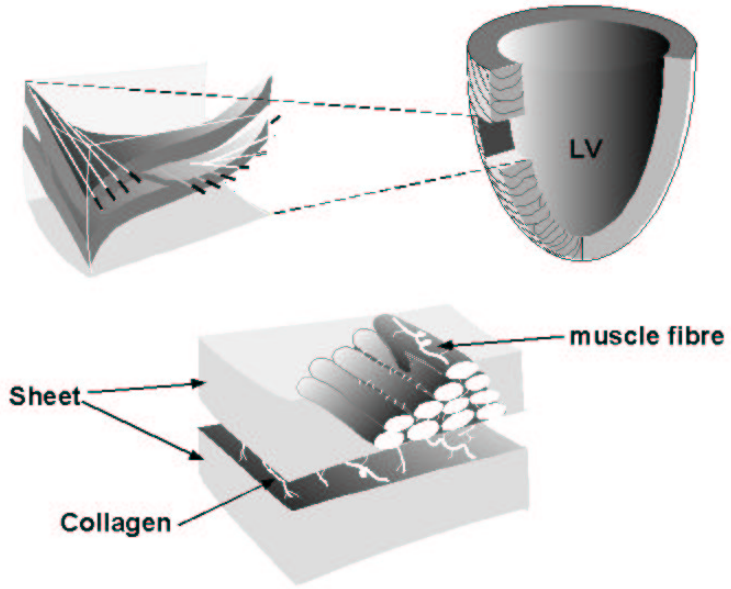

FIGURE 1.3: Schematic of myocardial microstructure illustrating the bundling of muscle fibres into sheets (Modified from LeGrice 1995).

have revealed highly nonlinear, anisotropic stress-strain behaviour which is typical of most soft biological tissues. The stress-strain properties along each of the microstructurally relevant directions are quite different, reflecting in part the organisation of collagen relative to these three axis. Figure 1.4 schematically summarises the typical stress-strain behaviour of myocardium when stretched along each of the three microstructural axes. The important feature of the response is the different limiting strain for elastic behaviour between each of the three axes.

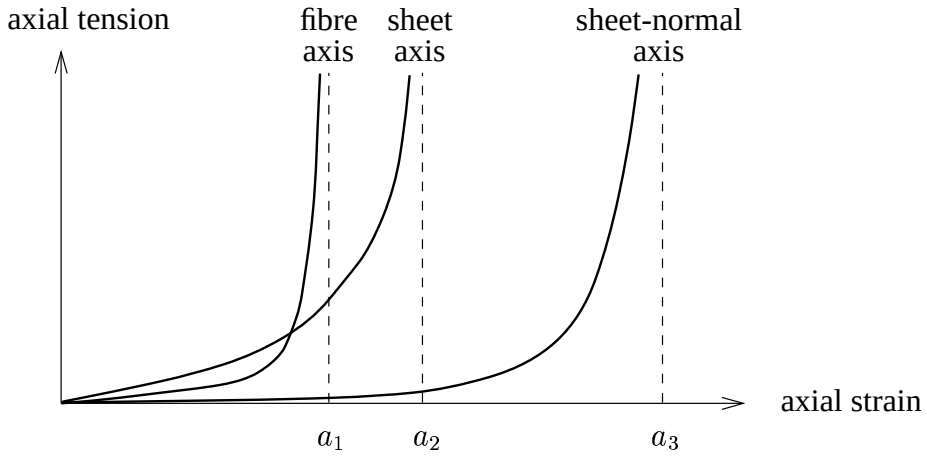

FIGURE 1.4: Typical nonlinear stress-strain response of ventricular myocardium. Note the highly nonlinear behaviour as the elastic limits are approached.

When the tissue is stretched along the fibre direction the limiting extension ratio is about 1.3, relative to a resting sarcomere length of approximately 1.95 μm for the unloaded muscle. The limiting extension ratio for the sheet axis is approximately 1.5. When stretched in the sheet normal direction very little tension is developed below an extension ratio of 1.5, but increases rapidly above this and irreversible damage is occurs when this ratio exceeds about 1.7 (Hunter, Nash & Sands 1997).

Variations in the axial limiting strains can be explained by the organisation of the extracellular connective tissue matrix. The high fibre stiffness is probably due to intracellular titin protein together with the tightly bound endomysial collagen coils that surround individual myocytes (Robinson, Geraci, Sonnenblick & Factor 1988*a*). As the tissue is stretched along the fibre axis, these coils straighten and it is the taut length of the collagen that determines the limiting strain (MacKenna, Omens & Covell 1996, MacKenna, Omens, McCulloch & Covell 1994). In contrast the relatively low sheet-normal stiffness is most likely to be due to the sparse array of perimysial collagen links in the

cleavage planes between myocardial sheets (LeGrice, Smaill, Chai, Edgar, Gavin & Hunter 1995).

Residual Strain and Stress in the Ventricular Wall

The ventricular wall in the absence of external loads is not completely stress free. Omens & Fung (1990) demonstrated this by radially cutting an equatorial cross-sectional ring, and observing how it sprang open into an arc when the so-called *residual stress* was relieved. Several studies suggest that the residual stresses give rise to more uniform transmural distributions of end-diastolic myocardial stress (Guccione, McCulloch & Waldman 1991, Nevo & Lanir 1994, Rodriguez, Omens, Waldman & McCulloch 1993). Although, during systole, Guccione, Costa & McCulloch (1995) found that the residual stresses were negligible compared to the large stresses produced by the contraction mechanisms, Rodriguez et al. (1993) concluded that residual stress may significantly impact systolic function by affecting end-diastolic sarcomere length and the subsequent force of active contraction.

1.1.3 Cardiac Function

The heart contains a unique electrical conduction system which provides a coordinated rhythmical electrical wavefront though the myocardium. At the wavefront each muscle cell is excited in turn, generating contractile forces. Activation normally begins spontaneously in the pacemaker cells of the *sinoatrial (SA) node*, which lies between the vena cava and the right atrium (see Figure 1.1). From the SA node, the activation wave spreads firstly though the RA followed by the LA causing them to contract and pump blood into their respective ventricles, before collecting at the *atrioventricular (AV) node*. The AV node is the only electrical pathway between the atria and the ventricles, it conducts slowly allowing enough time for the atrial blood to be pumped into the ventricles prior to ventricular contraction. The ventricular myocardium is activated via the *AV bundle* (otherwise known as the *common bundle*, or *bundle of His*), which bifurcates into *left* and right *bundle branches* at the top of the interventricular septum. Both branches travel down the septum and curl around the apical regions of their respective ventricles. From there the bundles divide into networks of fast conducting Pukinje fibres, which spread over and deliver the electrical impulse to the inner surface of the ventricles, the

endocardium. The activation wavefront then travels to the outer myocardium, the *epicardium*.

In terms of mechanical function the cardiac cycle has two major phases, *ventricular systole* which is the period of contraction, and *ventricular diastole* in which the heart relaxes and fills again ready for the next cycle. The Wiggers diagram in Figure 1.5 illustrates the relationship between the activation wavefront and the phases of the cardiac cycle. At the start of systole the ventricular pressure begins to rise due to atrial contraction. Following atrial contraction the mitral and aortic valves close, preventing any change in blood volume in the ventricles. The activation wavefront propagates though the ventricular myocardium causing the cells to produce contractile force which increases the ventricular pressure. This phase is referred to the as the *isovolumic contraction* phase and ends when the ventricular pressure exceeds that in the arteries and the aortic and pulmonary valves open. The following sytolic phase is called *rapid ejection* as the blood surges with an abrupt decrease in ventricular volume. After the rapid ejection phase there is a longer period of *reduced ejection* as the aortic pressure declines. The remaining systolic interval is called *protodiastole* which ends with the closure of the semilunar valves.

Following systole, the diastolic phase begins with a period of *isovolumic relaxation*, during which ventricular pressure decreases. The atrioventricular valves open when the ventricular pressure falls below the atrial pressure, and results in the *rapid filling phase* during which the ventricular walls rebound elastically from their contracted and compressed state. This is closely followed by the slow filling phase known as *diastasis*, corresponding to a gradual increase in atrial and ventricular pressures. The final phase of ventricular diastole coincides with atrial systole, which gives a final surge of blood into the ventricles before the atrioventricular valves close.

1.2 Myocardial Infarction

The heart also requires its own continuous supply of blood for oxygen and metabolic fuel (West 1985), which is delivered by the coronary arteries. *Occlusion* or obstruction of a coronary artery causes impaired function in the region supplied by that vessel within seconds. Occlusion is often caused by coronary artery disease in which cholesterol forms deposits inside the arteries of the heart (Menotti & Lanti 2003). After 15

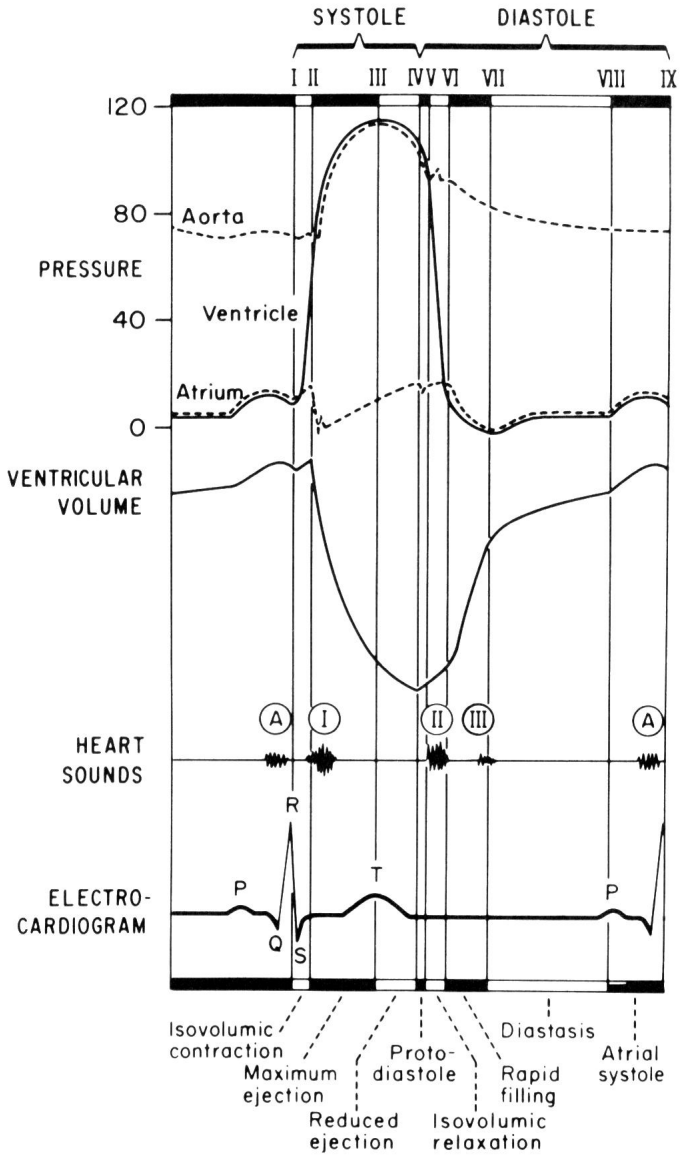

FIGURE 1.5: Wiggers diagram illustrating the eight primary phases of the cardiac cycle. The top three traces show the pressure in the aorta, LV and atria in millimetres of mercury. The following trace represents the LV volume. The lower two traces indicate the relative timings of the sounds heard via a stethoscope, and an ECG trace. The Wiggers diagram illustrates the relationship between the electrical wave in the myocardium, the resultant mechanical deformation and the consequential change in pressure in the heart chambers. Reproduced from Katz (1992).

minutes permanent damage, or *myocardial infarction* begins. Approximately 1.5 million people experience myocardial infarction in the Unites States each year (American Heart Association 2002). Of those, more than a third die, accounting for one quarter of all deaths in that country. Sixty percent of patients die within the first hour, usually before reaching hospital. Their deaths are usually because the myocardial infarct has interrupted the normal coordinated electrical activation of the heart muscle. The uncoordinated electrical activations, called *arrhythmias,* can generally be controlled once the patient is hospitalised. Mechanical rupture of the wound is the leading cause of in-hospital mortality.

If the patient is fortunate enough to survive the initial event, their long term chances of survival depend on the healing of the infarct and the remodelling of both the infarct and the remaining myocardium.

In the days and weeks following myocardial infarction the damaged area undergoes *necrosis,* the death and removal of muscle cells, followed by *fibrosis,* the building of collagen fibres. The collagen content increases steadily for six weeks or more. During the remodelling process the size of the infarct may increase or decrease. Local stretching and thinning of an infarct increases the surface area of the wound contributing to both cardiac rupture and to overall dilation of the left ventricle. Progressive decreases in the size of infarcts have also been reported, indicating that scar contraction may occur similar to that observed in healing skin(Fishbein, Maclean & Maroko 1978).

Once the myocardial tissue is damaged, the contractile function is permanently impaired (Akaishi, Weintraub, Schneider, Klein, Agarwal & Helfant 1986). The key structural component of the infarcted region, collagen, is a very stiff protein(Fung 1981). Hence the increase of collagen within an infarct results in the infarct being passively stiffer along the collagen fibre directions than the surrounding myocardium (Holmes 1995).

1.3 CMISS

The numerical methods developed for this thesis were implemented within the CMISS software package. CMISS is the product of 30 years of collective work by bioengineering researchers and their graduate students at the University of Auckland. CMISS is a modular mathematical modelling environment that includes finite element, boundary el-

ement, collocation methods and visualisation modules. The name CMISS is an acronym for Continuum Mechanics, Image analysis, Signal processing and System identification.

The computational kernel of CMISS is written primarily in Fortran and the visualisation module in C. The CMISS command language module is a Perl interpreter. CMISS currently runs on many platforms including SGI's Irix, IBM's Aix, Sun's Solaris, HP/-Compaq's Tru64 and Linux on the x86 and ARM41 architectures. The development work for this thesis was completed on an SGI 02, the computational work was carried out on SGI Origin 3400 and IBM pSeries 690 multiprocessor supercomputers. Examples of the CMISS command and input files are included in Appendices B and C. CMISS is currently available free for academic use from `www.cmiss.org`. The data and input files required to complete the simulations performed in this thesis are also available from that site.

Within the period of this work, simulations were performed on several generations of computers from different vendors. Since these machines are not directly comparable, neither are the computational times taken for different tasks completed on different machines. Therefore the timing information within this thesis is presented together with the machine used to indicate the computational magnitude of the task.

1.4 Experimental Work

The Auckland University Bioengineering Institute includes members of, and works closely with, the Department of Physiology at the University of Auckland's School of Medicine. The surgical and experimental work detailed here was performed in the Department of Physiology by Dr Ian LeGrice and co-workers with the approval of the University of Auckland Animal Ethics Committee.

Chapter 2

Finite Deformation Elasticity

Continuum mechanics deals with the movement of materials when subjected to applied forces. The motion of a continuous and deformable solid can be described by a continuous displacement field resulting from a set of forces acting on the solid body. In general, the displacements and forces may vary continuously with time, but for the present purpose a two-state quasi-static analysis will be discussed. The initial unloaded state of the material is referred to as the *reference* or *undeformed* state as the displacements are zero everywhere. The material then reconfigures due to applied loads and reaches an equilibrium state referred to as the *deformed* state. The concepts of *strain*, a measure of length change or displacement gradient, and *stress*, the force per unit area on an infinitesimally small plane surface within the material, are of fundamental importance for finite deformation elasticity theory.

The equations that govern the motion of deformable materials can be derived in the following four steps.

1. **Kinematic relations**, which define the components of the strain tensor in terms of displacement gradients, and, for incompressible materials, define the incompressibility constraint.

2. **Stress equilibrium**, or equations of motion derived from the laws of conservation of linear momentum and conservation of angular momentum

3. **Constitutive relations**, which express the relationship between stress and strain

and must be established from experimental measurement, subject to certain theoretical restrictions.

4. **Boundary conditions**, which specify the external loads or displacement constraints acting on the deforming body.

The first two steps define relationships which hold for all materials and will be detailed in Sections 2.1 and 2.2, respectively. The third step is concerned with relations determined experimentally for a particular material and is explained in Section 2.3. The application of boundary constraints is introduced in Section 2.4 and will be dealt with further in Chapter 3, which describes the solution of the governing equations. In the first instance equations and quantities of interest are referred to rectangular cartesian coordinates. It is often convenient, however, to utilise other systems of coordinates. Section 2.5 extends the theory to refer to general curvilinear coordinates.

2.1 Kinematic relations

The key to analysing strain in a material undergoing large displacements and deformation is to establish two coordinate systems and the relationship between them. The first is a material coordinate system to effectively tag individual particles in the body. The second is a fixed spatial coordinate system. Deformation is quantified by expressing the spatial coordinates of a material particle in the deformed state, as a function of the coordinates of the same particle in the undeformed state. Length changes of material segments can then be determined from the known deformation fields and thus strain tensors may be calculated.

2.1.1 Material versus spatial coordinates

Deformation is defined by the movement of *material particle*s, which can be thought of as small non-overlapping quantities of material that occupy unique points within the undeformed body. For this reason a method of labelling the particles is required. One convenient method is to define each material particle, $\mathbf{X}$, by a set of rectangular cartesian coordinates, $(X_1 X_2 X_3)$, in the undeformed body. As the body deforms the coordinate

axes deform with it and so orthogonal coordinate axes in the undeformed state will not in general be orthogonal in the deformed configuration. These coordinates are referred to as *material (or Lagrangian) coordinate*s because as the body deforms, a unique material particle is always identified by the same coordinate values.

Each point in space may be defined by a set of *spatial (or Eulerian) coordinates* relative to a fixed reference cartesian coordinate system. A particular spatial point, $\mathbf{x}$, with coordinates, $(x_1 x_2 x_3)$, may identify different material particles as they pass through the point, $\mathbf{x}$, during the deformation. Conversely, a fixed material particle, $\mathbf{X}$, may move to several spatial positions during the deformation. It should be noted that the material coordinates, $\mathbf{X}$, may be chosen to coincide with the rectangular cartesian spatial coordinates, $\mathbf{x}$, in the undeformed state.

2.1.2 Deformation and strain

To quantify the deformation of a material it is necessary to consider the change in length of *material segments*, or sets of adjacent material particles within the body. In Figure 2.1, an infinitesimal material line segment, $d\mathbf{X}$, in the undeformed body, B_0, has components dX^1, dX^2 and dX^3 with respect to global rectangular cartesian coordinates (Y_1, Y_2, Y_3). In the deformed body, B, the same material particles that constituted $d\mathbf{X}$ have reconfigured (due to applied loads) into $d\mathbf{x}$, which has components dx^1, dx^2 and dx^3 with respect to (Y_1, Y_2, Y_3). The deformation is quantified by the *deformation gradient tensor*, which carries the line segment, $d\mathbf{X}$, into $d\mathbf{x} = \mathbf{F}d\mathbf{X}$, or in component form,

$dx^i = F^i_M dX^M$. The deformation gradients are defined in Equation 2.1.

$$F^i_M = \frac{\partial x_i}{\partial X_m} \tag{2.1}$$

Any deformation can be split into two parts: a rigid body rotation and a stretch. This *polar decomposition* can be represented mathematically by considering the deformation gradient tensor to be a product, $\mathbf{F} = \mathbf{RU}$, of an orthogonal *rotation tensor*, $\mathbf{R}$, and a symmetric positive definite *stretch tensor*, $\mathbf{U}$. Thus the undeformed line segment components dX^M are stretched into $dy^L = U^L_M dX^M$ before being rotated into $dx^i =$

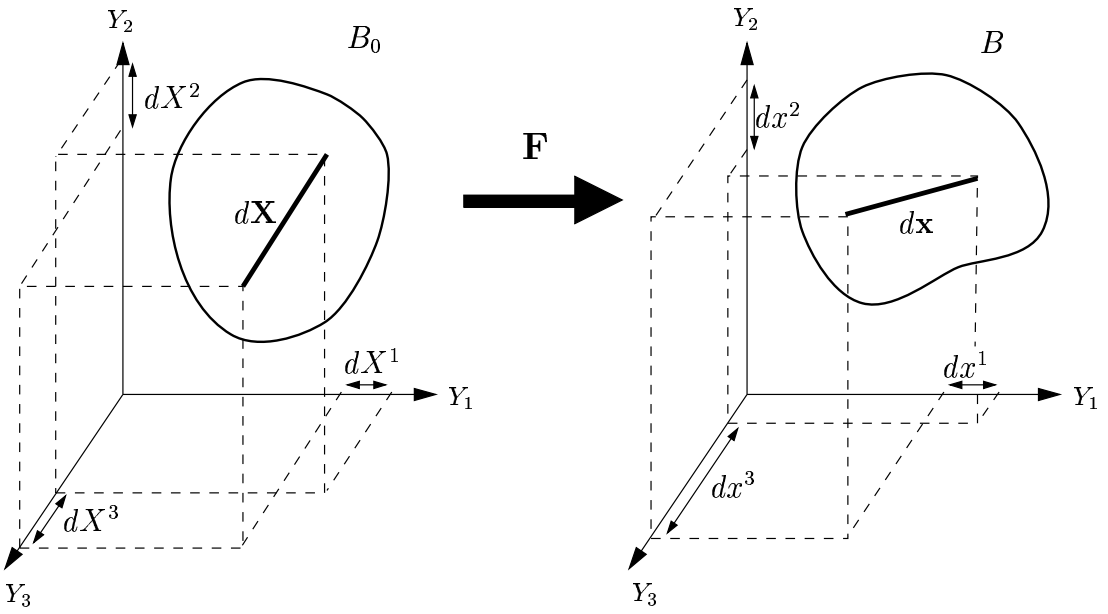

FIGURE 2.1: The deformation gradient tensor, $\mathbf{F}$ carries line segment $d\mathbf{X}$ into $d\mathbf{x}$.

$R^i_L dy^L$. Equivalently the line segment could be rotated first and then stretched, but for the present purpose it is more convenient to interpret the stretch in terms of material coordinates and then relate the stretched material lines to the spatial coordinates through the rotation tensor, $\mathbf{R}$. For further details on polar decomposition refer to (Atkin & Fox 1980, Sec. 1.4) or (Spencer 1980, Sec. 2.5). It is important to note here that the stretch tensor, $\mathbf{U}$, contains a complete description of the material strain, independent of any rigid body motion.

Strain in a deforming body is determined by measuring segment length changes. Equation 2.2 uses Pythagoras to determine the arc length of the deformed segment $d\mathbf{x}$.

$$ds^2 = dx^i dx^i = d\mathbf{x}^T d\mathbf{x} = (\mathbf{F}d\mathbf{X})^T \mathbf{F}d\mathbf{X} = d\mathbf{X}^T \mathbf{F}^T \mathbf{F} d\mathbf{X} = d\mathbf{X}^T \mathbf{C} d\mathbf{X} \tag{2.2}$$

where

$$\mathbf{C} = \mathbf{F}^T \mathbf{F} = \left\{ \frac{\partial x_k}{\partial X_M} \frac{\partial x_k}{\partial X_N} \right\} \tag{2.3}$$

Equation 2.3 defines *Green's deformation tensor* or the *right Cauchy-Green deforma-*

tion tensor[1] (Atkin & Fox 1980, p. 12), which indicates how each component of the undeformed line segment $d\mathbf{X}$ contributes to the squared length of the deformed line segment $d\mathbf{x}$. The deformation tensor $\mathbf{C}$ is related to the stretch tensor $\mathbf{U}$ in Equation 2.4 using the polar decomposition theorem.

$$\mathbf{C} = \mathbf{F}^T\mathbf{F} = (\mathbf{RU})^T\mathbf{RU} = \mathbf{U}^T\mathbf{R}^T\mathbf{RU} = \mathbf{U}^T\mathbf{U} = \mathbf{U}^2 \tag{2.4}$$

since $\mathbf{R}$ is orthogonal $(\mathbf{R}^T = \mathbf{R}^{-1})$ and $\mathbf{U}$ is symmetric. Note that like $\mathbf{U}$, $\mathbf{C}$ is symmetric and positive definite and that both $\mathbf{U}$and $\mathbf{C}$ are expressed in terms of material coordinates.

One method for computing the stretch tensor $\mathbf{U}$ from the deformation gradient tensor $\mathbf{F}$ is to first calculate $\mathbf{C} = \mathbf{F}^T\mathbf{F}$, then calculate the eigenvalues $(\lambda_1)^2$, $(\lambda_2)^2$ and $(\lambda_3)^2$, and orthogonal eigenvectors $\mathbf{s}_1$, $\mathbf{s}_2$ and $\mathbf{s}_3$ of $\mathbf{C}$ using a similarity transformation (Fox 1967, p. 239). $\mathbf{U}$ may then be constructed using 2.5.

$$\mathbf{C} = \Omega\Lambda^2\Omega^T = \Omega \begin{bmatrix} (\lambda_1)^2 & 0 & 0 \\ 0 & (\lambda_2)^2 & 0 \\ 0 & 0 & (\lambda_3)^2 \end{bmatrix} \Omega^T \quad \mathbf{U} = \Omega\Lambda\Omega^T = \Omega \begin{bmatrix} \lambda_1 & 0 & 0 \\ 0 & \lambda_2 & 0 \\ 0 & 0 & \lambda_3 \end{bmatrix} \Omega^T \tag{2.5}$$

where the columns of Ω are the orthonormal eigenvectors of $\mathbf{C}$ and are the *principal axes of stretch*, and λ_i are the *principal stretches* (there are no shear terms when the deformation is referred to the principal axes). Note that since $\mathbf{C}$ is a real symmetric matrix, the eigenvectors are orthogonal and therefore Ω is an orthogonal matrix, $\left(\Omega^T\Omega = \mathbf{I}\right)$. In essence, the similarity transformation diagonalises $\mathbf{C}$ and the positive square root of the resulting diagonal matrix is used to compute the stretch tensor $\mathbf{U}$.

The two orthogonal tensors $\mathbf{R}$ and Ω, derived from $\mathbf{F}$, have quite different physical interpretations. $\mathbf{R}$ describes the rigid body rotation component of the deformation with no information about the material stretching. On the other hand, the columns of Ω are the orientations of the principal stretch axes *relative to the material coordinates*.

In three-dimensions the deformation tensor is a 3×3 matrix. There are three invariants (scalar combinations of the components of $\mathbf{C}$, which remain unchanged under coordi-

[1]The *left Cauchy-Green deformation tensor* $\mathbf{B} = \mathbf{F}\mathbf{F}^T$ is also defined, but is not useful here since it is not independent of rigid body rotation.

nate rotations at a given state of deformation. These principal invariants are given in Equation 2.6 (see (Atkin & Fox 1980, Sec. 1.4)).

$$I_1 = \mathrm{tr}\mathbf{C} \qquad I_2 = \frac{1}{2}\left[(\mathrm{tr}\mathbf{C})^2 - \mathrm{tr}\mathbf{C}^2\right] \qquad I_3 = \mathrm{det}\mathbf{C} \tag{2.6}$$

where the trace of $\mathbf{C}$, denoted by $\mathrm{tr}\mathbf{C}$, is the sum of the diagonal terms, $\mathbf{C}_{MM}$, and the determinant of $\mathbf{C}$, $\mathrm{det}\mathbf{C}$, is a measure of volume change.

The similarity transformation of 2.5 may be used to express the invariants of $\mathbf{C}$ in terms of the principal stretch ratios as in Equation 2.7.

$$\begin{aligned} I_1 &= (\lambda_1)^2 + (\lambda_1)^2 + (\lambda_3)^2 \\ I_2 &= (\lambda_1)^2 (\lambda_2)^2 + (\lambda_2)^2 (\lambda_3)^2 + (\lambda_3)^2 (\lambda_1)^2 \\ I_3 &= (\lambda_1)^2 (\lambda_2)^2 (\lambda_3)^2 \end{aligned} \tag{2.7}$$

Equation 2.8 is the additional kinematic constraint that must be imposed on the deformation field for incompressible materials. This is discussed further in Section 2.3.

$$\mathrm{det}\mathbf{C} = I_3 = (\lambda_1\lambda_2\lambda_3)^2 = 1 \tag{2.8}$$

Equation 2.9 shows how the Lagrangian *Green's strain tensor*, with respect to rectangular cartesian coordinates, is related to the right Cauchy-Green deformation tensor (Spencer 1980, p. 72).

$$\mathbf{E} = \frac{1}{2}(\mathbf{C} - \mathbf{I}) \tag{2.9}$$

2.2 Stress equilibrium

Having established the kinematic framework for finite deformation analysis, the next step is to consider the governing force and momentum balances which follow from Newton's laws of motion. In order to apply these equations to materials which undergo large deformations, it is necessary to define stress tensors and the way they enter into the governing equations.

2.2.1 Stress tensors

Stress is defined as the force per unit area acting on an infinitesimally small plane surface. If the line of action of the force is normal to the plane then a *normal* or *axial* stress results, whereas a *shear* stress arises when the line of action of the force is tangential to the plane. The quantities of force and area can be referred either to the reference (undeformed) or deformed configurations, which leads to three important ways of representing stress in a deforming body, namely using the Cauchy, first or second Piola-Kirchoff stress tensors. Refer to Malvern (1969, p. 220) for a more complete explanation.

1. **The Cauchy stress tensor**, denoted σ^{ij}, represents the force measured per unit deformed area acting on an element of surface in the deformed configuration. The first index indicates the direction of the normal to the surface on which σ^{ij} acts and the second index indicates the direction of the stress component. It should be noted that the Cauchy stress tensor is symmetric for non-polar materials (see Section 2.2.2) and that in rectangular cartesian coordinates, σ^{ij} are also the physical components of stress.

2. **The first Piola-Kirchhoff stress tensor**, denoted s^{Mj}, represents the force acting on an element of surface in the deformed configuration but measured per unit undeformed area. The first index is written in uppercase as it refers to the normal of the surface in the undeformed state, and is thus a material coordinate index. The second index denotes the direction of the force acting on the deformed material, and is a spatial coordinate index. For this reason the first Piola-Kirchhoff stress tensor is generally not symmetric. It is sometimes referred to as the Lagrangian stress tensor and is often used in experimental testing where force is measured in the deformed tissue, but the area over which it acts is measured in the undeformed tissue.

3. **The second Piola-Kirchhoff stress tensor**, denoted T^{MN}, represents the force measured per unit undeformed area, $\mathbf{P}$, acting on an element of surface in the undeformed configuration. This force may be determined from the actual force, $\mathbf{p}$, in the same way that the undeformed material vector, $d\mathbf{X}$, is determined from the deformed material vector, $d\mathbf{x}$. Specifically $\mathbf{P} = \mathbf{F}^{-1}\mathbf{p}$ just as $d\mathbf{X} = \mathbf{F}^{-1}d\mathbf{x}$ (Malvern 1969, p. 222). The primary use of the second Piola-Kirchhoff stress

tensor is for representing material behaviour at a point, independent of rigid body motion. This is discussed further in Section 2.3, which describes relationships between stress and strain tensors at a point. The main idea here is that the second Piola-Kirchhoff stress tensor is defined solely in terms of material coordinates, just as for Green's strain tensor. Note that the second Piola-Kirchhoff stresses must be transformed into first Piola-Kirchhoff stresses for use in the equilibrium equations, which require a spatial frame of reference.

Equations 2.10 and 2.11 define the relationships between the second Piola-Kirchhoff, first Piola-Kirchhoff and Cauchy stress tensors.

$$\begin{aligned} \mathbf{S} = J\mathbf{F}^{-1}\Sigma \qquad \mathbf{T} = \mathbf{S}\left(\mathbf{F}^T\right)^{-1} &= J\mathbf{F}^{-1}\Sigma\left(\mathbf{F}^T\right)^{-1} \\ s^{Mj} = J\frac{\partial X_M}{\partial x_j}\sigma^{ij} \qquad T^{MN} = s^{Mj}\frac{\partial X_N}{\partial x_j} &= J\frac{\partial X_M}{\partial x_i}\sigma^{ij}\frac{\partial X_N}{\partial x_j} \end{aligned} \tag{2.10}$$

or inversely

$$\begin{aligned} \mathbf{S} = \mathbf{T}\mathbf{F}^T \qquad \Sigma = \tfrac{1}{J}\mathbf{F}\mathbf{S} \qquad &= \frac{1}{J}\mathbf{F}\mathbf{T}\mathbf{F}^T \\ s^{Mj} = T^{MN}\frac{\partial x_j}{\partial X_N} \quad \sigma^{ij} = \tfrac{1}{J}\tfrac{\partial x_i}{\partial X_M}s^{MJ} \quad &= \frac{1}{J}\frac{\partial x_i}{\partial X_M}T^{MN}\frac{\partial x_j}{\partial X_N} \end{aligned} \tag{2.11}$$

where J is the Jacobian of the transformation from reference to deformed coordinates, defined in Equation 2.12. Note from Equation 2.12 that the second Piola-Kirchhoff stress tensor is symmetric whenever the Cauchy stress tensor is symmetric.-

$$J = \mathrm{det}\mathbf{F} = \sqrt{I_3} = \lambda_1\lambda_2\lambda_3 \tag{2.12}$$

2.2.2 Conservation laws and the principle of virtual work

Conservation of mass

The conservation of mass principle relates the mass densities in the undeformed and deformed bodies (denoted by ρ_0 and ρ, respectively) given in Equation 2.13 (Oden 1972,

p. 15).

$$\int_{V_0} \rho_0 dV_{0=} \int_V \rho dV = \int_{V_0} \rho J dV_0 \tag{2.13}$$

Thus for arbitrary volumes, mass density for the undeformed and deformed bodies are related using Equation 2.14.

$$\rho_0 = J\rho = \sqrt{I_3}\rho \tag{2.14}$$

Conservation of linear momentum

Following Malvern (1969, Sec. 5.3), for a given set of particles, the time rate of change of the total linear momentum equates to the vector sum of all the external forces acting on the particles of the set. This is expressed mathematically in Equation 2.15, where $\mathbf{t}$ is the traction vector (external surface forces per unit area), $\mathbf{b}$ represents the body forces (per unit mass), and the rate of change of momentum is written in terms of the material derivative (d/dt) and the velocity vector $\mathbf{v}$.

$$\int_S \mathbf{t} dS + \int_V \rho \mathbf{b} dV = \frac{\mathrm{d}}{\mathrm{d}t} \int_V \rho \mathbf{v} dV \tag{2.15}$$

Cauchy's formula, defined in Equation 2.16, projects the components of a stress vector $\mathbf{t}$ (the force per unit area acting on some deformed surface dS, with unit normal $\hat{\mathbf{n}} = \hat{n}_j \mathbf{i}_j$) onto the set of orthogonal base vectors for the rectangular cartesian reference coordinate system, $\mathbf{i}_j$.

$$\mathbf{t} dS = \sigma^{ij} n_i \mathbf{i}_j dS \tag{2.16}$$

where σ^{ij} are components of the Cauchy stress tensor and are physical stresses, since $\mathbf{i}_j$ are unit vectors.

Cauchy's formula is substituted into Equation 2.15 to form Equation 2.17, which is appropriate for a material with constant density. Note that Equation 2.17 is written in component form where the body force and velocity vectors have components $\mathbf{b} = b^j \mathbf{i_j}$

and $\mathbf{v} = v^j \mathbf{i_j}$, respectively.

$$\int_S \sigma^{ij} \hat{n}_i dS + \int_V \rho \left(b^j - \frac{\mathrm{d}v^j}{\mathrm{d}t} \right) dV = 0 \tag{2.17}$$

Applying the divergence theorem to Equation 2.17 yields Equation 2.18.

$$\int_V \left[\frac{\partial \sigma^{ij}}{\partial x_i} + \rho b^j - \rho f^j \right] dV = 0 \tag{2.18}$$

where $f^j = \frac{\mathrm{d}v^j}{\mathrm{d}t}$ are components of the acceleration vector.

If Equation 2.18 is to be valid for arbitrary volumes the integrand must vanish (it is assumed here that the integrand is continuous). This results in Equation 2.19, which is the component form of *Cauchy's first law of motion* for rectangular cartesian coordinates.

$$\frac{\partial \sigma^{ij}}{\partial x_i} + \rho b^j = \rho f^j \tag{2.19}$$

It is often convenient to express Cauchy's first law of motion in terms of the second Piola-Kirchhoff stress components as in Equation 2.20. This can be determined by substituting Equations 2.11 and 2.14 into Equation 2.19 and assuming that there are no spatial gradients of density. Note that the term in parenthesis is simply the first Piola-Kirchhoff stress, s^{Mj}.

$$\frac{\partial}{\partial X_m} \left(T^{MN} \frac{\partial x_j}{\partial X_N} \right) + \rho_0 b^j = \rho_0 f^j \tag{2.20}$$

For static equilibrium of the material, important in solid mechanics, the right-hand-side acceleration term in Equation 2.19 vanishes, and in the absence of body forces this relation reduces to the statement of stress equilibrium in Equation 2.21 for rectangular cartesian coordinates.

$$\frac{\partial \sigma^{ij}}{\partial x_i} = 0 \qquad \text{or} \qquad \frac{\partial}{\partial X_M} \left(T^{MN} \frac{\partial x_j}{\partial X_N} \right) = 0 \tag{2.21}$$

Conservation of angular momentum

The conservation of angular momentum equates the time rate of change of the total angular momentum for a set of particles to the vector sum of the moments of the external forces acting on the system. For stress equilibrium of non-polar materials, this principle is equivalent to the symmetry condition on the Cauchy stress tensor, namely $\sigma^{ij} = \sigma^{ji}$ (see Malvern (1969, Sec. 5.3) or Spencer (1980, Sec. 7.5) for a full derivation). Note that if the Cauchy stress tensor is symmetric (as is the case for the non-polar materials being considered here), the second Piola-Kirchhoff stress tensor is also symmetric as a direct consequence of Equation 2.10. This implies that there are only six independent components of stress — three normal components and three shear components.

Principle of virtual work

Now consider a body of volume V and surface S loaded by a surface traction $\mathbf{s}$ which is in equilibrium with the internal stress vector $\mathbf{t}$. If the body is subjected to an arbitrarily small displacement $\delta\mathbf{v}$, which satisfies compatibility and any displacement boundary conditions specified on S (where $\delta\mathbf{v}$ must be zero), then the principle of virtual work can be expressed in the form of Equation 2.22 (see Malvern (1969, Sec. 5.5) or Marsden & Hughes (1983, p. 168)).

$$\int_{S_2} \mathbf{s} \cdot \delta\mathbf{v} dS = \int_{S} \mathbf{t} \cdot \delta\mathbf{v} dS \tag{2.22}$$

where S_2 is the portion of the boundary that is not subjected to displacement boundary conditions.

The virtual displacements may be resolved into components $\delta\mathbf{v} = \delta v_j \mathbf{i}_j$. Cauchy's formula (Equation 2.16) is then substituted into the virtual work equation (Equation 2.22) to yield Equation 2.23.

$$\int_{S_2} \mathbf{s} \cdot \delta\mathbf{v} dS = \int_{S} \sigma^{ij} \hat{n}_i \delta v_j dS \tag{2.23}$$

The right-hand-side surface integral in Equation 2.23 is transformed into a volume inte-

gral using Gauss' theorem (Fung 1965, p. 117) to give Equation 2.24.

$$\int_{S_2} \mathbf{s} \cdot \delta\mathbf{v} dS = \int_V \left[\frac{\partial \sigma^{ij}}{\partial x_i} \delta v_j + \sigma^{ij} \frac{\partial \delta v_j}{\partial x_i} \right] dV \tag{2.24}$$

Cauchy's first law of motion (Equation 2.19) is substituted into the volume integral in Equation 2.24 to give Equation 2.25. Moreover, Equation 2.11 is used to express Equation 2.25 in terms of the second Piola-Kirchhoff stress tensor, as written in Equation 2.26.

$$\int_V \sigma^{ij} \frac{\partial \delta v_j}{\partial x_j} dV = \int_V \rho \left(b^j - f^j \right) \delta v_j dV + \int_{S_2} \mathbf{s} \cdot \delta\mathbf{v} dS \tag{2.25}$$

$$\int_V T^{MN} \frac{1}{J} \frac{\partial x_j}{\partial X_M} \frac{\partial \delta v_j}{\partial X_N} dV = \int_V \rho \left(b^j - f^j \right) \delta v_j dV + \int_{S_2} \mathbf{s} \cdot \delta\mathbf{v} dS \tag{2.26}$$

To solve the virtual work equations it is necessary to evaluate the surface integral on the right-hand-side of Equation 2.26. This is outlined in Section 2.4. The next step, however, is to express the stress components in terms of the deformation to characterise the material behaviour. This is addressed in Section 2.3 through the use of constitutive relations.

2.3 Constitutive relations

Unlike the previously described kinematic relations and stress equilibrium equations that hold for most materials, constitutive relations characterise individual materials and their response to external loads. In the context of finite deformation elasticity, constitutive equations are used to represent the behaviour of a material through empirical relationships between experimentally observed stress and strain tensors. This section will only treat constitutive equations concerned with the mechanical behaviour of materials.

There are several important considerations which should be addressed when formulating constitutive laws. Perhaps the most important is that they are robust enough to predict behaviour in various experimental situations using different samples of the same type of material. It is unreasonable, however, to expect to simulate all aspects of a material's

behaviour with one set of constitutive equations. For this reason the most important and relevant behavioural features should be identified for the particular application and it is these features that the constitutive relations should approximate. The resulting equations will be more concise, numerically efficient and thus more suitable for use in large scale computer models.

It is essential that constitutive laws are based on experiments using real materials, but certain theoretical restrictions must be observed. Firstly, constitutive equations must be independent of the choice of coordinate system, since they characterise the constitution of individual materials and not the frame of reference from which they are observed. However, they can be expressed in terms of components relative to different coordinate systems. Thus rigid-body motions should play no role in the constitutive law (this is known as the *axiom of objectivity*, see Eringen (1980, p. 163)). Mathematically, this is satisfied by postulating the existence of a strain energy function, W, to be a scalar potential that depends on the components of either the right Cauchy-Green deformation tensor or Green's strain tensor (defined in Equations 2.3 and 2.9, respectively). Components of the second Piola-Kirchhoff stress tensor are given by the derivatives of $W(\mathbf{C})$ or $W(\mathbf{E})$ with respect to the components of $\mathbf{C}$ or $\mathbf{E}$, respectively. Equation 2.27 defines the components of the second Piola-Kirchhoff stress tensor when W is expressed in terms of Green's strain components, E_{MN}, referred to X_M-material coordinates (Green & Adkins 1970, p. 6).

$$T^{MN} = \frac{1}{2}\left(\frac{\partial W}{\partial E_{MN}} + \frac{\partial W}{\partial E_{NM}}\right) \tag{2.27}$$

Material symmetry imposes further theoretical restrictions on the form of the constitutive law. Certain types of material possess no preferred direction, exhibiting rotational symmetry about all directions and reflectional symmetry with respect to all planes. These materials are *isotropic*. For isotropic materials, the strain energy is constant for all orientations of the coordinate axes, or mathematically $W(\mathbf{C}) = W(\mathbf{Q}\mathbf{C}\mathbf{Q}^T)$, where $\mathbf{Q}$ is any constant orthogonal tensor. Thus the strain energy is an invariant function of $\mathbf{C}$. It can be shown that any invariant function of $\mathbf{C}$ can be expressed as a function of the three principal invariants of $\mathbf{C}$, which are defined in Equation 2.6 (see Spencer (1980, Sec. 10.2)). This reduces the functional form of the strain energy function to $W = W(I_1, I_2, I_3)$.

For incompressible materials a further restriction on the form of the constitutive law can be imposed. In this case the additional kinematic constraint $I_3 = 1$ (Equation 2.8) is applied. Spencer (1980, p. 141) notes that it is not sufficient to set $I_3 = 1$ in the constitutive equation, since certain derivatives of W tend to infinity in the limiting case of an incompressible material. This problem is overcome by introducing an arbitrary Lagrange multiplier λ into the constitutive equation. The unspecified strain energy term $\overline{W}$ is limited to be a function of I_1, I_2 only. Thus for isotropic, incompressible materials, Equation 2.28 shows the functional form of the strain energy function.

$$W = \overline{W}\left(I_1, I_2\right) + \lambda\left(I_3 - 1\right) \tag{2.28}$$

The mechanical effect of the incompressibility condition is to give rise to a reaction stress referred to as the *hydrostatic pressure* (denoted by p), which does not contribute to the deformation of the body. In other words, the addition of a hydrostatic pressure to an incompressible elastic body indeed alters the stress, but does not in any way affect the strain energy of the material. Equation 2.28 may be substituted into Equation 2.27 and rearranged to give the components of stress with respect to X_M-material coordinates, expressed in Equation 2.29 (Spencer 1980, Sec. 10.2). Note that $\frac{\partial I_3}{\partial E_{MN}} = 2\delta^{MN}$, where δ^{MN} is the *Kronecker delta,* which is equal to one if the indices M and N are the same and zero otherwise. In addition, the arbitrary Lagrange multiplier is chosen to be $\lambda = -\frac{1}{2}p$ in the constitutive equation (Equation 2.30) to ensure that the additional component in the diagonal terms of the stress tensor is a true hydrostatic stress.

$$T^{MN} = \frac{1}{2}\left(\frac{\partial \overline{W}}{\partial E_{MN}} + \frac{\partial \overline{W}}{\partial E_{NM}}\right) - p\delta^{MN} \tag{2.29}$$

where, for isotropic, incompressible materials

$$\frac{\partial \overline{W}}{\partial E_{MN}} = \frac{\partial \overline{W}}{\partial I_1}\frac{\partial I_1}{\partial E_{MN}} + \frac{\partial \overline{W}}{\partial I_2}\frac{\partial I_2}{\partial E_{MN}} \tag{2.30}$$

A suitable form of $\overline{W}\left(I_1, I_2\right)$ must then be chosen, based on experimental observations of the material. Certain types of rubber exhibit almost isotropic behaviour and are referred to as *Mooney-Rivlin* materials. Equation 2.31 characterises this type of material using material constants (mechanical properties) c_1 and c_2 which must be estimated ex-

perimentally. A subset of the Mooney-Rivlin materials are the *Neo-Hookean* materials, which are characterised by setting $c_2 = 0$ in Equation 2.31.

$$\overline{W}(I_1, I_2) = c_1 (I_1 - 3) + c_2 (I_2 - 3) \tag{2.31}$$

Note that the use of $(I_1 - 3)$ and $(I_2 - 3)$ ensures that the strain energy is zero when the strain, $\mathbf{E}$, is zero. This is demonstrated by using Equation 2.9 to show that $\mathbf{C} = \mathbf{I}$ for zero strain, in which case Equation 2.6 reduces to $I_1 = I_2 = 3$ and $I_3 = 1$.

Alternatively a *transversely isotropic* material possesses a single preferred direction at every point. These materials exhibit rotational symmetry about the preferred axis and reflectional symmetry with respect to all planes containing this axis. Green & Adkins (1970, p. 28) have extended the above approach by allowing W to depend on the strain invariants K_1 and K_2 associated with the plane of isotropy.

A major objection to the above approaches to the formulation of constitutive equations is that the parameters bear no direct relation to the underlying structure of the material. An approach which incorporated parameters that directly reflect mechanical or structural properties of the material would potentially yield a more reliable constitutive relation. In addition, variations in material properties could be more easily understood in terms of the effect on the behaviour of the material. Section 4.4.3 details the development of a microstructurally based constitutive law for passive heart tissue.

2.4 Boundary constraints and surface tractions

All terms in Equation 2.26 have now been defined apart from the right-hand-side integral involving the surface traction vector $\mathbf{s}$. If external surface pressures are applied, this integral must be evaluated for those portions of the boundary that sustain the loads. In the absence of boundary pressures this term vanishes.

Consider a deforming surface, with unit normal $\hat{\mathbf{n}} = \hat{n}_j \mathbf{i}_j$. If the surface is loaded by a pressure, $p_{(appl)}$ (a physical stress), then the surface traction vector has components $\mathbf{s} = p_{(appl)} \hat{n}_j \mathbf{i}_j$ and the right-hand-side surface integral of Equation 2.26 is evaluated

using Equation 2.32.

$$\int_{S_2} \mathbf{s} \cdot \delta\mathbf{v} dS = \int_{S_2} p_{(appl)} \hat{n}_j \delta v_j dS \tag{2.32}$$

This surface integral is then substituted into Equation 2.26 to yield the governing equations for finite deformation elasticity with respect to rectangular cartesian coordinates given in Equation 2.33.

$$\int_V T^{MN} \frac{1}{J} \frac{\partial x_j}{\partial X_m} \frac{\partial \delta v_j}{\partial X_N} dV = \int_V \rho \left(b^j - f^j \right) \delta v_j dV + \int_{S_2} p_{(appl)} \hat{n}_j \delta v_j dS \tag{2.33}$$

It then remains to solve Equation 2.33 in terms of the unknown virtual displacements δv_j, subject to any displacement boundary conditions. For geometrically simple bodies with straight-forward material behaviour, Equation 2.33 can be used in its present form. However, for more complex shapes and material laws it is often convenient to take advantage of different coordinate systems. Section 2.5 details how the quantities and governing equations that have been defined thus far may be generalised for curvilinear coordinate systems.

2.5 Curvilinear coordinate systems

A material point may be represented by coordinates with respect to a general curvilinear coordinate system. These coordinates are related to the reference rectangular cartesian coordinates using a set of *base vectors* which are unique to the particular curvilinear coordinate system. Tensor quantities such as strain and stress can be transformed to refer to the new system of coordinates using *metric tensors*, which are defined by inner products of base vectors and represent measures of the physical lengths of coordinate increments. Base vectors and metric tensors can thus be used to express the governing equilibrium equations with respect to a general set of curvilinear coordinates.

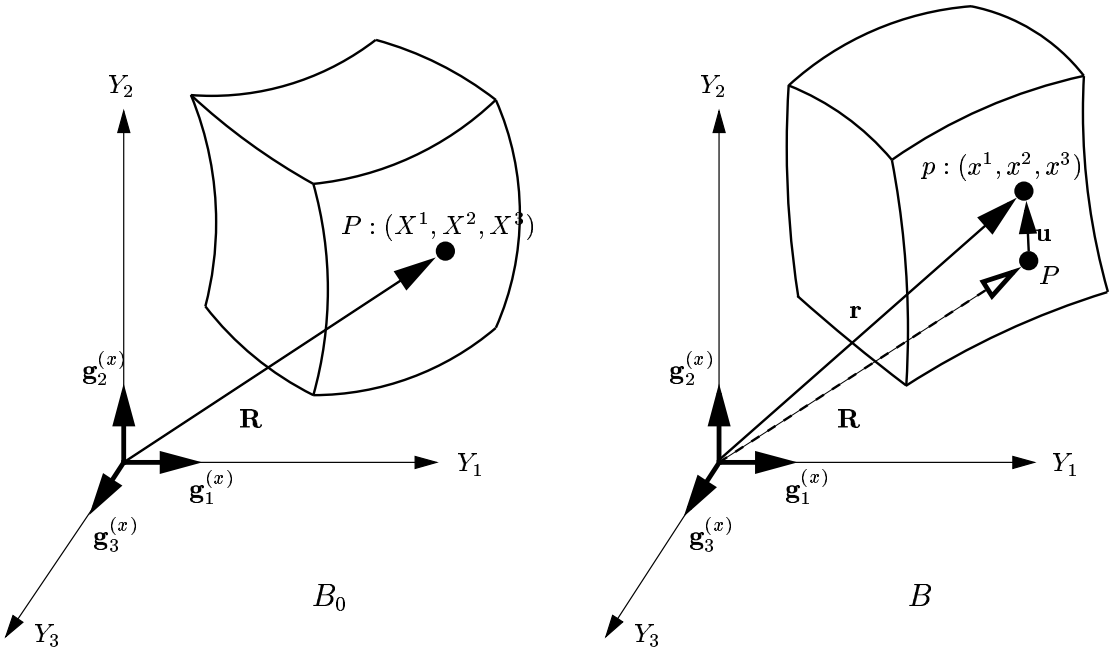

FIGURE 2.2: Coordinate systems used in a kinematic analysis of large deformation elasticity.

2.5.1 Base vectors and metric tensors

In Figure 2.2 a set of reference rectangular cartesian coordinates (x^1, x^2, x^3) define the position of a *material point* p, with position vector $\mathbf{r} = x^i \mathbf{g}_i^{(x)}$, in the deformed body B. $\mathbf{g}_i^{(x)} = \mathbf{i}_i$ are the unit base vectors for the rectangular cartesian coordinate system (Y_1, Y_2, Y_3). In the undeformed configuration B_0, (X^1, X^2, X^3) are the reference rectangular cartesian coordinates of the same material point P with position vector $\mathbf{R} = X^i \mathbf{g}_i^{(x)}$. The displacement vector $\mathbf{u}$ of the material point is defined in equation Equation 2.34 .

$$\mathbf{r} = \mathbf{R} + \mathbf{u} \tag{2.34}$$

For convenience, a set of reference coordinates $(\theta^1, \theta^2, \theta^3)$ may be defined to describe the material point p in the deformed body with respect to a general curvilinear coordinate system. The *covariant base vectors* for the curvilinear reference coordinate system, $\mathbf{g}_k^{(\theta)}$,

are defined to be the derivatives of the position vector $\mathbf{r}$ with respect to each of the θ_k coordinates, as written in Equation 2.35 . Thus the covariant base vectors for the θ_k-coordinate system are parallel to θ_k-coordinate lines.

$$\mathbf{g}_k^{(\theta)} = \frac{\partial x_i}{\partial \theta_k} \mathbf{g}_i^{(x)} \tag{2.35}$$

The components of the *covariant metric tensor*, denoted by $g_{ij}^{(\theta)}$, with respect to the θ_k-coordinate system are defined to be the inner products of the covariant base vectors. The covariant metric tensor with respect to the θ_k-coordinate system is defined in Equation 2.36.

$$g_{ij}^{(\theta)} = \mathbf{g}_i^{(\theta)} \cdot \mathbf{g}_j^{(\theta)} = \frac{\partial x_k}{\partial \theta_i} \frac{\partial x_k}{\partial \theta_j} \tag{2.36}$$

By definition, another set of vectors $\{\mathbf{g}_{(\theta)}^i\}$ are orthogonal to $\{\mathbf{g}_i^{(\theta)}\}$ using the relations given in Equation 2.37.

$$\mathbf{g}_{(\theta)}^i \cdot \mathbf{g}_j^{(\theta)} = \delta_j^i \tag{2.37}$$

where δ_j^i is the Kronecker delta.

These vectors are referred to as *contravariant base vectors* and are perpendicular to θ_k-coordinate surfaces. For example $\mathbf{g}_{(\theta)}^3$ is normal to a (θ_1, θ_2)-surface since it is orthogonal to both $\mathbf{g}_1^{(\theta)}$ and $\mathbf{g}_2^{(\theta)}$ from Equation 2.37.

The components of the *contravariant metric tensor* with respect to the θ_k-coordinate system are defined in Equation 2.38.

$$g_{(\theta)}^{ij} = \mathbf{g}_{(\theta)}^i \cdot \mathbf{g}_{(\theta)}^j = \frac{\partial \theta_i}{\partial x_k} \frac{\partial \theta_j}{\partial x_k} \tag{2.38}$$

The contravariant metric tensor may be used to relate the contravariant and covariant base vectors using Equation 2.39. For reference, the contravariant and covariant metric tensors with respect to the θ_k-coordinate system are related using Equation 2.40 (Green

& Adkins 1970, p. 2).

$$\mathbf{g}^i_{(\theta)} = g^{ir}_{(\theta)}\mathbf{g}^{(\theta)}_r \tag{2.39}$$

$$g^{ir}_{(\theta)}g^{(\theta)}_{rj} = \delta^i_j \tag{2.40}$$

Material axes for anisotropic materials

Anisotropic materials possess different material properties in different material directions. It is often convenient to identify the material coordinate axes with structurally important directions. For example myocardial tissue has a fibrous-sheet structure (see Section 1.1.2) and it is convenient to model it as an orthotropic material with one axis aligned with the muscle fibre direction, another with the sheet axis and the third orthogonal to these two axes. *Non-homogeneous* materials possess different material properties at different locations in a body. For non-homogeneous, anisotropic materials the orientation of the material axes may vary with location and so it is no longer convenient to identify the material axes in the undeformed body with the reference coordinates (X_1, X_2, X_3). Instead, a new material coordinate system (v_1, v_2, v_3) is introduced which is aligned with certain structural features of the material. For myocardium, a natural set of material axes are formed by identifying ν_1 with the muscle fibre direction, ν_2 with the sheet direction and ν_3 with the sheet-normal direction.

The base vectors for the ν_α-coordinate system may be chosen to be orthogonal in the undeformed state. This is convenient in myocardium, for example, where the ν_α-coordinates are chosen to line up with the fibre, sheet and sheet-normal directions, which are orthogonal in the undeformed state. However, the ensuing deformation dictates that they are not orthogonal, in general, in the deformed configuration. For this reason it is necessary to define base vectors and metric tensors for the ν_α-coordinate system in both the undeformed and deformed states. $\mathbf{A}^{(\nu)}_\alpha$, $\mathbf{A}^\alpha_{(\nu)}$ and $\mathbf{a}^{(\nu)}_\alpha$, $\mathbf{a}^\alpha_{(\nu)}$ denote the base vectors in the undeformed and deformed configurations, respectively. The metric tensors are denoted by $A^{(\nu)}_{\alpha\beta}$, $A^{\alpha\beta}_{(\nu)}$ and $a^{(\nu)}_{\alpha\beta}$, $a^{\alpha\beta}_{(\nu)}$ in the undeformed and deformed configurations, respectively. Recall that subscripted indices refer to covariant quantities and superscripted indices refer to contravariant quantities, and note that Greek symbols are used to denote individual ν_α material coordinates. They are computed in an analogous fashion to those for the θ_k-coordinate system defined in Equations 2.35 and 2.40. The base vectors and metric tensors for the ν_α-coordinate system are listed in Equation 2.41. Note that the

undeformed covariant base vectors, $\mathbf{A}_\alpha^{(\nu)}$, can be defined to be unit vectors by choosing the ν_α-coordinates to be a measure of physical arc-length in the undeformed state.

$$\begin{array}{rclcl} \mathbf{A}_\alpha^{(\nu)} &=& \frac{\partial X_k}{\partial \nu_\alpha}\mathbf{g}_k^{(x)} & & \\ \mathbf{A}_{(\nu)}^{\alpha}\cdot\mathbf{A}_\beta^{(\nu)} &=& \delta_\beta^\alpha & & \\ A_{\alpha\beta}^{(\nu)} &=& \mathbf{A}_\alpha^{(\nu)}\cdot\mathbf{A}_\beta^{(\nu)} &=& \frac{\partial X_k}{\partial \nu_\alpha}\frac{\partial X_k}{\partial \nu_\beta} \\ A_{(\nu)}^{\alpha\beta} &=& \mathbf{A}_{(\nu)}^{\alpha}\cdot\mathbf{A}_{(\nu)}^{\beta} &=& \frac{\partial \nu_\alpha}{\partial X_k}\frac{\partial \nu_\beta}{\partial X_k} \\ \mathbf{A}_{(\nu)}^{\alpha} &=& A_{(\nu)}^{\alpha\beta}\mathbf{A}_\beta^{(\nu)} & & \\ A_{(\nu)}^{\alpha\rho}A_{\rho\beta}^{(\nu)} &=& \delta_\beta^\alpha & & \end{array} \qquad \begin{array}{rclcl} \mathbf{a}_\alpha^{(\nu)} &=& \frac{\partial x_k}{\partial \nu_\alpha}\mathbf{g}_k^{(x)} & & \\ \mathbf{a}_{(\nu)}^{\alpha}\cdot\mathbf{a}_\beta^{(\nu)} &=& \delta_\beta^\alpha & & \\ a_{\alpha\beta}^{(\nu)} &=& \mathbf{a}_\alpha^{(\nu)}\cdot\mathbf{a}_\beta^{(\nu)} &=& \frac{\partial x_k}{\partial \nu_\alpha}\frac{\partial x_k}{\partial \nu_\beta} \\ a_{(\nu)}^{\alpha\beta} &=& \mathbf{a}_{(\nu)}^{\alpha}\cdot\mathbf{a}_{(\nu)}^{\beta} &=& \frac{\partial \nu_\alpha}{\partial x_k}\frac{\partial \nu_\beta}{\partial x_k} \\ \mathbf{a}_{(\nu)}^{\alpha} &=& a_{(\nu)}^{\alpha\beta}\mathbf{a}_\beta^{(\nu)} & & \\ a_{(\nu)}^{\alpha\rho}a_{\rho\beta}^{(\nu)} &=& \delta_\beta^\alpha & & \end{array} \tag{2.41}$$

2.5.2 Measures of strain and stress in curvilinear coordinates

Equations 2.9 and 2.29 express Green's strain tensor and the second Piola-Kirchhoff stress tensor, respectively, with respect to rectangular cartesian coordinates. The material coordinates required in these relations were chosen to align with the rectangular cartesian coordinates in the undeformed reference state. Alternatively, stress and strain tensors may be referred to ν_α-material coordinates as in Equations 2.42 and 2.43, respectively, using the metric tensors for the ν_α-material coordinate system (Equation 2.41). Note that if the ν_α-material coordinates are chosen to coincide with the rectangular cartesian coordinates, $a_{\alpha\beta}^{(\nu)}$ reduces to $C_{\alpha\beta}$ and both $A_{\alpha\beta}^{(\nu)}$ and $A_{(\nu)}^{\alpha\beta}$ reduce to $\delta_{\alpha\beta}$.

$$E_{\alpha\beta} = \frac{1}{2}\left(a_{\alpha\beta}^{(\nu)} - A_{\alpha\beta}^{(\nu)}\right) \tag{2.42}$$

$$T^{\alpha\beta} = \frac{1}{2}\left(\frac{\partial \overline{W}}{\partial E_{\alpha\beta}} + \frac{\overline{W}}{E_{\beta\alpha}}\right) - pA_{(\nu)}^{\alpha\beta} \tag{2.43}$$

Cauchy's formula for rectangular cartesian coordinates (Equation 2.16) is generalised in Equation 2.44 to express the components of the stress vector $\mathbf{t}$ acting on a deformed surface dS, with normal $\mathbf{n} = n_i\mathbf{g}_{(\theta)}^i$, in terms of the components of the Cauchy stress tensor.

$$\mathbf{t}dS = t^j\mathbf{g}_j^{(\theta)}dS = \sigma^{ij}n_i\mathbf{g}_j^{(\theta)}dS \tag{2.44}$$

For this research the constitutive law is based on the material structure (see Section

4.4.3) and so it is convenient to compute components of the second Piola-Kirchhoff stress tensor with respect to the undeformed ν_α-material coordinates, as in Equation 2.43. It is therefore more appropriate to express the stress vector in terms of the second Piola-Kirchhoff stress components.

Nanson's theorem (Equation 2.45) maps the deformed spatial (world) coordinate area, dS, into the area of the same material surface in the undeformed state, dS_0, with unit normal $\mathbf{N} = N_\alpha \mathbf{a}^\alpha_{(\nu)}$ (Malvern 1969, p. 169).

$$\frac{1}{J} F^i_\alpha n_i dS = N_\alpha dS_0 \qquad \text{or} \qquad F^T \mathbf{n} dS = J \mathbf{N} dS_0 \tag{2.45}$$

Substituting Nanson's theorem and Equation 2.11 into Equation 2.44 results in an alternative form of Cauchy's formula, written in Equation 2.46.

$$\mathbf{t} dS = T^{\alpha\beta} F^j_\beta N_\alpha \mathbf{g}^{(\theta)}_j dS_0 \tag{2.46}$$

Equation 2.46 defines the form of Cauchy's formula used in Section 2.5.3 to generalise the governing equations developed in Section 2.2.2 to curvilinear coordinates.

Physical components of stress and strain in curvilinear coordinates

The components of the Cauchy stress tensor (σ^{ij} in Equation2.44) are in general not physical stresses since the base vectors $\mathbf{g}^{(\theta)}_j$ are not necessarily unit vectors. To obtain physical stress components, these covariant base vectors must be normalised and the components of the normal $\mathbf{n}$ must be referred to the unit contravariant base vectors as in Equation 2.47.

$$\mathbf{n} = n_i \mathbf{g}^i_{(\theta)} = \sum_i \sqrt{g^{ii}_{(\theta)}} n_i \left(\frac{\mathbf{g}^i_{(\theta)}}{\sqrt{g^{ii}_{(\theta)}}} \right) \qquad \text{(no implicit summation)} \tag{2.47}$$

where $\sqrt{g^{ii}_{(\theta)}} n_i$ are the covariant components of the *unit* normal vector, relative to the *unit* contravariant base vectors, written in parenthesis. Equation 2.47 is then substituted

into Equation 2.44 to form Equation 2.48.

$$\mathbf{t} = \sum_{ij} \sigma^{ij} \frac{1}{\sqrt{g^{ii}_{(\theta)}}} \left(\sqrt{g^{ii}_{(\theta)}} n_i \right) \sqrt{g^{(\theta)}_{jj}} \left(\frac{\mathbf{g}^{(\theta)}_j}{\sqrt{g^{(\theta)}_{jj}}} \right) \qquad \text{(no implicit summation)} \quad (2.48)$$

where $\frac{\mathbf{g}^{(\theta)}_j}{\sqrt{g^{(\theta)}_{jj}}}$ are *unit* covariant base vectors.

By comparing Equation 2.48 with Equation 2.16, the physical components of the Cauchy stresses, denoted here as $\sigma^{(ij)}$, may be calculated using Equation 2.49. Note that the matrix of physical stresses is symmetric since the Cauchy stress tensor is symmetric (see Section 2.2.2), but $\sigma^{(ij)}$ are not the components of a tensor.

$$\sigma^{(ij)} = \sigma^{ij} \frac{\sqrt{g^{(\theta)}_{jj}}}{\sqrt{g^{ii}_{(\theta)}}} \qquad \text{(no implicit summation)} \quad (2.49)$$

Components of physical Green's strain are related to the tensor components of Equation 2.42 in a slightly different manner. The relation defined in Equation 2.50 and incorporates the undeformed covariant metric tensor for the ν_α-coordinate system, $A^{(\nu)}_{\alpha\beta}$. Note that like the physical stresses, the physical strain components form a symmetric matrix, but are not (in general) tensor components.

$$E_{(\alpha\beta)} = E_{\alpha\beta} \sqrt{A^{(\nu)}_{\beta\beta} A^{(\nu)}_{\alpha\alpha}} \qquad \text{(no implicit summation)} \quad (2.50)$$

Recall that earlier the base vectors of the ν_α-coordinate system were chosen to be orthonormal. In this case, the undeformed metric tensor $A^{(\nu)}_{\alpha\beta}$ consists of the components of the identity matrix, and the Green's strain tensor is comprised of physical strain components. If, however, strains were to be transformed to refer to reference θ_k-coordinates (for which the base vectors are generally not unit vectors), then the tensor components would not be physical components of strain. In this situation, physical strain components could be computed using a relation similar to Equation 2.50 with the covariant metric tensor $g^{(\theta)}_{ij}$ substituted in place of $A^{(\nu)}_{\alpha\beta}$ in Equation 2.50.

2.5.3 Equilibrium equations in curvilinear coordinates

Cauchy's formula for curvilinear coordinates (Equation 2.46) may be substituted into Equation 2.15 to yield a statement of conservation of linear momentum appropriate for curvilinear coordinates. This is written in Equation 2.51 and has been expressed in terms of the components of the second Piola-Kirchhoff stress tensor with respect to ν_α-material coordinates.

$$\int_{S_0} T^{\alpha\beta} F^j_\beta N_\alpha \mathbf{g}^{(\theta)}_j dS_0 + \int_{V_0} \rho_0 \mathbf{b} dV_0 = \frac{\mathrm{d}}{\mathrm{d}t} \int_{V_0} \rho_0 \mathbf{v} dV_0 \tag{2.51}$$

where Equation 2.13 has been used to transform the volume integrals to be taken over the undeformed volume instead of the deformed volume.

The next step is to transform the surface integral in Equation 2.51 into a volume integral using the divergence theorem (Sokolnikoff 1964, p. 264). Equation 2.52 defines the transformation.

$$\int_{S_0} T^{\alpha\beta} F^j_\beta N_\alpha \mathbf{g}^{(\theta)}_j dS_0 = \int_{V_0} \bigtriangledown \cdot \left(T^{\alpha\beta} F^j_\beta \mathbf{g}^{(\theta)}_j \right) dV_0 = \int_{V_0} \left(T^{\alpha\beta} F^j_\beta \right)\big|_\alpha \mathbf{g}^{(\theta)}_j dV_0 \tag{2.52}$$

where "$|_\alpha$" denotes *covariant differentiation* with respect to the ν_α-material coordinate (defined in Equation 2.57).

The resulting linear momentum balance is written in Equation 2.53.

$$\int_{V_0} \left[\left(T^{\alpha\beta} F^j_\beta \right)\big|_\alpha \mathbf{g}^{(\theta)}_j + \rho_0 \mathbf{b} - \rho_0 \mathbf{f} \right] dV_0 = 0 \tag{2.53}$$

where $\mathbf{f} = \frac{\mathrm{dv}}{\mathrm{d}t}$. Note that ρ_0, $\mathbf{v}$ and $\mathbf{f}$ are assumed to be continuous throughout V_0.

For arbitrary volumes, the integrand in Equation 2.53 vanishes resulting in Equation 2.54, which is a general form of Cauchy's first law of motion appropriate for curvilinear coordinates.

$$\left(T^{\alpha\beta} F^j_\beta \right)\big|_\alpha \mathbf{g}^{(\theta)}_j + \rho_0 \mathbf{b} = \rho_0 \mathbf{f} \qquad \text{or} \qquad \left(T^{\alpha\beta} F^j_\beta \right)\big|_\alpha + \rho_0 b^j = \rho_0 f^j \tag{2.54}$$

where the body force and acceleration vectors have components $\mathbf{b} = b^j \mathbf{g}^{(\theta)}_j$ and $\mathbf{f} = f^j \mathbf{g}^{(\theta)}_j$, respectively. Note that this reduces to Equation 2.20 if the ν_α-material coor-

dinate are chosen to coincide with the rectangular cartesian reference coordinates in the undeformed state and the θ_k-coordinates are chosen to be the rectangular cartesian coordinates.

Now, recalling the principle of virtual work in Equation 2.22, the virtual displacements may be expressed in terms of covariant components $\delta\mathbf{v} = \delta v_j \mathbf{g}^j_{(\theta)}$ with respect to the base vectors of the θ_k-reference coordinate system. Similarly, the surface traction vector may be written in terms of its contravariant components using $\mathbf{s} = s^j \mathbf{g}^{(\theta)}_j$. Substituting these components together with the expression for the traction vector given in Equation 2.46, transforms the virtual work equations into Equation 2.55.

$$\int_{S_2} s^j \delta v_j dS = \int_{S_0} T^{\alpha\beta} F^j_\beta N_\alpha \delta v_j dS_0 \tag{2.55}$$

Gauss' theorem (Fung 1965, p. 117) is used to expand the right-hand-side surface integral in Equation 2.55 into the volume integral in Equation 2.56.

$$\int_{S_2} s^j \delta v_j dS = \int_{V_0} \left[\left(T^{\alpha\beta} F^j_\beta\right)\big|_\alpha \delta v_j + T^{\alpha\beta} F^j_\beta \, \delta v_j|_\alpha \right] dV_0 \tag{2.56}$$

where $\delta v_j|_\alpha$ is the covariant derivative of the virtual displacement with respect to the ν_α-material coordinate and is defined in Equation 2.57.

$$\delta v_j|_\alpha = \frac{\partial \delta v_j}{\partial \nu_\alpha} - \Gamma^i_{j\alpha} \delta v_i \tag{2.57}$$

where

$$\Gamma^i_{j\alpha} = \frac{\partial}{\partial \nu_\alpha}\left(\mathbf{g}^{(\theta)}_j\right) \cdot \mathbf{g}^i_{(\theta)} = \frac{\partial}{\partial \nu_\alpha}\left(\frac{\partial x_k}{\partial \theta_j}\right)\frac{\partial \theta_i}{\partial x_k} \tag{2.58}$$

are called *Christoffel symbols of the second kind* which are non-tensor quantities that arise through partial differentiation of base vectors. As expressed here, they are not symmetric with respect to the two lower indices since j is a spatial coordinate and α is a material coordinate.

Cauchy's first law of motion Equation 2.54 can be used to eliminate the second derivative terms in Equation 2.56 and reduce it to Equation 2.59. Notice that in this expression of the virtual work principle, the stress components are referred to material ν_α-material

coordinates, while the displacement components are referred to the θ_k-reference coordinates.

$$\int_{V_0} T^{\alpha\beta} F^j_\beta \, \delta v_j|_\alpha \, dV_0 = \int_{V_0} \rho_0 \left(b^j - f^j\right) \delta v_j dV_0 + \int_{S_2} s^j \delta v_j dS \tag{2.59}$$

The final step is to evaluate the right-hand-side surface integral, as discussed in Section 2.5.4.

2.5.4 Surface tractions in curvilinear coordinates

The right-hand-side surface integral of Equation 2.59 is evaluated by expressing the contravariant components of the traction vector, s^j, in terms of the pressure loads acting on the external surfaces of the deforming body. In the absence of boundary pressures this integral vanishes.

At this stage, it is convenient to introduce one further system of material coordinates that describe the geometry of the deforming body. They are referred to as the *finite element material coordinates*,

(ξ_1, ξ_2, ξ_3), and are described fully in Section 3.1.5. The base vectors and metric tensors for the ξ_M-material coordinate system are defined in Equation 3.20.

Consider a pressure load, $p_{(appl)}$ (a physical stress), acting on the deforming (ξ_1, ξ_2)-coordinate surface. The unit normal to this surface is given by $\hat{\mathbf{n}} = \frac{\mathbf{g}^3_{(\xi)}}{\sqrt{g^{33}_{(\xi)}}}$ (since the contravariant vectors for the ξ_M-coordinate system are not necessarily unit vectors). The surface traction vector is expressed in Equation 2.60.

$$\mathbf{s} = p(appl)\hat{\mathbf{n}} = p_{(appl)} \frac{\mathbf{g}^3_{(\xi)}}{\sqrt{g^{33}_{(\xi)}}} = p(appl) \frac{\mathbf{g}^{3M}_{(\xi)}}{\sqrt{g^{33}_{(\xi)}}} \mathbf{g}^{(\xi)}_M = p(appl) \frac{g^{3M}_{(\xi)}}{\sqrt{g^{33}_{(\xi)}}} \frac{\partial \theta_j}{\partial \xi_M} \mathbf{g}^{(\theta)}_j = s^j \mathbf{g}^{(\theta)}_j \tag{2.60}$$

where the contravariant components of the surface traction vector are given by

$$s^j = p_{(appl)} \frac{g^{3M}_{(\xi)}}{\sqrt{g^{33}_{(\xi)}}} \frac{\partial \theta_j}{\partial \xi_M} \tag{2.61}$$

The right-hand-side surface integral of Equation 2.59 may now be computed using Equation 2.62.

$$\int_{S_2} s^j \delta v_j dS = \int_{S_2} p_{(appl)} \frac{g^{3M}_{(\xi)}}{\sqrt{g^{33}_{(\xi)}}} \frac{\partial \theta_j}{\partial \xi_M} \delta v_j dS \tag{2.62}$$

where the integral is performed over the portion of deformed surface that is subject to pressure boundary constraints.

Finally, Equation 2.62 is incorporated into Equation 2.59 to yield the equilibrium equations that govern large deformation elasticity, written in Equation 2.63.

$$\int_{V_0} T^{\alpha\beta} F^j_\beta \, \delta v_j|_\alpha \, dV_0 = \int_{V_0} \rho_0 \left(b^j - f^j \right) \delta v_j dV_0 + \int_{S_2} p_{(appl)} \frac{g^{3M}_{(\xi)}}{\sqrt{g^{33}_{(\xi)}}} \frac{\partial \theta_j}{\partial \xi_M} \delta v_j dS \tag{2.63}$$

Equation 2.63 is the starting point for the analysis of a body undergoing large elastic deformations. To be useful for practical applications, the virtual displacements are expressed in terms of an interpolation of nodal parameters which may be determined using a nonlinear Galerkin finite element method (see Chapter 3). Moreover, to be applicable to the heart, the relationship between the stress and strain (Equation 2.43) must be based on experimental observations of myocardium under physiological conditions (see Section 4.4.3).

Chapter 3

The Finite Element Method For Finite Elasticity

To analyse stress in an body undergoing large elastic deformations the equations that govern finite deformation elasticity, developed in Chapter 2, must be solved. For materials with regular geometries and simple material properties this may be done analytically (an example of this is presented in Section 4.2). However, for most practical applications materials behave nonlinearly and assume complex shapes. Irregular domains may be discretised into a number of smaller regular *elements*, over which quantities of interest (for example the geometric coordinates of a point) are continuously approximated. The two main types of interpolation functions used in this thesis are linear Lagrange and cubic Hermite basis functions. Section 3.1 details these interpolation schemes and their use in one, two and three spatial dimensions.

In order to accurately and efficiently resolve quantities of interest that vary dramatically it is often necessary to vary the consistency of the discretisation. Section 3.1.4 describes a method to include irregular connections whilst maintaining continuity of the approximation throughout the domain.

It is often convenient, if not necessary, to use several different coordinate systems for the FEM for finite deformation elasticity. For example, stress components are most conveniently expressed with respect to a system of material coordinates aligned with structural features of the body, whereas the geometry best expressed using a system of curvilinear reference coordinates. Section 3.1.5 defines FE material coordinate systems

in terms of the global rectangular cartesian coordinate system.

For each element, the equations governing finite deformation elasticity are expressed in terms of known material properties and the unknown displacements of the element vertices (referred to as *nodes*). To formulate these equations many integrals must be evaluated and often this cannot be done analytically. Gaussian quadrature (described in Section 3.2) is a suitable numerical integration scheme for use with FE analysis.

Element contributions are assembled into a global system of equations to ensure that the solution is compatible across element boundaries. The system of nonlinear equations (defined in Section 3.3) are solved, subject to boundary constraints, to yield a set of deformed nodal coordinates from which deformation patterns are approximated using interpolation. Section 3.4 describes nonlinear techniques used to solve the equations. To reduce solutions times, the computation of the element contributions to the global equations is distributed across a number of processors, which may be a cluster of workstations or a high performance computer.

3.1 Interpolation using basis functions

Basis functions, also known as *shape* or *interpolation functions*, may be used to approximate quantities of interest (for example geometric or solution variables) that vary over a particular domain. They consist of sets of polynomials of different degrees, depending on the desired accuracy of the approximation (generally the higher the degree, the better the approximation). This thesis uses two main types of interpolation functions — namely the linear Lagrange and cubic Hermite basis functions. The higher order cubic Hermite basis functions are used to approximate quantities of interest that possess large spatial gradients, whereas linear Lagrange basis functions are used to approximate variables that do not vary appreciably. This section provides an overview of the properties of each basis type and the way they can be combined to approximate field variables in two- and three-dimensions. For further information see Zienkiewicz & Taylor (1994, Chap. 7).

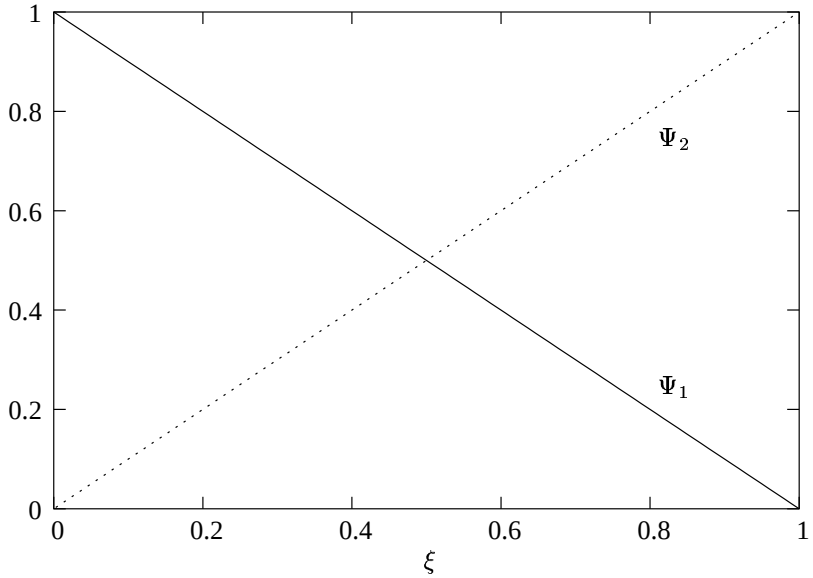

FIGURE 3.1: Linear Lagrange basis functions

3.1.1 Linear Lagrange basis functions

Consider an arbitrary scalar function, u, with $u = u_1$ and $u = u_2$ at opposite ends of a one-dimensional domain. A linear approximation of u, along the domain can then be defined using Equation 3.1, by introducing a normalised measure of distance, ξ, with $\xi = 0$ at one end (where $u = u_1$ say) and $\xi = 1$ at the other end of the domain (where $u = u_2$).

$$u(\xi) = (1 - \xi)u_1 + \xi u_2 \qquad (0 \leq \xi \leq 1) \tag{3.1}$$

The boundary points of the domain are variously referred to as *element vertices*, *element nodes* or *nodal points* and the values of u at element nodes, namely u_1 and u_2, are referred to as *nodal parameters*. In Equation 3.1, a weighting function is associated with each of the nodal parameters. These weighting functions are straight lines that vary between 0 and 1 as shown in Figure 3.1. They are referred to as the *linear Lagrange basis functions* and are defined in Equation 3.2.

$$\Psi_1(\xi) = (1 - \xi) \qquad \Psi_2(\xi) = \xi \tag{3.2}$$

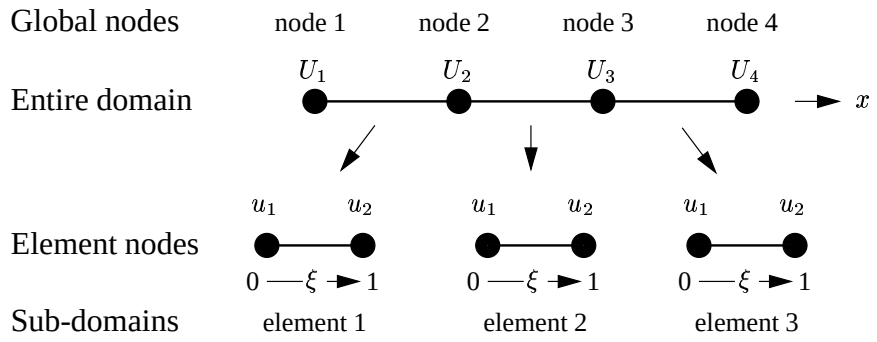

FIGURE 3.2: The scalar field, *u*, may be approximated over an entire domain by using piecewise polynomials over a set of smaller domains.

More complex variations of u (with larger spatial gradients, say) may be approximated using piecewise linear polynomials over smaller domains, called *elements*. The union of the set of smaller sub-domains must cover the entire domain of interest without overlapping. Adjacent elements share nodal parameters for their description of u as shown in Figure 3.2, which ensures that the approximation of u is continuous throughout the entire domain.

Equation 3.1 holds over each of the three elements in Figure 3.2. In the first element $u_1 = U_1$ and $u_2 = U_2$, whereas in the second element $u_1 = U_2$ and $u_2 = U_3$. This ensures that the quantity u is implicitly continuous between elements since in the first element $u(1) = U_2$ and in the second element $u(0) = U_2$ using Equation 3.1. Similarly, in the third element, $u_1 = U_3$ and $u_2 = U_4$, ensuring continuity between the second and third elements with $u = U_3$ at the junction node.

It is now clear that u may be approximated by a continuous piecewise parametric description in terms of the normalised element coordinate, ξ. In order to express u in terms of the physical coordinate, x, the relationship between x and ξ must be defined for each element. It is convenient to define the spatial coordinate, x, as an interpolation of the nodal values of x. Thus the dependence of u on x is defined by the parametric expressions in Equation 3.3.

$$u(\xi) = \sum \Psi_n(\xi) u_n \qquad x(\xi) = \sum \Psi_n(\xi) x^n \tag{3.3}$$

Note that in Equation 3.3, summation is implied over all element nodes (there are only 2 for this one-dimensional case) and that $x(\xi)$ provides the mapping between the math-

ematical space, $0 \leq \xi \leq 1$ and the physical space $x_1 \leq x \leq x_2$.

3.1.2 Cubic Hermite basis functions

Like the linear Lagrange basis functions, cubic Hermite interpolation functions provide continuity of the variable of interest across element boundaries. In addition, they provide continuity in the first derivative with respect to arc length, which is what makes them different from cubic Lagrange basis functions. For this reason Hermite bases are ideal for representing a smoothly varying curve or surface over some domain of interest.

To approximate the field quantity, u, using a one-dimensional cubic Hermite basis, two element nodes are required, over which four nodal quantities must be defined. Two of these are the values of u at the element nodes, namely u_1 and u_2, just as for the linear Lagrange basis functions. The additional two quantities are the first derivatives of u with respect to the normalised element coordinate, ξ. These two parameters are denoted by $\left(\frac{\mathrm{d}u}{\mathrm{d}\xi}\right)_1$ and $\left(\frac{\mathrm{d}u}{\mathrm{d}\xi}\right)_2$, where the subscripts refer to the element node at which the derivative is defined.

A one-dimensional cubic Hermite basis incorporates the four cubic polynomials listed in Equation 3.4 and illustrated in Figure 3.3. Note that the subscripted indices on the basis functions refer to the element node number and the superscripted indices signify whether the basis function is associated with the value of u (superscript 0) or its derivative (superscript 1) at the node.

$$\begin{array}{lcllcl} \Psi_1^0(\xi) & = & 1 - 3\xi^2 + 2\xi^3 & \Psi_2^0(\xi) & = & \xi^2(3 - 2\xi) \\ \Psi_1^1(\xi) & = & \xi(\xi - 1)^2 & \Psi_2^1(\xi) & = & \xi^2(\xi - 1) \end{array} \tag{3.4}$$

Equation 3.5 defines how u may be approximated in one-dimension using the four cubic Hermite basis functions with their associated nodal parameters.

$$u(\xi) = \Psi_1^0(\xi)u_1 + \Psi_1^1(\xi)\left(\frac{\mathrm{d}u}{\mathrm{d}\xi}\right)_1 + \Psi_2^0(\xi)u_2 + \Psi_2^1(\xi)\left(\frac{\mathrm{d}u}{\mathrm{d}\xi}\right)_2 \tag{3.5}$$

To make cubic Hermite basis functions useful in practice, one further modification is necessary. Instead of using the nodal derivative $\left(\frac{\mathrm{d}u}{\mathrm{d}\xi}\right)_n$ that depends on the local element

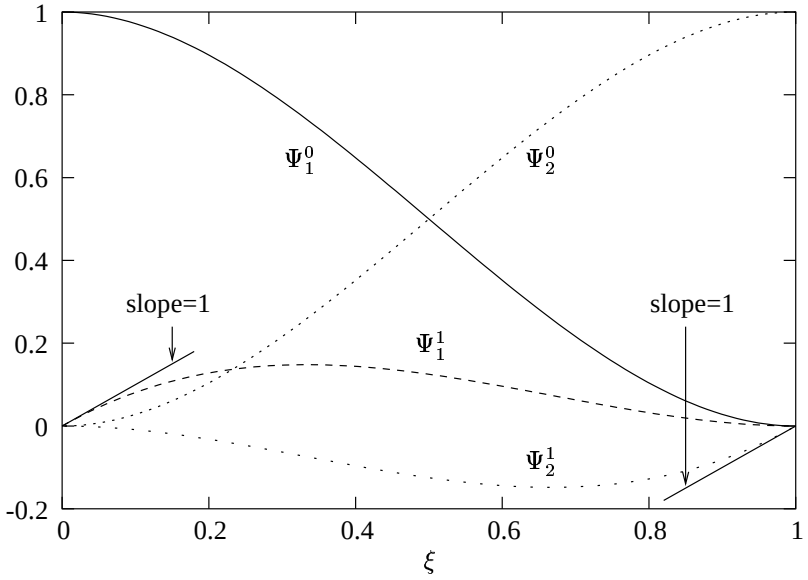

FIGURE 3.3: Cubic Hermite basis functions

ξ-coordinate in the two adjacent elements, it is more useful to define a global node derivative $\left(\frac{\mathrm{d}u}{\mathrm{d}s}\right)_N$, where s is the arc-length and N is the global node number. Equation 3.6 is then used to calculate the ξ-coordinate derivative.

$$\left(\frac{\mathrm{d}u}{\mathrm{d}\xi}\right)_n = \left(\frac{\mathrm{d}u}{\mathrm{d}s}\right)_N \cdot \left(\frac{\mathrm{d}s}{\mathrm{d}\xi}\right)_n \tag{3.6}$$

where $\left(\frac{\mathrm{d}s}{\mathrm{d}\xi}\right)_n$ is an *element scale factor* which scales the arc-length derivative of global node N to the ξ-coordinate derivative of element node n. Note that it is always convenient to associate the element node n in element e with the global node N using a connectivity matrix $\Delta(n,e) = N$. The result is that $\left(\frac{\mathrm{d}u}{\mathrm{d}s}\right)$ is implicitly constrained to be continuous across element boundaries rather than $\left(\frac{\mathrm{d}u}{\mathrm{d}\xi}\right)$.

3.1.3 Interpolation in two- and three-dimensions

Two- and three-dimensional basis functions can simply be constructed from tensor products of the one-dimensional bases described above.

To approximate u over a two-dimensional domain, the *bilinear Lagrange* interpolation scheme may be used. This scheme consists of the four polynomials shown in Figure 3.4

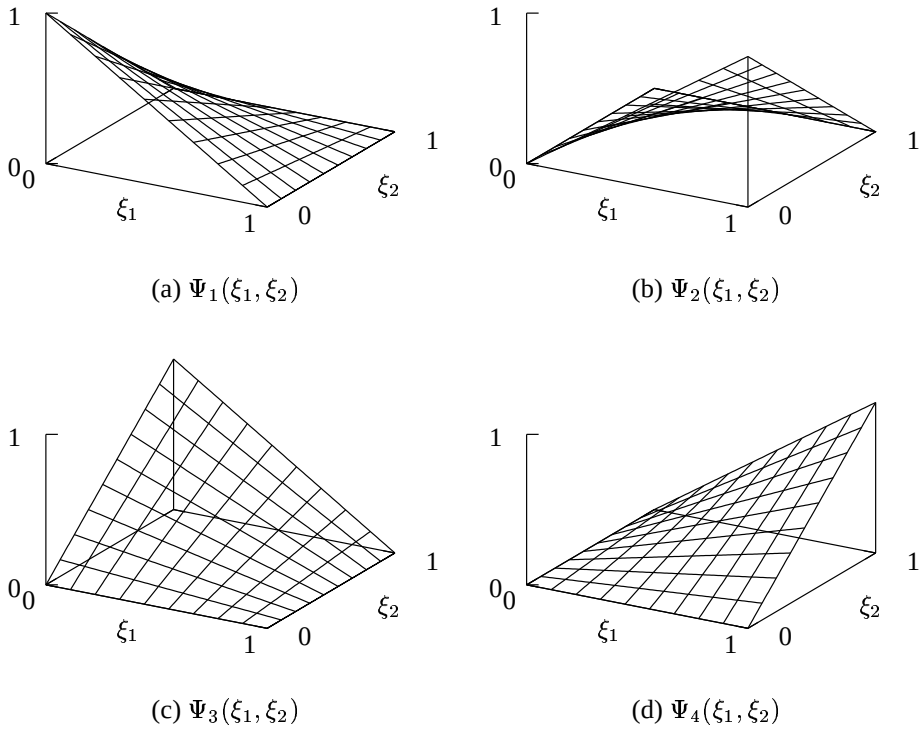

(a) $\Psi_1(\xi_1, \xi_2)$ (b) $\Psi_2(\xi_1, \xi_2)$

(c) $\Psi_3(\xi_1, \xi_2)$ (d) $\Psi_4(\xi_1, \xi_2)$

FIGURE 3.4: Two-dimensional bilinear basis functions.

, and is constructed by taking the tensor product of individual one-dimensional linear Lagrange interpolations in the ξ_1 and ξ_2 directions as outlined in Equation 3.7.

$$\begin{aligned}
\Psi_1(\xi_1, \xi_2) &= \Psi_1^L(\xi_1)\Psi_1^L(\xi_2) &= (1-\xi_1)(1-\xi_2) \\
\Psi_2(\xi_1, \xi_2) &= \Psi_2^L(\xi_1)\Psi_1^L(\xi_2) &= \xi_1(1-\xi_2) \\
\Psi_3(\xi_1, \xi_2) &= \Psi_1^L(\xi_1)\Psi_2^L(\xi_2) &= (1-\xi_1)\xi_2 \\
\Psi_4(\xi_1, \xi_2) &= \Psi_2^L(\xi_1)\Psi_2^L(\xi_2) &= \xi_1\xi_2
\end{aligned} \tag{3.7}$$

where $\Psi_1^L(\xi)$ and $\Psi_2^L(\xi)$ are the one-dimensional linear Lagrange basis functions described in Section 3.1.1.

Four nodal parameters, $u_1, ..., u_4$, are associated with the two-dimensional basis functions and are the values of u defined at the element vertices. The approximation of u is

given in Equation 3.8.

$$u(\xi) = \Psi_1(\xi_1, \xi_2)u_1 + \Psi_2(\xi_1, \xi_2)u_2 + \Psi_3(\xi_1, \xi_2)u_3 + \Psi_4(\xi_1, \xi_2)u_4 \tag{3.8}$$

As for the one-dimensional case, the geometry of the element is defined in terms of interpolations of nodal positions $(x^n, y^n)\,, n = 1...4$. Equation 3.9 is then used to provide the mapping between the mathematical space (ξ_1, ξ_2) and the physical space (x, y).

$$x(\xi_1, \xi_2) = \sum \Psi_n(\xi_1, \xi_2)x^n \qquad y(\xi_1, \xi_2) = \sum \Psi_n(\xi_1, \xi_2)y^n \tag{3.9}$$

Using a similar procedure, the eight polynomials that constitute a three-dimensional trilinear Lagrange basis have been constructed in Equation 3.10 and used to approximate u over a three-dimensional element in Equation 3.11.

$$\begin{aligned}
\Psi_1(\xi_1, \xi_2, \xi_3) &= (1-\xi_1)(1-\xi_2)(1-\xi_3) & \Psi_2(\xi_1, \xi_2, \xi_3) &= \xi_1(1-\xi_2)(1-\xi_3) \\
\Psi_3(\xi_1, \xi_2, \xi_3) &= (1-\xi_1)\xi_2(1-\xi_3) & \Psi_4(\xi_1, \xi_2, \xi_3) &= \xi_1\xi_2(1-\xi_3) \\
\Psi_5(\xi_1, \xi_2, \xi_3) &= (1-\xi_1)(1-\xi_2)\xi_3 & \Psi_6(\xi_1, \xi_2, \xi_3) &= \xi_1(1-\xi_2)\xi_3 \\
\Psi_7(\xi_1, \xi_2, \xi_3) &= (1-\xi_1)\xi_2\xi_3 & \Psi_8(\xi_1, \xi_2, \xi_3) &= \xi_1\xi_2\xi_3
\end{aligned} \tag{3.10}$$

and

$$\begin{aligned}
u(\xi_1, \xi_2, \xi_3) &= \sum \Psi_n(\xi_1, \xi_2, \xi_3)u_n \qquad n = 1...8 \\
x_i(\xi_1, \xi_2, \xi_3) &= \sum \Psi_n(\xi_1, \xi_2, \xi_3)x_i^n \qquad x_i \in \{x, y, z\}
\end{aligned} \tag{3.11}$$

The construction of two- and three-dimensional basis functions involving cubic Hermite interpolation can be achieved using the above procedure, with one modification for the derivative terms. To approximate u using a two-dimensional bicubic Hermite basis, the four quantities listed in Equation 3.12 must be defined at each element node, totalling 16 nodal parameters per element.

$$u, \quad \frac{\partial u}{\partial \xi_1}, \quad \frac{\partial u}{\partial \xi_2}, \quad \frac{\partial^2 u}{\partial \xi_1 \partial \xi_2} \tag{3.12}$$

The need for the second-order cross-derivative term can be explained as follows. Since

u is cubic in both ξ_1 and ξ_2 independently, then the derivative $\frac{\partial u}{\partial \xi_1}$ is quadratic in ξ_1 and cubic in ξ_2. The cubic variation of u with ξ_2 is specified by the four nodal parameters u_1, $\left(\frac{\partial u}{\partial \xi_2}\right)_1$, u_3, and $\left(\frac{\partial u}{\partial \xi_2}\right)_3$, defined at element vertices one and three respectively. However, since $\frac{\partial u}{\partial \xi_1}$ is cubic in ξ_2, as stated above, and is entirely independent of these four parameters, four additional parameters are required to specify this cubic. Two of these are specified by $\left(\frac{\partial u}{\partial \xi_1}\right)_1$ and $\left(\frac{\partial u}{\partial \xi_1}\right)_3$, and the remaining two are the second-order cross-derivative terms, $\left(\frac{\partial^2 u}{\partial \xi_1 \partial \xi_2}\right)_1$ and $\left(\frac{\partial^2 u}{\partial \xi_1 \partial \xi_2}\right)_3$. Similar reasoning explains the need for $\frac{\partial^2 u}{\partial \xi_1 \partial \xi_2}$ to be defined at element vertices two and four.

The bicubic Hermite interpolation of the field quantity u is written out in full form in Equation 3.13 using the one-dimensional cubic Hermite basis functions defined in Equation 3.4, and the 16 nodal parameters described above.

$$
\begin{aligned}
u(\xi_1,\xi_2) = {} & \Psi_1^0(\xi_1)\Psi_1^0(\xi_2)u_1 && + \Psi_2^0(\xi_1)\Psi_1^0(\xi_2)u_2 \\
+ {} & \Psi_1^0(\xi_1)\Psi_2^0(\xi_2)u_3 && + \Psi_2^0(\xi_1)\Psi_2^0(\xi_2)u_4 \\
+ {} & \Psi_1^1(\xi_1)\Psi_1^0(\xi_2)\left(\frac{\partial u}{\partial \xi_1}\right)_1 && + \Psi_2^1(\xi_1)\Psi_1^0(\xi_2)\left(\frac{\partial u}{\partial \xi_1}\right)_2 \\
+ {} & \Psi_1^1(\xi_1)\Psi_2^0(\xi_2)\left(\frac{\partial u}{\partial \xi_1}\right)_3 && + \Psi_2^1(\xi_1)\Psi_2^0(\xi_2)\left(\frac{\partial u}{\partial \xi_1}\right)_4 \\
+ {} & \Psi_1^0(\xi_1)\Psi_1^1(\xi_2)\left(\frac{\partial u}{\partial \xi_2}\right)_1 && + \Psi_2^0(\xi_1)\Psi_1^1(\xi_2)\left(\frac{\partial u}{\partial \xi_2}\right)_2 \\
+ {} & \Psi_1^0(\xi_1)\Psi_2^1(\xi_2)\left(\frac{\partial u}{\partial \xi_2}\right)_3 && + \Psi_2^0(\xi_1)\Psi_2^1(\xi_2)\left(\frac{\partial u}{\partial \xi_2}\right)_4 \\
+ {} & \Psi_1^1(\xi_1)\Psi_1^1(\xi_2)\left(\frac{\partial^2 u}{\partial \xi_1 \partial \xi_2}\right)_1 && + \Psi_2^1(\xi_1)\Psi_1^1(\xi_2)\left(\frac{\partial^2 u}{\partial \xi_1 \partial \xi_2}\right)_2 \\
+ {} & \Psi_1^1(\xi_1)\Psi_2^1(\xi_2)\left(\frac{\partial^2 u}{\partial \xi_1 \partial \xi_2}\right)_3 && + \Psi_2^1(\xi_1)\Psi_2^1(\xi_2)\left(\frac{\partial^2 u}{\partial \xi_1 \partial \xi_2}\right)_4
\end{aligned}
\tag{3.13}
$$

To ensure derivative continuity throughout the spatial domain as well as the ξ-coordinate space, the global node derivatives need to be specified with respect to physical arc-length. There are now two arc-lengths to consider. Arc-lengths along the ξ_1- and ξ_2-coordinates are measured by s_1 and s_2, respectively. Thus the one-dimensional scale factors in Equation 3.6 are extended in Equation 3.14 for two-dimensional interpolation.

$$
\begin{aligned}
\left(\frac{\partial u}{\partial \xi_1}\right)_n &= \left(\frac{\partial u}{\partial s_1}\right)_N \cdot \left(\frac{\mathrm{d}s_1}{\mathrm{d}\xi_1}\right)_n \\
\left(\frac{\partial u}{\partial \xi_2}\right)_n &= \left(\frac{\partial u}{\partial s_2}\right)_N \cdot \left(\frac{\mathrm{d}s_2}{\mathrm{d}\xi_2}\right)_n
\end{aligned}
\tag{3.14}
$$

with the additional cross-derivative scale factor

$$\left(\frac{\partial^2 u}{\partial\xi_1\partial\xi_2}\right)_n = \left(\frac{\partial^2 u}{\partial s_1\partial s_2}\right)_N \cdot \left(\frac{\mathrm{d}s_1}{\mathrm{d}\xi_1}\right)_n \cdot \left(\frac{\mathrm{d}s_2}{\mathrm{d}\xi_2}\right)_n \tag{3.15}$$

where $\left(\frac{\mathrm{d}s_1}{\mathrm{d}\xi_1}\right)_n$ and $\left(\frac{\mathrm{d}s_2}{\mathrm{d}\xi_2}\right)_n$ are element scale factors which scale the arc-length derivatives of global node N to the ξ-coordinate derivatives of element node n, as for the one-dimensional case. Again N is related to n using the connectivity mapping, $\Delta(n, e)$.

A further condition must governs the choice of scale factors to ensure that u is C^1 continuous across element boundaries. A sufficient condition is that the scale factor at a node in one element is the same as the scale factor at the same node in an adjacent element (Bradley, Pullan & Hunter 1997). In other words the scale factors should be *nodally based* so that the same scale factor is used for all elements in which a node lies. Any choice of scale factor will provide C^1 continuity across element boundaries, but it is convenient to choose the average of the two arc-lengths adjacent to the given global node. This is because it is often computationally desirable to uniformly space the ξ coordinate with respect to arc-length (for example to evenly space out the computational points of a Gaussian quadrature scheme across elements). However if adjacent element arc-lengths differ largely, average arc-length scale factors may cause the arc-length to be too long in one element and too short in the other. Another choice of scale factor is the *harmonic mean*, given in Equation 3.16 for . The harmonic mean is smaller than the arithmetic mean and is therefore more useful when the mesh contains neighbouring elements of markedly different sizes.

$$\frac{1}{H} \equiv \frac{1}{n}\sum_{i=1}^{n}\frac{1}{x_i}$$

or for the case of interest when $n = 2$

$$H(x_1, x_2) = \frac{2x_1x_2}{x_1 + x_2} \tag{3.16}$$

Three-dimensional tricubic Hermite basis functions may be constructed in a similar

manner by introducing a triple cross derivative with respect to all three element coordinates as in Equation 3.17.

$$\left(\frac{\partial^3 u}{\partial\xi_1\partial\xi_2\partial\xi_3}\right)_n = \left(\frac{\partial^3 u}{\partial\xi_1\partial\xi_2\partial\xi_3}\right)_N \cdot \left(\frac{\mathrm{ds}_1}{\mathrm{d}\xi_1}\right)_n \cdot \left(\frac{\mathrm{ds}_2}{\mathrm{d}\xi_2}\right)_n \cdot \left(\frac{\mathrm{ds}_3}{\mathrm{d}\xi_3}\right)_n \tag{3.17}$$

3.1.4 Irregular Meshes - Hanging Nodes

In this thesis some of the phenomena of interest vary dramatically over a relatively small portion of the solution domain, for example, the properties of soft tissue surrounding an infarct. In order to resolve those quantities accurately, the discretisation of the domain in the area of interest must be sufficiently fine and the order of the polynomial interpolation sufficiently high. Meeting that criterion and uniformly discretising the entire domain is often computationally inefficient or infeasible. *Hanging nodes* also referred to as *improper*, *slave* or *constrained nodes* provide a means of connecting regions of varying discretisation.

Hanging nodes are proper nodes for an element which uses them as vertices[1] and their field values contribute directly to these element stiffness matrices. However, their field values are interpolated from neighbouring elements where they do not correspond to an element vertex.

In the solution process the degrees of freedom of a hanging node are constrained to be values interpolated from the neighbouring elements in order to enforce continuity of the approximation across the inter-element boundaries. The constrained degrees of freedom are eliminated from the discrete system of global equations. Figure 3.5 demonstrates the use of a hanging node to create an irregular linear Lagrange mesh.

In the system of equations for the example presented in Figure 3.5, there are no equations for the constrained node degrees of freedom. The equations for the proper nodes 5 and 6 are modified to include the coefficients associated with the hanging node, node 8.

For a hanging node in a cubic Hermite mesh, as in the linear Lagrange example, u is interpolated from the adjacent element. The nodal arc length derivative value $\left(\frac{\mathrm{du}}{\mathrm{ds}}\right)$ is also evaluated from the adjacent element.

[1] "Vertex" here implies that the element node weights a corresponding element basis function (i.e. it could be a mid side node for an element that directly used midside nodes).

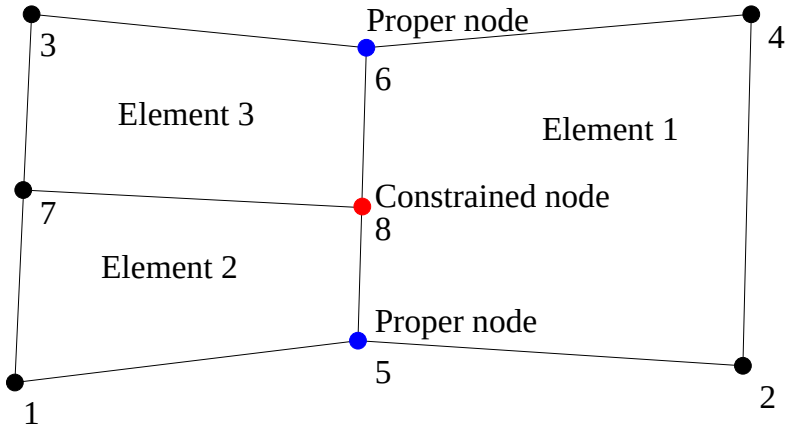

FIGURE 3.5: A Hanging node in a linear Lagrange domain mesh. The nodal parameter u at the constrained node is constrained to be the value of u interpolated from the proper nodes in element 1.

The scale factors $\left(\frac{\mathrm{ds}}{\mathrm{d}\xi}\right)$ for the connected elements must be chosen to satisfy the condition that $\frac{\frac{\mathrm{du}}{\mathrm{d}\xi}}{\frac{\mathrm{ds}}{\mathrm{d}\xi}}$ is continuous across the element boundaries to ensure that the domain mesh varies smoothly and is continuous.

Note this criterion does not maintain strict C^1 continuity, that is continuity of $\frac{\partial u}{\partial \zeta}$, across the element boundaries. In fact it is not possible with the FEM implementation used in this thesis to create a C^1 continuous irregular mesh using cubic Hermite elements. However, although C^1 continuity is desirable it is not absolutely necessary.

3.1.5 Finite element material coordinates

When modelling the geometry of a deforming body using the FEM, it is convenient to define a system of normalised element coordinates within each element, (ξ_1, ξ_2, ξ_3). These coordinates are material coordinates because they are embedded in the body and deform with the material as it deforms. Thus, in general the ξ_M-material coordinates are not orthogonal. With reference to Figure 3.6, consider a material point P with rectangular cartesian coordinates (X_1, X_2, X_3) in the undeformed body B_0. Equation 3.18 may be used to map the ξ_M-material coordinates of P into the undeformed spatial coordinates using the values (and derivatives, for high order interpolation) of the geometric

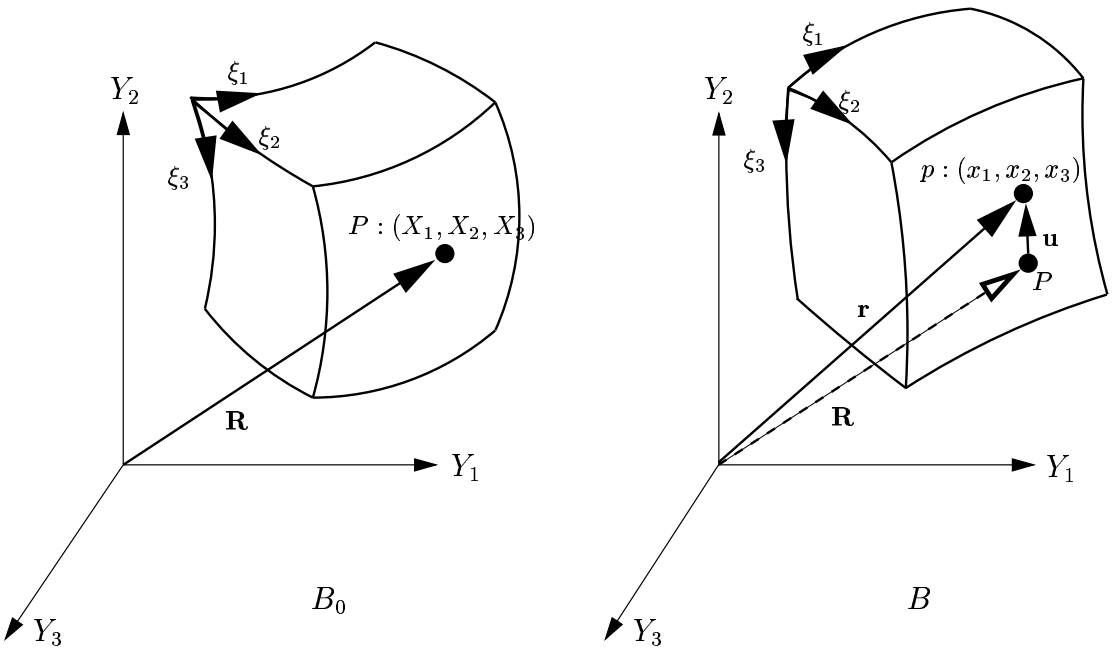

FIGURE 3.6: The finite element material coordinate system (ξ_1, ξ_2, ξ_3).

coordinates for the n element parameters in the undeformed state, X_i^n.

$$X_i = \Psi_n(\xi_1, \xi_2, \xi_3) X_i^n \tag{3.18}$$

where $\Psi_n(\xi_1, \xi_2, \xi_3)$ are the chosen three-dimensional basis functions (see Section 3.1).

A subsequent deformation causes the material point to undergo a displacement $\mathbf{u}$. In the deformed body B, the material point is labelled p and has rectangular cartesian coordinates (x_1, x_2, x_3). Again the ξ_M-material coordinates may be used to describe the deformed geometry of the element using the mapping given in Equation3.19.

$$x_i = \Psi_n(\xi_1, \xi_2, xi_3) x_i^n \tag{3.19}$$

where x_i^n are the element nodal values (and derivatives) of the i-th geometric coordinate in the deformed state.

The covariant base vectors and metric tensors for the ξ_M-coordinate system are defined in Equation 3.20 for the undeformed and deformed states. Contravariant base vectors and metric tensors for the ξ_M-coordinate system may be determined in an analogous

fashion to those for the ν_α-coordinate system in Equation 2.41, and again the metric tensors may be used to raise or lower indices.

$$\begin{array}{rclcrcl} \mathbf{G} & = & \frac{\partial X_k}{\partial \xi_M}\mathbf{g}_k^{(x)} & & \mathbf{g}_M^{(\xi)} & = & \frac{\partial x_k}{\partial \xi_M}\mathbf{g}_k^{(x)} \\ G_{MN}^{(\xi)} & = & \mathbf{G}_M^{(\xi)} \cdot \mathbf{G}_N^{(\xi)} & = & \frac{\partial X_k}{\partial \xi_M}\frac{\partial X_k}{\partial \xi_N} & g_{MN}^{(\xi)} & = & \mathbf{g}_M^{(\xi)} \cdot \mathbf{g}_N^{(\xi)} & = & \frac{\partial x_k}{\partial \xi_M}\frac{\partial x_k}{\partial \xi_N} \end{array} \tag{3.20}$$

3.2 Gaussian quadrature

The calculation of surface and volume integrals is essential when using the FEM. Often these integrals can not be determined analytically, especially when dealing with nonlinear problems such as finite elastic deformations. For this reason an efficient and accurate numerical method to determine the element integrals is required. The Gauss-Legendre quadrature integration scheme (hereafter referred to as Gaussian quadrature) satisfies these criteria by approximating an integral by a weighted sum of integrand evaluations using specified sets of independent variables.

3.2.1 Integration in one-dimension

The one-dimensional integral given in Equation 3.21 is approximated by a weighted sum of integrand evaluations, where w_i are the weighting factors and $\xi^{(i)}$ are the points at which the integrand, $f(\xi)$, is evaluated. These sampling points are commonly termed *Gauss points*. The error in the approximation is denoted by E_I, where I is the order of the quadrature scheme.

$$\int_0^1 f(\xi)d\xi = \sum_{i=1}^{I} w_i f(\xi^{(i)}) + E_I \tag{3.21}$$

To exactly integrate a cubic polynomial, two Gauss points are required. This is proven as follows. A general cubic polynomial incorporates four coefficients and may be written in the form shown in Equation 3.22.

$$f(\xi) = a + b\xi + c\xi^2 + d\xi^3 \tag{3.22}$$

Substituting Equation 3.22 into the integral on the left-hand-side of Equation 3.21 yields Equation 3.23.

$$\int_0^1 f(\xi)d\xi = a\int_0^1 1d\xi + b\int_0^1 \xi d\xi + c\int_0^1 \xi^2 d\xi + d\int_0^1 \xi^3 d\xi \tag{3.23}$$

This integral may be approximated using two Gauss points as shown in Equation 3.24.

$$\int_0^1 f(\xi)d\xi = w_1 f(\xi^{(1)}) + w_2 f(\xi^{(2)}) \tag{3.24}$$

To determine the $\xi^{(i)}$ positions and associated w_i weights, each integral on the right-hand-side of Equation 3.23 is evaluated analytically. The same integrals are then expanded using Equation 3.24, where the function f is chosen to be the corresponding integrand. The result is a set of four equations in four unknowns, as detailed in Equations 3.25 - 3.28.

$$\int_0^1 1d\xi = 1 = w_1 + w_2 \qquad \text{since } f(\xi) = 1 \tag{3.25}$$

$$\int_0^1 \xi d\xi = \frac{1}{2} = w_1\xi^{(1)} + w_2\xi^{(2)} \qquad \text{since } f(\xi) = \xi \tag{3.26}$$

$$\int_0^1 \xi^2 d\xi = \frac{1}{3} = w_1\left(\xi^{(1)}\right)^2 + w_2\left(\xi^{(2)}\right)^2 \qquad \text{since } f(\xi) = \xi^2 \tag{3.27}$$

$$\int_0^1 \xi^3 d\xi = \frac{1}{4} = w_1\left(\xi^{(1)}\right)^3 + w_2\left(\xi^{(2)}\right)^3 \qquad \text{since } f(\xi) = \xi^3 \tag{3.28}$$

The four Equations 3.25 - 3.28 are expressed in terms of the four unknowns, $\xi^{(1)}$, $\xi^{(2)}$, w_1 and w_2, and may be solved to determine the positions and weights (listed in Equation 3.29) unique to the quadrature scheme involving two Gauss points. Implicit in this derivation is the fact that Equation 3.24 is exactly satisfied since the four integrals on the

right-hand-side of Equation 3.23 are used in Equations 3.25 - 3.28 to calculate the Gauss positions and weights. Thus a polynomial of degree three can be exactly integrated using a Gaussian quadrature scheme with two Gauss points.

$$\begin{array}{rclcl} \xi^{(1)} & = & \frac{1}{2} - \frac{1}{2\sqrt{3}} & \qquad & w_1 = \frac{1}{2} \\ \xi^{(2)} & = & \frac{1}{2} + \frac{1}{2\sqrt{3}} & & w_2 = \frac{1}{2} \end{array} \tag{3.29}$$

This idea is extended when treating higher order polynomials. A Gaussian quadrature scheme with N sampling points (Gauss points) associated with N weights will exactly integrate a polynomial of degree $2N-1$. Note that if there are more than N Gauss points a polynomial of degree $2N-1$ will also be exactly integrated, although needless calculations will be performed reducing the efficiency of this scheme. Conversely, if the scheme incorporates less than N Gauss points (say $M < N$) then the error term in Equation 3.21 will be of the order of ξ to the $2M^{th}$ power. For example three Gauss points will exactly integrate a fifth order polynomial, but if only two Gauss points are chosen for the integration scheme, then E_I will be of the order of ξ^4.

3.2.2 Integration in two- and three-dimensions

To approximate surface and volume integrals using Gaussian quadrature, one-dimensional schemes are set up in each direction. Consider the function $f(\xi_1, \xi_2)$ which depends on the two variables ξ_1 and ξ_2 defined to lie in the surface of interest. The surface integral of f over its domain can be approximated by the two-dimensional Gaussian quadrature scheme expressed in Equation 3.30.

$$\int_0^1 \int_0^1 f(\xi_1, \xi_2) d\xi_2 d\xi_1 = \int_0^1 \left(\sum_{i=1}^{I} w_i f(\xi_1, \xi_2^{(i)}) + E_I \right) d\xi_1 = \sum_{i=1}^{I} \sum_{j=1}^{J} w_i w_j f(\xi_1^{(j)} \xi_2^{(i)}) + E_{IJ} \tag{3.30}$$

where a quadrature scheme with I Gauss points and weights is firstly employed in the ξ_2 direction ($\xi_2^{(i)}$ and w_i, respectively) followed by a scheme with J Gauss points and weights for the ξ_1 direction ($\xi_1^{(j)}$ and w_j, respectively). Note that the error term depends

on the choice of quadrature schemes in the ξ_1 and ξ_2 directions separately which, in general, may be different.

Similarly in three-dimensions, Equation 3.31 shows how to approximate a volume integral of $f(\xi_1, \xi_2, \xi_3)$ using Gaussian quadrature schemes with I, J and K Gauss points and weights in the ξ_3, ξ_2 and ξ_1 directions, respectively.

$$\int_0^1 \int_0^1 \int_0^1 f(\xi_1, \xi_2, \xi_3) d\xi_3 d\xi_2 d\xi_1 = \sum_{i=1}^{I} \sum_{j=1}^{J} \sum_{k=1}^{K} w_i w_j w_k f(\xi_1^{(k)}, \xi_2^{(j)}, \xi_3^{(i)}) + E_{IJK} \quad (3.31)$$

It should be noted that the limits on the integrals performed throughout this section have purposely been chosen as 0 and 1 for the following reason. For FE calculations, integrals are generally performed over the physical coordinate space of each element. The basis functions described in Section 3.1 map the spatial coordinates into the mathematical ξ-coordinate space and so the element integrals can also be transformed using the appropriate Jacobian. Thus the integrals required are now performed over the ξ_i-coordinate space for which $0 \leq \xi_i \leq 1$. Moreover, the integrands are polynomial-like, hence Gaussian quadrature is an ideal integration scheme for FE analysis.

3.3 Galerkin finite element equations for finite elasticity

The equations that govern large elastic deformations of deformable materials have been developed in Chapter 2. The framework has now been set to apply the Galerkin FEM to the stress equilibrium equations developed in Section 2.5.3. Additional constraints arise if the material is incompressible in nature, and if surface pressures are prescribed on external faces.

3.3.1 Galerkin equilibrium equations

The virtual displacement fields δv_j in Equation 2.63 are approximated by a FE displacement field in Equation 3.32 using interpolation functions Ψ_n developed in Section 3.1.

$$\delta v_j = \Psi_n(\xi_1, \xi_2, \xi_3) \delta v_j^n \quad (3.32)$$

where δv_j^n are arbitrary virtual nodal displacements.

Equation 3.32 is substituted into the equilibrium equations that govern finite deformation elasticity (Equation 2.63) and each component δv_j^n is considered in turn in Equation 3.33.

$$\int_{V_0} T^{\alpha\beta} F_\beta^j \, \Psi_n|_\alpha \, dV_0 = \int_{V_0} \rho_0 \left(b^j - f^j\right) \Psi_n dV_0 + \int_{S_2} p_{(appl)} \frac{g_{(\xi)}^{3M}}{\sqrt{g_{(\xi)}^{33}}} \frac{\partial \theta_j}{\partial \xi_M} \Psi_n dS \quad (3.33)$$

To evaluate the integrals in Equation 3.33, they must first be transformed from the reference coordinate space to the ξ_M-coordinate space using the appropriate Jacobian. The transformed integrals are written in Equation 3.34.

$$\begin{aligned} \iiint_{V_0} T^{\alpha\beta} F_\beta^j \, \Psi_n|_\alpha \sqrt{G^{(\xi)}} \, d\xi_3 d\xi_2 d\xi_1 = \iiint_{V_0} \rho_0 \left(b^j - f^j\right) \Psi_n \sqrt{G^{(\xi)}} \, d\xi_3 d\xi_2 d\xi_1 \\ + \iint_{S_2} p_{(appl)} \, g_{(\xi)}^{3M} \frac{\partial \theta_j}{\partial \xi_M} \, \Psi_n \sqrt{g^{(\xi)}} \, d\xi_2 d\xi_1 \end{aligned} \quad (3.34)$$

where $\sqrt{G^{(\xi)}} = \sqrt{\det\{G_{ij}^{(\xi)}\}}$ and $\sqrt{g^{(\xi)}} = \sqrt{\det\{g_{ij}^{(\xi)}\}}$ are the three-dimensional coordinate transformation Jacobians with respect to the undeformed and deformed configurations, respectively. Note that the surface integral is transformed by substituting $J_{2D} d\xi_2 d\xi_1$ for dS, where the two-dimensional Jacobian with respect to deformed coordinates is given by $J_{2D} = \sqrt{g^{(\xi)} g_{(\xi)}^{33}}$ (Oden 1972, p. 245).

The three-dimensional integrals in Equation 3.34 are evaluated over the undeformed volume and the two-dimensional integral is computed over the portion of the deformed surface (denoted S_2) for which external pressure loads are applied. These integrals are replaced by a sum of integrals over the collection of element domains which constitute the FE model. Element integrals are evaluated numerically using Gaussian quadrature (Section 3.2) and adjusted by the scale factors associated with the chosen interpolation scheme (see the discussion on scale factors in Section 3.1.3). Components of the second Piola-Kirchhoff stress tensor, $T^{\alpha\beta}$, are evaluated at each Gauss point using the constitutive equations (Equation 2.43) and the strain energy is calculated using the appropriate form of the strain energy function (see Sections 2.3 and 4.4.3 for further details).

Element integrals are then assembled back into Equation 3.34 to yield a global system of equations, in which there are three equations for each node of the FE mesh (one for each spatial coordinate direction). The unknown variables are the three coordinate displacements (or equivalently locations) for each node of the FE mesh, thus forming a square system. Note that this formulation is *isoparametric*, as it uses the same basis functions for the deformed coordinates (solution variables) as for the undeformed geometry (independent variables) (Zienkiewicz & Taylor 1994, p. 160). Further equations and unknowns arise if the material is incompressible (see Section 3.3.2) and pressure constraints are applied to external surfaces (see Section 3.3.3).

3.3.2 Galerkin incompressibility constraint

Equation 3.34 is sufficient to solve for the unknown nodal geometric displacements δv_j^n. For incompressible materials, an additional scalar hydrostatic pressure field is introduced into the constitutive equations (see Section 2.3). The extra constraint necessary to determine the parameters of the hydrostatic pressure field arise from the requirement that $I_3 = 1$ for incompressible materials. To reflect volume changes, the additional kinematic constraint $\sqrt{I_3} - 1 = 0$ is incorporated into the global system.

To be consistent when calculating stress components and to avoid numerical ill-conditioning, Oden (1972, p. 239) suggests that the interpolation scheme chosen to describe the deformed geometric coordinates should be of higher order than that chosen to approximate the hydrostatic pressure field. This arises because the strain energy contribution to stress components is related to the first derivatives of the geometric displacement fields, whereas the hydrostatic pressure directly contributes to the stress components (Equation 2.43). To be compatible the two contributions should vary in a similar manner.

For trilinear interpolation of the deformed geometric solution variables, the hydrostatic pressure field must be approximated using a piecewise constant scalar field to satisfy the compatibility condition. One auxiliary parameter is introduced per element and is simply the hydrostatic pressure within the element. One kinematic incompressibility constraint per element is introduced to produce a square system of equations, with matching numbers of unknowns and constraints. For a Galerkin formulation, the form

of the incompressibility constraints is given in Equation 3.35.

$$\int\int\int_{V_e} \left(\sqrt{I_3} - 1\right) \Psi^p \sqrt{G^{(\xi)}} d\xi_3 d\xi_2 d\xi_1 = 0 \tag{3.35}$$

where V_e denotes the domain of the element and Ψ^p are the basis functions used to approximate the three-dimensional hydrostatic pressure field ($\Psi^p = 1$ for constant element based pressure interpolation). Note that the undeformed three-dimensional Jacobian, $\sqrt{G^{(\xi)}}$, is introduced since the integrals are evaluated with respect to the undeformed configuration.

Alternatively, if cubic Hermite interpolation functions are used for the unknown geometric displacements, the compatibility condition permits trilinear interpolation of the hydrostatic pressure field. The desirable feature of this scheme is that the hydrostatic pressure field is implicitly piecewise continuous across element interfaces, which is essential for determining continuous stress distributions. The nodal hydrostatic pressure variables are determined using Galerkin constraints of the form in Equation 3.35, applied at each vertex of the element. In this case, the weighting functions Ψ^p are chosen to be the trilinear basis functions of Equation 3.10, and the hydrostatic pressure field is implicitly piecewise continuous across element interfaces.

3.3.3 Explicit pressure boundary constraints for the finite element equations

To ensure that the stress field on the external boundaries of the body exactly matches the applied pressure loads, an extra constraint may be introduced for each applied surface pressure. These ideas were originally introduced by McCulloch (1986) and have also been described by Costa, Hunter, Rogers, Guccione, Waldman & McCulloch (1996*b*), so a brief summary is included here.

For the case of element based interpolation of the hydrostatic pressure field, extra degrees of freedom are required to satisfy these constraints. The hydrostatic pressure field is thus extended to vary quadratically across each element (for convenience this variation is chosen to be in the ξ_3-direction), as in Equation 3.36.

$$P^e(\xi_3) = \sum_{i=0}^{2} P_i^e \Psi_i^P(\xi_3) \tag{3.36}$$

where

$$\Psi_0^P(\xi_3) = 1 \qquad \Psi_1^P(\xi_3) = \xi_3 \qquad \Psi_2^P(\xi_3) = 2\xi_3(\xi_3 - 1) \tag{3.37}$$

The constant hydrostatic pressure element variables, p_0^e, remain unchanged (see Section 3.3.2) and are determined using an element constraint of the form in Equation 3.35. The two extra element parameters, p_1^e and p_2^e, are determined by introducing the explicit surface traction constraints in Equation 3.38 into the global system.

$$\begin{aligned} \sigma_{(wall)}^{(33)}\Big|_{\xi_3=0} + p_{(in)} &= 0 \\ \sigma_{(wall)}^{(33)}\Big|_{\xi_3=1} + p_{(out)} &= 0 \end{aligned} \tag{3.38}$$

where $p_{(in)}$ and $p_{(out)}$ are the applied pressure loads at the centre of the $\xi_3 = 0$ and $\xi_3 = 1$ faces, respectively, and $\sigma_{(wall)}^{(33)}$ is the physical component of Cauchy stress normal to the centre of the deformed (ξ_1, ξ_2) face, which is defined in Equation 3.39.

$$\sigma_{(wall)}^{(33)} = \left(T^{\alpha\beta} \frac{1}{J} \frac{\partial \nu_\gamma}{\partial V_\alpha} \frac{\partial \nu_\eta}{\partial V_\beta} \right) \frac{\partial w_3}{\partial \nu_\gamma} \frac{\partial w_3}{\partial \nu_\eta} \tag{3.39}$$

where V_α and ν_γ denote the undeformed and deformed microstructural material coordinates, respectively, and w_3 denotes the (ξ_1, ξ_2) wall normal coordinate.

In Equation 3.39, the physical component of stress normal to the (ξ_1, ξ_2) surface is computed using two coordinate transformations. Firstly, the term in parenthesis transforms components of the second Piola-Kirchhoff stress tensor (referred to microstructural material coordinates in the undeformed state) into physical components of Cauchy stress referred to deformed microstructural material coordinates. This is achieved using the Jacobian and the deformation gradients with respect to the ν_α-material coordinate system. The second transformation computes the physical Cauchy stress component normal to the deformed (ξ_1, ξ_2) surface using derivatives of the wall normal coordinate with re-

spect to the ν_α-material coordinates.

For the case of trilinear Lagrange hydrostatic pressure interpolation, there are no explicit pressure boundary constraints and the applied boundary pressures contribute only to the equilibrium equations for finite deformation elasticity (Equation 3.34). The nodal hydrostatic pressure variables are determined using additional incompressibility constraints, of the form in Equation 3.35 (see Section 3.3.2).

The global nonlinear system is comprised of Equations 3.34 and 3.35, combined with Equation 3.38 if explicit pressure boundary constraints are required. The final step in the analysis is to solve the FE equations using a suitable nonlinear solution method. Section 3.4 briefly describes one common solution technique, known as Newton's method.

3.4 Solving the nonlinear finite element equations using Newton's method

The FEM for finite deformation elasticity requires a system of nonlinear equations to be solved over the domain of interest. It is convenient to rearrange the equations into a set of residuals (with zeroes on the right-hand-side), which must be minimised with respect to the set of solution variables. This set consists of the positions (or equivalently, the displacements) and arc-length derivatives in each of the coordinate directions, at each global node of the FE mesh. For incompressible problems additional variables arise from the description of the hydrostatic pressure throughout the domain as discussed in Section 3.3.2.

The residual equations are made up of rearranged forms of Equations 3.34 and 3.35. Additional residuals of the form in Equation 3.38 arise if explicit pressure boundary constraints are required to determine additional element based hydrostatic pressure variables. Equation 3.34 provides one equation for each coordinate direction (superscript j) at each node of the FE mesh (subscript n), plus additional equations associated with arc-length derivatives in each direction at each node. Further residuals arise from the incompressibility constraint (Equation 3.35) and any explicit pressure boundary constraints (Equation 3.38). Note that in all cases there are the same number of residuals as there are solution variables, comprising a square system of equations.

The residuals can be minimised using a nonlinear optimisation technique, such as Newton's method. As detailed below, this technique minimises a set of residuals using their first derivatives with respect to each of the solution variables to determine the parameter space search direction for the next solution iteration. For a more detailed description of Newton's method see Acton (1970, p. 367).

Consider the system of n nonlinear equations of the form $f_i(\mathbf{x}) = 0$, $(i = 1, \ldots, n)$, where $\mathbf{x}$ are the solution variables. With an initial estimate of the solution $\{x_i\} = \{a_i\}$, each function can be expanded about $\mathbf{a}$ in n-space using Taylor's series. Retaining only the linear terms in this expansion yields Equation 3.40, where $\{\delta_i\}$ represents the set of deviations from $\mathbf{a}$.

$$\begin{array}{ccccccccccc} f_1(\mathbf{a}) & + & \frac{\partial f_1}{\partial x_1}(\mathbf{a})\delta_1 & + & \frac{\partial f_1}{\partial x_2}(\mathbf{a})\delta_2 & + & \cdots & + & \frac{\partial f_1}{\partial x_n}(\mathbf{a})\delta_n & = & 0 \\ f_2(\mathbf{a}) & + & \frac{\partial f_2}{\partial x_1}(\mathbf{a})\delta_1 & + & \frac{\partial f_2}{\partial x_2}(\mathbf{a})\delta_2 & + & \cdots & + & \frac{\partial f_2}{\partial x_n}(\mathbf{a})\delta_n & = & 0 \\ \vdots & & & & & & & & & & \vdots \\ f_n(\mathbf{a}) & + & \frac{\partial f_n}{\partial x_1}(\mathbf{a})\delta_1 & + & \frac{\partial f_n}{\partial x_2}(\mathbf{a})\delta_2 & + & \cdots & + & \frac{\partial f_n}{\partial x_n}(\mathbf{a})\delta_n & = & 0 \end{array} \tag{3.40}$$

or

$$\mathbf{J}(\mathbf{a})\delta = -\mathbf{f}(\mathbf{a}) \tag{3.41}$$

where $\mathbf{J}$ is the Jacobian of derivatives evaluated at $\mathbf{a}$, and is defined in Equation 3.42 in terms if the solution variables $\mathbf{x}$.

$$\mathbf{J}(\mathbf{x}) = \begin{bmatrix} \frac{\partial f_1}{\partial x_1} & \frac{\partial f_1}{\partial x_2} & \cdots & \frac{\partial f_1}{\partial x_n} \\ \frac{\partial f_2}{\partial x_1} & \frac{\partial f_2}{\partial x_2} & \cdots & \frac{\partial f_2}{\partial x_n} \\ \vdots & & & \vdots \\ \frac{\partial f_n}{\partial x_1} & \frac{\partial f_n}{\partial x_2} & \cdots & \frac{\partial f_n}{\partial x_n} \end{bmatrix} \tag{3.42}$$

Equation 3.41 is a system of *linear* equations that can be solved using direct solvers such as the LU decomposition method (Press, Flannery, Teukolsky & Vetterling 1989, Sec. 2.3), which is suitable for small systems, or iterative solvers such as the generalised minimum residual (GMRES) method (Saad & Schultz 1986), which is more suitable for

large systems of equations. The solutions to the linear system are the set of deviations $\{\delta_i\}$, which are used to calculate the new approximation to the solution variables of the nonlinear system from the initial solutions a_i, using Equation 3.43.

$$x_i = a_i + \delta_i \qquad i = 1, \ldots, n \tag{3.43}$$

Convergence of Newton's method is highly dependent on the nonlinearity of the functions and the choice of the initial solution. For initial solutions sufficiently close to the true solution, convergence is quadratic. However, for more distant initial solutions, convergence of Newton's method is not guaranteed, especially when the functions possess large gradients with respect to the solution variables.

The initial solution for the FE equations for finite deformation analysis is chosen to be the undeformed mesh. Thus for small loads, which produce small displacements, convergence is likely. For larger loads the likelihood of convergence may be improved by splitting up the applied loads into incremental load steps, and applying them sequentially. This requires a nonlinear optimisation at each step, where the final solution from the previous load step is used as the initial solution for the current load step.

Section 6.4 details the implementation of the finite element method for finite elasticity, using Newton's method to solve the nonlinear system of equations. These techniques are used in Chapters 6 and 7 to analyse strain and stress in the deforming heart ventricles.

Chapter 4

Previous Mathematical Modelling of Cardiac Ventricular Mechanics

In comparison with typical engineering structures the mechanical behaviour of the heart is extremely complex. In order to understand how the heart functions it is necessary to use engineering mechanics techniques based upon mathematical models. Mathematical models have contributed greatly to our understanding of ventricular cardiac mechanics over the last few decades. They have evolved from simple axisymmetric shapes with isotropic, homogeneous material properties (Wong & Rautaharju 1968) to geometrically accurate models (Nielsen, Le Grice, Smaill & Hunter 1991) with detailed descriptions of the fibrous sheet microstructure of the myocardium (LeGrice, Smaill & Hunter 1992) and simulations of the cardiac cycle (Nash & Hunter 2001). With each improvement in the models has come greater understanding of cardiac function. This chapter provides a review of the significant steps in the evolution of cardiac ventricular modelling that have led to the developments described in this work, more detailed reviews of cardiac biomechanics modeling may be found in Yin (1981) and McCulloch (1995). Yin (1985) also presents are good review of cardiac ventricular models based on the finite element method.

To date most attention has been paid to the function of the the left ventricle because it provides the vital function of pumping oxygenated (pulmonary) blood to the systemic circulation. It was reported as early as 1915 (Starling 1915) that LV ejection rose with increased cavity volume at the end of diastole. He also suggested that the end-diastolic muscle fibre length was the most likely mechanism behind “The Law of the Heart”.

More recent studies (ter Keurs, Rijnsburger, van Heuningen & Nagelsmit 1980) have confirmed that the the force developed during isometric contraction increases with muscle stretch. These findings indicate that mathematical models of ventricular function must first predict physiologically realistic end-diastolic fibre strains in order to model ejection.

4.1 Thin Walled Models

Models for determining the ventricular wall stress were proposed as early as the late 1800's, but in the absence of computers they were based on analytical techniques. Woods (1892) modeled the LV as a simple thin-walled sphere with uniform internal pressure. The model approximated myocardial tension to be proportional to the product of pressure and radius. Similar techniques were used by Sandler & Dodge (1963) to model the ventricle as an axisymmetric ellipsoid, expressing the the wall stress in terms of wall thickness, the principal radii of curvature and the cavity pressure. These models are limited by the assumption that the thickness of the wall is much less than the radii of curvature, and by the omission of material properties. Nevertheless, estimates of the principal wall stresses could be obtained with simple measurements of ventricular pressure and geometry.

4.2 Axisymmetric Cylinder Models

A better first approximation of the LV's diastolic behavior is to model it as a homogeneous thick-walled cylinder with an internal pressure loading, applied torsion and extension. The myocardial tissue is assumed to be incompressible, isotropic and linearly elastic. Rivlin (1950, p.175) derived physical Cauchy stress components using the theory of finite deformation elasticity (presented in Chapter 2) for this model. Stress distributions based on Rivlin's analysis are compared with those computed using the Finite Element Method (Chapter 3) in Figure 4.1 for an example model (Table 4.1). The FE model model incorporated a single element with tricubic Hermite interpolation of the radial coordinate and trilinear Lagrange interpolation of the circumferential and longitudinal coordinates. Whilst both analysis techniques yield similar solutions for the

model presented, specialised analysis developed for simple geometries do not extend well to more complex geometries and deformation patterns (McCulloch 1986, Costa, Hunter, Rogers, Guccione, Waldman & McCulloch 1996*a*, Costa et al. 1996*b*).

Parameter	Value
External radius (cm)	1.5
Internal radius (cm)	1.0
Axial extension ratio	1.2
Cylinder length(cm)	1.0
Material Properties (kPa)	2.0, 6.0
External Pressure (kPa)	0.0
Internal Pressure (kPa)	1.5

TABLE 4.1: Model parameters for the closed form and FE analyses presented in Figure 4.1. The material is Mooney-Rivlin.

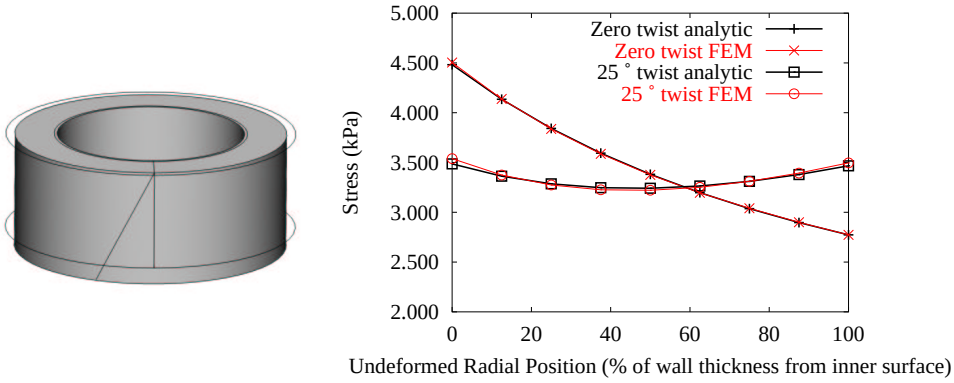

FIGURE 4.1: Axisymmetric cylinder model of an incompressible, isotropic and linearly elastic material (Table 4.1). The application of torsion reduces the transmural gradient of circumferential stress.

Despite its over-simplification of the physiology, this model revealed that an applied twist serves to reduce and balance the transmural distribution of circumferential stress. The heart twists and untwists of its own accord throughout the cardiac cycle. This alludes to the significance of the myocardium's microstructure.

Axi-symetric models also served in the development of constitutive laws for myocardium. Janz & Grimm (1973) developed a finite element model that characterised passive myocardium by a nonlinear constitutive relation.

The cylindrical models do not represent the geometry of the LV, and they are not closed at one end, therefore physiological loading conditions are difficult to simulate on such a simple model.

4.3 Axisymmetric Prolate-Spheroidal Models

Since the left ventricular geometry resembles a prolate spheroid, this can be taken advantage of. The *prolate-spheroidal* coordinate system, shown in Figure 4.2, is described by a *focus* or *focal length* d, two angular coordinates μ,θ and a measure of distance from the origin of the coordinate system λ. By formulating the FE model in prolate-spheroidal coordinates few degrees of freedom are required to model an axisymmetric thick walled prolate.

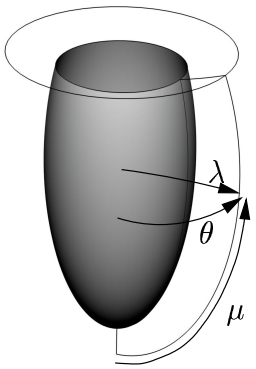

FIGURE 4.2: An axisymmetric prolate-spheroidal model.

These models have been very successful in elucidating some of the mechanisms of cardiac mechanics. McCulloch (1986) investigated the effects of the helical fibrous structure of the myocardium by comparing isotropic models with anisotropic models with realistic fibre fields, and confirmed that experimental observations were consistent with material anisotropy. It was also found in the anisotropic models that ventricular torsion resulted which substantially reduced the unrealistically high transmural gradients of fibre stress and strain that isotropic models had predicted. However, the axisymmetric models do not fully represent the complex LV geometry nor the RV at all, thus their usefulness is limited.

4.4 Anatomical Prolate-Spheroidal Models

To further understand ventricular mechanics a geometrically and structurally more realistic continuum model is necessary. The University of Auckland anatomical prolate-spheroidal canine model was developed by many researchers with significant steps being achieved through a sequence of doctoral theses (Hunter 1975, Nielsen 1987, LeGrice 1992, Nash 1998).

4.4.1 Geometry and Fibres

Nielsen (1987) used a rig (described in detail in Section 5.1.1) to complete the first detailed study of ventricular geometry and myocardial muscle fibre orientation. He then fitted a prolate-spheroidal finite element model to the geometric data and another nodally interpolated field to represent fibre data. The prolate-spheroidal coordinate system was chosen in the original model for its ventricle-like shape in order to reduce the number of degrees of freedom in the model. The canine ventricular continuum model shown in Figure 4.3 has since served as the basis for numerous studies of ventricular behaviour, both electrical and mechanical, by research groups around the world (Eason, Schmidt, Dabasinskas, Siekas, Aguel & Trayanova 1998, Huiskamp 1998).

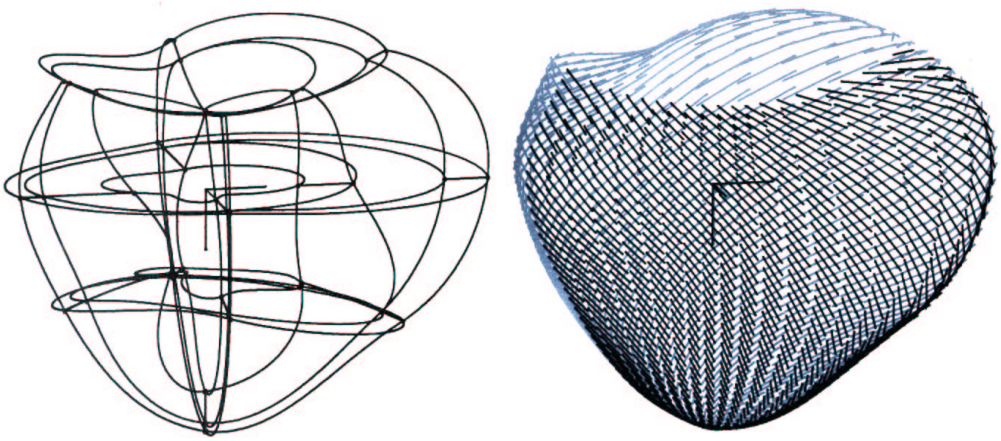

FIGURE 4.3: The first anatomically accurate continuum ventricular model (Nielsen 1987). Left: Prolate-spheroidal mesh. Right: Fitted epicardial fibre field.

4.4.2 Sheets

At that time the myocardial fibres were thought to be a uniformly branching continuum and material properties were therefore modelled as transversely isotropic. Then LeGrice (1992) showed by drying thin apex-base transmural segments that the myocardial fibres are in fact bound more tightly with some neighbouring fibres than others. The interconnections are arranged such that the fibres form a discrete laminar structure or sheets (Section 1.1.2). In the transmural plane, myocardial sheets run from endocardium to epicardium in a characteristic pattern which varies at different ventricular sites. Figure 4.4 shows an example specimen segment before and after drying to reveal the laminar sheet structure.

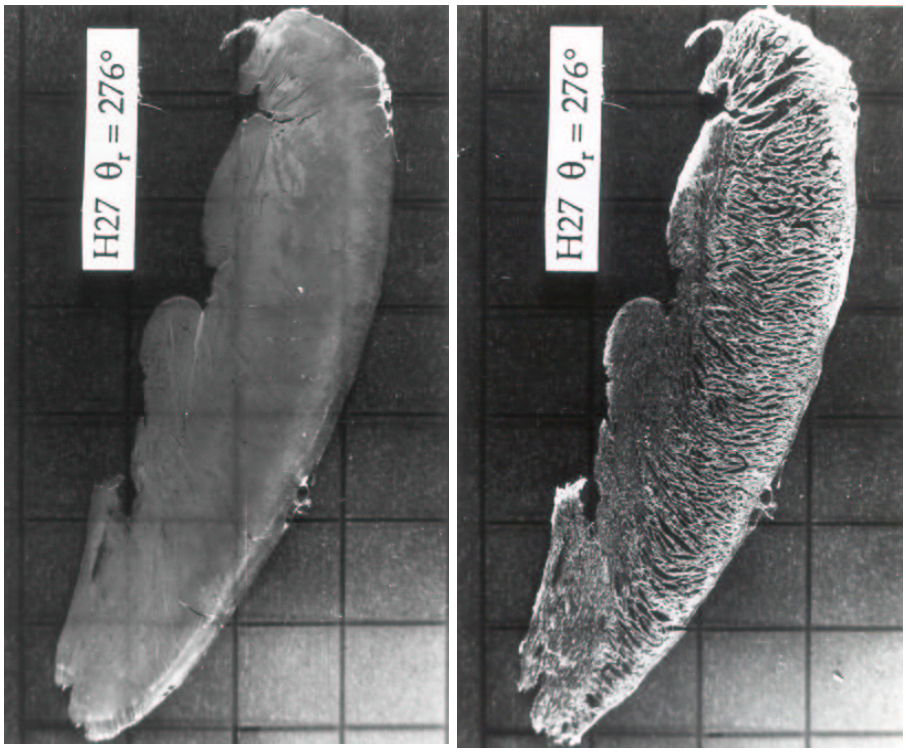

FIGURE 4.4: Longitudinal-transmural ventricular sections from a canine LV free wall, Left: Before drying. Right: After drying (LeGrice 1992).

LeGrice extended the anatomical ventricular canine model to incorporate a field representation of the laminar organisation of the myocardium. The techniques used to collect the data and fit the sheet field are described in more detail in Section 5.1.2 where they are repeated in the work for this thesis.

4.4.3 Mechanical Simulation

Nash (1998) used the LeGrice model and the finite element method based on finite elasticity theory to compute the ventricular deformation throughout the heart cycle. It is this last model developed at the University of Auckland that provides the starting point for the work completed in this thesis, and therefore this model is described in detail in the following sections.

In directions tangential to the local endo- or epicardial surface, the interpolation was cubic Hermite for the radial coordinate and linear Lagrange for the angular coordinates. In the transmural direction, all coordinates were interpolated linearly. The local finite element parametric coordinates were chosen to lie in the circumferential, longitudinal (apex-to-base) and transmural (though-wall) directions, respectively (see Figure 4.5).

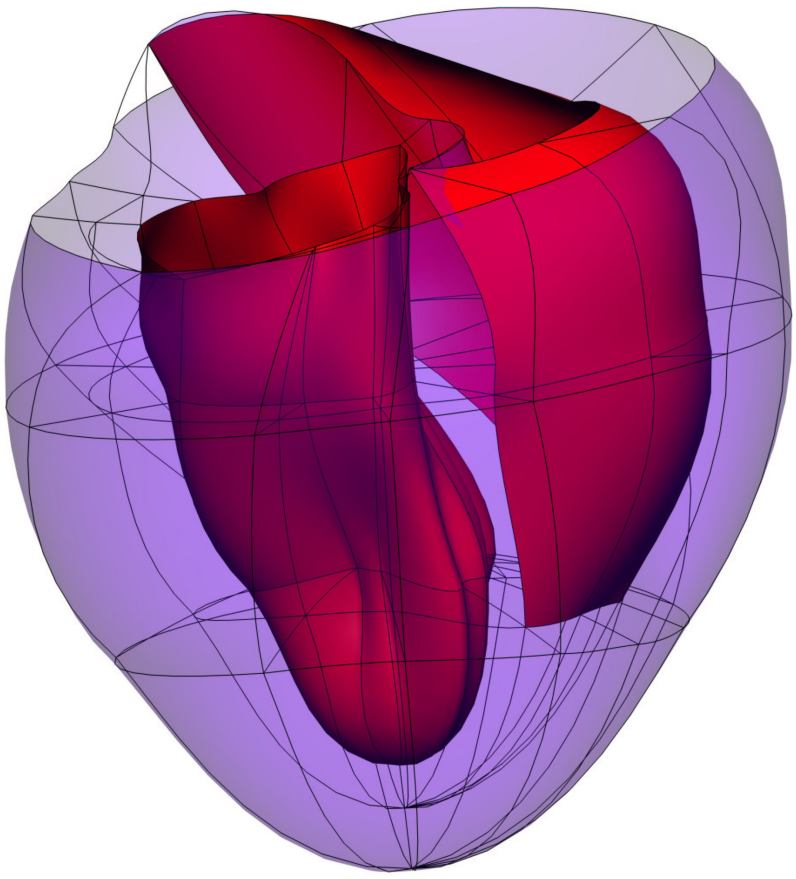

FIGURE 4.5: The anatomical prolate-spheroidal canine ventricular model.

The "Pole-Zero" Constitutive law for Myocardium

The nonlinear viscoelastic and poroelastic nature of myocardial tissue has been modelled before (Huyghe, Arts, van Campen & Reneman 1992, Yang & Taber 1991), but for simplicity this aspect of the material properties was neglected and the myocardium treated as an incompressible, elastic solid. For an incompressible material the components of the second Piola-Kirchhoff stress tensor are given by the derivatives of the strain energy function $W(\mathbf{E})$ (Equation 2.29) with respect to the components of $\mathbf{E}$ and a hydrostatic pressure, which does not contribute to the deformation, and hence strain energy of the material.

The parameters of such a constitutive law can be obtained directly from experiment without reference to the underlying tissue structure. But an approach which incorporates parameters that directly reflect mechanical or structural properties of the material yields a more useful constitutive relation. For example, observed spatial variation in collagen distributions can be related to material constitutive parameters.

Based on the stress-strain properties of ventricular myocardium described in Section 1.1.2, a constitutive law which incorporates material properties that can be directly estimated from the tissue was developed (Nash & Hunter 2001). The *pole-zero strain energy function* for myocardium is given by Equation 4.1.

$$\begin{aligned} W &= k_{11}\frac{E_{11}^2}{|a_{11}-E_{11}|^{b_{11}}} + k_{22}\frac{E_{22}^2}{|a_{22}-E_{22}|^{b_{22}}} + k_{33}\frac{E_{33}^2}{|a_{33}-E_{33}|^{b_{33}}} \\ &\quad + k_{12}\frac{E_{12}^2}{|a_{12}-E_{12}|^{b_{12}}} + k_{13}\frac{E_{13}^2}{|a_{13}-E_{13}|^{b_{13}}} + k_{23}\frac{E_{23}^2}{|a_{23}-E_{23}|^{b_{23}}} \end{aligned} \tag{4.1}$$

where the constitutive parameters (a's, b's and k's) have the following interpretations:

- the $a_{\alpha\beta}$ are the *limiting strains* or *poles* for each mode of deformation. They are physical properties of the tissue that may be measured directly from microstructural observations. In particular, MacKenna et al. (1994) used elastica theory on the collagen helices aligned with the myofibres to determine the yield strain (pole) of $a_{11} = 0.52$ along the fibre axis. Alternatively, these yield strains can be estimated by fitting the model directly to experimental stress-strain data (Smaill & Hunter 1991).

- the $b_{\alpha\beta}$ are related to the curvature of the uniaxial stress-strain relationships for each mode of deformation. These have been estimated using the biaxial test results of Smaill & Hunter (1991).

- the $k_{\alpha\beta}$ weight the contribution of the corresponding mode of deformation to the total strain energy of the material.

The terms in Equation 4.1 are naturally split into six groups, one for each mode of deformation. These groups correspond to the six independent terms of the Green's strain tensor. The first three terms refer to the *axial* modes of deformation, fibre, sheet and sheet-normal denoted 11, 22 and 33, respectively. The remaining terms relate to modes of *shear* deformation between the microstructural axes, fibre/sheet, fibre/sheet-normal and sheet/sheet-normal denoted by the subscripts 12, 13 and 23, respectively. The parameters associated with the axial terms were estimated using a combination of microstructural observations, biaxial tension tests and non-invasive magnetic resonance imaging (MRI) data. The shear parameters were determined using a biophysical model that assumes that certain shear deformations are strongly correlated to certain axial modes of deformation (Appendix A). The parameters used are given in table 4.2.

Type	Axial Properties	Shear Properties
Coefficients (kPa)	k_{11} 1.937	k_{12} 1.0
	k_{22} 0.028	k_{13} 1.0
	k_{33} 0.312	k_{23} 1.0
Poles	a_{11} 0.523	a_{12} 0.731
	a_{22} 0.681	a_{13} 0.731
	a_{33} 1.037	a_{23} 0.886
Curvatures	b_{11} 1.351	b_{12} 2.0
	b_{22} 5.991	b_{13} 2.0
	b_{33} 0.398	b_{23} 2.0

TABLE 4.2: Material properties of myocardium for the pole-zero constitutive law used in the canine model. Note that the poles, $a_{\alpha\beta}$, and curvatures, $b_{\alpha\beta}$, are dimensionless, but the coefficients, $k_{\alpha\beta}$, have units of stress.

Residual Strain and Stress in the Ventricular Wall

The concepts of residual stress and strain in the ventricular muscle were introduced in Section 1.1.2. To accurately predict myocardial stress the pre-existing stress in

the reference state of the model must be accounted for. The residual strains within the myocardium may be approximated by introducing the concept of a *growth tensor* (Rodriguez, Hoger & McCulloch 1994). The growth tensor, denoted $\mathbf{F_g}$, modifies the deformation gradient tensor of Equation 2.1 to account for the differences between the no-load state and the stress-free state of the ventricular wall.

$$F_M^i = \frac{\partial x_i}{\partial X_N} \cdot F_{gNM} \tag{4.2}$$

The elements of the growth tensor express deformation gradients relating the unloaded and stress-free states with respect to the microstructural material coordinates. The diagonal elements of $\mathbf{F_g}$ define the initial extension ratios due to the residual strains for the fibre, sheet and sheet-normal axes, respectively. The off-diagonal elements represent the residual shear deformation gradients.

Applying the growth tensor to a body upsets the internal equilibrium, because the created non-zero strain field is incompatible with the zero stress state. Therefore the residual stresses necessary for equilibrium with the modified strain field need to be determined. This is achieved by solving the model in the absence of external loads. This requires a stress-free reference configuration to which the computed strains (and hence stresses) are referred. However, the stress-free reference configuration is not available and is therefore approximated by the unloaded, residually stressed state for this solution procedure. This is reasonable since the displacements due to the residual stresses are presumably small (the effect of cutting the wall radially, to examine the deformation arising from these residual stresses, is discussed in Section 6.3.2).

The initial distribution of applied residual strain is listed in Table 4.3, the values were derived from Rodriguez et al. (1993).

Boundary Conditions

The model was used to simulate passive inflation to physiologically realistic LV and RV end-diastolic pressures of 1.0 kPa and 0.2 kPa, respectively.

The central RV epicardial node on the basal ring (shown by a ■in Figure 4.6) was fixed in the circumferential direction to prevent rigid body rotations, and the three apical

nodes (▲) were constrained to lie on the long axis of the LV for compatibility.

It was found that in the absence of any radial constraints the model predicted excessive radial expansion and wall thickening, and consequently the basal ring descended towards the apex to maintain tissue incompressibility. To counter this non-physiological behaviour a so called *pericardial-constraint* was applied by fixing the the radial (λ) coordinate of the epicardial nodes (●). Katz (1992, p. 366) commented that the pericardial sac plays an important role in limiting ventricular filling due to its low compliance.

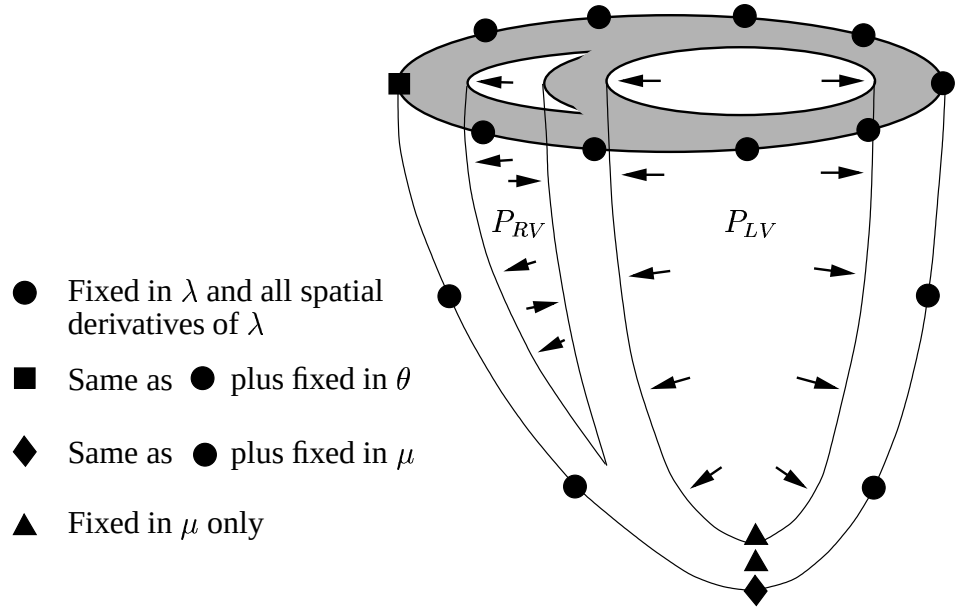

FIGURE 4.6: Schematic of the boundary conditions applied to the anatomical prolate model.

Ventricular region	Transmural location	Initial fibre extension ratio, λ_f^0
Equator	LV endocardium	0.95
	LV/RV epicardium	1.05
	RV endocardium	1.00
Base, Apex	all	1.00

TABLE 4.3: Initial fibre extension ratios applied to model residual strain in the passive myocardium.

4.4.4 Summary

The previously developed model of the canine ventricles successfully incorporated an anatomical description of the ventricular geometry and the non-homogeneous laminar microstructure. A fully orthotropic pole-zero constitutive law based upon the three-dimensional architecture of the myocardium was used to account for the nonlinear material response of resting cardiac muscle. However the model has the following limitations which prevent accurate representation of modes of deformation:

- The apical and basal anatomy is not accurately represented.
- The model is formulated in the prolate-spheroidal coordinates which constrains the motion of the apex to the axis of the coordinate system.
- The pericardial constraint boundary condition is excessively rigid.
- Myocardial fibres that lie oblique to the ventricular wall surfaces such as occur near the apex were not accounted for.
- The myocardial tissue is modelled as incompressible, but physiologically it is slightly compressible particularly in the subendocardium.
- Regional variations in material properties were not modelled.

A new porcine model is presented in the next two chapters to overcome some of these limitations.

Chapter 5

A Finite Element Model of the Porcine Ventricles

The pig is now the principal large animal used experimentally because the regional distribution of coronary vessels, extent of collateralisation and the heart to body weight ratio are more similar to humans than dogs (Bloor, White & Lammers 1986). Animal rights issues have also had an influence upon the which species can be used experimentally. Therefore it is necessary to have a computational model of the porcine ventricles to model and interpret experimental findings. The previous canine model made use of several simplifications in order to ensure that it was computationally efficient, including using the prolate-spheroidal coordinate system. Since the canine model was developed computer technology has improved dramatically rendering earlier simplifications no longer necessary. The porcine ventricular model developed in this thesis also seeks to address some of the deficiencies of the earlier model. It is developed in rectangular-cartesian coordinates and includes an accurate description of the basal region geometry.

5.1 Data Acquisition

The heart specimens were obtained from anesthetised pigs via a median sternotomy using the procedures detailed in Nielsen et al. (1991) with the exceptions that anesthesia was induced with Zoletil and maintained with 2.5% halothane in oxygen. The heart was then prepared for morphologic measurements which are detailed in the following

sections.

5.1.1 Ventricular Geometry and Myocardial Fibre Angle Measurement

The ventricular geometry and myocardial fibre angles of a 24 kg pig heart were measured by LeGrice and coworkers in a manner similar to the earlier study performed on the canine heart (LeGrice 1992).

To prepare the heart for measurement, the atria were removed and a stainless steel spindle was inserted through the fibrous tissue between the mitral and aortic valves and though the apex. Pins attached to a plate on the end of the spindle were passed though the valve orifices into the left and right ventricular cavities. The ventricular cavities were then filled with silicone rubber under water. The endplate assembly ensured that the heart was firmly located with respect to the spindle even as parts of the myocardium were later dissected away.

The spindle was inserted in a specially designed rig (Figure 5.1)[1]. For each data point measurement, a vertically mounted probe was wound down until its tip touched the surface of the heart. A small lamp projected the shadow of a horizontal pin, attached to the side of the probe near the tip, onto the myocardial surface. The probe was rotated about its axis to align the shadow with the fibre direction. The rig was attached to a computer which recorded the the spindle angle, probe height and rotation in cylindrical polar coordinates at the operators command. However, the rotation of the pin was not the same as myocardial fibre angle since the shadow was projected on an inclined myocardial surface. This was accounted for in subsequent post-processing of the data.

Data was acquired at 5 mm intervals from apex to base and 4 degree increments in the spindle angle. To record fibre angles though the heart wall, after each complete revolution of data acquisition, a layer of tissue approximately 0.5 mm thick was removed over the entire surface. The axial and radial coordinates were reproducible to 0.3 mm and the angular coordinate to 1.2 degrees.

The rig design prevented accurate acquisition of the heart's base plane geometry because the probe approaches the base tangentially. It was not possible to accurately digitise the

[1]The rig was initially designed and built by Peter Hunter during post-doctoral work at Oxford University. Later, Nielsen (1987) added a mechanism for computerised data acquisition.

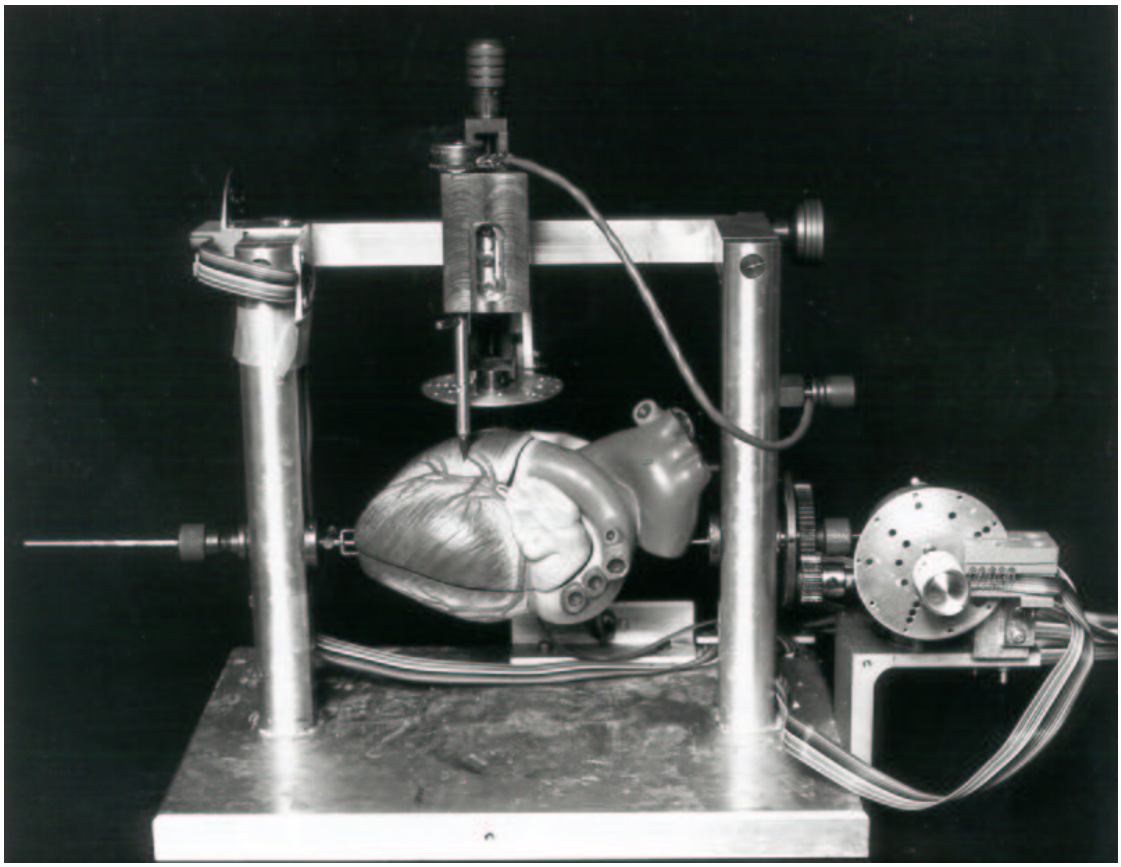

FIGURE 5.1: The ventricular geometry and myocardial fibre angle acquisition rig (loaded with a plastic anatomical model).

valve ring geometry with this rig, nor measure fibre angles in the base plane. Therefore another three-dimensional digitisation device called a *FaroArm* produced by Faro Technologies Inc[2]. was also used. The FaroArm, shown in Figure 5.2, is a multiple axis articulated arm with a spherical working volume. Each joint has a rotary transducer. The signals from these transducers are sent to a computer which acquires the rectangular cartesian coordinates of the probe tip within an accuracy of 75 μm. The FaroArm was used to digitise the epicardial valve orifice geometry and the basal regions that were unreachable with the rig.

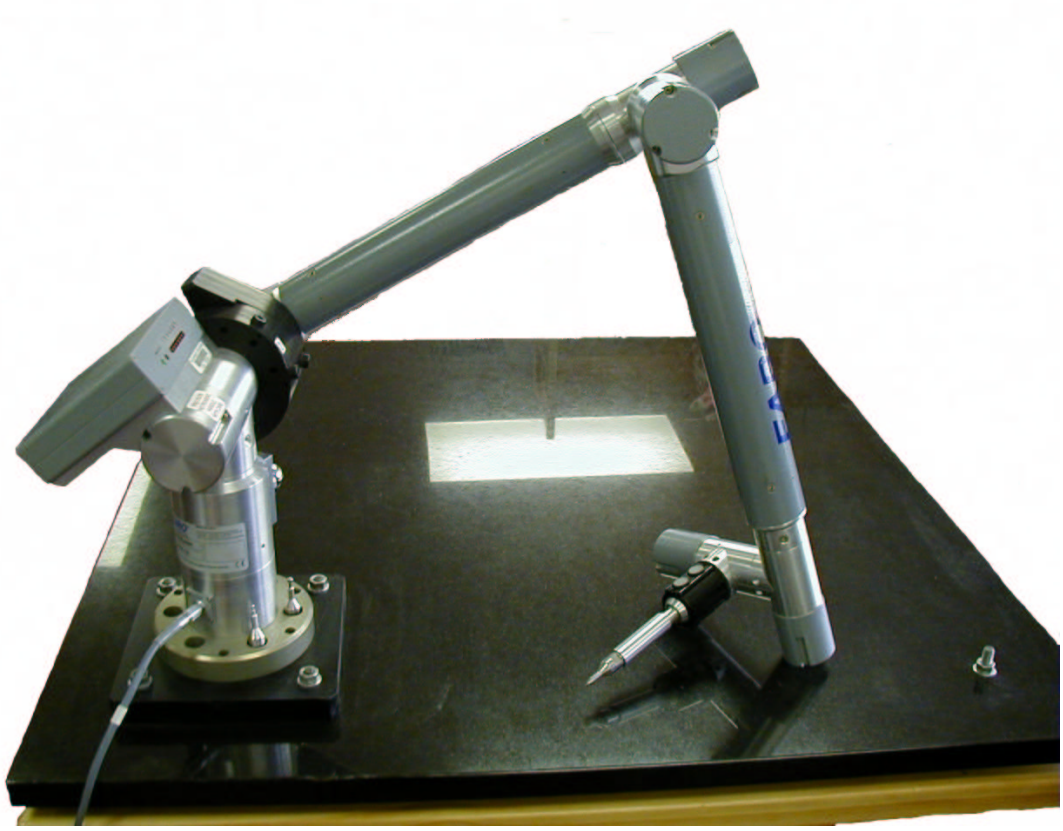

FIGURE 5.2: The FaroArm used to digitise the valve ring geometry

In order to be able to combine the two sets of data, three reference pins were inserted into the myocardium, two near the base in each ventrical's free wall, and the other near the apex. The pin's locations were digitised using both the rig and the FaroArm. A transformation matrix to rotate and translate the FaroArm data to align with the rig data

[2] `http://www.faro.com`

was computed using a nonlinear optimisation. The sum of the squared distances between the reference points in each data set was minimised to 0.2 mm. Figure 5.3 shows the combined epicardial data sets and reference points.

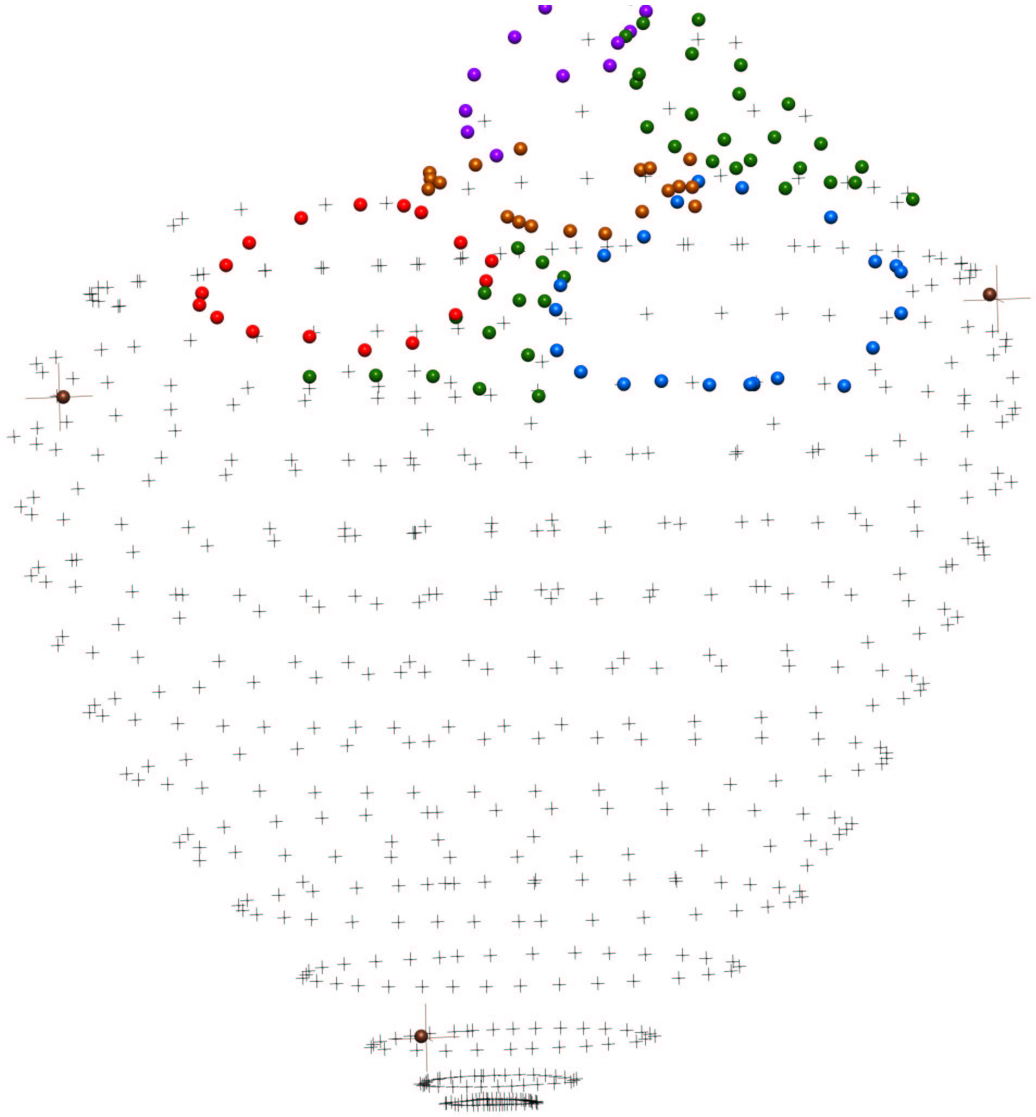

FIGURE 5.3: Combined epicardial data sets and reference points from the rig and the FaroArm. The rig data is plotted using crosses and the FaroArm data using spheres. The mitral valve data is red, the aortic brown, tricuspid blue, and the pulmonary valve data is purple. The green data are epicardial surface points that were unreachable in the rig, between the valves and the top of the pulmonary outflow tract.

The myocardial fibre angles in the basal region of the RV free wall and the top of the

pulmonary outflow tract could not be measured in the rig because the base was nearly tangential to the probe. Instead reference pins were inserted into the pulmonary outflow tract, digitised in the rig and then that piece of tissue was dissected out. The removed piece of myocardium was then pinned onto a cylinder and placed in the rig to measure the fibre angles relative to a pair of the reference pins.

5.1.2 Myocardial Sheet Angle Measurement

Another heart from a 25 kg pig was prepared as described above, since the fibre orientation measurement technique prevented the sheet orientation data from being acquired from the same heart.

The surface geometry was measured along 30 meridians spaced at 12 degree intervals around the heart. Base-apex transmural segments were cut from the heart along each of these meridians in the (x,r)-plane. Initially wedges were cut from the RV free wall exposing the silicon rubber cast of the RV. The geometry of the RV free wall endocardium was then recorded along the same meridians on the cast. The RV cast was then removed and the geometry of the RV septal endocardium was recorded. Finally the LV free wall and septal myocardium was cut into 30 segments along the meridian and the LV endocardial geometry was measured from the silicone cast of the LV lumen.

To reveal the transmural and circumferential myocardial sheet organisation a technique of cutting and drying full length (apex to base) frozen sections was used. A longitudinal transmural section was cut from each of the 30 wedges described above. 80 μm thick sections were then cut from corresponding surfaces of each myocardial wedge using a sledge microtome. These sections were carefully floated onto a 120 mm x 60 mm x 1 mm polycarbonate sheet. The specimen plate was then drained and placed on a transparent acetate sheet marked with a 10 mm square grid representing the (x,r)-plane. The slide was oriented so that shallow epicardial cuts that had been made around the circumference of the heart near the apex and base were aligned with the appropriate axial coordinates on the grid below and so that the radial coordinates matched those measured on the geometry rig. In this way the section was positioned in the (x,r)-plane, in the identical location that it was before being removed from the intact heart. Digital images of the sections were taken before and after drying were compared to check for shrinkage. For meridians transecting both RV free wall and septum, a section was cut

from each block and these were processed together on the same slide.

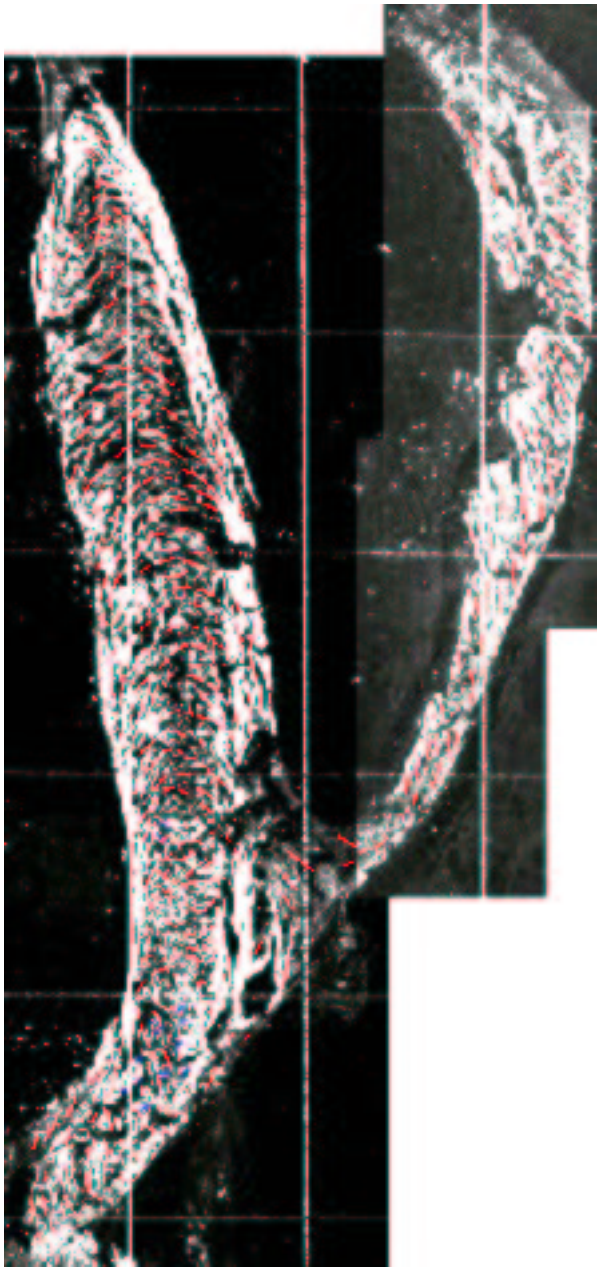

FIGURE 5.4: Longitudinal-transmural ventricular section after drying, with sheet orientation vectors. To the left is the inter-ventricular septum and the RV free wall is shown on the right.

Digital image analysis was used to quantify the sheet orientations. The analysis was per-

formed on a Macintosh computer using the public domain NIH Image program[3]. The muscle layer orientations were recorded from the 30 transverse sections with approximately 550 observations recorded from each section. At each observation point a short vector was drawn parallel to the local sheet direction using the computer mouse. The cylindrical polar coordinates of the point was recorded along with the vector orientation. Since the camera lens system limited the maximum area of section imaged at one time it was necessary to process several images to cover the whole section. Figure 5.4 shows a dried ventricular section prepared for measurement.

5.2 Model Creation

The design of the finite element model presented here varies significantly from those presented to date. With the increased computational power available it is possible to include more physiological detail in the model while still retaining a reasonable solution time. The model developed in this thesis increases the order of the geometric and microstructure interpolation to fully tricubic Hermite, and changes the reference coordinate system to rectangular cartesian for reasons provided below. An innovative mesh design and alterations to the computational implementation have allowed the total number of nodes and elements to be reduced from the number required in the anatomical prolate model presented in Section 4.4.3, while capturing more detailed ventricular physiology.

5.2.1 Coordinate System

Like most of the ventricular models developed to date the Auckland canine model took advantage of the left ventricle-like prolate-spheroidal coordinate system to reduce the number of degrees of freedom in the model. However, the use of the prolate-spheroidal coordinate system imposes constraints on the model that may not be completely physiological. The prolate-spheroidal coordinate system imposes limits on the geometry of the model. For example, the complicated geometry of the basal region cannot be accurately represented and the apex is constrained to lie on the axis of the coordinate system. Deficiencies in the geometric description result in non-physiological boundary

[3]Developed at the U.S. National Institutes of Health and available from `http://rsb.info.nih.gov/nih-image`

conditions being applied and less physiological model behaviour, such as the "pericardial constraint" which prevents radial expansion during diastole. The rectangular-cartesian coordinate system was chosen for the development of a new porcine model since the computational efficiency aspect of the model no longer outweighs the need for including more physiological complexity. Using rectangular-cartesian coordinates also increases the usability of the model for other research efforts within the Auckland University Bioengineering Institute and the wider Physiome project[4].

Before fitting, the geometric data was transformed from the original cylindrical-polar coordinates to rectangular cartesian coordinates. The *z*-axis is aligned with the axis of the cylindrical polar coordinate system in which the data was acquired, from base to apex. The *x*- and *y*-axes lie in the base plane.

5.2.2 Geometric and Field Fitting With Finite Elements

Measured data is usually in the form of a non-uniform discrete data set. However, mathematically it is more useful to have the information as a continuous field. The node points of a finite element model define continuous fields which can be evaluated at any point within the domain using the standard interpolation formula given in Equation 3.1. To represent the measured discrete data set with a continuous finite element model, the model must be *fitted* to minimise the difference between to the two representations.The choice of measure for the difference or *error* depends upon the field to be fitted and desired qualities in the final result.

First we shall consider the *geometric fitting problem*, where given a set of data defining the geometry, the nodal positions and derivatives, for a given mesh, must be found that minimises the error in the mesh approximation to the data.

For each point in a set of rectangular cartesian data with geometric locations z_d, $d = 1, ..., D$, a point on the mesh with the shortest distance to that data point can be found. This point is termed the *orthogonal projection* of the data point onto the mesh. The length of the orthogonal projection provides the measure of error, illustrated in Figure 5.5.

To calculate the ξ coordinate of a data point projection, ξ_d, a non-linear iterative procedure is required. Given a starting ξ position for the data point projection, the geometric

[4] `http://www.bioeng.auckland.ac.nz/physiome/physiome.php`

position is given by the standard interpolation Equation 3.3. An error function can then be set up as the Euclidean distance between this point and the actual position of the data point. The local ξ position that minimises this function can then be found using the Newton-Raphson root finding method on the derivative of this function. This ξ position is effectively the orthogonal projection of the data point onto the finite element.

Geometric fitting is just a particular case of field fitting, in which the fields are the geometric coordinates. The general *field fitting problem* can then be formulated as a minimisation procedure in which the objective is to minimise the sum of squared differences over all the data points, between the known value at each data point, u_d, and the finite element field approximation evaluated at the projected ξ_d position of the data point, $u(\xi_d)$, *i.e.*,

$$\min F(u) = \sum_{d=1}^{D} [u(\xi_d) - u_d]^2 \tag{5.1}$$

The field value at a given ξ location $u(\xi_d)$ can be interpolated from the nodal field values (u_n) of the element by Equation 5.2.

$$u(\xi_d) = \varphi_n(\xi_d) u_n \tag{5.2}$$

where $\varphi_n(\xi_d)$ represents basis function n evaluated at ξ_d. The sum of squared differences

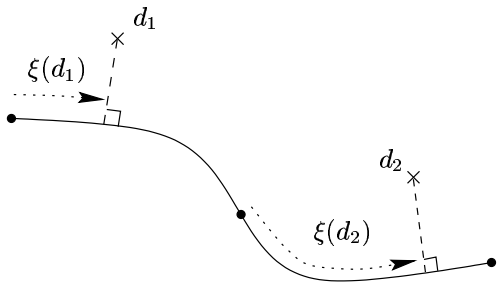

FIGURE 5.5: Schematic of orthogonal data point projections. The dashed lines show the projections onto a mesh, and their positions in parametric coordinates ξ_d are illustrated within each element.

between this value and the measured value u_d for all the data points ($d = 1, .., D$) is

$$\Upsilon = \sum_{d=1}^{D} \left(\varphi_n(\xi_d) u_n - u_d\right)^2 \tag{5.3}$$

Minimising Υ with respect to the nodal parameters u_m results in

$$\frac{\partial \Upsilon}{\partial u_m} = 2 \sum_{d=1}^{D} \left(\varphi_n(\xi_d) u_n - u_d\right) \varphi_m(\xi_d) = 0 \qquad m, n = 1, \ldots, N \tag{5.4}$$

$$\text{or} \qquad \left(\sum_{d=1}^{D} \varphi_m(\xi_d) \varphi_n(\xi_d) \right) u_n = \sum_{d=1}^{D} \varphi_m(\xi_d) u_d \qquad m, n = 1, \ldots, N \tag{5.5}$$

This can then be assembled into a global system of equations $E_{mn} u_n = F_m$ where

$$\begin{aligned} E_{mn} &= \sum_{d=1}^{D} \varphi_m(\xi_d) \varphi_n(\xi_d) \\ F_m &= \sum_{d=1}^{D} \varphi_m(\xi_d) u_d \end{aligned} \tag{5.6}$$

and u_n are the unknown field values at each finite element node n. The solution of this system of equations gives the fitted nodal field values and derivatives.

During this fitting process the scale factors and data point projections are held constant, therefore the resultant mesh may not completely minimise the error. Hence it is necessary to iteratively apply the fitting procedure in order to obtain a mesh that best fits the data. The fit can be considered converged when the root mean squared, RMS, error in the fit does not change significantly between iterations. The RMS error of the fit is defined as

$$\text{RMS error} = \sqrt{\frac{\sum_{d=1}^{D} \|u(\xi_d) - u_d\|^2}{D}} \tag{5.7}$$

The fitting algorithm used in this thesis is as follows:

1. Define an initial mesh (and calculate the initial scale factors).
2. Calculate the initial data point projections and initial error in the mesh.
3. Repeat until converged or the maximum number of iterations is exceeded:

- Fit the mesh by applying the fitting procedure;
- Update the scale factors to be harmonic mean arc-lengths based on the new mesh;
- Recalculate the data point projections on the new mesh.

Sobelov Smoothing

If the objective function is only measured in terms of deviation from the data points as in Equation 5.1 and in some locations there is a lack of data points, the finite element field representation may deviate in an undesirable manner without affecting the objective function. This can be treated by introducing a smoothness constraint (Young, Hunter & Smaill 1989) by adding a second term to the objective function.

$$\min F(u) = \sum_{d=1}^{D} [u(\xi_d) - u_d]^2 + \int_{\Omega} g(u(\xi)) d\xi \tag{5.8}$$

The first term in Equation 5.8 measures the error in the data from the surface while the second term measures the deformation of the surface. The deformation is measured using a p^{th} order weighted Sobelov norm (Terzopoulos 1986) defined by

$$g_{p,w}(x) = \sum_{q=0}^{p} \sum_{i,j(i+j=q)}^{n} \omega_{ij} \left\| \frac{\partial^q x}{\partial \xi_1^i \partial_2^j} \right\|_2 \tag{5.9}$$

where ω_{ij} are the weighting values applied to the component of $g(x)$. The addition to the objective function, called the *Sobelov value*, is defined as

$$G(x) = \int_{\Omega} g(x) d\Omega$$

where Ω is the mesh domain.

For a two-dimensional surface, the smoothing constraint is given by

$$\begin{array}{ll} \int_\Omega g(u(\xi))d\xi = \int_\Omega & \alpha \left(\left\| \frac{\partial u}{\partial \xi_1} \right\|_2 + \left\| \frac{\partial u}{\partial \xi_2} \right\|_2 \right) \\ & \beta \left(\left\| \frac{\partial^2 u}{\partial \xi_1^2} \right\|_2 + 2 \left\| \frac{\partial^2 u}{\partial \xi_1 \partial \xi_2} \right\|_2 + \left\| \frac{\partial^2 u}{\partial \xi_2^2} \right\|_2 \right) d\xi \end{array} \tag{5.10}$$

The parameter α controls the tension of the surface and parameter β controls the degree of surface curvature. The weighting values α and β are chosen manually to ensure the fitted fields vary physiologically (Young et al. 1989).

5.2.3 Valve Rings

The valve rings form the basis of the basal skeleton, the structure to which the ventricles are attached. Therefore their location and geometry in the model are important. The first step in creating the full ventricular model was to model the geometry of each of the valve annuli. One-dimensional cubic Hermite elements were fitted to the epicardial valve orifice data collected with the FaroArm. The number of nodes and their initial positions were chosen to facilitate their inclusion in the full ventricular mesh.

Fits of each of the fitted orifices are plotted in Figure 5.6, their relative locations are shown in Figure 5.7, and Table 5.1 lists the results of each fit.

The degrees of freedom that described these elements were included as fixed parameters in the fitting of the ventricular surface meshes.

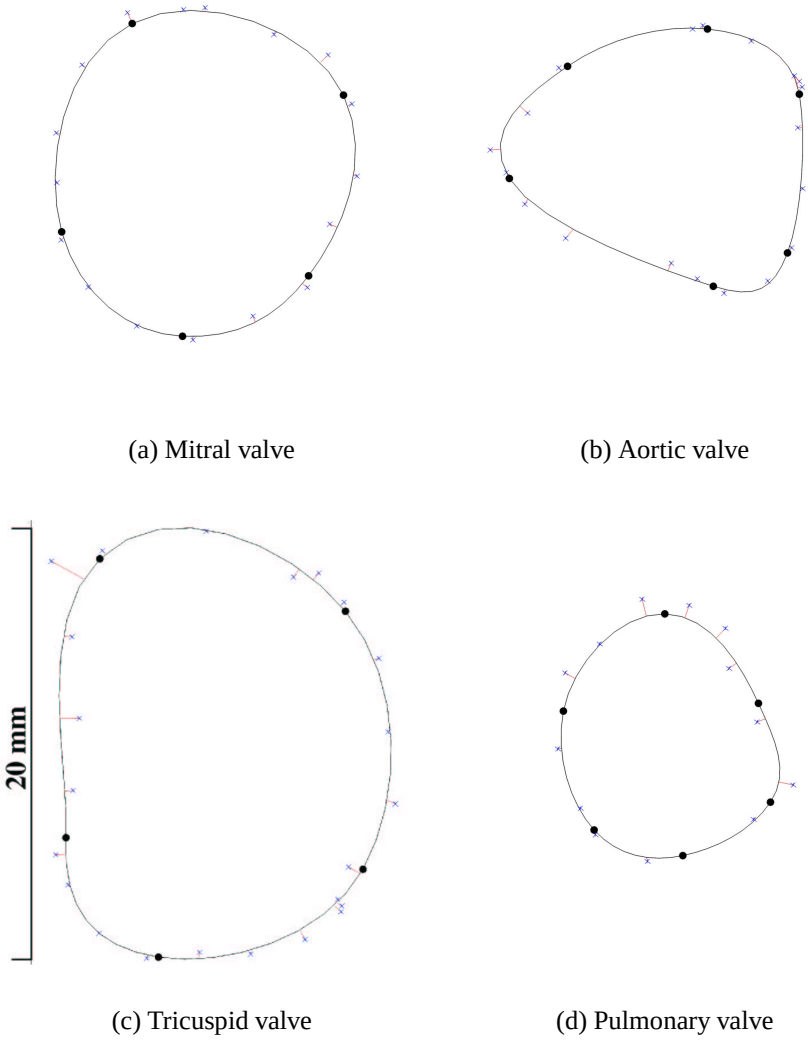

(a) Mitral valve (b) Aortic valve

(c) Tricuspid valve (d) Pulmonary valve

FIGURE 5.6: Fitted valve orifice geometries with raw data and error projections. The four valves are plotted using the same scale.

5.2.4 Left Ventricular Endocardium

The left ventricular endocardial surface was fitted with 54 bicubic Hermite elements. The elements at the apex are collapsed along one side by using the same node twice to

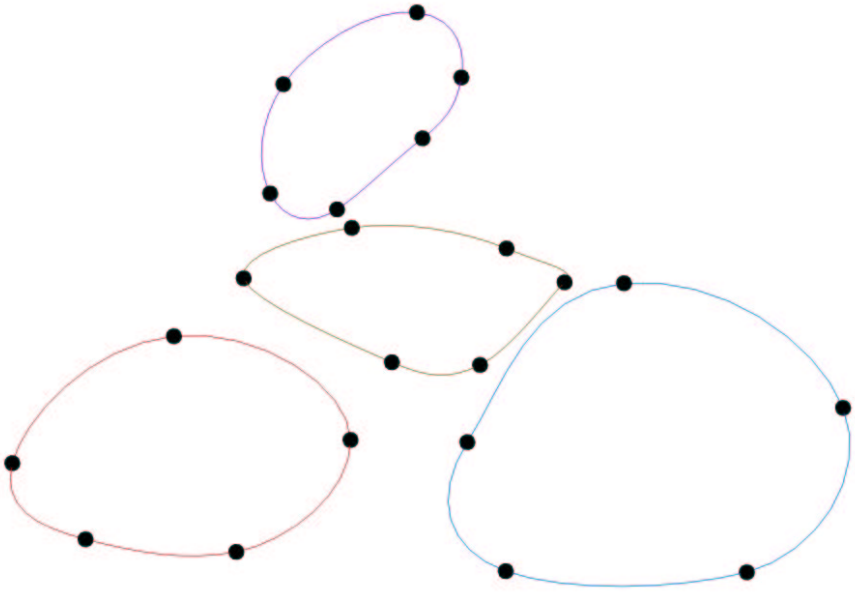

FIGURE 5.7: A projected view from the basal short-axis plane of the fitted valve ring geometries. The mitral valve is red, the aortic brown, tricuspid blue, and the pulmonary valve is purple.

Valve Orifice	Nodes	Data Points	RMS Error (mm)
Mitral	5	17	0.47
Aortic	6	19	0.75
Tricuspid	5	23	0.83
Pulmonary	6	13	0.75

TABLE 5.1: Summary of valve orifice fitting results.

form triangular elements. There are 9 versions of the derivative degrees of freedom at the apical node.

The nodal derivatives and element scale factors determined from the mitral and aortic annuli fits were fixed input variables for the corresponding degrees of freedom in the ventricular surface mesh.

An element has been omitted on the septal wall side between the two valves. That is where the connective tissue that forms the bridge between the valves is attached. The surface mesh is designed such that it can be connected into the full volume mesh later.

Surface data corresponding the papillary muscle is included in the fitting but tendon data is ommited. The mesh design and Sobelov smoothing have the effect of truncating the papillary muscles to bumps on the surface.

The parametric coordinate ξ_1 is aligned approximately circumferentially and the ξ_2 coordinate longitudinally. Figures 5.8 and 5.9 plot the fitted LV endocardial geometry, 888 data points were used in the fit with a resultant RMS error of 0.93 mm.

5.2.5 Right Ventricular Endocardium

36 bicubic Hermite elements were used to fit the right ventricular endocardial surface. The parametric coordinate ξ_1 is aligned approximately circumferentially and the ξ_2 coordinate longitudinally. The tricuspid valve orifice degrees of freedom already determined were fixed in the fit. The previously fitted pulmonary valve orifice was not included this surface mesh. A hanging node was used at the top of the pulmonary outflow tract to provide the degrees of freedom necessary to represent the orifice without the extra computational expense of an extra column of elements from apex to base.

The RV endocardial geometry fit used 327 data points, and had an accuracy of RMS 1.37 mm. Figures 5.10 and 5.11 show the fitted geometry.

Two versions of the derivative variables are used to join the septal and free wall surfaces where the connection is not smoothly continuous. Along the lower edge of the cavity the two versions of nodal derivatives with respect to ξ_1, for the septal and free wall surfaces, are constrained to be equal and opposite. Similarly at the surfaces connection between the two valve orifices.

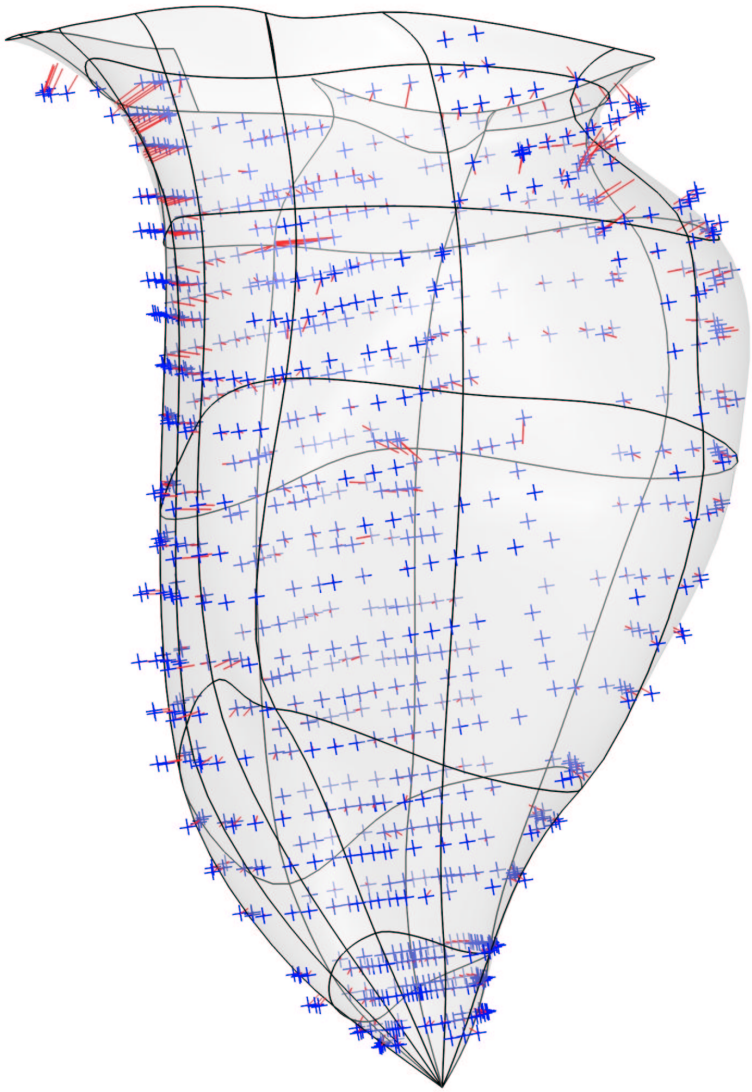

FIGURE 5.8: Fitted left ventricular endocardial surface geometry with raw data and error projections.

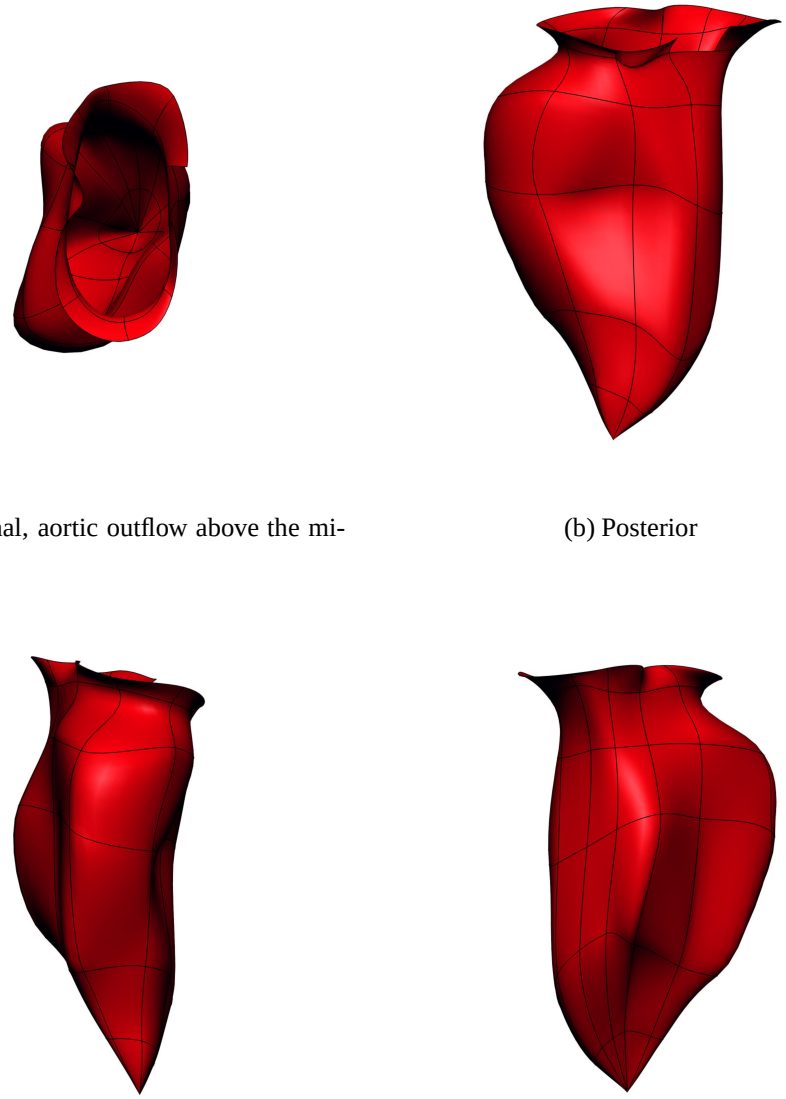

(a) Coronal, aortic outflow above the mitral inlet

(b) Posterior

(c) LV free wall

(d) Septum and anterior

FIGURE 5.9: The fitted left ventricular endocardial surface.

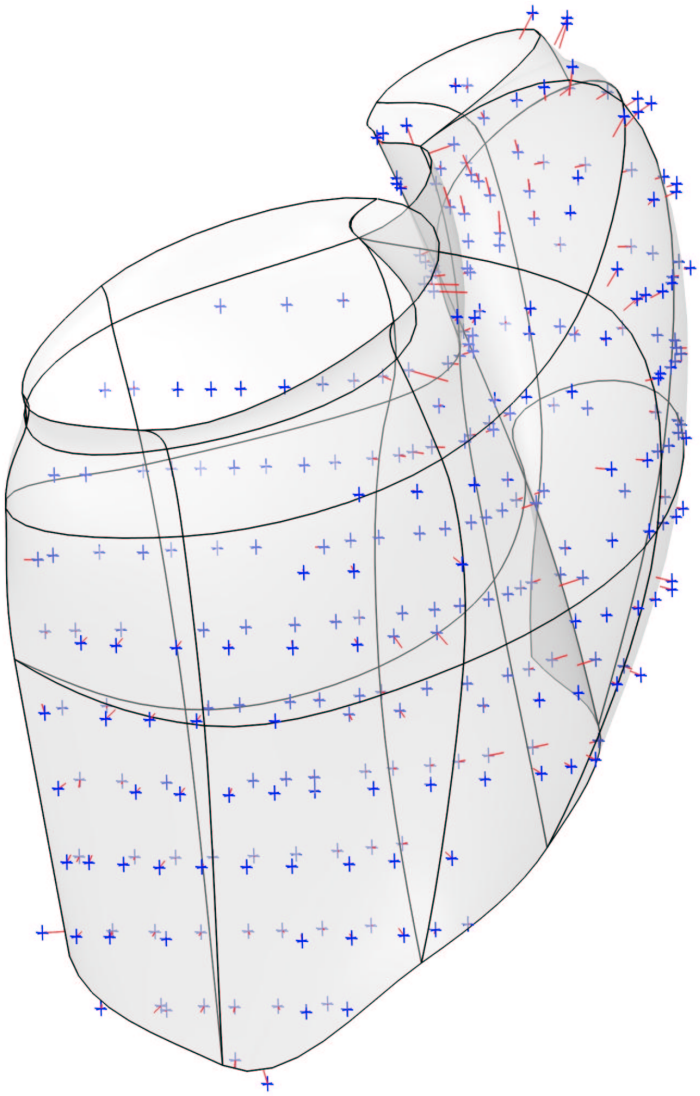

FIGURE 5.10: Fitted right ventricular endocardial surface geometry with raw data and error projections.

5.2.6 Epicardium

The epicardial surface was fitted with 63 bicubic Hermite elements. The mitral, aortic and tricuspid valve orifices degrees of freedom were fixed to the values already used in the LV and RV endocardial surface fits for compatibility. The pulmonary valve orifice was fitted since the mesh does not extend completely to the digitised annulus. As with the RV endocardial surface fit, a hanging node was used at the top of the pulmonary outflow tract to provide the degrees of freedom necessary to represent the orifice.

The parametric coordinate ξ_1 is aligned approximately circumferentially and the ξ_2 coordinate longitudinally. However, the complicated basal geometry prevents the construction of a completely C^1 continuous mesh. Instead, multiple versions of the derivative quantities are employed to provide the necessary connections between the annuli. Multiple versions of the derivative variables are also used at the apical node.

Plots of the fitted epicardial geometry are presented in Figures 5.12 and 5.13. 575 data points were used in the fit which had an RMS accuracy of 0.55 mm.

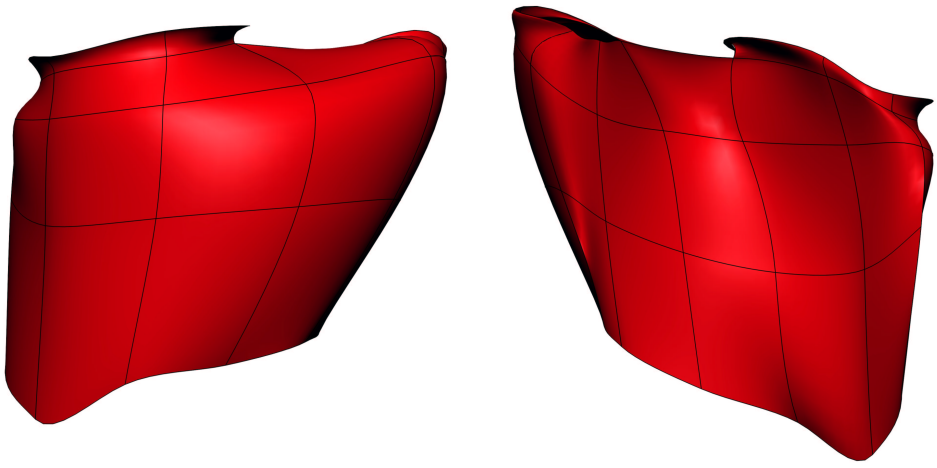

(a) RV free wall (b) Septal wall

FIGURE 5.11: The fitted right ventricular endocardial surface.

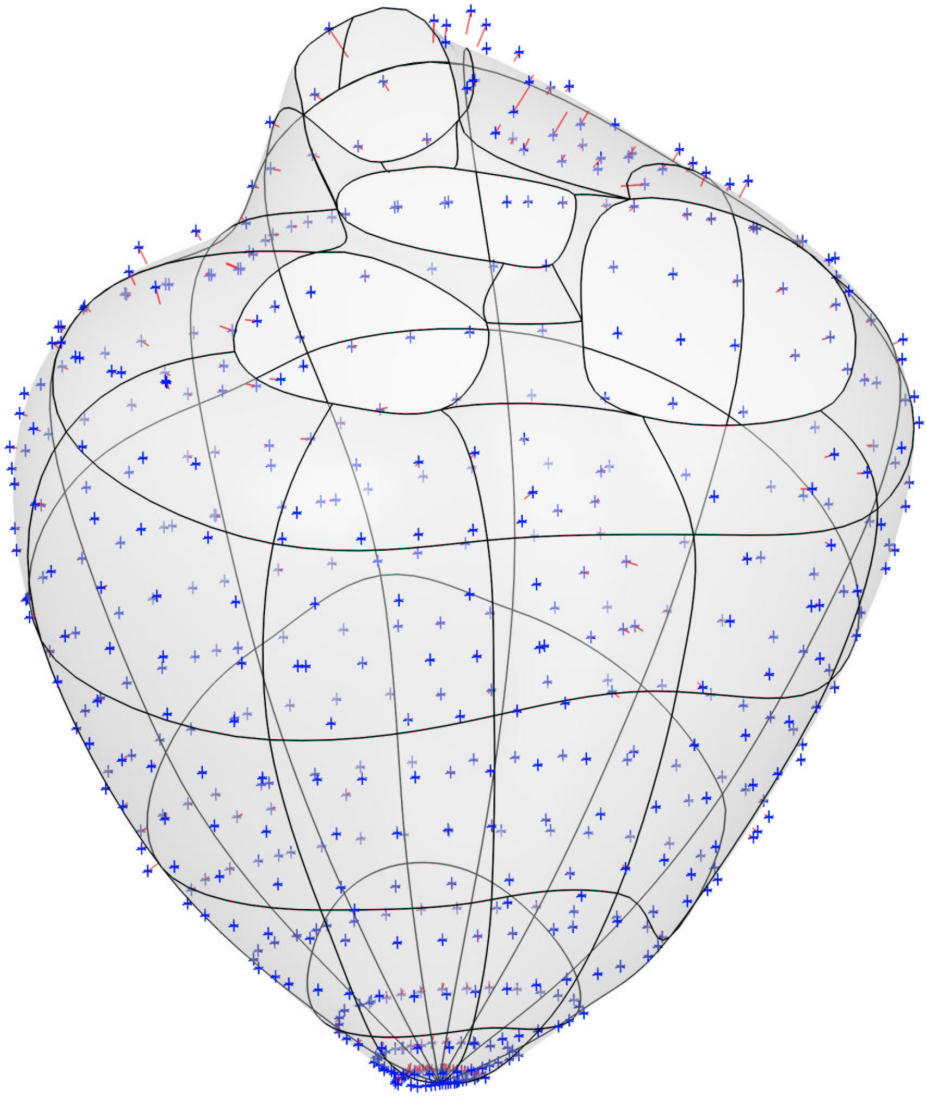

FIGURE 5.12: Fitted epicardial surface geometry with raw data and error projections.

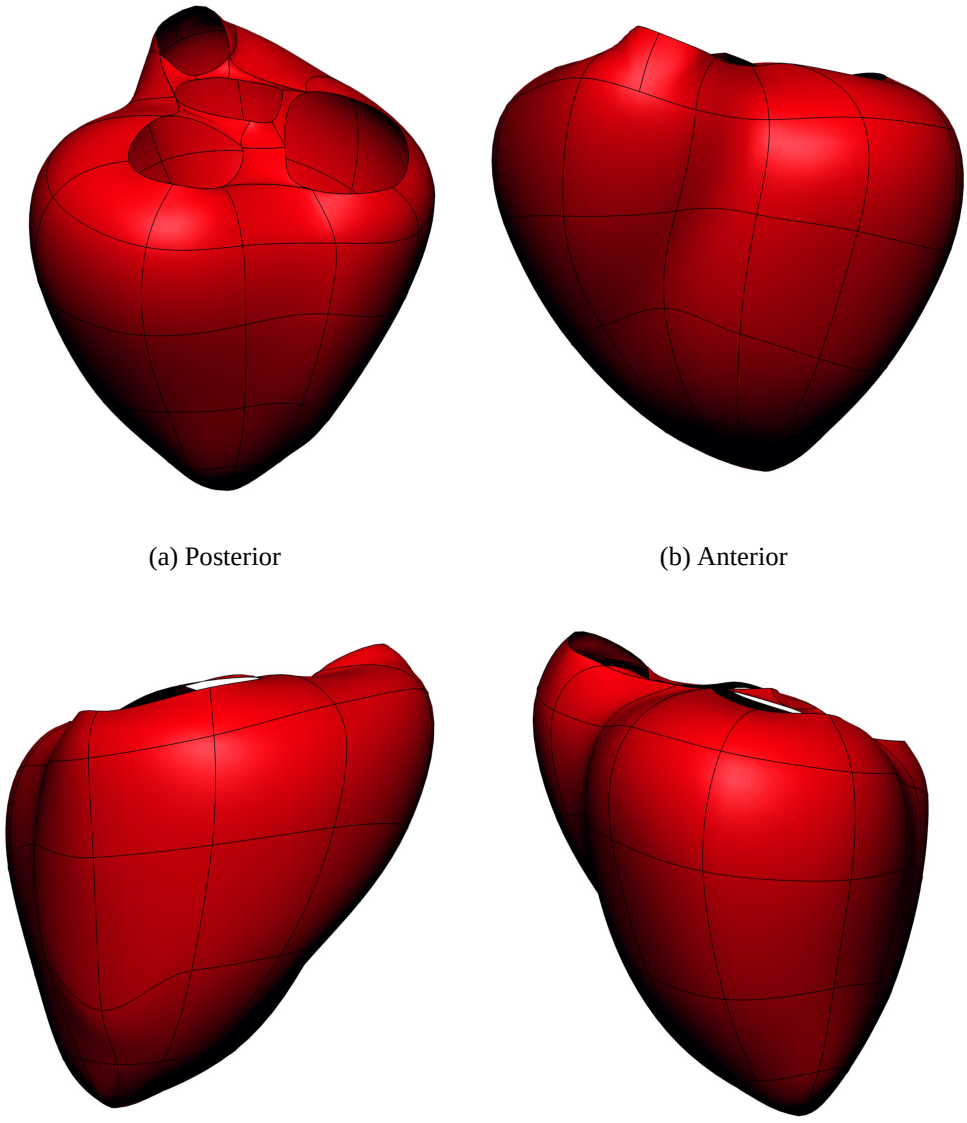

(a) Posterior

(b) Anterior

(c) RV free wall

(d) LV free wall

FIGURE 5.13: The fitted epicardial surface.

5.2.7 From Surfaces to a Volume Model

Creating a volume mesh from the three fitted surfaces required a consolidation of the common degrees of freedom and the introduction of new degrees of freedom to complete the transmural connections as shown in Figure 5.14.

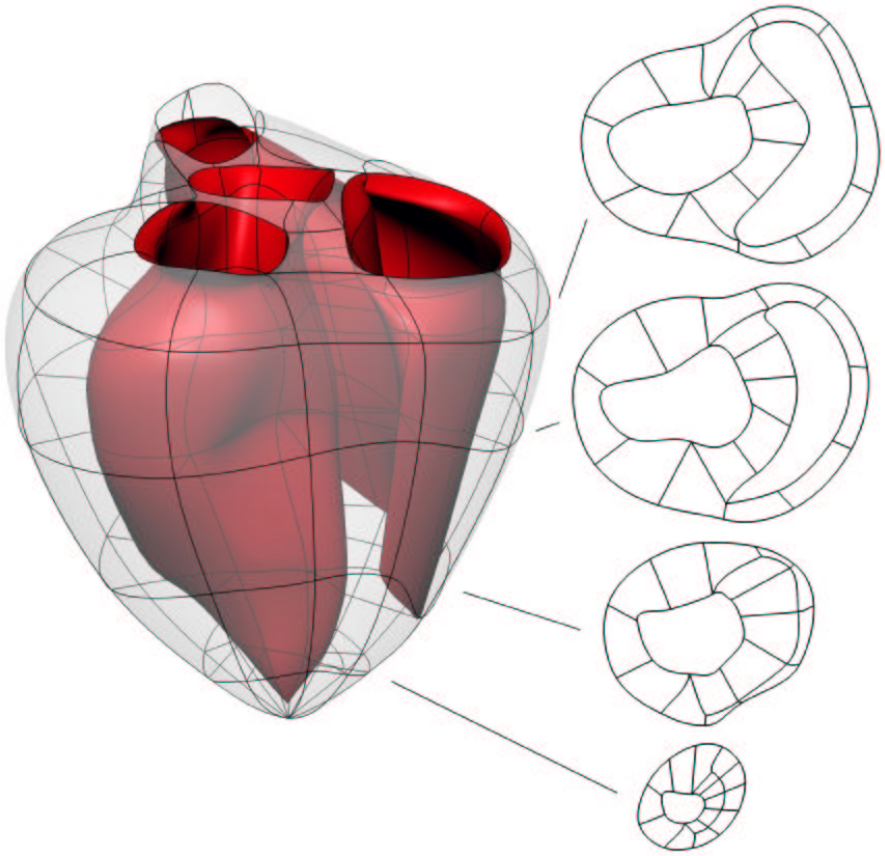

FIGURE 5.14: Connection of fitted surfaces to form the volume mesh. Two-dimensional projections of the mesh topology at the inter-element locations are plotted on the right.

Throughout the mesh construction process the nodal locations have been carefully chosen to ensure that the resultant volume elements are as nearly cuboid as possible. In fact quite some iteration between the surface mesh fits and the volume mesh were required to produce the final meshes presented here.

In the final volume mesh ξ_1 is aligned circumferentially, ξ_2 longitudinally and ξ_3 radially outward. Multiple versions were used connect the interventricular septum to the

ventricular free walls as illustrated in Figure 5.15. Geometrically equivalent derivatives in adjacent elements with inconsistent parametric coordinates were constrained to be the same, likewise with the corresponding elemental scale factors. C^1 continuity is not maintained across these element boundaries.

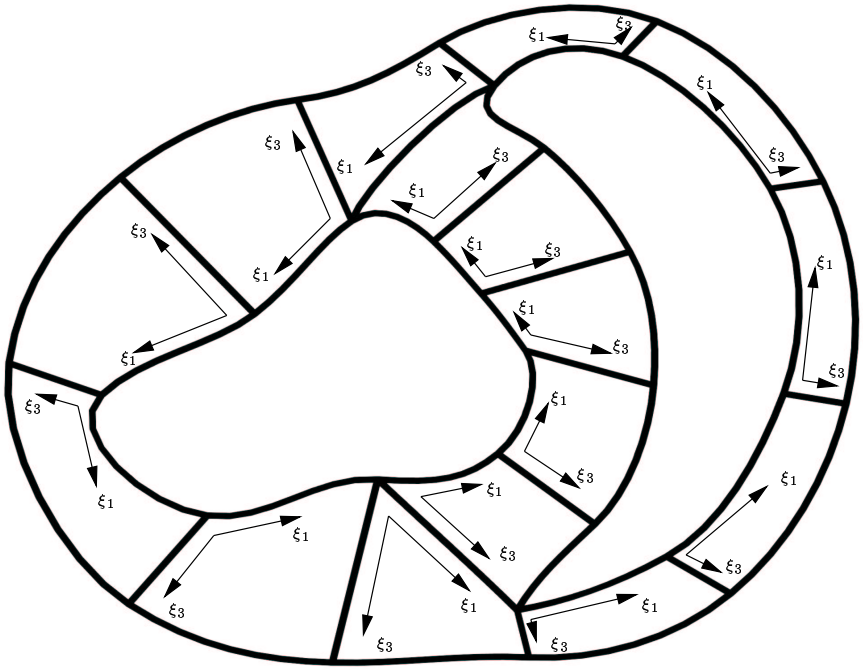

FIGURE 5.15: A plan view of the transmural element connectivity and parametric coordinates.

The remaining degrees of freedom necessary to complete the volume element between the mitral and aortic valve orifices were determined manually since no data was acquired in that region.

Apex

To date most ventricular models have treated the apex as thick walled, similar to the rest of the LV free wall (Section 4.5). In reality the wall tapers steeply to a thin collagenous

membrane as shown in Figure 5.16(a). We hypothesize that this feature is mechanically significant and might serve as a type of hinge. Therefore the LV endocardial apex geometry has been modeled more accurately. The rate of inclination of the wall thickness depends upon the extent of trabeculation in any given region. The model does not account for trabeculation, nor is there any data at the very apex because the spindle protruded though it. Therefore the LV endocardial apex surface was manually adjusted to model the observed anatomy more accurately. Figure 5.16(b) shows a cross-section though the model in a fashion similar to the photograph in Figure 5.16(a).

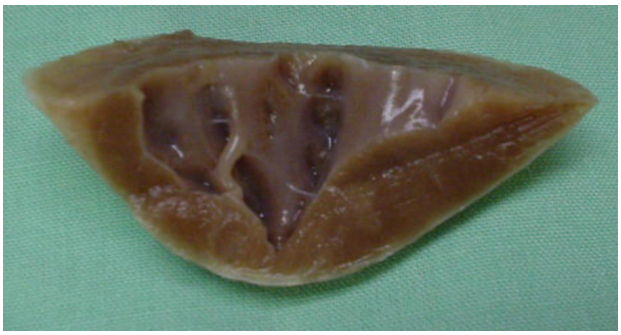

(a) Sagital LV cross-section

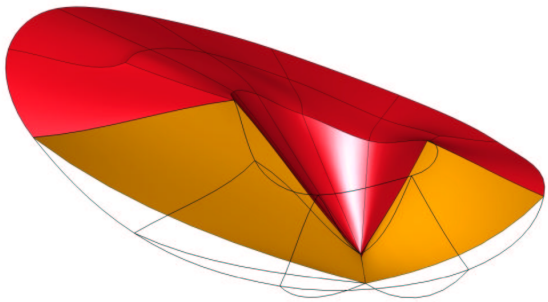

(b) Sagital section of the model

FIGURE 5.16: Apical cross sections from a porcine heart and the model. The model endocardial and top surfaces are red, the transmural cut face is yellow.

The resulting geometric fit is a very good representation of the original data set. The upper pulmonary outflow tract would benefit from more degrees of freedom, but is acceptable for the work anticipated in the near future. The final geometric degree of freedom

count is presented is Table 5.2. The model is 58.54 mm from apex to base. The fitted myocardial volume is 83.1 cc, The LV and RV cavity volumes are 22.7 cc and 15.9 cc respectively.

Nodes	Versions	Fields (*x*,*y*,*z*)	GDOF
114	1	3	2736
15	2	3	675
23	3	3	1518
3	4	3	261
1	9	3	192
1	26	3	549
157		Total	5931

Elements	88

TABLE 5.2: Geometric degrees of freedom

5.2.8 Myocardial Fibre Structure

Fibre Angle Transformations

The fibre angle measurements were made relative to the circumferential direction of the heart. Previous models incorporating fibre angle data from this rig have aligned the ξ_1 direction with the circumferential direction, allowing the measured angles to be fitted directly as rotations from the ξ_1 direction (Nielsen 1987, LeGrice 1992, Nash 1998). The model geometry defined in this thesis does not enforce ξ_1 to be solely circumferential, in order to better represent the geometry. Consequently the fibre angle data must be pre-processed before fitting as a field defined relative to ξ_1.

The correction angle, θ, that must be added to the measured fibre angle is the angle between the ξ_1 direction and the circumferential direction in the (ξ_1, ξ_2) plane (see Figure 5.17). The circumferential vector $\mathbf{g_c}$ is a linear combination of the vectors in the ξ_1 and ξ_2 directions, $\mathbf{g}_1$ and $\mathbf{g}_2$ (Equations 5.11, 5.12, 5.13).

$$\mathbf{g}_1 = \frac{\partial x_k}{\partial \xi_1}\mathbf{i_k} \tag{5.11}$$

$$\mathbf{g}_2 = \frac{\partial x_k}{\partial \xi_2}\mathbf{i_k} \tag{5.12}$$

$$\mathbf{g_c} = a\mathbf{g}_1 + b\mathbf{g}_2 \tag{5.13}$$

or

$$\mathbf{g_c} = a\frac{\partial x_k}{\partial \xi_1}\mathbf{i_k} + b\frac{\partial x_k}{\partial \xi_2}\mathbf{i_k} \tag{5.14}$$

For g_c to be oriented in the circumferential direction a and b must be chosen such that the component in the $\mathbf{i}_3$ direction is zero.

$$a\frac{\partial x_3}{\partial \xi_1} + b\frac{\partial x_3}{\partial \xi_2} = 0 \tag{5.15}$$

or

$$\frac{a}{b} = -1\frac{\frac{\partial x_3}{\partial \xi_2}}{\frac{\partial x_3}{\partial \xi_1}} \tag{5.16}$$

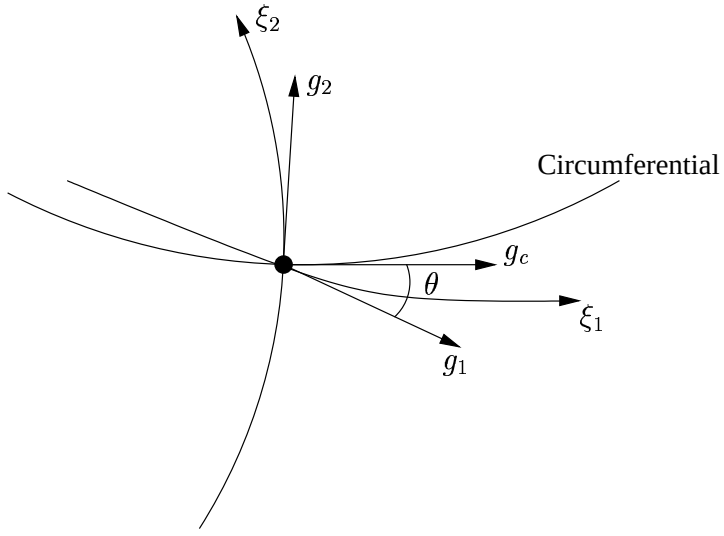

FIGURE 5.17: Fibre angle correction for non-circumferential ξ_1 direction.

The correction angles to be applied to the measured fibre angles can then be calculated from Equation 5.17.

$$\theta = cos^{-1}(\mathbf{g_c} \cdot \mathbf{g}_1) \tag{5.17}$$

where $\mathbf{g}_1$ and $\mathbf{g_c}$ have been normalised to unit length.

Fibre Field

The process of fitting the fibre field was the same as that used by LeGrice (1992). The three-dimensional fibre field parameters were found by first fitting the LV endocardial, RV endocardial and epicardial surface fibre distributions using bicubic Hermite interpolation. The transmural myocardial fibre angles were then fitted to data while the longitudinal and circumferential surface parameters were fixed. The transmural interpolation of the fibre field was also cubic Hermite, providing a fully tricubic Hermite representation of the fibre field.

Previous models have used cubic Hermite interpolation only for the transmural fibre parameters (Nielsen 1987, LeGrice 1992, Nash 1998). Longitudinal and circumferential fibre orientation have been represented using linear Lagrange interpolation. Bicubic Hermite interpolation was used here because it avoided the extra complexity of mixed basis function types between adjacent elements where parametric coordinate consistency is not maintained (see Figure 5.18). The additional computational expense is not significant. The fibre field interpolation and connectivity is the same as used for the geometric fields.

A predominant fibre direction is not visible in the collagenous basal skeleton that connects the valve orifices. Therefore the fibre field was not fitted in the elements corresponding to the basal skeleton.

Due to the inability to measure fibre angles accurately in the basal region there was little data to fit to around the base. On the specimen it was observed that the fibres tend to continue in the same direction over the base to as they did along the wall. The application of Sobelov smoothing enforced this constraint in the fit, providing a fibre field that resembled the observed fibre distribution about the valve orifices well. The RMS errors for the fibre field fits are reported in Table 5.3. Plots of the fitted fields are

given in Figures 5.20, 5.21 and 5.22. The fitted fibre orientations for the porcine heart are quite similar to those measured in the earlier canine model, a helical pattern from -60 degrees on the epicardium through to +90 degrees at the endocardium.

The ξ_1, ξ_2 planes of the LV, septum and RV connective elements shown in Figure 5.18 are not parallel with the epi- and endocardial surfaces as elsewhere, therefore non-zero imbrication angles were applied within those elements to provide continuous flow of the fibre field through those elements. A two dimensional projection of the fibres, Figure 5.19, illustrates the flow of the fibres achieved around the margins where the right ventricle joins the septum.

Fibre Field Fit	Data Points	RMS error (radians)
LV endocardium	622	0.27
RV endocardium	153	0.18
Epicardium	754	0.22
Transmural myocardium	4386	0.29

TABLE 5.3: Fibre field fit RMS errors.

5.2.9 Myocardial Sheet Structure

As for the fibre angle data, the experimentally measured sheet angle must first be transformed to an angle that defines the orientation of the sheet with coordinates attached

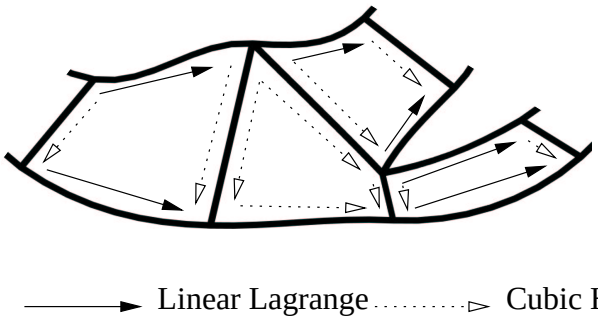

FIGURE 5.18: A bilinear Lagrange-cubic Hermite fibre field would require the LV, septum and RV connection elements to use cubic Hermite-linear Lagrange-cubic Hermite for a consistent cubic Hermite interpolation of the transmural fibre parameters.

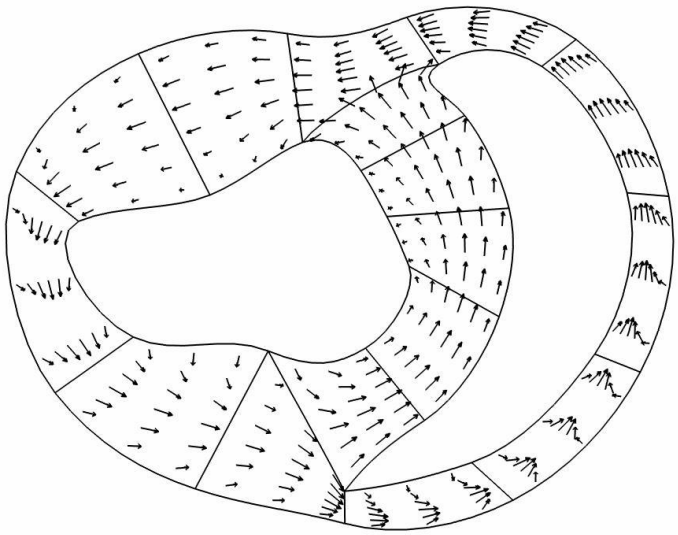

FIGURE 5.19: Fibre direction vectors projected onto a two-dimensional cross-section of the pig heart model. All fibres are drawn as vectors with the same length, so the more axially aligned fibres in the subepicardium and subendocardium have a smaller projection onto this plane than the more circumferentially aligned midwall fibres. The apparent inward orientation of some of the subepicardial and subendocardial fibres reflects the taper of the wall (out of the plane of this projection) and does not indicate a non-zero imbrication angle. Notice the flow of fibres around the margins where the right ventricle joins the septum.

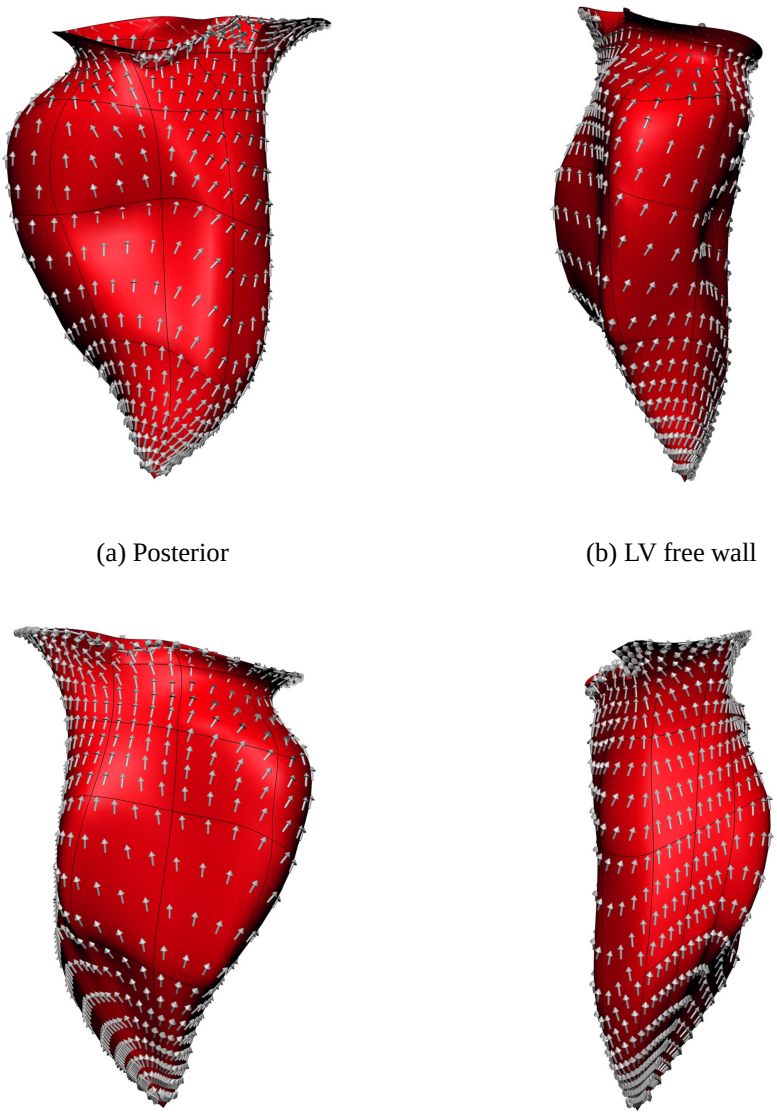

(a) Posterior

(b) LV free wall

(c) Anterior

(d) Septum

FIGURE 5.20: LV endocardial fitted fibre field.

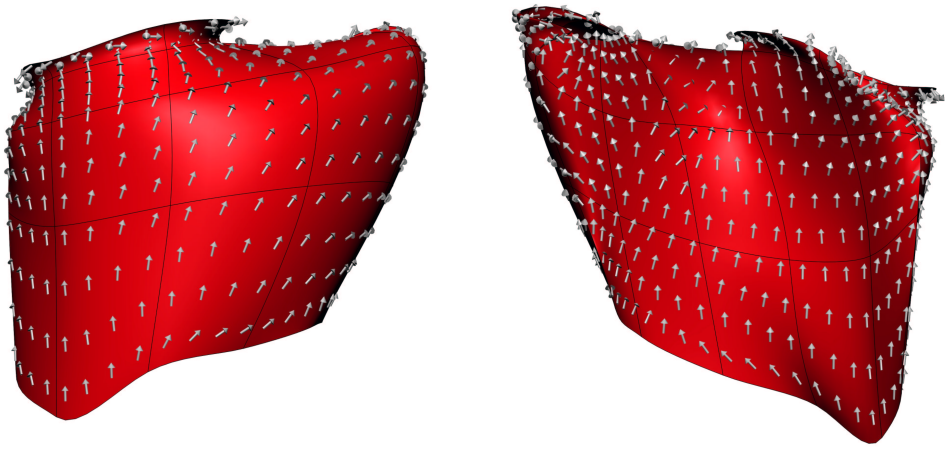

(a) Free wall (b) Septal wall

FIGURE 5.21: RV endocardial fitted fibre field.

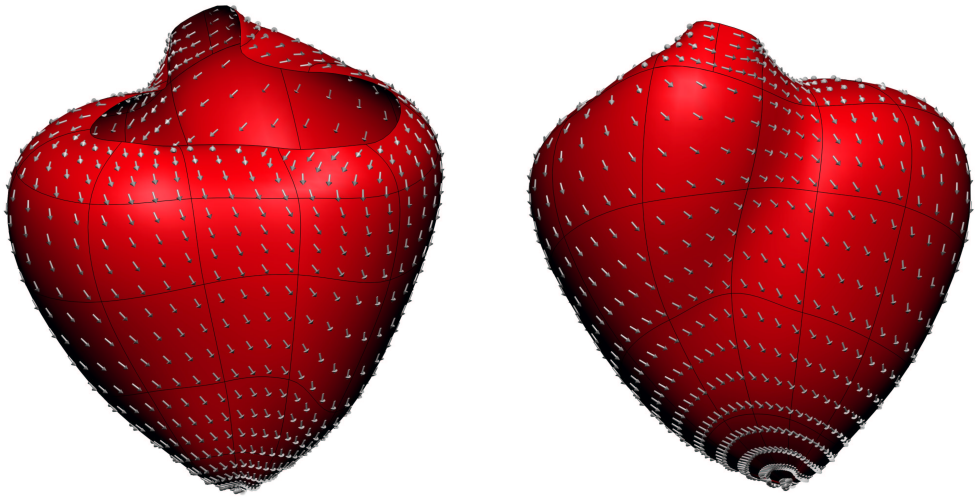

(a) Posterior (b) Anterior

FIGURE 5.22: Epicardial fitted fibre field.

to the heart itself. In order to calculate the transformations another FEM model of the specimen geometry from which the sheet angles were measured is required.

Sheet Data Specimen Model

In order to take advantage of the model built earlier and to avoid repeating the model making process outlined in Sections 5.2.3 through 5.2.7, the fitting algorithm was modified to enable the degrees of freedom associated with the external surfaces of a volume mesh to be fitted, while the remaining degrees of freedom were not considered. Thus the complete model from the previous section with some rotation and translation to align anatomical features, was used as the initial mesh. The geometry of the exterior faces, epicardium, LV endocardium and RV endocardium were then each fitted to the corresponding data sets recorded from the segments described in Section 5.1.2. Both specimens were of similar size and shape resulting in a good fit for the second geometric model. The final RMS values of the fit are listed in Table 5.4, and the model is presented in Figure 5.23. The valve orifice geometry was not measured for the sheet data specimen because sheet orientations could not be identified in the basal skeleton beyond the ventricular myocardium.

Geometric Field Fit	Data Points	RMS error (mm)
LV endocardium	589	0.56
RV free wall endocardium	148	0.87
RV septal wall endocardium	133	0.62
Epicardium	318	0.56

TABLE 5.4: RMS errors of sheet specimen geometric fit.

Sheet Angle Transformations

$\boldsymbol{\beta}'$ is defined to be a unit vector lying at the intersection of the myocardial sheet plane and the (x,r)-plane and makes an angle β' with the radial axis at that point. β' is the angle measured experimentally. The unit vector $\boldsymbol{\beta}$ lies on the myocardial sheet plane orthogonal to the fibre vector $\boldsymbol{\alpha}$. Thus

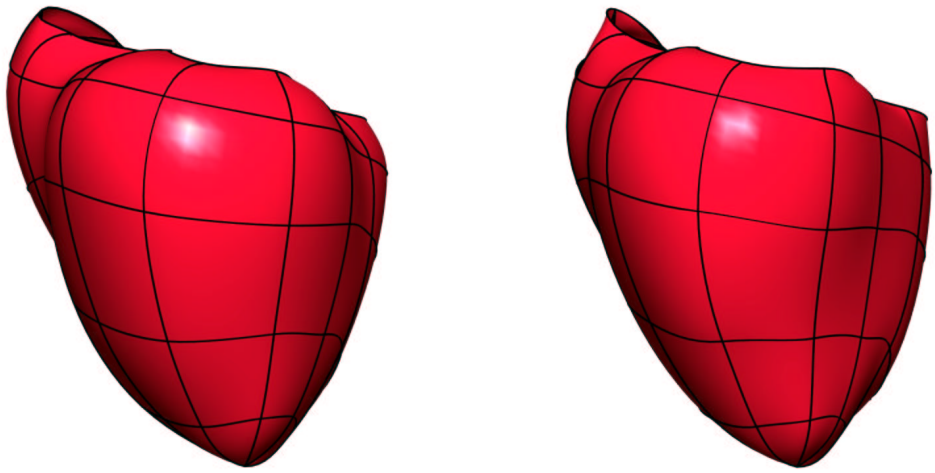

(a) Initial mesh, original fibre and geometry specimen

(b) Fitted sheet data specimen

FIGURE 5.23: Plots of the model geometries for the initial mesh and the fitted sheet data specimen. The sheet specimen geometry is used in the post processing of the recorded sheet orientation data. (a) The initial mesh of the specimen from which the geometry and fibre data was obtained. (b) The fitted mesh geometry of the specimen from which the sheet orientation data was measured. Both plots are to the same scale. The specimens were very similar in size and shape.

$$\boldsymbol{\beta} = \mathbf{n} \times \boldsymbol{\alpha} \tag{5.18}$$

where

$$\mathbf{n} = \frac{\boldsymbol{\alpha} \times \boldsymbol{\beta}'}{|\boldsymbol{\alpha} \times \boldsymbol{\beta}'|} \tag{5.19}$$

and

$$\boldsymbol{\beta}' = \begin{bmatrix} 1 & 0 & 0 \\ 0 & \cos\theta & -\sin\theta \\ 0 & \sin\theta & \cos\theta \end{bmatrix} \begin{bmatrix} -\sin\beta' \\ \cos\beta' \\ 0 \end{bmatrix} \tag{5.20}$$

A unit vector normal to the (ξ_1, ξ_2)-plane is

$$\mathbf{u} = \frac{\mathbf{g}_1 \times \mathbf{g}_2}{|\mathbf{g}_1 \times \mathbf{g}_2|} \tag{5.21}$$

The *sheet angle* β is defined to be the angle subtended by $\boldsymbol{\beta}$ and $\mathbf{u}$ and lies in the (p, u)-plane, hence:

$$\beta = \tan^{-1} \frac{\boldsymbol{\beta}_\mathbf{p}}{\boldsymbol{\beta}_\mathbf{u}} \tag{5.22}$$

where $\boldsymbol{\beta}_\mathbf{p}$ and $\boldsymbol{\beta}_\mathbf{u}$ are the components of $\boldsymbol{\beta}$ in the p- and u-directions, respectively.

Thus, given the measured sheet angel β' and the fibre orientation $\boldsymbol{\alpha}$ together with the heart geometry, the following sequence of computations is used to find the sheet angle β

- $\boldsymbol{\beta}'$ from Equation 5.20
- $\mathbf{n}$ from Equation 5.19

- $\boldsymbol{\beta}$ from Equation 5.18
- $\mathbf{g}_1$ and $\mathbf{g}_2$ from Equations 5.11 and 5.12
- $\mathbf{u}$ from Equation 5.21
- $\mathbf{p}$ from $\mathbf{u} \times \boldsymbol{\alpha}$
- β from Equation 5.22

Sheet Field

The sheet angle data was fitted by a tricubic Hermite field to the transformed sheet orientation values β at corresponding ξ locations in the original fibre and geometry model. The sheet field was fitted with an RMS error of 0.49 using 8360 data points.

The implementation of the transformations and fitting technique were tested and validated by transforming and fitting generated raw data with simple patterns, such as zero and 45 degree angles, then plotting cross-sections of the fitted fields to confirm the fields represented the original data. The tricubic Hermite field has enough degrees of freedom to adequately describe the transmural variation of sheet orientation.

Cross section plots of the fitted sheet fields are presented in Figure 5.24. The fitted sheets are aligned predominantly radially, but curve to align more tangentially to the external surfaces. The transmural sheet curvature appears less marked than in the earlier canine heart.

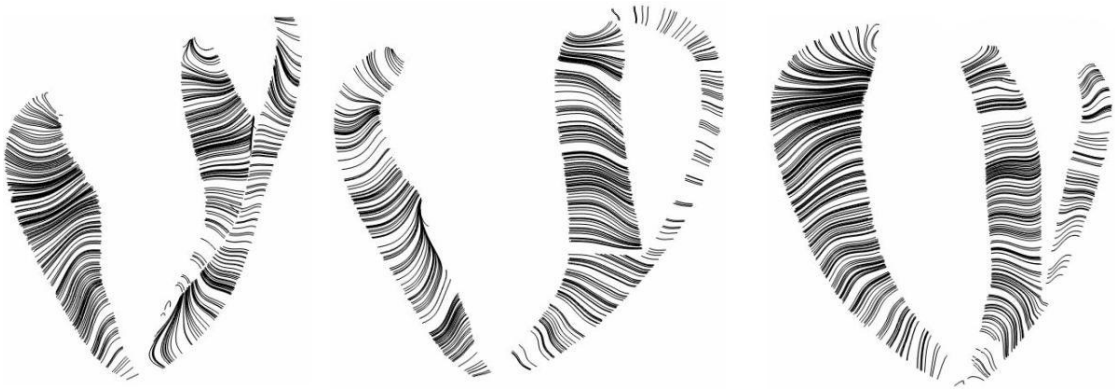

FIGURE 5.24: Fitted sheet orientations, shown in three longitudinal sections through the heart. The sheets are predominantly radially aligned. The apparent discontinuities are actually only an artifact of the rendering technique at the element boundaries.

Chapter 6

Simulating Ventricular Mechanics using the Finite Element Model of Porcine Ventricles

This chapter presents the use of the porcine ventricular model to simulate passive inflation and predict the myocardial distributions of stress and strain. The validity of the FEM and finite elasticity techniques presented in Chapters 2 and 3 for modelling ventricular mechanics have been rigorously tested (McCulloch 1986, Nash 1998). The following selection of modelling and solution techniques draws heavily upon that body of work.

6.1 Solution Fields

There are four fields to solve for, the displacements in each geometric coordinate, x, y and z, and the hydrostatic pressure. For each field an appropriate set of interpolation functions must be chosen. The interpolation functions must be able to represent the solution fields with the required accuracy. A desirable feature of the model is that the predicted stress and strain distributions are also spatially C^o-continuous.

In this model the myocardial stress components are derived from components of the strain tensor, the hydrostatic pressure field and the material properties of the ventricular tissue. Therefore these quantities must be spatially continuous throughout the model to

achieve C^o-continuity of myocardial stress. Trilinear Lagrange is the lowest order interpolation that will provide adequate resolution and continuity of the hydrostatic pressure field. To be consistent when calculating components of stress the interpolation scheme for the geometric solution fields should be of a higher order than the interpolation scheme for the hydrostatic pressure field (Section 3.3.2). For this reason and for their ability to resolve the deformation fields accurately, tricubic Hermite interpolation is used for all three geometric displacement fields. As for the model geometry multiple versions of the derivative dependent variables are necessary to connect elements with inconsistent parametric coordinates.

6.2 Displacement Boundary Conditions

The anatomical model presented in this thesis was designed to provide the ability to apply more physiological boundary conditions than in earlier ventricular model simulations. Although the earlier prolate-spheroidal coordinate system based models had the benefit of the model geometry and deformations aligned with the coordinate system directions, allowing for the direct application of boundary conditions to modes of deformation, the coordinate system imposed constraints on the modes of deformation itself (Section 4.4.3). The anatomical rectangular cartesian model makes no assumption about the relationship of the model geometry or deformation with the global coordinate system. The model accurately represents the basal skeleton which serves as the point of connection of the ventricles with the body. Therefore the node positions and derivatives which form the perimeter of the ventricular myocardium were fixed. The elements corresponding to the collagenous inter-valve basal skeleton are omitted because their material properties are unknown and are not thought to contribute significantly to the deformation of the ventricular wall. It was also discovered that fixing the derivatives of the apex nodes improved the convergence of the solution procedure at higher cavity pressures. Fixing the apex derivatives has the effect of making the region immediately adjacent to the nodes more rigid, which is consistent with the observation that the apex is more collagenous than the ventricular wall. This is discussed further in the following section that describes the material properties. Figure 6.1 shows the applied boundary conditions.

These boundary conditions are also consistent with experimental protocols for inflat-

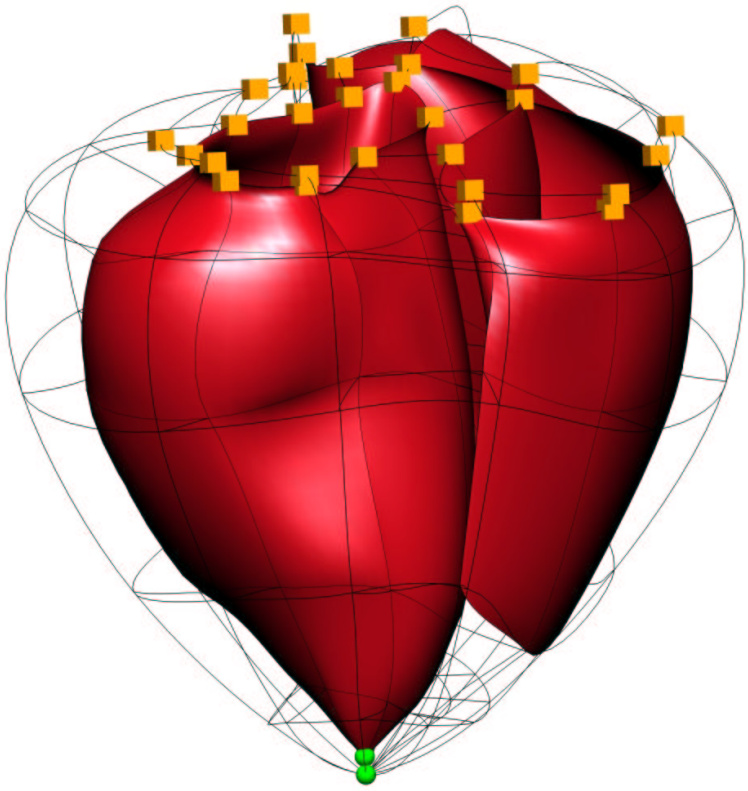

FIGURE 6.1: Displacement boundary conditions. The cubes represent nodes at which all the degrees of freedom are fixed, both location and curvature. The spheres represent nodes at which only the derivatives are fixed.

ing excised hearts, as illustrated by the experimental rig for investigating ventricular mechanics using MRI shown in Figure 6.2.

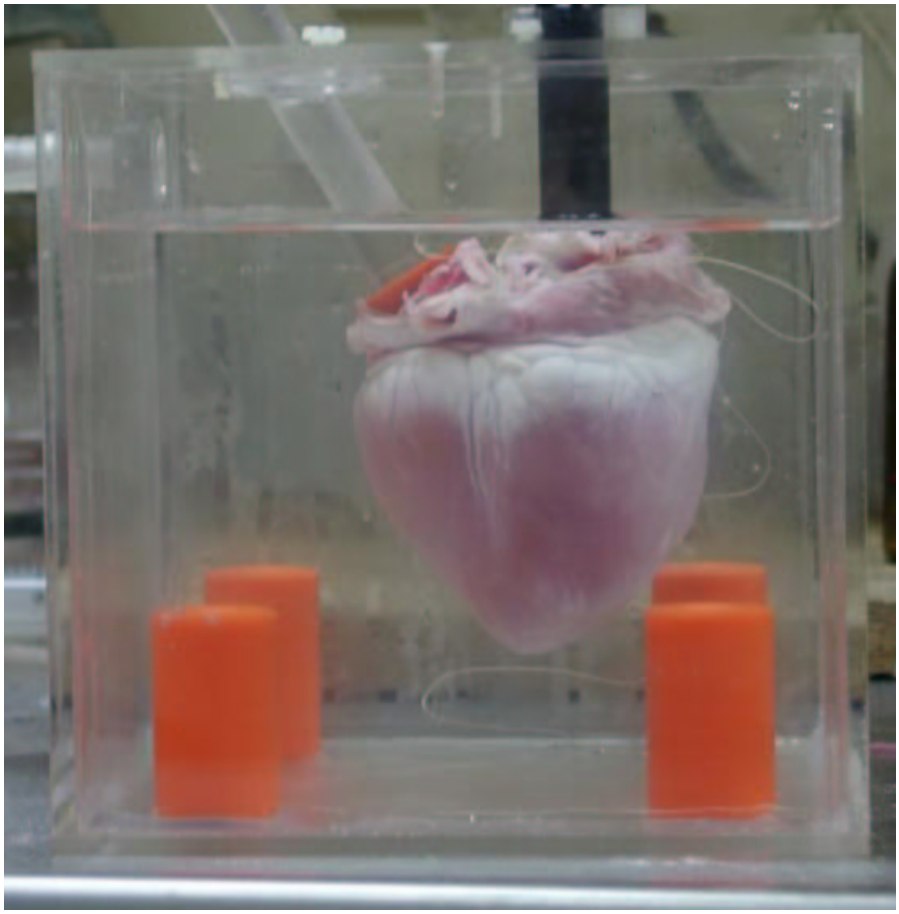

FIGURE 6.2: An experimental heart preparation for examining passive ventricular deformation. The ventricles are attached to the rig via tubes that also supply fluid to the cavities to apply pressure. MRI techniques are then used to examine the ventricular deformation under various loading conditions. (Presented with permission, K. Augenstein, thesis in progress)

Earlier models have included a pericardial constraint to limit the circumferential bulging (Section 4.4), whilst perhaps having some physiological merit, its application has not been consistent with the physiology. The form of the pericardial constraint applied to the anatomical prolate canine model is too restrictive. A less restrictive alternative would be to apply the pericardial pressures to the epicardial surfaces. These pressures vary significantly throughout the cardiac cycle and their measurement has been a topic of considerable discussion (Tyson, Maier, Olsen, Davis & Rankin 1984, Tyberg & Smith

1990, Hamilton, Dani, Semlacher, Smith, Kieser & Tyberg 1994). A superior alternative would be to couple the ventricular model to a model of the pericardial sac.

It is preferential to omit the influence of the pericardial sac than to model it incorrectly, since much of the experimental data available in the literature is from excised hearts, or from procedures that involve incising the pericardial sac to obtain access to the ventricles. Therefore no pericardial constraint is applied in this work. Without the ability to force a desired deformation through the application of rigid boundary conditions such as the "pericardial constraint", the role of the microstructure and its material properties becomes considerably more important.

Following the application of the boundary conditions there are 3110 solution degrees of freedom in the model to solve for.

6.3 Material Properties

6.3.1 Constitutive Law

The pole-zero strain energy function for myocardium, Equation 4.1, was used to model the stress-strain behaviour of the ventricular myocardium. Estimates for several of the pole-zero constitutive law parameters have been made using material testing and elastica theory as described in Section 4.4.3. However, to date the regional variation in myocardial material properties, evident from the regional variation in the microstructure and its constituents, has not been characterised. It was discovered that the material parameter set used in the earlier canine model did not yield a model that was numerically stable under physiological loading when applied to the current model. The reasons for this are not well understood, but may be due to a lack of adequate stiffness in certain regions of the model. Since it was found that increasing the stiffness in several regions of the model enabled it to simulate physiological loading without becoming numerically unstable. The regions that needed modifying were consistent with regions that do in fact exhibit increased collagen densities (and hence the stiffness of the extracellular matrix).

The regions that required modification were portions of the RV free wall and septal wall interface, the base and the apex. An attempt was made to describe the regional variation in material properties using trilinear-Lagrange interpolation, but the model became

numerically unstable. The variation of multiple constitutive parameters within the elements may have resulted in portions of tissue with non-viable properties. Variation of the material properties on an element by element basis, which provides a piecewise constant description, proved successful. The modified elements are shown in Figure 6.3. In the modified regions the sheet and sheet-normal constitutive parameters were set equivalent to the fibre direction parameters. For the apex, the now stiff isotropic material description is consistent with the observation that the apex is a more collagenous region without a discernible microstructure orientation. At the lower RV free wall the modified material properties are representative of the increased trabeculation and the less structured alignment of fibres at the septal wall interface. Similarly the modified basal element is in a region where an increased collagen density is observed.

The constitutive parameters used in the pole-zero law were chosen such that the fibre term parameters were consistent with those obtained from material testing and used in the earlier canine model. The sheet and sheet-normal term parameters were chosen to provide the relationships between the normal direction terms observed experimentally in the physiological strain range. Namely, marginally stiffer in the sheet direction than the fibre direction, and much more compliant in the sheet-normal direction than the fibre direction. For ease of interpretation and through lack of quantitative data the coefficients $k_{\alpha\beta}$ were set equivalent while the curvatures $b_{\alpha\beta}$ and poles $a_{\alpha\beta}$ were manipulated to provide the desired strain energy contribution relationships for the normal direction terms.

Recent triaxial shear testing of myocardial tissue (Dokos, Smaill, Young & LeGrice 2002) has begun to provide insights into the shear behaviour of ventricular myocardium. The testing rig measured the force required to deform cubes of myocardium excised from the ventricular mid wall. Simple shear deformation also imposes strain in the directions normal to the shear plane. The Dokos experiments determined that the simple shear deformation is resisted by the elastic elements aligned with the microstructural axes of the tissue. Therefore the data acquired in that series of experiments cannot be used to determine the shear term parameters in the pole-zero law because they need to be independent of other modes of deformation. The triaxial testing rig is currently under going modification to enable the imposition of pure shear, which will provide the stress-strain relationship for the shear modes independent of any other modes of deformation. The experiments to date do, however, indicate the validity of the previous assumption

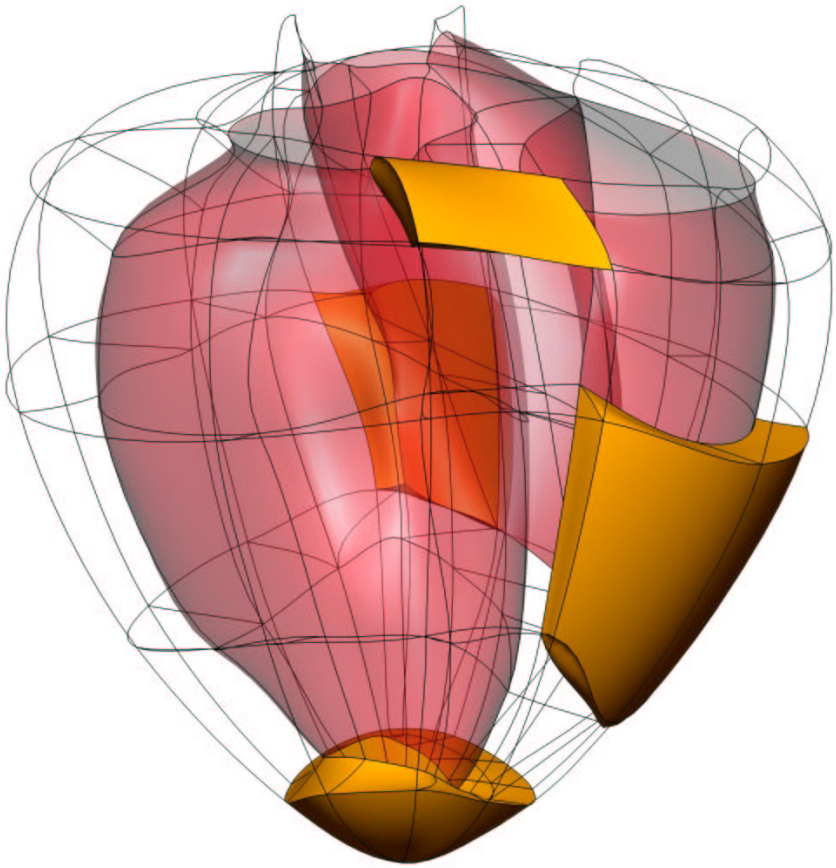

FIGURE 6.3: Regional variation of material parameters. Material properties in the sheet and sheet-normal directions are set equivalent to the fibre direction in the shaded elements. The modified elements are in the lower RV free wall, base and apex.

that the shear behaviour is strongly correlated with the axial behaviour. Therefore the *fibre distribution model* (Nash & Hunter 2001) (Appendix A) for calculating the shear poles from the axial parameters was used. The shear coefficients and curvature terms were assigned to reflect the assumption that these modes of deformation to not contribute significantly to the strain energy of the myocardium. Table 6.1 lists the material properties used in this model[1].

Type	Axial Properties	Shear Properties
Coefficients (kPa)	k_{11} 2.0	k_{12} 1.0
	k_{22} 2.0	k_{13} 1.0
	k_{33} 2.0	k_{23} 1.0
Poles	a_{11} 0.523	a_{12} 0.73
	a_{22} 0.523	a_{13} 0.73
	a_{33} 1.037	a_{23} 1.18
Curvatures	b_{11} 1.351	b_{12} 2.0
	b_{22} 1.9	b_{13} 2.0
	b_{33} 6.0	b_{23} 2.0

TABLE 6.1: Material properties of myocardium for the pole-zero constitutive law used in the porcine model.

6.3.2 Residual Stress and Strain

The concepts of residual stress and strain in the ventricular muscle were introduced in Section 1.1.2, and a suitable method for incorporating these properties into a ventricular model by the use of a growth tensor was presented in Section 4.4.3. Using data from studies that have quantified residual strain distributions in intact ventricular muscle (Omens & Fung 1990, Rodriguez et al. 1993) a trilinear Lagrange initial fibre extension ratio field was generated with the nodal values presented in Table 6.2 and shown in Figure 6.4.

To restore internal equilibrium within the ventricular myocardium the model is solved without any external loading. The residual stresses and strains in the unloaded ventricular model at equilibrium, or *reference state*, are presented in Figure 6.5.

[1]The pole-zero constitutive law parameters presented here vary from those presented in Appendix D, because work subsequent to the submission of the paper led to changes in the parameter set.

Ventricular region	Transmural location	Initial fibre extension ratio, λ_f^0
Equator	LV endocardium	0.95
	LV epicardium	1.05
	RV endocardium	1.00
	RV epicardium	1.00
Base, Apex	all	1.00

TABLE 6.2: Initial fibre extension ratios applied applied to model residual strain in the passive myocardium.

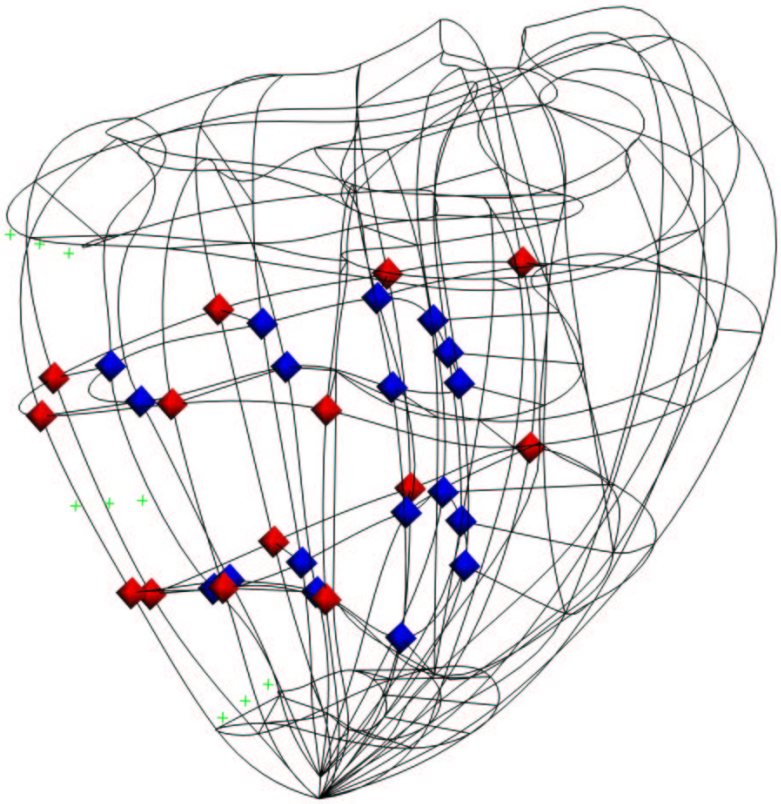

FIGURE 6.4: Applied initial residual fibre strain field. Red diamonds mark the nodes at which an initial fibre extension is applied, blue diamonds mark nodes with an applied initial fibre compression. No initial residual strains are applied at unmarked nodes. The green crosses indicate the regions in which the reference state stresses and strains are plotted in Figure 6.5.

The introduction of residual fibre strain into the equatorial region of the model results in a residual sheet-normal strain also being produced to satisfy the incompressibity constraint. The sheet and shear components of strain remain largely unchanged. The resultant residual fibre strain is similar to that reported by Costa, May-Newman, Farr, O'Dell, McCulloch & Omens (1997) and the shear strains are similarly small. However, the induced sheet and sheet-normal residual strains do not the resemble reported data, which indicates that the imposed residual stress distribution may be overly simplistic.

The only significant residual stress produced is in the fibre direction. The residual sheet-normal strain does not result in any notable residual stress because the material is relatively compliant along the sheet-normal axis. The maximum residual fibre stress is small compared to maximum end-diastole and end-systolic fibre stresses.

In order to assess the extent to which the imposed residual stresses represent those actually occurring, a model simulation of the opening angle experiments (Omens & Fung 1990) was performed on a slice of the porcine ventricular model. The resultant simulated opening angle was approximately 10 degrees, which is less than the 25 degree opening angles observed experimentally in canine hearts (Costa et al. 1997). The compressive behaviour of myocardium is not well quantified and may significantly influence the deformation in the opening angle experiment.

6.4 Computational Techniques

Deformation of the ventricular mechanics model is governed by the theory of finite deformation elasticity (Chapter 2). A system of nonlinear equations is assembled and solved in CMISS using the FEM (Chapter 3) and Newton's method (Section 3.4), which incorporates the sparse SuperLU[2] method to solve the resulting set of linear equations. Convergence is achieved when both the ratio of *unconstrained* to *constrained residuals* and the sum of solution vector increments for the current Newton iteration are less than a prescribed *error tolerance*. Constrained residual equations are associated with degrees of freedom for which the boundary conditions have been fixed (thus these equations are removed from the problem). Unconstrained residuals are associated with the solution variables which are to be determined.

[2] `http://www.nersc.gov/ xiaoye/SuperLU/`

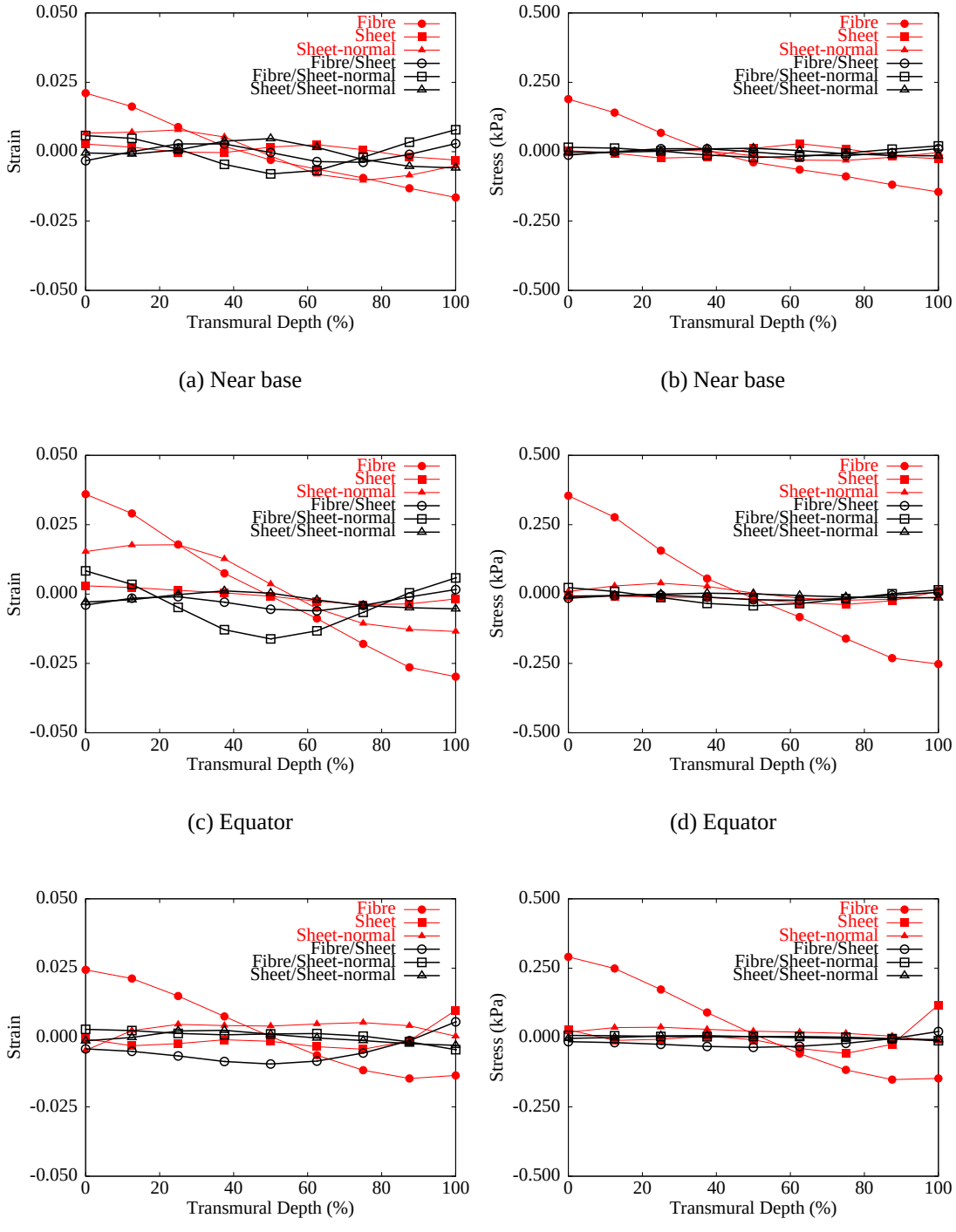

(a) Near base

(b) Near base

(c) Equator

(d) Equator

(e) Near apex

(f) Near apex

FIGURE 6.5: Residual fibre strains and stresses in the unloaded, reference state, lateral LV free wall. (a), (c) and (e) show the strains, (b), (d) and (f) the stresses in the material coordinate system. The sampling locations are plotted in Figure 6.4

Several sections of the solution algorithm lend themselves well to a multiprocessor computer architecture, in particular the determination of the element stiffness matrices and the solution of the system of linear equations. For the most part the development of this cardiac model was performed on SGI Origin type multiprocessor machines. Parallel processing of the algorithm was implemented to obtain the best performance from this architecture, and did exhibit linear speed-up with increased processor count. However shortly before the completion of this thesis a newer IBM pSeries 690 supercomputer became available. The different architecture design and newer technology executed the algorithm implementation sufficiently differently that the parallelisation code designed on the earlier machine was no longer suitable. In fact a single processor executed the algorithm quicker than any multiprocessor combination on the earlier machine. Further redesign of the parallisation code could therefore potentially reduce the execution time significantly. However, for the purposes of this study the single processor solution times were considered adequate. The model results presented in the following sections were completed on the IBM pSeries 690 supercomputer on a single processor.

6.5 Passive Inflation

The anatomical rectangular cartesian porcine ventricular model was inflated to LV and RV end-diastolic pressures of 1 kPa and 0.2 kPa respectively, to simulate the first portion of passive diastolic filling during the cardiac cycle. A physiologically end-diastolic LV cavity pressure is nearer 2kPa but attempts to simulate inflation to higher cavity pressures were unsuccessful due to the material property short comings discussed in Section 6.3.1. Despite the reduced cavity pressures the model still serves to provide insight into the mechanical behaviour of the ventricles and the role of the microstructure in its deformation. Unfortunately the lower pressure loads limit the comparisons that can be made with results in the literature to assess the suitability and accuracy of the model.

The simulation took approximately 30 minutes on a single processor on an IBM pSeries 690.

6.5.1 Cardiac Coordinate Strains

Radiopaque marker beads have been used (Waldman, Fung & Covell 1985, Omens, May & McCulloch 1991) to measure the deformation in a small

region of myocardium. The results of an experimental study on isolated pig hearts (Holmes 1995) are presented with the predicted model strains for comparison in Figure 6.6. The strains are presented in the coordinate system used for the experimental work referred to as the *cardiac coordinate system* or *wall coordinates*. In this more topologically relevant coordinate system the axes are aligned with the circumferential, longitudinal and outward radial directions of the ventricles. The model normal strains

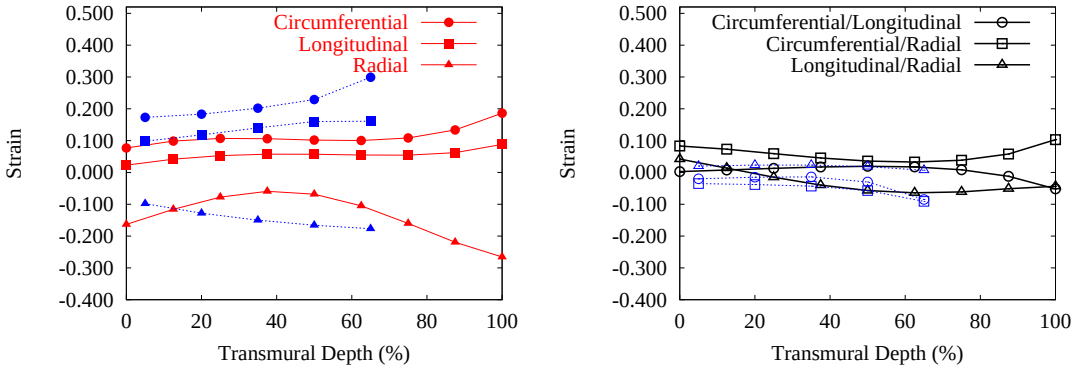

(a) Normal strains

(b) Shear strains

FIGURE 6.6: Cardiac coordinate strains in the equatorial lateral LV free wall at end-diastole, an LV cavity pressure of 1 kPa. The sampling locations are plotted in Figure 6.4. The predicted strains are approximately the same magnitude and exhibit similar trends to the experimental pressure-strain data of Holmes (1995), shown in blue with the same symbols for each strain component.

agree reasonably well with the experimental results, while the shear components do not follow quite so similar trends.

The apex-base length of the model increased from 58.54 mm to 60.27 mm a change of 2.96%. Measuring the base to apex twist with anti-clockwise rotations being positive when viewed from the apex towards the base, the model twist was 4 degrees.

Further analysis of the deformation using microstructural information provides more

understanding of the ventricular mechanics taking place in the model.

6.5.2 Microstructure Coordinate Strains

To gain more insight into the model behaviour it is necessary to interpret the deformations with respect to the microstructural axes. By analysing each of the deformation components the role of the microstructure in the global ventricular deformation and the applicability of the constitutive law can be examined. The end-diastolic material stresses and strains are presented in Figures 6.8, 6.9 and 6.10 in a variety forms to aid in their interpretation. The fibre and sheet orientations in the equatorial region of the lateral LV free wall are plotted in Figure 6.7 and are referred to in the following interpretation of the material coordinate stresses and strains.

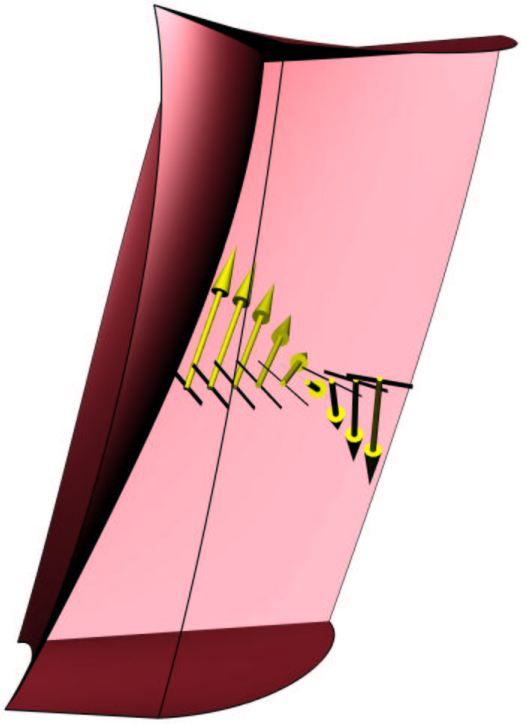

FIGURE 6.7: Anterior view of the fibre and sheet orientations in the equatorial region of the lateral LV free wall. The fibres are directed into the page with the sheet orientations plotted at their origin. The sheets are radially aligned in the outer third of the wall and become more longitudinally aligned towards the endocardium.

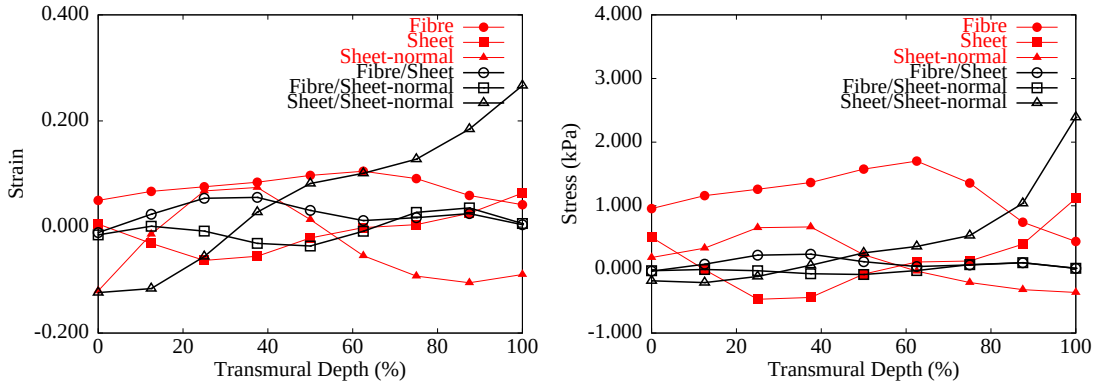

(a) Near base

(b) Near base

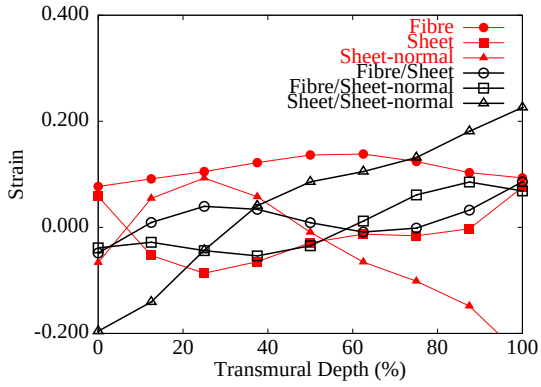

(c) Equator

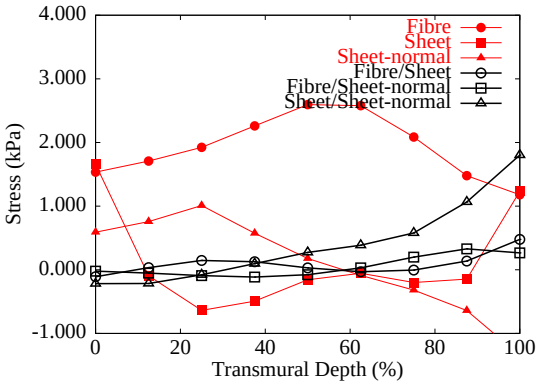

(d) Equator

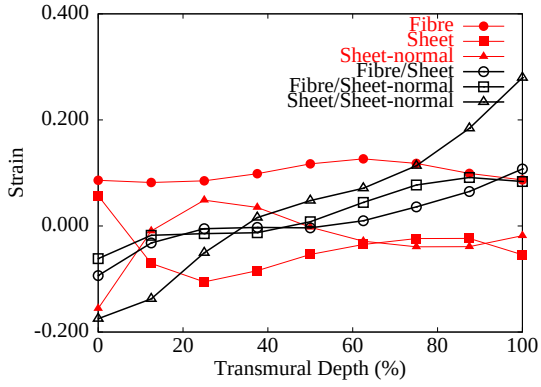

(e) Near apex

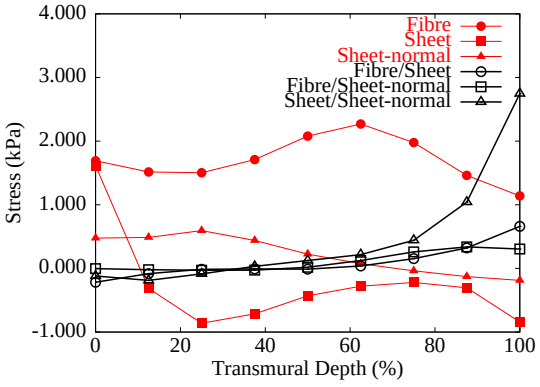

(f) Near apex

FIGURE 6.8: Fibre strains and stresses in the lateral LV free wall at end-diastole. (a), (c) and (e) show the strains, (b), (d) and (f) the stresses in the material coordinate system. The sampling locations are plotted in Figure 6.4.

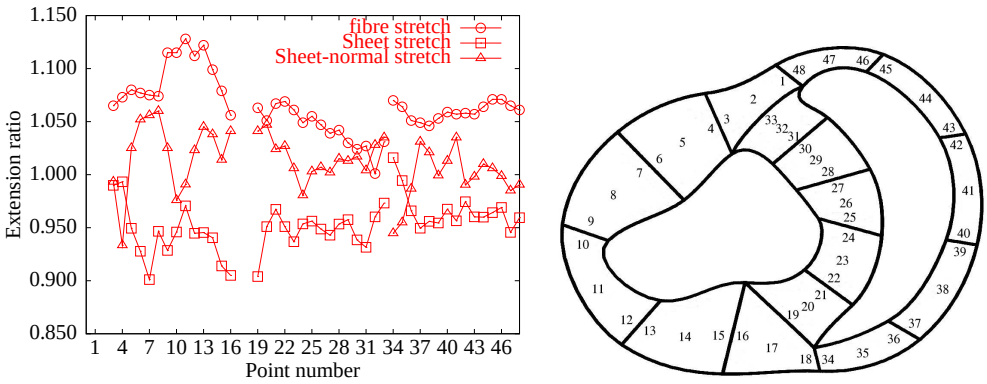

FIGURE 6.9: Circumferential distribution of fibre, sheet and sheet-normal stretch at equatorial midwall locations shown on the right. The numbers on the horizontal axis refer to Gauss point locations in the sequence around the heart shown by the figure on the right. Note that strain components at locations 1,2,17,18 are omitted from the plot because the fibre orientations are not in the circumferential direction.

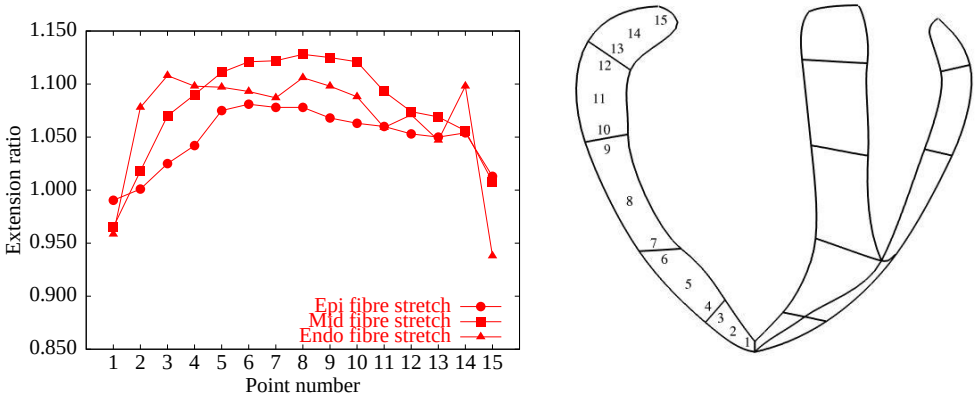

FIGURE 6.10: Base-apex distribution of fibre stretch in the subepicardium, midwall and subendocardium. The stretch in the basal elements is influenced by the applied boundary conditions, and the apical deformation is limited by the stiff isotropic material and the apical derivative boundary condition.

- Fibre strain - The fibre extension ratios reach physiological end-diastolic values of about 1.1 in the LV free wall. There is small transmural variation peaking at the midwall and decreasing at the sub-epi and sub-endocardial surfaces (Figures 6.8 and 6.10). The circumferential distribution of fibre stretch (6.10) reflects the circumferentially varying wall thickness. The peak fibre strain occurs between the regions where the LV free wall is thickened by the bulge of the papillary muscles (6.9). The minimum fibre strain occurs where the wall is thickest at the junction of the right ventricle with the septum. The fibre stresses are significantly greater than the other stress components (Figure 6.8) reflecting the constitutive law parameters chosen to model the increased stiffness of myocardium along the direction of the fibre axis

- Sheet strain - The sheets are aligned predominantly radially (Figure 6.7) except in the subepi and subendocardial regions where they rotate to be tangential to the surfaces. The sheet strains vary consistent with the sheet orientations, in the midwall the sheet strains are negative as the sheets are compressed by the radial pressure loading, while close to the surfaces the sheets are stretched as they bear some of the load in the base-apex direction (Figure 6.8). The change in sheet orientation gives rise to large subepi and subendocardial stresses that indicate the constitutive law parameters might not be suitable for the sheet direction term in these regions.

- Sheet-normal strain - The sheet orientations dictate the mode of deformation in the sheet-normal direction. In the regions where the sheets are aligned radially, they are pulled apart by longitudinal deformation. In the subepi and endocardium the sheets are aligned tangential to the surface planes and hence pressed together by the radial loading (Figure 6.8). The large sheet-normal stresses in the sub-endocardium again highlight the shortcomings of a homogeneous material description and incompressible material model to represent the myocardium.

- Fibre/Sheet shear strain - The shearing between sheets in the fibre direction is not a significant mode of deformation and does not generate any stress in the myocardium (Figure 6.8).

- Fibre/Sheet-normal shear strain - The shearing across the sheets in the fibre direction is not a significant mode of deformation either and does not contribute any

stress to the myocardium (Figure 6.8).

- Sheet/Sheet-normal - The shearing between sheets in the sheet direction is a significant mode of myocardial deformation, but does not generate significant stress because the sheets are only bound loosely together. This mode of shearing between the sheets enables significant wall thickening and thinning throughout the cardiac cycle without creating significant stress. The change in sign transmurally of this deformation component (Figure 6.8) is consistent with the change in orientation of the sheets transmurally (Figure 6.7). The large sub-endocardial shear stress associated with this mode of deformation may not be physiologically reasonable, but without more constitutive property data it is not possible to do better at the moment.

6.6 Active Contraction

Following end-diastole an electrical wave propagates through the ventricular myocardium exciting the myocites causing them to contract and generate force. To model the isovolumic contraction and ejection phases of the cardiac cycle, the forces generated by the contracting cells must also be calculated and added to the passive three-dimensional stress tensor of Equation 2.43. For the purposes of this research it is assumed that the muscle fibres only generate force in the direction of their longitudinal axes, hence only one term needs to be added to the passive stress tensor. Expressing the stress tensor with respect to the microstructural material axes makes only modification of the T^{11} component necessary, as given in Equation 6.1.

$$T^{\alpha\beta} = \frac{1}{2}\left(\frac{\partial W}{\partial E_{\alpha\beta}} + \frac{\partial W}{\partial E_{\beta\alpha}}\right) - pA^{\alpha\beta}_{(v)} + T\delta^{\alpha}_{1}\delta^{\beta}_{1} \tag{6.1}$$

where $T = (t, \lambda_{11}, [Ca^{2+}]_i)$ is the active tension generated by a fibre at time, t.

For the development of the anatomical prolate canine model the active contraction tension was calculated from a cell model implemented at the Gauss points within the FEM for finite elasticity solution procedure. Since then an extensive framework for solving cellular models using a *collocation method* (Hunter et al. 1997) has been developed

within CMISS. The new framework enables the solution of more complex cell models and will ultimately serve full coupling of the electro-mechanics problem. At the time of this research the electrical coupling in three dimensions was still under development, hence only cell-tissue coupled mechanics is considered here. Therefore, the dynamic $[Ca^{2+}]_i$ heterogeneities, due to the spread of electrical excitation are not taken into account.

The collocation method implemented in CMISS is not described here in detail because without consideration of the electrical problem it can be reduced to the evaluation of the cell model at the FEM Gauss points. The point of difference from the earlier canine model is the adoption of the extensible cellular modelling framework to drive the ventricular mechanics simulation. This also enables the investigation of the suitability of different cardiac cell models for coupling to the continuum ventricular model.

Two models for determining the active tension generated by a fibre were investigated, the *fading memory model* (Bergel & Hunter 1979, Hunter 1995) and the more complex Hunter-McCulloch-ter Keurs or *HMT* (Hunter, McCulloch & ter Keurs 1998). The steady state $\left[\mathrm{Ca}^{2+}\right]$-tension relationship function derived from the fading memory model is given in Equation 6.2.

$$T\left(\lambda, \mathrm{Ca}_{actn}\right) = \frac{\left(\mathrm{Ca}_{actn} \cdot \left[\mathrm{Ca}^{2+}\right]_{max}\right)^{h}}{\left(\mathrm{Ca}_{actn} \cdot \left[\mathrm{Ca}^{2+}\right]_{max}\right)^{h} + \left(c_{50}\right)^{h}} \cdot T_{\mathrm{ref}} \cdot \left[1 + \beta\left(\lambda - 1\right)\right] \tag{6.2}$$

where

- $\left[\mathrm{Ca}^{2+}\right]_{max} = 2.5$ mM is the intracellular calcium concentration for maximal activation.
- Ca_{actn} is a non-dimensional parameter which represents the level of activation.
- $c_{50} = 1.25$ mM is the intracellular calcium concentration at which the isometric tension is 50% of its maximum.
- $h = 3$ is the Hill coefficient, determining the shape of the saturation curve.
- $T_{\mathrm{ref}} = 100$ kPa is the isometric, actively developed tension at $\lambda = 1$ and saturating intracellular calcium.

- $\beta = 1.45$ is the non-dimensional slope parameter for the maximally activated isometric tension-λ relationship.

The HMT isometric $\left[\mathrm{Ca}^{2+}\right]$-tension relationship is not presented in detail here because it proved unsatisfactory for reasons detailed in the following section.

The tension generated by the cell models is dependent upon the extension ratios of the fibres, hence the deformation during systole is dependent upon the model deformation at end-diastole. As indicated earlier there are several shortcomings of the model at end-diastole, which must be taken into account when examining any model predictions from the systolic simulations.

6.6.1 Isovolumic Contraction

Isovolumic contraction was modelled by a sequence of quasi-static mechanics solutions coupled to the cell models at increasing states of activation.

The maintainence of the constant cavity volume was achieved via an alternative technique to the earlier work of Nash (1998). Rather than coupling the ventricular wall mesh to meshes of the cavities and solving a coupled multiple region problem, an iterative approach was used. Meshes of the end-diastolic cavity spaces were created to evaluate their volumes. If the ventricular wall contraction reduced the cavity volume, an increase in the cavity pressure boundary condition to restore the volume was estimated, and the problem resolved. This approach had the benefit of not requiring any equations to be simultaneously solved for the cavity regions and being simpler to implement in rectangular cartesian coordinates, but increased the number of solution steps required, which was not a large penalty.

Convergence for the coupled HMT-ventricle model could not be a achieved for an LV cavity pressure above 2.6 kPa. The reason for this appeared to be that the HMT cell model is more sensitive to the tissue extension ratios, creating large tension gradients across the ventricular wall.

The fading memory model deforms the LV into a more physiological spherical shape while HMT squeezed the LV into a more elongated shape. This suggests that the circumferential tensions from HMT were too high relative to the subepi- and subendocardial tensions, which in turn might be because the predicted end-diastolic transmural strain

variation is too large. An effort was made to modify the HMT parameters to reduce the sensitivity to the tissue extension ratios (specifically β_0), but the result remained similar. Therefore only the fading memory model results are presented and discussed here. The deformed end-diastolic and end-isovolumic contraction models are plotted in Figure 6.11.

The LV cavity volume was maintained at its end-diastolic volume of 33 ml while the active tension along the fibre axes was increased. Several studies have reported end-isovolumic contraction cavity pressures of approximately 15kPa (Waldman et al. 1985, LeGrice, Takayama & Covell 1995), but model convergence could not be achieved for cavity pressures beyond 9.6 kPa. Again this appears to be related to the lack of adequate regional variation of material properties. Considerable testing of the model using a variety of constitutive laws, material properties and boundary conditions suggests that a inhomogeneous parameter set is necessary to improve the robustness of the model.

During this isovolumic contraction simulation the apex-base twist was 23.4 degrees from the end-diastolic state, and the apex-to-base length of the model decreased slightly to 60.12 mm from 60.27 mm.

The isovolumic contraction phase of the simulation took approximately 4 hours on a single processor on an IBM pSeries 690.

6.6.2 Ejection

Ideally an accurate model of the fluid mechanics within the ventricles and the great vessels would provide for the correct impedance behaviour during ejection. Although such models are in development, they are not yet mature enough to accurately simulate the pressure loading within the ventricular cavities during ejection. Instead the cavity pressure was gradually decremented, solving for the ventricular wall deformation at each step. The active tension generated by the cell model was kept at the level obtained at the end-isovolumic contraction. Hence the quasi-static solutions are representative of the deformation at a given pressure loading and myocardial activation level, but the sequence of solutions may not be representative of the actual cardiac sequence. Nevertheless, the solutions do provide insight into the mechanical behaviour of the ventricular wall during systole and are a valid for examining the end-systolic state.

At end-systole, zero LV cavity pressure, the LV cavity reduced to a volume of 17 ml from 33 ml. The ejection fraction of 48% compares favourably with the values reported in the literature, published figures vary with an average about 45% (Fann, Sarris, Ingels, Niczyporuk, Yun, Daughters, Derby & Miller 1991, Azhari, Weiss, Rogers, Siu, Zerhouni & Shapiro 1993). Plots of the model at the end of each of the phases of the simulated cardiac cycle are presented in Figure 6.11.

The circumferential distribution of the myocardial material stretch is plotted in Figure 6.12. The myocardium is contracted along the fibre axis direction by the myocyte activation, and expands in the sheet and sheet-normal directions because it is incompressible. The variation in the circumferential distribution of fibre stretch can be related to variations in the wall thickness and the fibre orientation. The end-systolic distributions of fibre stretch in the LV free wall a plotted in Figure 6.13. The average fibre extension ratio in the LV free wall is approximately 0.9, which is consistent with the experimental results of Rodriguez, Hunter, Royce, Leppo, Douglas & Weisman (1992) and Guccione, Le Prell, de Tombe & Hunter (1997). The variation in fibre strain in the subendocardium appears to be consistent with the variation in wall thickness. Further more, the incompressibility constraint is particularly non-physiological in the subendocardium and may skew the results in this region. The apex-base shortening of the model from the beginning till the end of ejection also compares well with published literature. The model predicts a length change of 3.47%, Rankin, McHale, Arentzen, Ling, Greenfield & Anderson (1976) reported an apex to base length change of 4.7% $\pm$0.3% from eight closed chest dogs, although the base was measured as the top of the left atrium in this case .

The apex-base twist during ejection was a slight untwisting of -0.6 degrees. The total twist from end-diastole to end-systole was then 22.8 degrees. This model result is consistent with reported values of about 20 degrees (Beyar, Yin, Hausknecht, Weisfeldt & Kass 1989).

Although there have been studies of the regional distribution of myocardial strain in dog (Rademakers, Rogers & Guier 1994, Villarreal, Lew, Waldman & Covell 1991, McCulloch & Omens 1991) the data is not suitable for a rigorous examination of the porcine model developed here. However, a project is currently underway at the University of Auckland Bioengineering Institute to comprehensively characterise the strain distribution in the porcine ventricles (Augenstein, McVeigh & Young 2001). The study in progress uses tagged MRI to measure the deformation of excised hearts during pas-

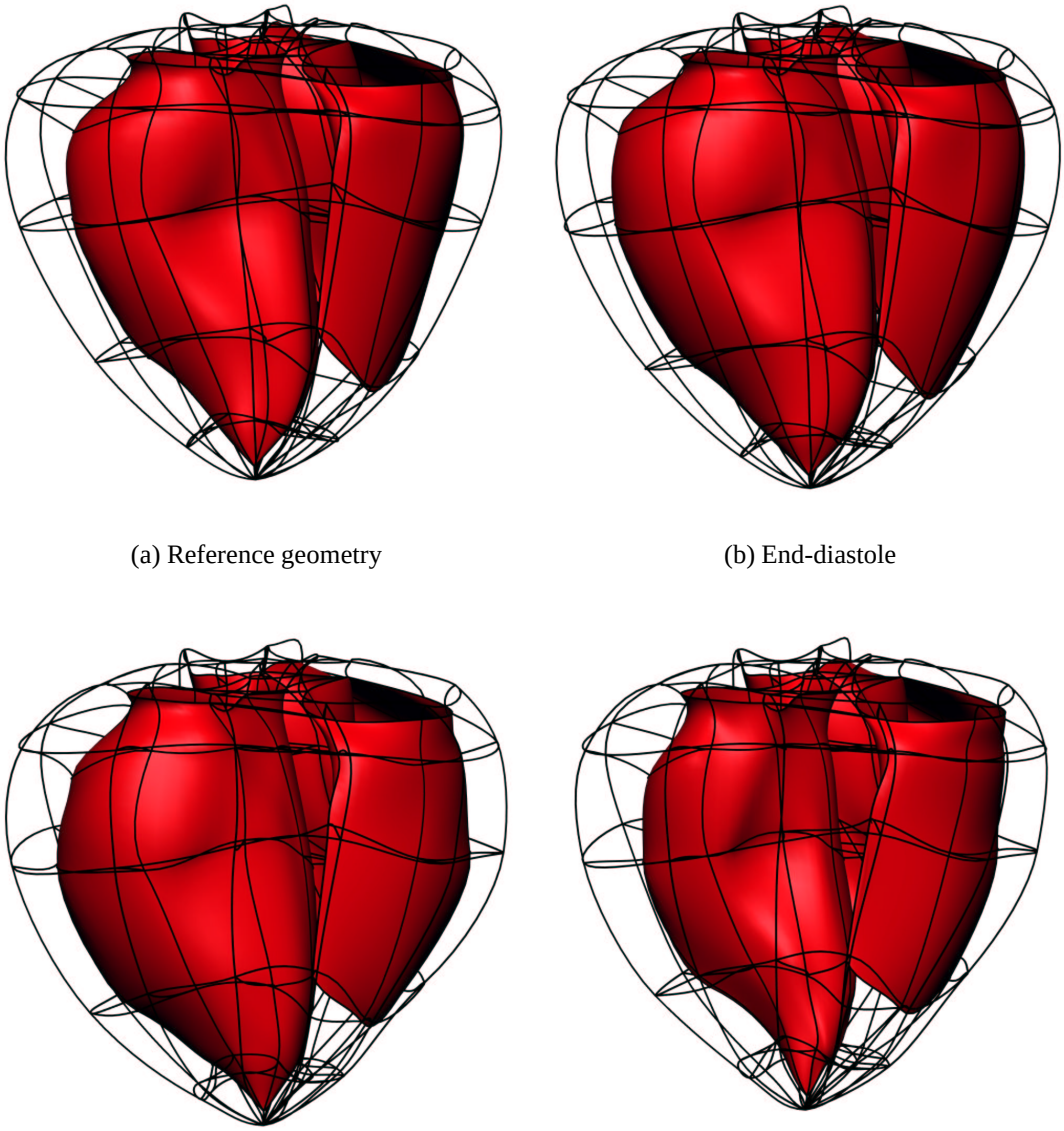

(a) Reference geometry

(b) End-diastole

(c) End-isovolumic contraction

(d) End-systole

FIGURE 6.11: Plots of the model deformation at the end of each phase in the simulated cardiac cycle.

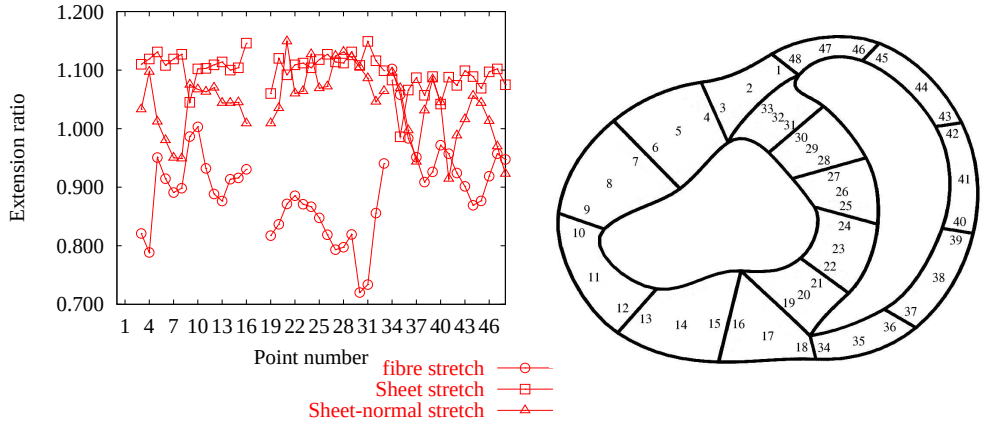

FIGURE 6.12: Circumferential distribution of fibre, sheet and sheet-normal stretch at equatorial midwall locations shown on the right at end-systole. The numbers on the horizontal axis refer to Gauss point locations in the sequence around the heart shown by the figure on the right. Note that strain components at locations 1,2,17,18 are omitted from the plot because the fibre orientations are not in the circumferential direction.

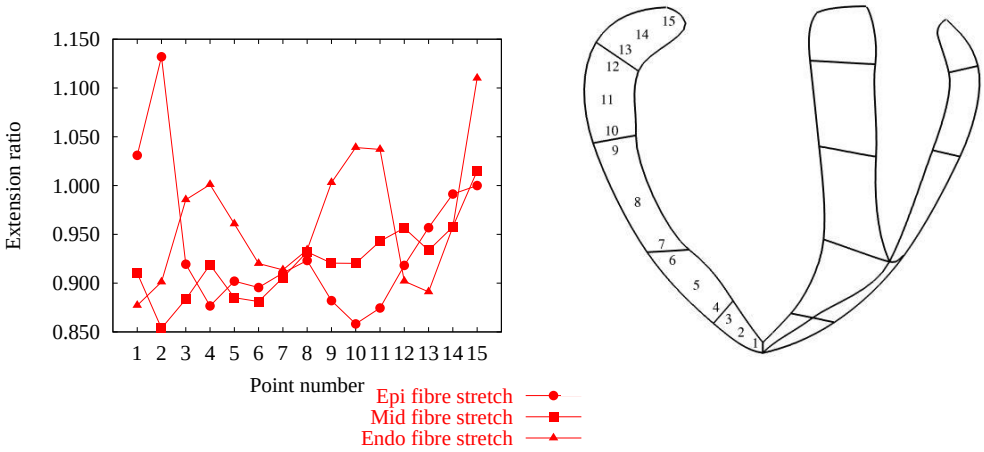

FIGURE 6.13: Base-apex distribution of fibre stretch in the subepicardium, midwall and subendocardium at end-systole.

sive inflation by a pumping device. The data will serve to determine the constitutive law parameters *in vivo* and further validate the porcine model developed here.

The ejection phase of the simulation took approximately 2 hours on a single processor on an IBM pSeries 690.

6.7 Numerical Verification

It is important to assess the sensitivity of the deformation solutions to the discretisation of the finite element mesh. If the mesh is too course the solution fields will lack the degrees of freedom required to accurately represent the actual deformation, rendering the results useless. Prior to designing the model presented here, experience was gained modelling single LV's as part of the study, presented in the following chapter, that experience suggested the use of the mesh discretisation and interpolation schemes used for this model. To confirm those design choices were in fact sound and the solutions are *converged*, that is, would not differ if the mesh was more finely discretised, the LV free wall was refined transmurally, since the strains vary most rapidly in that direction. Figure 6.14 shows the locally refined mesh, and the end-diastolic Gauss point strain distributions are plotted together for comparison in Figure 6.15.

Refinement of the model introduced another 400 solution degrees of freedom. 200 of which are at hanging nodes, and hence are explicitly mapped to genuine degrees of freedom, removing them from the system of equations (Section 3.1.4). Thus a total of 200 new degrees of freedom are are added to the system of equations. The elements within which the strains are evaluated do not contain any hanging nodes. The local refinement add added another 8 minutes to the total solution time.

The strain comparisons between the refined and original models presented in Figure 6.15, indicate that the unrefined mesh is a suitable model for investigating myocardial deformation. Refinement of the mesh does not alter the behaviour of the model significantly. However, the difference in the sub-endocardial sheet-normal strain should be kept in mind when interpreting the results of the unrefined model.

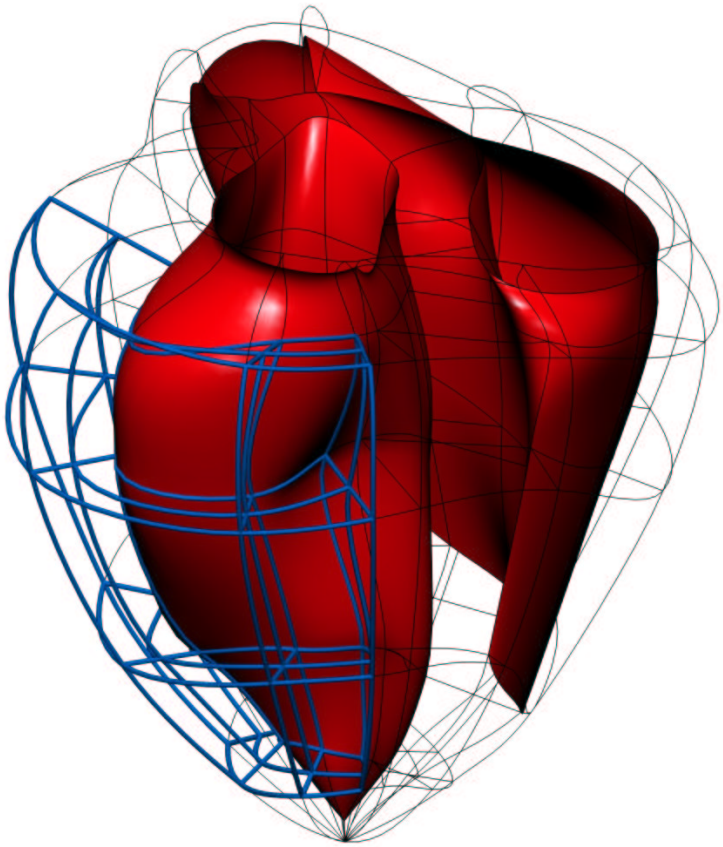

FIGURE 6.14: Transmural local refinement of the LV free wall.

6.8 Summary and Discussion

A new finite element mechanics model of the left and right ventricular myocardium has been developed. In contrast to an earlier prolate spheroidal model of the dog heart, the model is developed in rectangular cartesian coordinates and uses tricubic Hermite basis functions for the geometric coordinates. The fibrous-sheet structure of the pig heart was measured and fitted with parameters defined at the nodes of the finite element mesh. In comparison with the earlier dog heart model, this new pig heart model gives a much more accurate description of the base and valve ring geometry. The thin apex of the heart is also now modelled more accurately than in the previous model.

The model was used to simulate the cardiac cycle. The pole-zero constitutive law for myocardium formulated with respect to the underlying microstructure represented the ventricular myocardium stress-strain response. Physiological boundary conditions and myocite activation models simulated observed ventricular mechanics with an acceptable degree of accuracy.

At end-diastole the circumferential distribution of fibre stretch reflects the circumferentially varying wall thickness. The peak fibre strain occurs between the regions where the free wall is thickened by the bulge of the papillary muscles. The minimum fibre strain

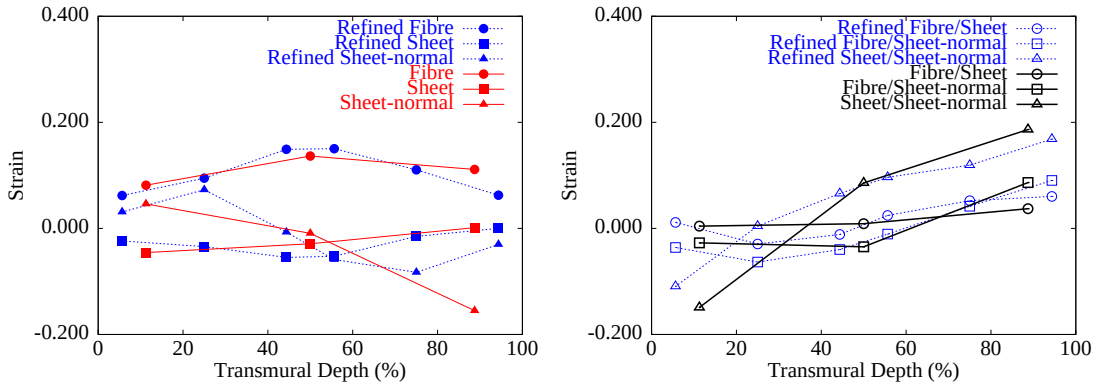

(a) Normal strains

(b) Shear strains

FIGURE 6.15: Gauss point fibre strains the equatorial lateral LV free wall at end-diastole. Refinement of the mesh yields little change in the predicted strains. (The sampling locations are connected linearly to clarify the data; the strains do not vary linearly between the Gauss points).

occurs where the wall is thickest at the junction of the right ventricle with the septum. Sheet strains are compressive because the sheets lie primarily in the transmural direction which thins during diastole. The sheet-normal direction is primarily in the base-apex direction and this is extended during diastole, yielding a positive sheet-normal stretch. The longitudinal distribution of fibre stretch is fairly uniform (within 5%, except at the base and apex) and with small transmural variations (also less than 5%).

The systolic deformation response exhibited physiological characteristics. An ejection fraction of 48% was predicted with an apex-base shortening of approximately 4%. The large ejection fraction is achieved through apex-base twist of 22.8 degrees and wall thickening of 33% in the equatorial region.

The choice of constitutive properties for the myocardium significantly effect the resultant deformation. The use of a homogeneous parameter set does not accurately represent reality. One approach to rectify this would be to experimentally determine the stress-strain relationship for tissue from many regions throughout the ventricles. Alternatively, formulation of growth laws to determine the required stiffnesses based upon stress and strain from cardiac cycle simulations may be sufficient. The later adaptive approach would also have the benefit of enabling remodelling simulations.

Further investigation of the sensitivity of the ventricular mechanics during diastole to the material parameters, is presented in an article accepted for publication included in Appendix D.

6.8.1 Limitations of the Model

As noted throughout this thesis many assumptions have been made to reduce the complexity of the model. These simplifications limit the applicability of the model predictions. The following are the major limitations of the model:

- The myocardial tissue is modelled as incompressible which is not completely accurate, particularly in the sub-endocardium (Krams, Sipkema & Westerhof 1989). This immediately limits the models ability to accurately predict strains in the sub-endocardium.
- The constitutive parameters used in the pole-zero constitutive law for myocardium are primarily based upon *in-vitro* biaxial tension tests of this sections of ventricu-

lar myocardium. These parameters would be better estimated using *in-vivo* techniques, possibly with deformation data from MRI along with pressure recordings.

- Transmural and regional variations of material properties are not included in the model presented here. The passive inflation simulations suggest regional variations of material properties must be modelled to successfully simulate the deformation of the apical and right ventricular regions and simulate physiological loading.

- The compressive response of myocardial tissue is poorly quantified. For this study it was approximated using a shallow linear strain energy function. Further experimental studies are required before the compressive myocardial response can be modelled.

- The papillary muscles are not yet modelled - an important omission that needs to be rectified in the future because the mechanical loads transmitted from the systolically loaded mitral valve to the apical free wall by the papillary muscles is an important aspect of ventricular mechanics during systole.

- The model of the fibrous-sheet structure of the heart presented here assumes that the fibres lie in planes tangent to the epicardial and endocardial surfaces. From LeGrice (1992) measurements, the out-of-plane deviation (imbrication angle) is less than 5 degrees for the bulk of the myocardium but is substantially greater than this for the regions of the myocardium close to the apex and base, where fibres spiral inward to provide continuity from epicardium to endocardium.

- The rigid boundary conditions applied at the base are not completely physiological. The basal skeleton does deform, though considerably less than the ventricular myocardium and valve orifices themselves change in diameter throughout the cardiac cycle. The model may also benefit from being coupled to a model of the pericardial sac which would alter the ventricular deformation by limiting the the radial expansion (Katz 1992) and increasing the apex-base lengthening.

- The current model does not include *myocardial fluid shifts* or *viscoelasticity* (Bache & Cobb 1977, Huyghe et al. 1992, Yang & Taber 1991).

Many of these issues are being actively researched both at the University of Auckland Bioengineering Institute and research groups abroad.

Chapter 7

A Finite Element Model of Myocardial Infarction

Until recently most efforts to model infarction (Section 1.2) have focussed on the impact of a noncontracting segment on overall ventricular function. The common approaches to modelling ischemic myocardium utilise material descriptions of passive myocardium, or normal myocardium with modifications such as reduced contractility, reduced maximal tension, or altered myofilament calcium sensitivity. The presence of myocardial scar tissue decreases the performance of the heart by (i) decreasing the amount of contracting myocardium contributing to ejection (Parmley, Chuck, Kivowitz, Matloff & Swan 1973), (ii) by stretching locally during systole, *(aneurysmal bulging,*) thereby reducing the stroke volume, and (iii) by interfering with the shortening and thickening of the adjacent myocardium (Janz & Waldron 1977, Lessick, Sideman, Azhari, Marcus, Grenadier & Beyar 1991, Guccione, Moonly, Moustakidis, Costa, Moulton, Ratcliffe & Pasque 2001). It has been concluded therefore that the decrease in cardiac performance post-infarction depends both on the scar size (Choong, Gibbons, Hogan, Franklin, Nolting, Mann & Weyman 1989, Pfeffer, Pfeffer, Fishbein, Fletcher, Spadaro, Kloner & Braunwald 1979) and the scar stiffness (Bogen, Rabinowitz, Needleman, McMahon & Abelmann 1980, Bogen, Needleman & McMahon 1984, Janz & Waldron 1977, Parmley et al. 1973, Swan, Forrester, Diamond, Chaterjee & Parmley 1972).

Holmes (1995) recognised that the term scar stiffness was too simplistic and attempted to determine the collagen fibre structure and its relationship to mechanical properties and deformation in myocardial scar. An experimental study was completed and a con-

stitutive law for infarcted myocardium proposed. Holmes also performed a limited investigation of the validity of the proposed constitutive relationship using a simple axisymetric prolate finite element model. A quote from the end point of that work sets the scene for the work carried out in this chapter:

> *We therefore collected three-dimensional regional strain data during passive inflation and digitized the three-dimensional geometry for these infarcted hearts to allow parameter estimation via a model optimization approach. At present, this validation awaits refinement of computational methods for handling the rapid changes in local geometry and material properties that occur over very short distances at the scar border.*

The work by Holmes et al. is described in more detail in the following sections. This chapter presents the computational methods developed for handling sharp changes in geometry and material properties. A model optimisation approach is then used to estimate parameters for the Holmes constitutive law for infarcted myocardium.

The pole-zero constitutive law has proven suitable for relating the deformation behaviour of normal myocardium to its microstructural constituents (Section 4.4.3). Therefore, the ability of the pole-zero law to represent the constitutive behavior of infarcted myocardium is also investigated here.

Following the development of the constitutive relationships for infarcted myocardium, a quantitative comparison is made of the end-diastolic states of the anatomical porcine model developed in Chapters 5 and 6 pre- and post infarction. The command file used for the following simulations is included in Appendix C.

7.1 Constitutive Laws for Infarcted Myocardium

7.1.1 Holmes Passive Infarction Mechanics Study Review

This section describes the relevant details of the study performed by Holmes et. al. upon which the models in this chapter are developed.

Experimental Work

Transmural infarcts were induced in the left ventricle of domestic farm pigs by ligation of an obtuse marginal branch of the left circumflex coronary artery. The animals were then left to recover. Three weeks later two sets of marker beads were implanted, one in the scar tissue and the second in the noninfarcted anterior wall of the left ventricle. A set of marker beads consisted of three columns of small (0.9-1.0 mm diameter) gold beads. Each column contained three or four beads 2-3 mm apart. The hearts were arrested and removed. The left atrium was opened and a balloon secured to a custom mitral plug was inserted (Figure 7.1).

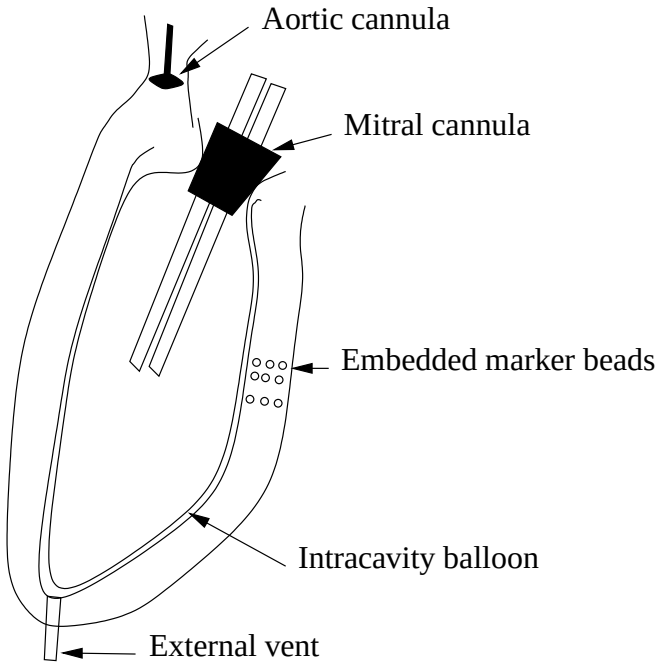

FIGURE 7.1: Diagram of the isolated arrested heart preparation used to study passive mechanics of the infarcted left ventricle.

The mitral plug was secured in the annulus by a suture. An aortic cannula was positioned above the valve leaflets and secured to prevent herniation of the balloon into the aorta. Pressure and volume data was acquired as the ventricle was inflated to a maximum pressure of 30 mmHg. Simultaneously the marker bead positions were recorded under flouroscopy using biplane video tape.

Upon completion of the data acquisition runs the left ventricles were filled with silicon

rubber which was allowed to harden. The fixed ventricle was then sliced into 5mm thick short axis slices. The epicardial and endocardial contours of each slice were traced onto transparencies, as well as the infarct boundaries which were grossly visible.

Transmural blocks of tissue were then removed from each of the bead sets for histology. The collagen content, collagen orientation and muscle fibre angles were measured at 0.5 mm increments from the epicardial surface to the endocardial surface through the infarcted blocks. The measurements were made at 1.0 mm increments through the normal myocardium blocks.

Holmes observed that most of the muscle in the infarct region had been replaced by collagen, which is in agreement with reports on humans (Smith, Feild & Rackley 1974). It was observed that within the scar there were several unique features that acted to increase the number of collagen fibres oriented along the circumferential direction, and presumably the ratio of overall circumferential to longitudinal stiffness in the scar.

- The transmural collagen fibre angle gradient in the scar was less steep than the muscle fibre gradient in noninfarcted muscle. Hence the collagen fibres were aligned more circumferentially than longitudinally within the inner half of the wall, where the stresses are expected to be highest.
- The scatter of the collagen fibre angles about the mean angle was greater in the sub-epi and sub-endocardium, where the mean angle was the farthest from circumferential. Thus even in these layers substantial numbers of collagen fibres were oriented more circumferentially than longitudinally.
- The collagen area fractions were highest in the midwall. Therefore the circumferential mean angles measured near the midwall represented more collagen fibres than the angles measured in the inner and outer wall.

Since the scar was composed primarily of large collagen fibres that resist stretch along their axes, Holmes predicted from these features that the large numbers of nearly circumferential fibres in the scar will result in a high ratio of circumferential to both longitudinal and radial stiffness in the scar tissue.

The positions of the marker beads were recorded as the cavity pressure was incremented. From the changes in the bead positions the deformation gradient tensor, $\mathbf{F}$, was calculated within each of the bead sets using the finite element method. The strains measured

during passive inflation supported the interpretation of the collagen structure. While the longitudinal strain in the scar was slightly greater than in the remote myocardium at any cavity pressure, the circumferential strain was smaller at all depths and pressures. A significant finding of the Holmes study was that radial strain was also similar in the scar and the remote myocardium.

Having measured the scar structure and deformation under controlled loading conditions and found them to agree generally with the concept that collagen fibres in the scar contribute significantly to its mechanical behavior by resisting axial deformation, Holmes formulated a constitutive law to test the hypothesis that the collagen density and distribution are the principle determinants of the scars material properties using a finite element model. The constitutive law formulation is presented in the following section.

Constitutive Law Formulation

Tendon and passive myocardium can be modelled as hyperelastic materials (Douglas, Rodriguez, O'Dell & Hunter 1991), for which the Cauchy stress tensor, Σ, can be related to the Lagrangian strain tensor E through a strain energy function W (Section 2.3). Following Choung & Fung (1986) Holmes employed a strain energy function of the form given in Equation 7.1 because a function for which most of the material constants could be determined from structural measurements was desired. The function contains an isotropic term and a set of terms related to the axial deformation of collagen fibres.

$$W = \frac{C_1}{2}\left(\mathrm{e}^{Q} - 1\right) \tag{7.1}$$

where

$$Q = C_2(I_1 - 3) + C_3(fibre\,strain\,terms)$$

At each transmural depth, the orientation of individual fibres, α_i, were expressed relative to the local mean fibre angle, θ_{mean}.

$$\alpha_i = \theta_i - \theta_{mean} \tag{7.2}$$

The axial strain of each fibre was given in terms of strain components in an axis system aligned with the mean fibre, cross-fibre and radial directions. It was observed that the large collagen fibres were all parallel with the local epicardial tangent plane, therefore the radial components of the fibre vectors were set to zero.

$$\begin{aligned}
\mathrm{E}_\alpha &= \mathbf{n}_\alpha \mathbf{E} \mathbf{n}_\alpha && (7.3)\\
&= \begin{bmatrix} \cos\alpha \\ \sin\alpha \\ 0 \end{bmatrix}^{\mathrm{T}} \begin{bmatrix} \mathrm{E_{ff}} & \mathrm{E_{fc}} & \mathrm{E_{fr}} \\ \mathrm{E_{cf}} & \mathrm{E_{cc}} & \mathrm{E_{cr}} \\ \mathrm{E_{rf}} & \mathrm{E_{rc}} & \mathrm{E_{rr}} \end{bmatrix} \begin{bmatrix} \cos\alpha \\ \sin\alpha \\ 0 \end{bmatrix} && (7.4)\\
&= \mathrm{E_{ff}} \cos^2\alpha + (\mathrm{E_{fc}} + \mathrm{E_{cf}}) \cos\alpha \sin\alpha + \mathrm{E_{cc}} \sin^2\alpha && (7.5)
\end{aligned}$$

Q was chosen to be formulated with respect to squared strain components, from Equation7.5,

$$\begin{aligned}
\mathrm{E}_\alpha^2 &= \mathrm{E_{ff}^2} \cos^4\alpha + \mathrm{E_{cc}^2} \sin^4\alpha \\
&\quad + (2\mathrm{E_{ff}}\mathrm{E_{cc}} + \mathrm{E_{fc}^2} + 2\mathrm{E_{fc}}\mathrm{E_{cf}} + \mathrm{E_{cf}^2}) \sin^2\alpha \cos^2\alpha \\
&\quad + (2\mathrm{E_{ff}}\mathrm{E_{fc}} + 2\mathrm{E_{ff}}\mathrm{E_{cf}}) \sin\alpha \cos^3\alpha \\
&\quad + (2\mathrm{E_{fc}}\mathrm{E_{cc}} + 2\mathrm{E_{cf}}\mathrm{E_{cc}}) \sin^3\alpha \cos\alpha
\end{aligned} \tag{7.6}$$

At a given depth a group of k individually measured fibre angles and an expression for the squared axial strain of each fibre were defined. To sum the contributions of the individual fibres, the fibre angle measurements were treated as a discrete distribution. The probability of finding a fibre at a given angle α is given by $\mathrm{h}(\alpha)$:

$$\mathrm{h}(\alpha) = \begin{cases} \frac{1}{\mathrm{k}} & \text{if } \alpha = \alpha_\mathrm{j},\ \mathrm{j} = 1, 2, ..., \mathrm{k} \\ 0 & \text{otherwise} \end{cases} \tag{7.7}$$

To account for potential variations in area fraction in different regions of the scar, the probability functions were weighted by the measured collagen area fraction, AF.

$$\mathrm{h}^{'}(\alpha) = \begin{cases} \frac{\mathrm{AF}}{\mathrm{k}} & \text{if } \alpha = \alpha_{\mathrm{j}},\ \mathrm{j} = 1, 2, ..., \mathrm{k} \\ 0 & \text{otherwise} \end{cases} \tag{7.8}$$

Summing the contributions of each fibre provides the fibre strain terms in Equation 7.1:

$$Q = C_2(I_1 - 3) + C_3 \left[\sum_{1}^{\mathrm{k}} \mathrm{h}^{'}(\alpha_{\mathrm{j}}) \mathrm{E}_{\alpha}^2(\mathrm{E}_{\mathrm{ff}}, \mathrm{E}_{\mathrm{fc}}, \mathrm{E}_{\mathrm{cf}}, \mathrm{E}_{\mathrm{cc}}, \alpha_{\mathrm{j}}) \right] \tag{7.9}$$

Expanding and rearranging

$$Q = C_2(I_1 - 3) + C_3 \left[\begin{array}{ll} & C_4 \mathrm{E}_{\mathrm{ff}}^2 \\ + & C_5 \mathrm{E}_{\mathrm{cc}}^2 \\ + & C_6(2\mathrm{E}_{\mathrm{ff}}\mathrm{E}_{\mathrm{cc}} + \mathrm{E}_{\mathrm{fc}}^2 + 2\mathrm{E}_{\mathrm{fc}}\mathrm{E}_{\mathrm{cf}} + \mathrm{E}_{\mathrm{cf}}^2) \\ + & C_7(2\mathrm{E}_{\mathrm{ff}}\mathrm{E}_{\mathrm{fc}} + 2\mathrm{E}_{\mathrm{ff}}\mathrm{E}_{\mathrm{cf}}) \\ + & C_8(2\mathrm{E}_{\mathrm{fc}}\mathrm{E}_{\mathrm{cc}} + 2\mathrm{E}_{\mathrm{cf}}\mathrm{E}_{\mathrm{cc}}) \end{array} \right] \tag{7.10}$$

where

$$\begin{aligned} C_4 &= \sum_{1}^{\mathrm{k}} \mathrm{h}^{'}(\alpha_{\mathrm{j}})(\cos\alpha_{\mathrm{j}})^4 \\ C_5 &= \sum_{1}^{\mathrm{k}} \mathrm{h}^{'}(\alpha_{\mathrm{j}})(\sin\alpha_{\mathrm{j}})^4 \\ C_6 &= \sum_{1}^{\mathrm{k}} \mathrm{h}^{'}(\alpha_{\mathrm{j}})(\sin\alpha_{\mathrm{j}})^2(\cos\alpha_{\mathrm{j}})^2 \\ C_7 &= \sum_{1}^{\mathrm{k}} \mathrm{h}^{'}(\alpha_{\mathrm{j}})(\sin\alpha_{\mathrm{j}})(\cos\alpha_{\mathrm{j}})^3 \\ C_8 &= \sum_{1}^{\mathrm{k}} \mathrm{h}^{'}(\alpha_{\mathrm{j}})(\sin\alpha_{\mathrm{j}})^3(\cos\alpha_{\mathrm{j}}) \end{aligned}$$

The constants C_4 through C_8 can be determined from the measured large collagen fibre distribution within the scar. The remaining three constants C_1, C_2 and C_3 scale the steepness of the exponential and the relative contributions of the large collagen fibres to the isotropic background.

Holmes estimated values for C_1, C_2 and C_3 of 0.5 kPa, 1 and 100 respectively from a series of trials using a simple axisymetric prolate model. The simple model was unable to represent the regional variation in material properties, so the entire myocardium was described with the constitutive relationship developed for the infarcted tissue.

In this chapter the computational methods required to determine the remaining three constants are developed and applied to experimental data provided by Holmes et. al.

7.1.2 Validating the Holmes Constitutive Relationship for Infarcted Myocardium

If the constitutive law for infarcted myocardium formulated by Holmes is a suitable representation of the scar tissue behavior, it is attractive because it is based directly upon physical measurements. However, there are three unknown scaling variables. To validate the infarcted material description the remaining variables must be determined and the model predictions compared to the experimental recordings. A parameter optimisation approach is used to determine values for the unknown constants.

Specimen Specific Geometric Model

A finite element model of the most typical specimen was made from the digitised ventricular surface data following the procedure described in Section 5.2.2. The specimen chosen was labeled scp04 in the Holmes study. The model was created in rectangular cartesian coordinates using tricubic Hermite interpolation with the techniques presented in Section 5.2.2. The parametric element coordinates were aligned the same as the models already presented, ξ_1 circumferentially, ξ_2 longitudinally and ξ_3 radially outward. A circumferential mesh resolution of eight elements was the lowest resolution that could represent the geometry suitably. Although there is little geometric variation longitudinally, four elements were chosen to keep the mesh resolution similar in all three direc-

tions. The epicardial and endocardial surfaces were fitted with RMS errors of 0.79 and 0.68 to 2782 and 1581 data points respectively.

A tricubic Hermite finite element mesh was also fitted to the infarct geometry for use with the material property description presented in the following section. The LV and infarct models are shown in Figure 7.2.

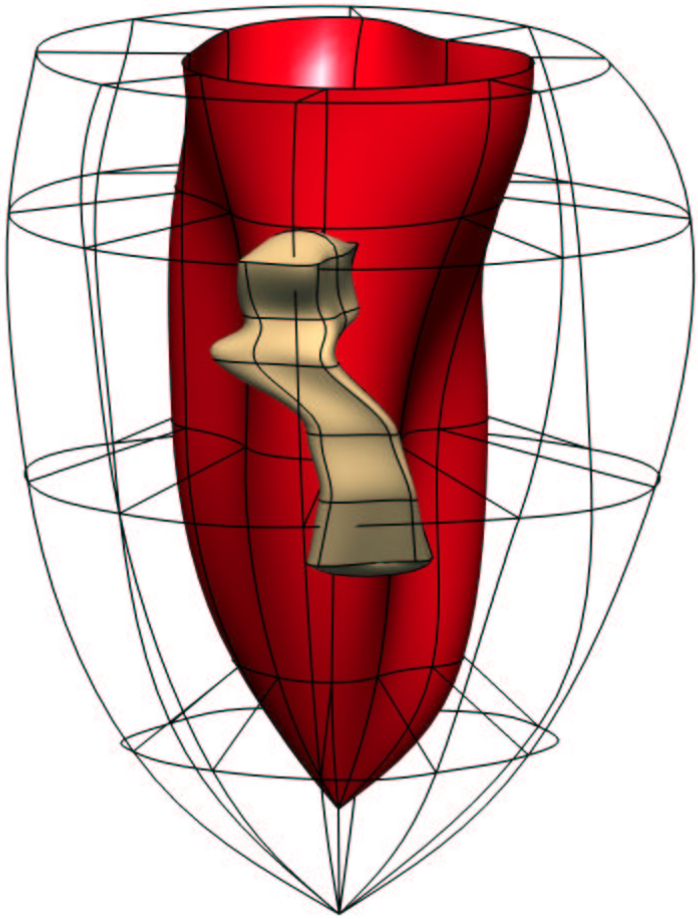

FIGURE 7.2: The fitted finite element model of the infarcted LV of specimen scp04 and the meshed infarction. The infarct mesh protrudes from the ventricular mesh slightly because each surface was fitted independently. The specimen is 62.25 mm from apex to base.

Spatially Varying Material Properties

The material properties of infarct tissue are dramatically different from the surrounding myocardium and the transitional border zone is relatively narrow. The finite element model must be capable of representing both the spatially varying material parameters and the deformation solution accurately. In order to achieve the required accuracy with a computationally efficient model, the hanging or constrained node method for high order cubic Hermite elements was developed (Section 3.1.4) along with a new framework for prescribing spatially varying model parameters within CMISS.

Although localised refinement provides more resolution of the dependent variables, it is not very convenient to describe the material parameter fields using nodally interpolated or element based fields. It would be a tedious task to align the node positions and element boundaries with the infarct geometry and determine the appropriate nodal or element values of the material parameters. Then if the desired mesh resolution were to be changed, the task would have to be repeated. These problems are overcome here by extending existing facilities within CMISS and applying them in a new way.

First, a common technique used by graphics programmers to map images or *textures* onto element meshes is used to map the material parameter data into the elements through the heart wall. The material parameter data for C_4 through C_8 was provided in terms of wall depth, but the wall may be modelled using any number of elements transmurally. Therefore each material parameter data set is represented as a texture field that is scaled to fit across the wall. The texture field is then sampled where the material parameter values are required. The transmural texture field values for the spatially varying parameters C_4, C_5 and C_6 are presented in Figure 7.3. The material parameter data was limited to wall depths from 20% through 80%, the properties for the remainder were estimated to be equivalent to the nearest data. As well as convenience this approach has another very appealing point. Since the material parameter description is independent of the finite element model, the same material parameter value is obtained at any given depth regardless of the number of transmural elements or their interpolation schemes.

The current CMISS implementation does not provide for the direct sampling of the material parameter textures at the Gauss points, where those quantities are required during the solution process. Rather than adding this feature, an intermediate step that may offer future benefits was introduced. CMISS contains a framework for solving cellular models (Section 6.6) and modelling electrical activation problems using collocation grids

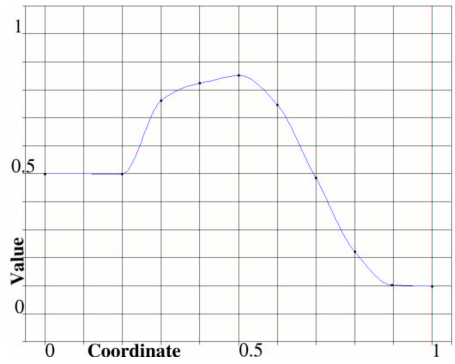

(a) C4

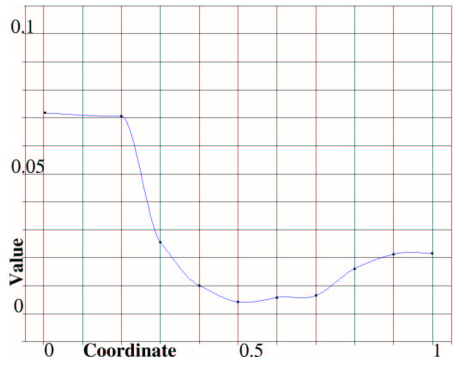

(b) C5

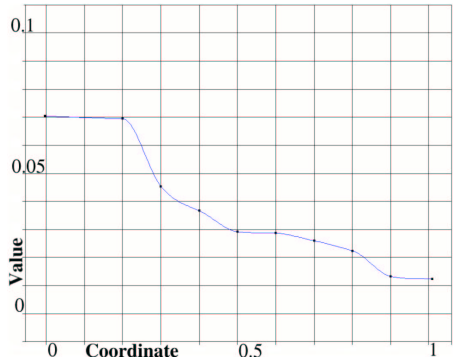

(c) C6

FIGURE 7.3: The material parameter texture fields for the spatially varying parameters C_4, C_5 and C_6. The texture fields are defined from 0 to 1, zero being at the endocardium and 1 at the epicardium. The parameter value texture field is scaled to span the extent of the model to which it applies and can span multiple elements.

embedded within finite elements (Hunter et al. 1997). The texture fields are evaluated at the grid points, and Gauss point values then interpolated from the grid points. With a sufficiently high resolution collocation grid the Gauss points are very close to the nearby grid points at which the material parameter was evaluated, interpolating from them provides an accurate estimate of the material parameter value at the Gauss point. The process is illustrated in Figure 7.4. Research is also progressing on solving distributed metabolism problems and cellular mechanics on the embedded grids. The mechanical material properties of the myocardium and infarct tissue are ultimately dependent upon cellular activity, therefore working on the framework to couple the large continuum mechanics models to the finer scale cellular models was an attractive direction to further develop CMISS.

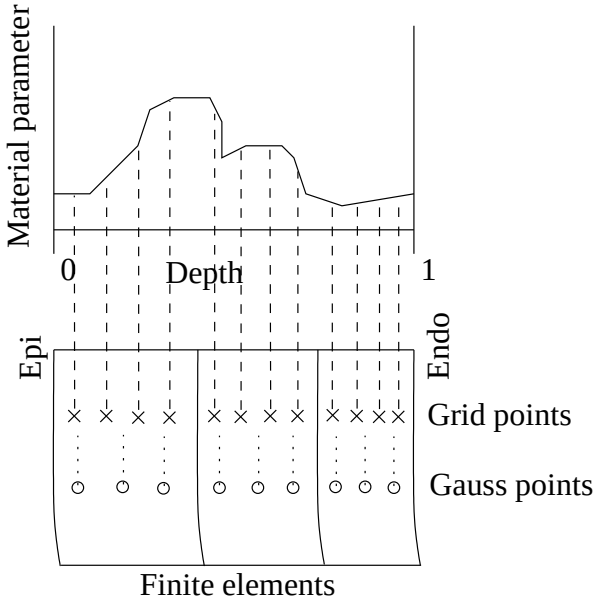

FIGURE 7.4: Material parameter fields are represented as textures that are scaled across the heart wall. The material parameter texture fields are evaluated at the embedded grid points then interpolated to the Gauss points.

In order to define the myocardium and scar tissue properties separately the grid points need to be divided into two groups, those inside the infarct and those in the normal myocardium. The transitional border zone was not modelled since data was not acquired in that region. The grouping was determined by evaluating whether or not the grid point position lay within the finite element mesh of the infarcted region or not. A Newton-Raphson root finding method was used to calculate the ξ-coordinates of each grid point

within each infarct element. Only the points with ξ-coordinates that were within the element i.e. between 0 and 1, were added to the infarct grid point group.

A transmural resolution of three elements was found to be adequate to represent the transmural variation in the material property fields. The mesh was also refined locally in the longitudinal and circumferential directions to retain cuboid elements and to provide a higher resolution of the dependent variable fields.

In summary, a localised refinement technique was developed for high order elements. The model was refined locally about the infarcted region to achieve a high resolution of the dependent variables and material parameters. A semi-automated procedure was developed to define the material parameters within the infarct. The method provides a mechanism for future coupling of mechanical constitutive law parameters to cellular scale models. Figure 7.5 shows the grid points within the infarct and a spatially varying material field parameter plotted.

The fibre angles were only accurately measured within the infarcted region and in another control region in the lower left anterior wall. That data was inadequate to fit a FE field description over the entire model. In the control region the fibre angle orientations were consistent with the data fitted in Section 5.2.8. The difference in geometry of the infarct specimen and the porcine model indicated that there was little to gain by mapping the porcine model fibre fields into the infarct specimen. Therefore a theoretical field was generated for evaluation of the constitutive law in the FEM. The fibre angle distribution was modelled as varying linearly from the -60 degrees at epicardium to +60 degrees on the endocardium. Within the infarcted region the fibre angle distribution was modified to +30 degrees on the endocardium to represent the more circumferential collagen fibre alignment measured within the scar tissue (Holmes 1995).

Material Parameter Estimation

The experimental ventricular pressure and strain data provide more information about the behavior of the scar tissue than the structural measurements alone. The remaining unknown material parameters were found by optimising their values to minimise the difference between the model deformation and the experimentally measured deformation.

The objective function was evaluated using the deformation at three transmural locations

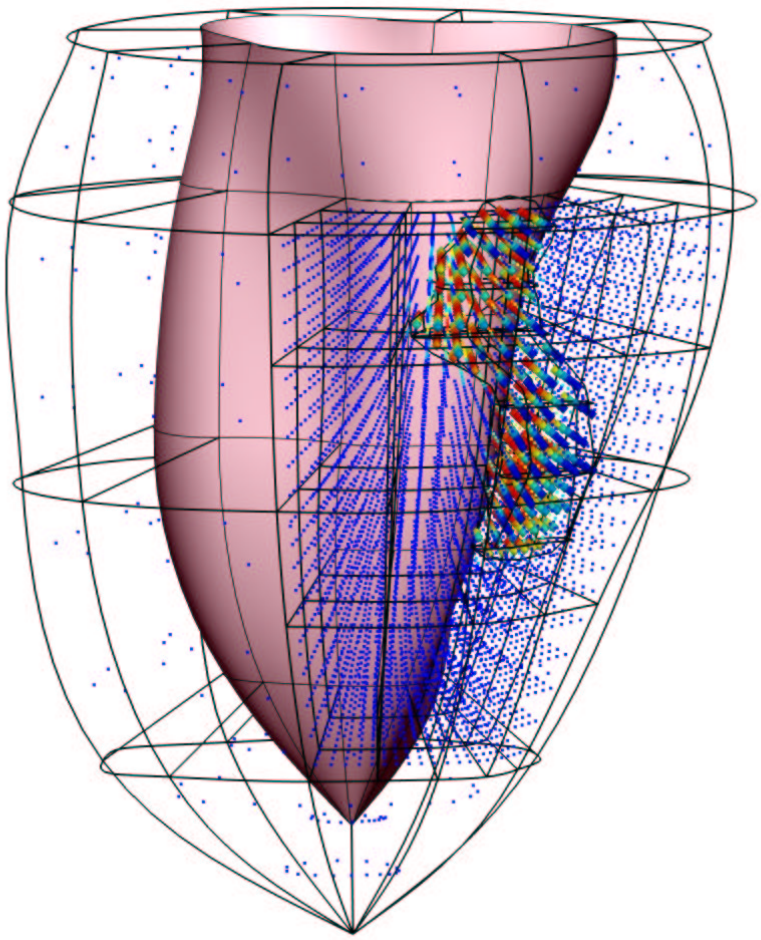

FIGURE 7.5: Grid point specification of material properties. The constitutive parameter C_4 is plotted on the grid points. The points within the infarct are plotted slightly larger.

compared with the experimental values at four prescribed ventricular cavity pressures. The three transmural locations chosen for comparison were at 5%, 35% and 65% wall depth from the epicardium, corresponding to the minimum, mid and maximum transmural extent of the experimental data set. The differences between the model strains and the experimental strains (*residuals*) were evaluated at cavity pressures of 5, 10, 15 and 20 mmHg, which correspond to the pressures at which the data was obtained experimentally. The optimisation problem was formulated to minimise the sum of squared residuals, Equation 7.11. The nonlinear optimisation problem was solved using a sequential programming method implemented within CMISS.

$$\min F(C_1, C_2, C_3) = \sum_{p=1}^{4} \sum_{d=1}^{3} [\mathrm{E}(5p, \xi_d) - \mathrm{E}(5p, d)]^2 \tag{7.11}$$

Following Holmes's approach the normal myocardium was modelled having a collagen area fraction of 0.4 and the collagen fibres are assumed to be parallel with the muscle fibres. Using a typical angular deviation of 15^{o} about the mean angle, a normal fibre angle distribution was generated and used to calculate the material parameters for the myocardium. The unknown constants C_1, C_2 and C_3 were set to the values chosen by Holmes using a systematic series of trials. The constants C_7 and C_8 were set to zero because they were on average two orders of magnitude smaller than C_4 and one order of magnitude smaller than C_5 and C_6. The structural constants used for normal myocardium are given in Table 7.1, and the strains in the noninfarcted region are presented in Figure 7.6.

Material Parameter	Value
C_1	0.5 kPa
C_2	2.5
C_3	100
C_4	0.0442
C_5	0.0006
C_6	0.0026
C_7	0
C_8	0

TABLE 7.1: Structural constants for normal myocardium.

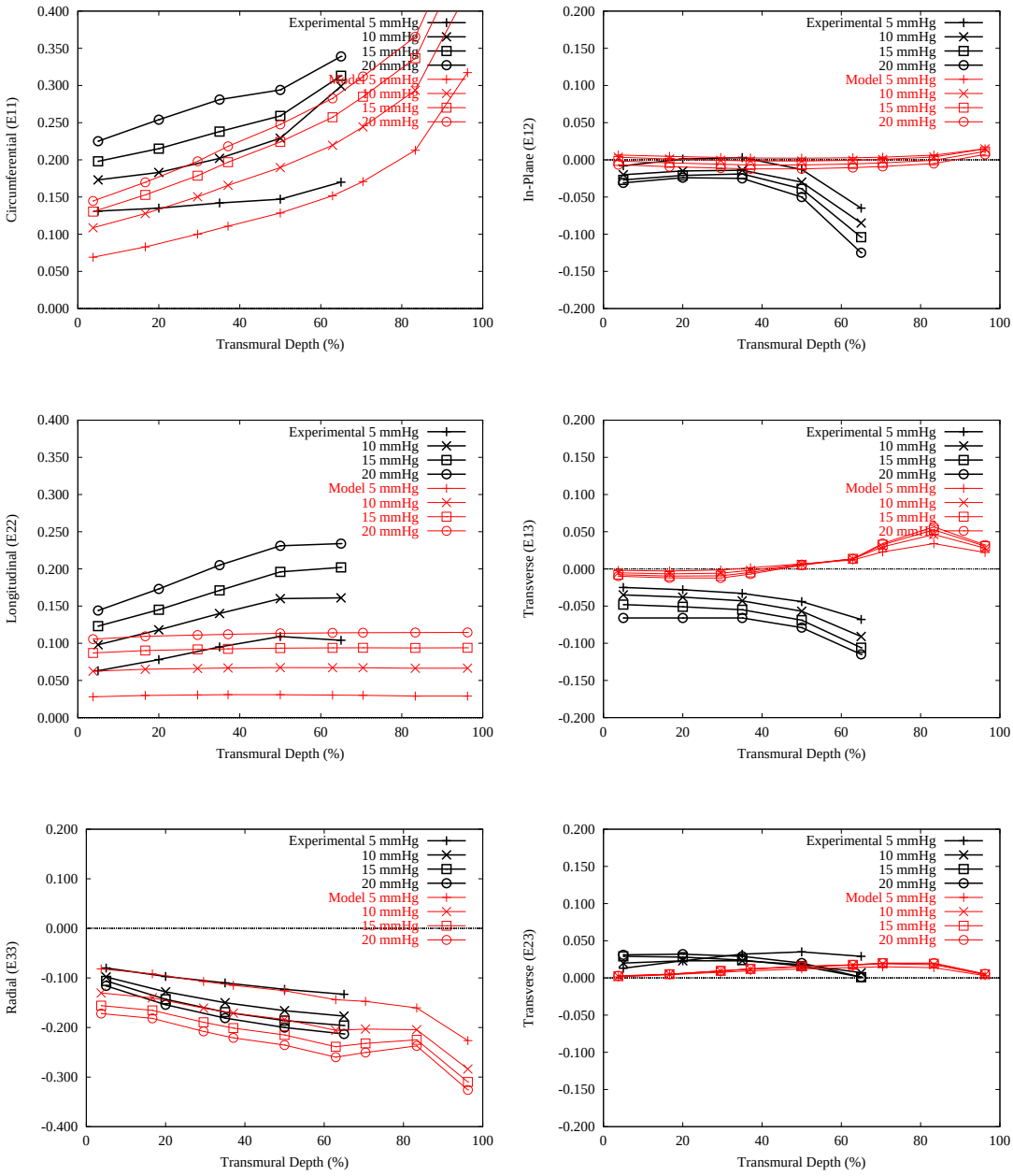

FIGURE 7.6: Strains in the noninfarcted myocardium using the parameters listed in Table 7.1 along with the experimentally measured strains. The normal strain components predicted by the model agree reasonably well with the experimental data, with the exception of the longitudinal strain component.

The predicted strains for normal myocardium agreed reasonably well with the measured values. The longitudinal however, strains did not exhibit the recorded increase from the epicardium through to the endocardium. This finding suggests perhaps there is a complex relationship between the effect of the rotating fibres, the isotropic term and the surrounding tissue that is not accurately reflected in the model. The incompressibity constraint may account for the minor oscillations in the model's radial strains. The shear behaviour of the model also differs from the measured data towards the endocardium. Again, this is likely due to the incompressibility constraint.

Observation of the microstructure and the experimental infarct strain results suggested that the longitudinal and radial strains within the infarct are not too dissimilar to those in the surrounding normal myocardium, while the circumferential strain is independent of the surrounding tissue. Prior to the optimisation runs this observation was investigated. Model simulations were performed examining the infarct strains while varying the constitutive law scaling parameters $C_1$and C_2 within the normal myocardium (see Figures 7.7 and 7.8). C_1, C_2 and C_3 for the scar tissue were chosen to be 0.5 kPa, 1.0 and 100 respectively.

The model reproduced the experimental relationship of infarct strains to normal myocardial strains. The longitudinal and radial strains were sensitive to the surrounding myocardium but the circumferential strain was not.

Since the purpose was to determine the unknown constants for infarcted myocardium it was undesirable to formulate the problem in a way that was sensitive to the choice of parameters in the normal myocardium. Therefore only the circumferential strain component was chosen to optimise against. The shear terms were not used because they were considerably smaller.

Results

The optimised values for C_1, C_2 and C_3 were 0.64 kPa, 1.44 and 106 respectively. This required 42 inflations of the model. The predicted strains in the infarcted region are presented with the experimental results in Figure 7.9.

The optimised parameter set does provide a reasonably accurate prediction of the circumferential infarct strain, although the predicted subendocardial circumferential strains

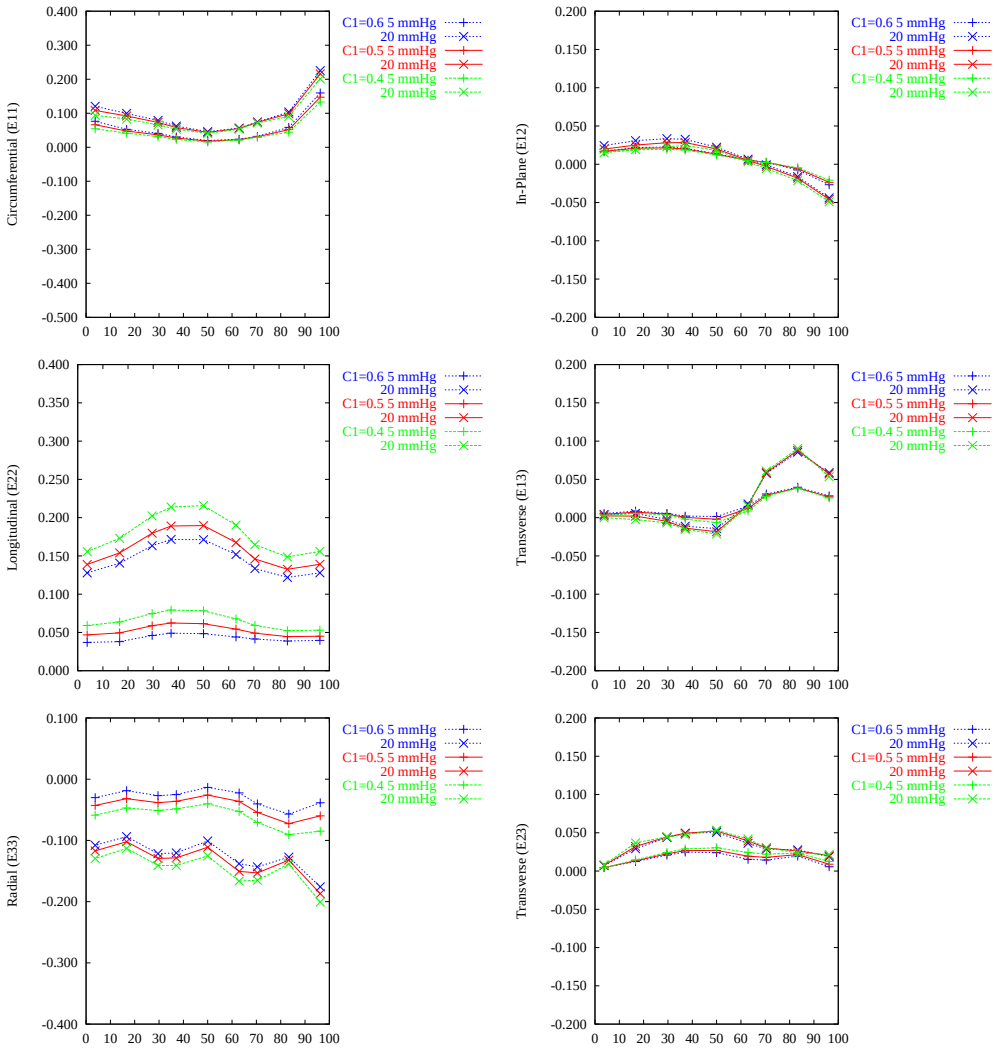

FIGURE 7.7: Sensitivity of model infarct strains to variation of the normal myocardium properties via the C_1 constant. The percentage transmural depth is measured on the abscissa.

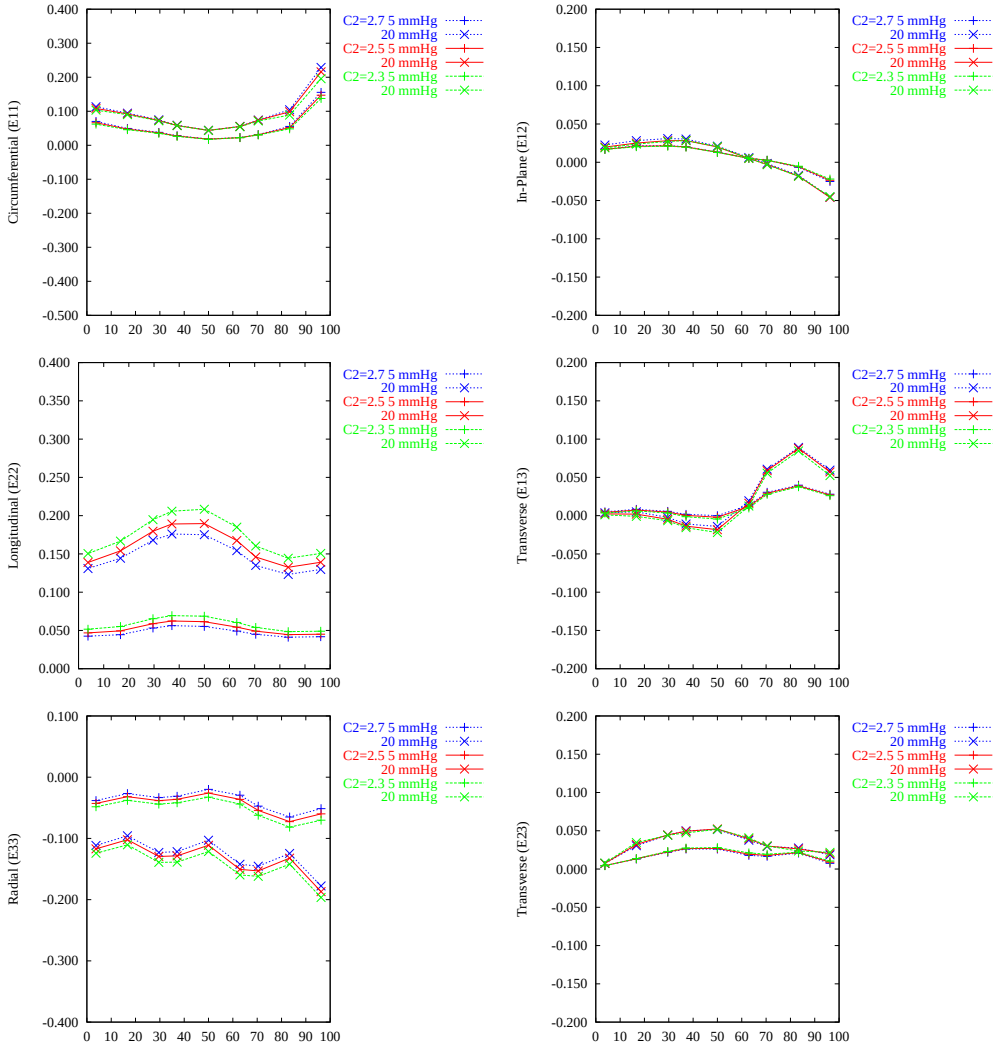

FIGURE 7.8: Sensitivity of model infarct strains to variation of the normal myocardium properties via the C_2 constant. The percentage transmural depth is measured on the abscissa.

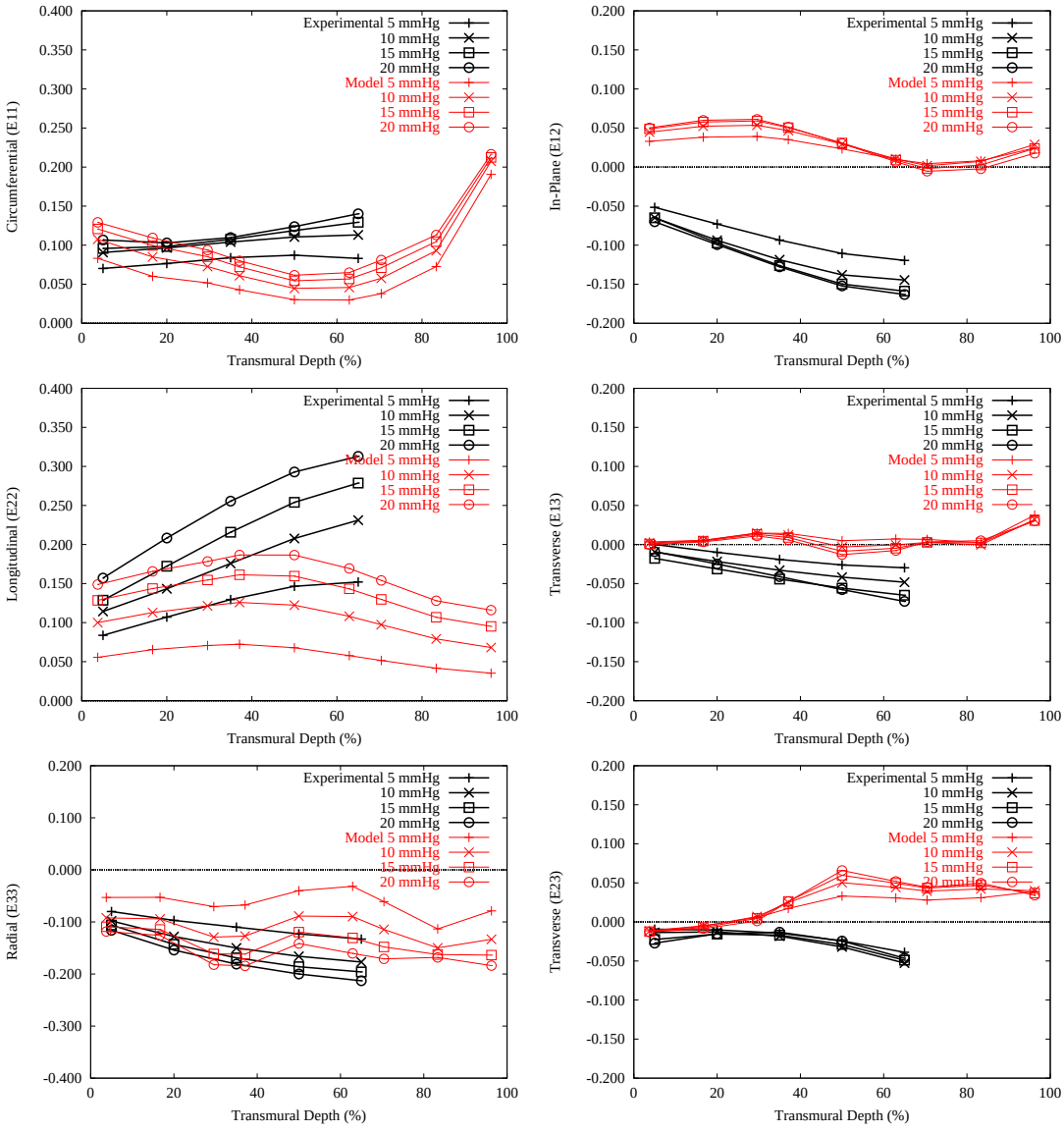

FIGURE 7.9: Optimised model and experimental pressure strain relationships within the infarct.

are slightly too high. The enforcement of the non-physiological incompressibility constraint is likely to have lead to the discrepancy between the experimental and predicted strains in the subendocardium. The incompressibility constraint may also be responsible for the oscillations in the radial strain component.

The nonphysiological transmural distribution of longitudinal strain indicates that the constitutive relationship does not accurately represent the complex relationship between the effect of the rotating fibres and the isotropic term. The constitutive law is founded upon collagen in the fibre direction being the stiffening component, with some inference of its role in the cross-fibre direction. Therefore further experimental work may be necessary to quantify the cross-fibre constitutive relationship. These results are discussed further in Section 7.1.4.

7.1.3 A Pole-Zero Constitutive Relationship for Infarcted Myocardium

The pole-zero constitutive law for myocardium (Section 4.4.3) directly relates microstructure to function. Current estimates for the constitutive parameters provide a good model for the material properties of normal myocardium, and research is in progress at the University of Auckland to further quantify the constitutive parameters. Therefore it is desirable to be able to also model infarction through the modification of the appropriate terms in the pole-zero law.

The pole-zero law was tested in place of the Holmes constitutive law in the same model and infarct geometry. However, the pole-zero law is dependent upon a laminar sheet field in the model but the sheet structure was not investigated in the Holmes study. Instead a physiological sheet field was generated. The generated sheet field shown in Figure 7.10 turns through 90 degrees from +45 degrees at the epicardial surface to -45 at the endocardial surface with respect to the radial axes.

A series of trials were performed to determine the constitutive law parameters that provided an acceptable match of the non-infarcted model with the experimental control data. Only the curvature constants for the normal direction terms b_{11}, b_{22} and b_{33} in equation 4.1 were modified, the values used in the following simulations for normal myocardium are listed in Table 7.2. The predicted strains are plotted with the experimental results for normal myocardium in Figure 7.11.

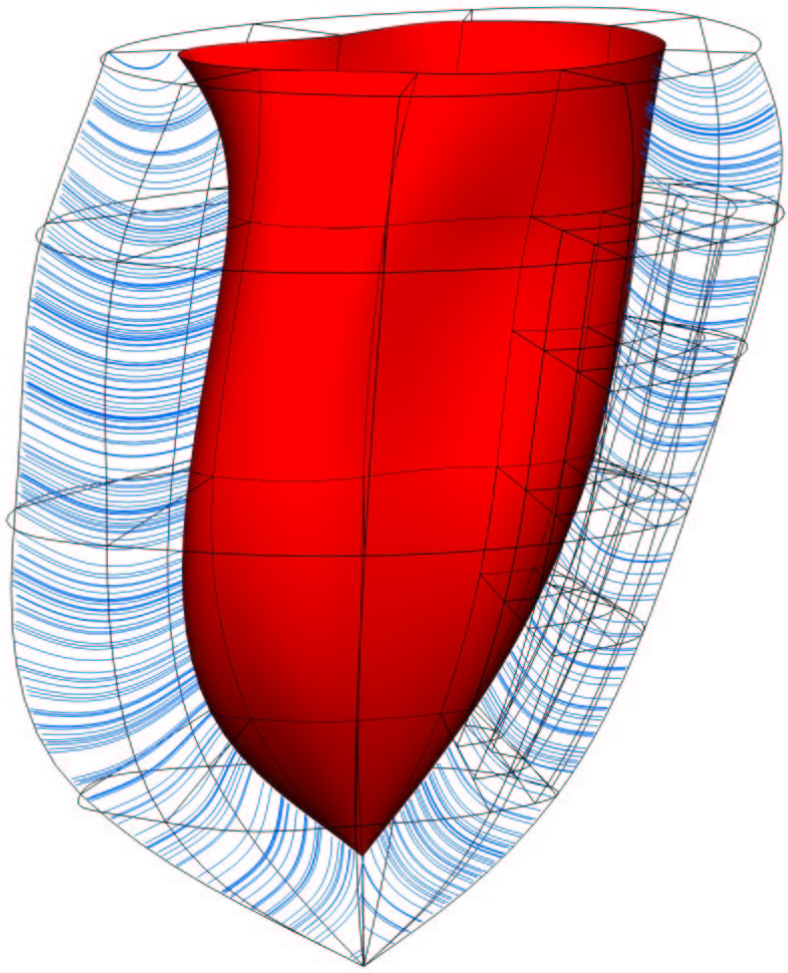

FIGURE 7.10: Generated sheet field for use with the pole-zero constitutive law, +45 degrees at the epicardial surface to -45 degrees at the endocardial surface with respect to the radial axes.

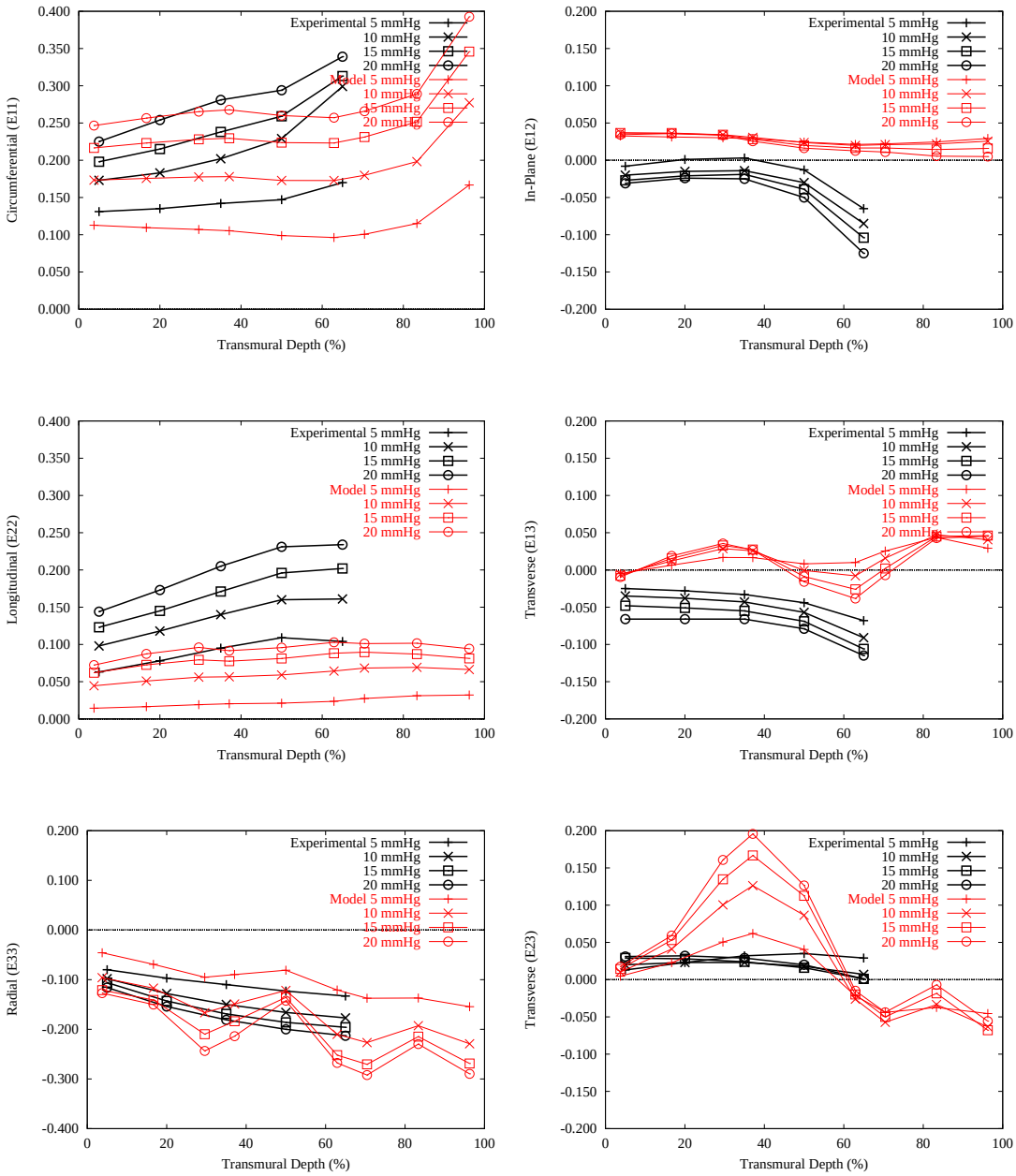

FIGURE 7.11: Experimental strains for normal myocardium and the predicted strains using the pole-zero constitutive law.

Type	Axial Properties	Shear Properties
Coefficients (kPa)	k_{11} 2.0	k_{12} 1.0
	k_{22} 2.0	k_{13} 1.0
	k_{33} 2.0	k_{23} 1.0
Poles	a_{11} 0.523	a_{12} 0.73
	a_{22} 0.523	a_{13} 0.73
	a_{33} 1.037	a_{23} 1.18
Curvatures	b_{11} 1.0	b_{12} 2.0
	b_{22} 1.2	b_{13} 2.0
	b_{33} 20.0	b_{23} 2.0

TABLE 7.2: Material properties of myocardium for the pole-zero constitutive law used in the porcine model.

The determination of parameters for the pole-zero law to model infarction is not suited to the optimisation approach used earlier with the Holmes constitutive law, because several parameters, potentially transmurally varying, must be found rather than a pair of constants. Nor are the quantitative structural measurements immediately useful for determining a suitable set of pole-zero law parameters. Nevertheless, an attempt is made to estimate the parameters based upon the observations of the collagen density and scatter along with the pressure strain data.

The observation that the circumferential strains are significantly reduced within the infarcted region suggests that the upper limit or pole of circumferential stretch may also be reduced. The midwall circumferential strain can be interpreted as largely strain along the fibre axis of the material coordinate system since those fibres are circumferentially oriented. The circumferential infarct strains do not increase beyond 0.1 therefore the fibre axis pole, a_{11} is estimated to be 0.15.

The range of circumferential strain with increasing cavity pressure is very small compared to the range exhibited in the noninfarcted tissue. This indicates a less gradual curvature is required for the fibre axis term, hence the curvature parameter b_{11} is reduced to 0.2. The stress strain relationships for normal and infarcted myocardium along the fibre axis are plotted in Figure 7.12 for comparison.

Holmes reported that the collagen fibres were more scattered towards the epicardial and endocardial surfaces than in the midwall, possibly contributing to the circumferential stiffness in regions where the fibres are not so circumferentially aligned. This obser-

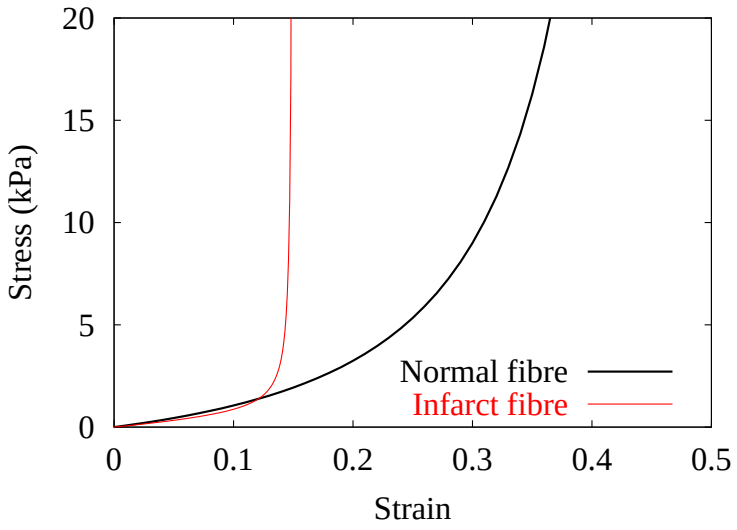

FIGURE 7.12: The stress strain relationships of the fibre axis term in the pole-zero law for normal and infarcted myocardium.

vation is incorporated by decreasing the pole for the deformation in the sheet-normal axis direction, a_{33}, in the subepi and subendocardial regions. The stiffness in the sheet-normal direction is not altered in the midwall because such a change would also modify the longitudinal strain response, which varied little between the infarcted and normal myocardium in the experiments. The sheet-normal strain limiting pole a_{33} was reduced to 0.7 in the subepicardium and 0.9 in the subendocardium, the transmural distribution of the pole is shown in Figure 7.13. The sheet-normal pole position in the subendocardium was decreased less because the more more circumferentially aligned fibres in that region caused the longitudinal strain response to be more greatly effected.

There are many more possible parameter variations that could be explored, but it was found that the above modifications to the pole-zero law constitutive parameters do provide a good model of the passive mechanical behaviour of an infarcted region. The model simulation results are presented in Figure 7.14.

The predicted circumferential strain agrees reasonably well with the experimentally measured values, Figure 7.14(a). The modifications to the infarcted region constitutive parameters do not significantly alter the longitudinal or radial deformation behaviour as desired, Figures 7.14(c and e). However, further material testing of myocardial scar tissue is needed to more accurately define the necessary spatial distribution of constitutive

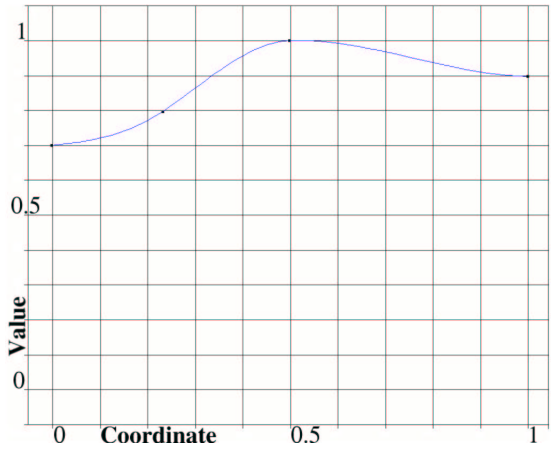

FIGURE 7.13: Transmural sheet-normal axis pole position distribution, 0.7 in the subepicardium and 1.0 at the midwall 0.9 at the subendocardium.

parameters.

The generated theoretical fibre and sheet fields within the normal myocardium may not be physiological enough to enable the correct shearing behaviour during inflation Figures 7.14(b,d and f) and hence the appropriate apex-base lengthening of the model Figure 7.14(c).

The incompressibility constraint and lack of regional variation of material properties probably contribute to the oscillations in the radial strain, Figure 7.14(e).

7.1.4 Discussion and Conclusions

The computational techniques developed for this study successfully enabled closer investigation of ventricular deformation behavior than has been possible previously. Despite the advances in computational technology, there is still a need to design models efficiently to maximise the accuracy of results. The hanging node method for high order elements has made detailed study of localised phenomena such as infarction computationally feasible using high order FE models of the ventricles.

The coupling of the continuum description of material properties to an embedded grid scheme along with the suite of cellular and graphical modelling tools available in CMISS provide a highly configurable method for prescribing spatially varying material properties. The coupling of the continuum and cellular modelling frameworks along with the

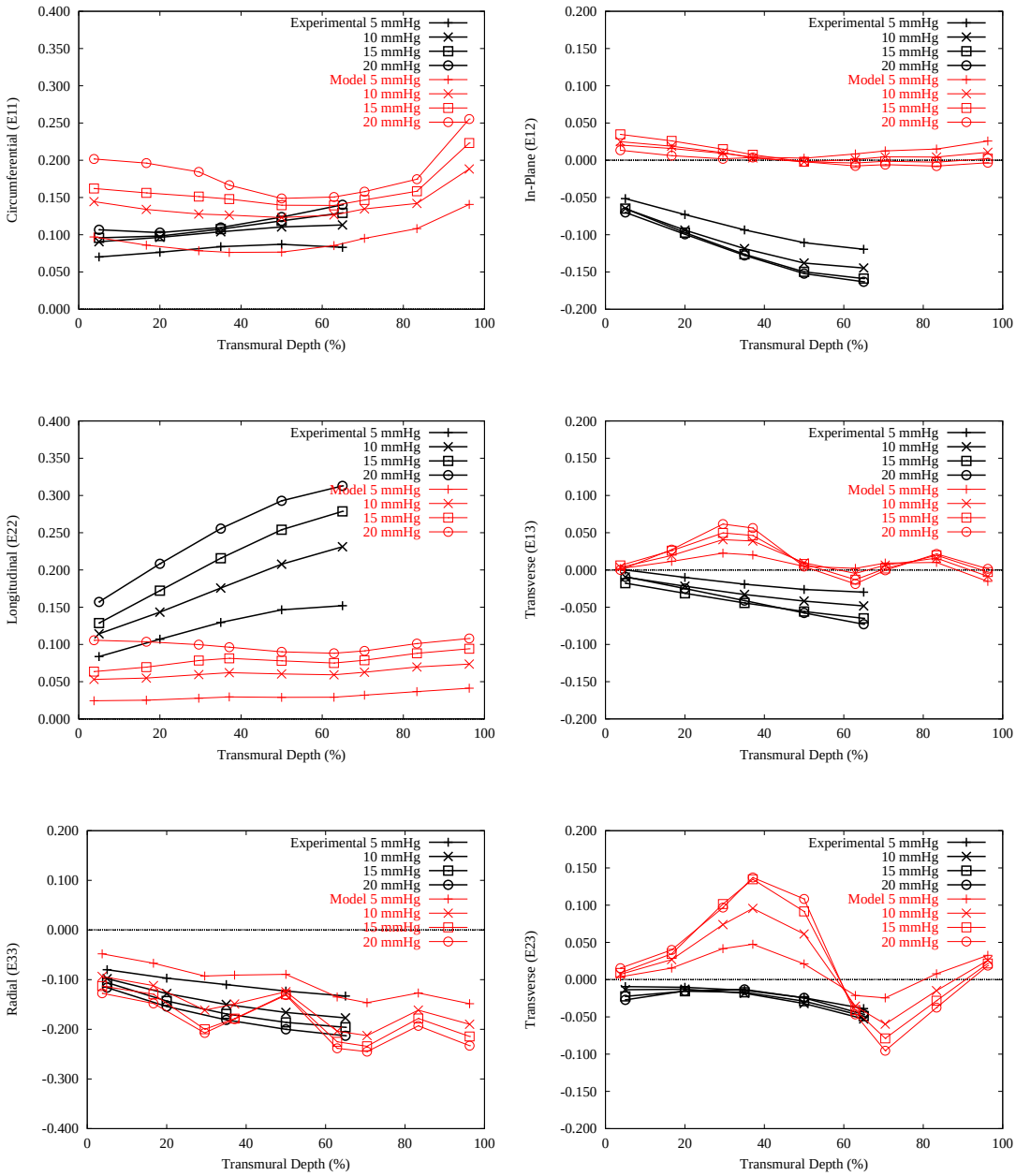

FIGURE 7.14: Predicted and experimental strains within the infarct with increasing cavity pressure.

visualisation tools is an on-going area of development in CMISS with many researchers contributing their expertise. These first steps toward coupling material properties structures also demonstrated the power of generalised modelling tools within a single framework for examining new problems.

Two constitutive laws for the modelling of infarcted myocardium were investigated using the same ventricular and infarct geometries. The Holmes constitutive law for infarcted myocardium has the benefit of being largely based upon structural measurements, but lacks description of microstructural features that play a significant role in the deformation behaviour. The isotropic plus fibre strain term formulation (Equation 7.1) neglects the laminar sheet arrangement of the microstructure and does not include the cross-fibre properties. These omissions may account for the nonphysiological transmural distribution of longitudinal strain exhibited by the model. The unrealistic longitudinal strain distribution could be created solely by varying the constant C_2. The effect of the infarct geometry was also examined using a rectangular shaped infarct, but the results remained unchanged. Therefore it appears that the Holmes constitutive law does not accurately represent the complex relationship between the rotating fibres and the isotropic background, or the isotropic background itself does not suitably describe the tissue within the subendocardium.

Modification of the pole-zero constitutive law for myocardium to also represent infarcted tissue is more attractive because it relates modes of deformation to microstructural features (Section 4.4.3) including the laminar sheets. The anisotropic constitute law provided a good fit to the experimental normal myocardial strains. Simple modifications to several of the infarcted region parameters, based upon Holmes's observations of the physiology, resulted in the infarcted ventricular model representing the significant features of the experimental study. The circumferential strain was significantly reduced locally, while the longitudinal and radial strain components remained largely unchanged. The fibre and sheet fields used in the model were generated based upon the Holmes data and commonly used average values. They were not specific to the geometry of the particular specimen and did not vary regionally as is observed in normal ventricular myocardium. Therefore some mismatch between the geometry and the sheet orientations could account for the discrepancy between the predicted and experimental shear strains. Ideally suitable pole-zero constitutive law parameters for infarcted myocardium would be determined through material testing testing techniques, to quantify

the stress-strain behaviour along each of the microstructural axes.

Both material law descriptions model the myocardium as incompressible. As discussed in Section 6.8.1 this immediately limits the achievable accuracy of the models since myocardium is slightly compressible particularly in the subendocardium. Furthermore the Holmes data indicated that the infarcted region actually increased in volume during inflation.

The pole-zero formulation for infarcted myocardium appears to provide a suitable model for investigating the effect of infarction upon ventricular mechanics.

7.2 The Anatomical Ventricular Porcine Model and Infarction

In this section the tools and techniques described above for modelling ventricular mechanics and infarction are applied to the model of the porcine ventricles developed in Section 5. A simulation and analysis of the end-diastolic state of the ventricles was presented in Chapter 6. Suitable parameters to represent infarcted myocardium using the the pole-zero constitutive law were determined in Section 7.1. Here an infarcted region is introduced into the anatomical model and the end-diastolic simulations results are compared with those obtained in Chapter 6 for the healthy model. The applied boundary conditions are the same, the basal skeleton displacements are fixed, and the LV and RV cavities are loaded to 1.0 kPa and 0.2 kPa respectively.

7.2.1 Material Properties

The size, shape and location of myocardial infarcts varies. The pole-zero constitutive parameters for infarcted tissue have been determined from data of completely transmural infarcts with a longitudinal orientation located between the papillary muscles in the LV free wall. Without further experimental analysis to determine the properties of a variety of different infarct types, the applicability of the constitutive parameters to other infarct geometries and locations cannot be known. Therefore the geometry of the infarct used here is designed to be similar to that induced by the coronary ligation experiments detailed in Section 7.1.1. Localised wall thinning is not considered.

The pole-zero constitutive law is used for both the normal and the infarcted myocardium. The constitutive parameters for the normal myocardium are the values determined in Section 6.3.1, and the infarcted region parameters are evaluated in Section 7.1.3.

The transmural fibre orientation within the infarcted region is modified to reflect the more circumferentially aligned fibres measured by Holmes (Section 7.1.1).

7.2.2 Localised Ventricular Mesh Refinement

The LV free wall is refined in the circumferential and transmural directions to more accurately resolve the strains in the infarcted region. The local refinement creates an additional 31 elements with another 800 degrees of freedom to be solved for. The refined model and the infarcted region with the modified constitutive parameters are shown in Figure 7.15.

7.2.3 Results

The passive inflation simulation was repeated using the refined mesh with and without the infarct present. The longitudinal and circumferential distributions of strain are compared to examine the global effect of the localised increase in circumferential stiffness caused by the infarction. The circumferential distributions of the material strains at the midwall are plotted in Figure 7.16. The midwall fibre orientations are close to circumferential and the sheets are radially aligned therefore the strains may also be interpreted as circumferential, longitudinal and radial.

The strains within the infarcted region are consistent with the experimental and model results presented in the previous sections. The predicted circumferential strain within the infarcted region is reduced while the radial and longitudinal strains remain unchanged. However immediately adjacent to the infarcted region the sheet strains peak unexpectedly. The material properties of the transitional border zone between the infarcted and normal myocardium were not modelled because of the lack of available data. Therefore no conclusions can be drawn regarding the increases in sheet strain in the adjacent myocardium.

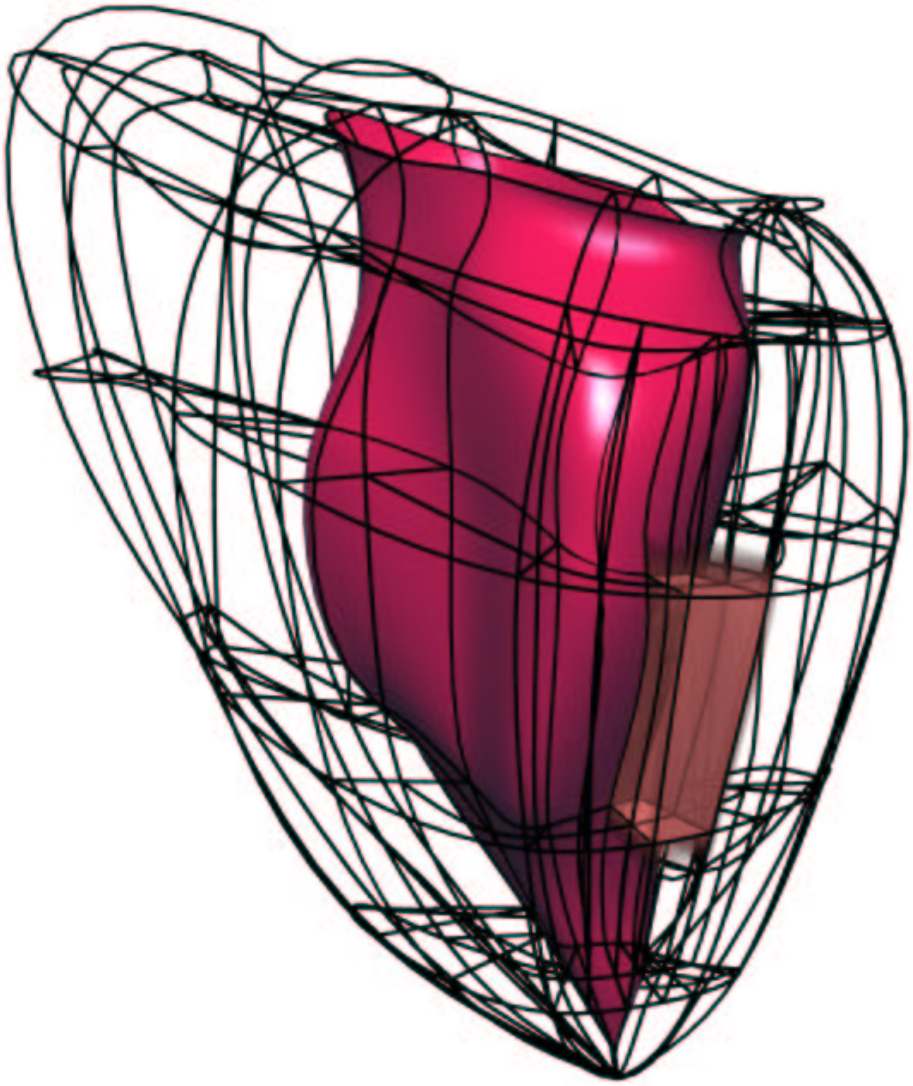

FIGURE 7.15: The anatomical porcine model with an infarcted region and localised refinement.

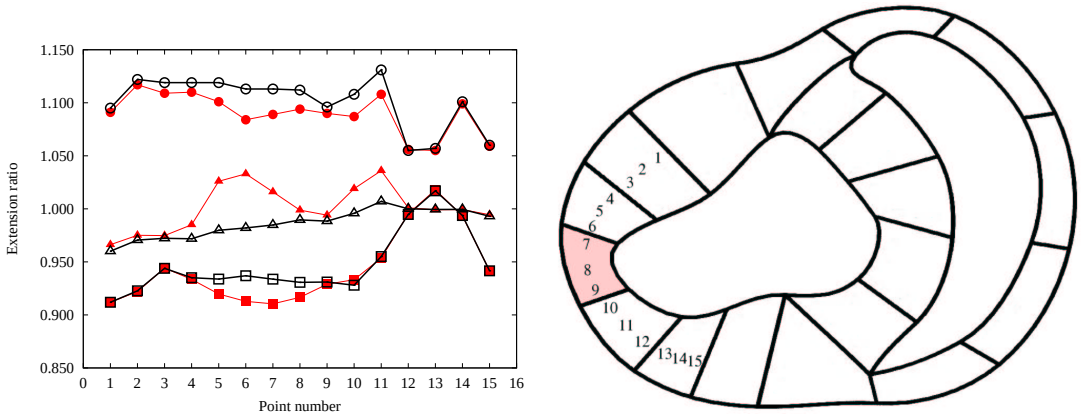

FIGURE 7.16: Circumferential distribution of fibre, sheet and sheet-normal stretch at equatorial midwall locations shown on the right for the healthy and infarcted models. The infarct element is shaded in the diagram on the right.

7.3 Discussion

There is little quantitative data published describing the histology and deformation behaviour of infarcted myocardium. The experimental study by Holmes was the only source available. Holmes also completed a modelling study to formulate a constitutive law for infarcted myocardium, but was limited by the modelling methods available. In this thesis the required techniques, listed below, have been developed and applied.

The proposed constitutive law for infarcted myocardium of Holmes did not adequately represent the deformation characteristics of the scar tissue. However, Holmes' measurements of infarct microstructure and strain behaviour enabled the estimation of suitable parameters for the pole-zero law to represent the scar tissue behaviour. The predicted strains using the estimated parameters indicate the pole-zero law for myocardium is also suitable for representing infarcted myocardium.

Since the pole-zero law is based upon the stress-strain properties of the microstructural constituents it is necessary to experimentally measure the material properties of infarct tissue to determine the parameters more quantitatively. The material properties of the transitional border zone must also be quantified to improve the accuracy of the models.

In summary, a first exploration of detailed myocardial infarction modelling using anatomically accurate models with microstructurally based material properties has been completed. For this study several new techniques have been developed and implemented

within the CMISS package, namely:

- The hanging or constrained node method for high order cubic Hermite finite elements (Section 3.1.4).
- The fitting degrees of freedom associated with external faces of volume elements to data (Section 5.2.9).
- The coupling of discrete cellular mechanics models to continuum models (Section 6.6).
- The evaluation of texture maps to prescribe material properties (Section 7.1.2).
- The mapping constraints to ensure C^0-continuity between cubic Hermite elements with inconsistent parametric coordinates (Section 5.2.7).
- The optimisation of constitutive law parameters using a three-dimensional finite element model (Section 7.1.2).

7.4 Future Work

The techniques and models developed in this thesis have provided initial insights into ventricular mechanics and the behaviour of infarcted myocardium. The new framework can now be used for future studies. In order to improve the accuracy and robustness of the models there are several key areas that require further work.

Firstly, the material properties of the myocardium need to be addressed. The material laws used in this thesis modelled myocardium as an incompressible material. This assumption may be significantly affecting the accuracy of the predicted subendocardial strains. Furthermore, the constitutive parameters in the pole-zero law are based upon *in-vitro* biaxial tension tests of ventricular myocardium. More suitable *in-vivo* testing techniques, such as MRI may soon yield better data for the determination of constitutive parameters. An investigation of the inhomogeneity of the ventricular myocardium's material properties would also aid the accuracy and robustness of the models.

The models developed here have excluded the papillary muscles. However, the papillary muscles do influence ventricular deformation. The next step in the development of the

geometry and loading conditions of the models is to include the papillary muscles and their link to the heart valves by the chordae.

Studies of the influence of the apical geometry upon ventricular mechanics, and possible constraints by the pericardium would also be interesting areas for further investigation.

Many of these issues are being actively researched by the University of Auckland Bioengineering Institute and other research groups.

Appendix A

Fibre Distribution Model for Cardiac Tissue

A biophysical model of cardiac muscle elasticity has been formulated to help understand the correlation between the axial and shear parameters of the pole-zero constitutive law for myocardium (Hunter et al. 1997). The main assumption of this *fibre distribution model* is that three families of fibrous connective tissue (mainly collagen) are responsible for storage of the total strain energy of the myocardium. This implies that some axial and shear deformations must be strongly correlated since they involve the same underlying collagen microstructure. The fibre orientations within each family is assumed to be normally distributed about a mean direction, which is aligned with one of the microstructural material axes (see Figure A.1). Note that in the following description the term 'fibre' refers to a collagen connection within a fibre family and not a cardiac muscle fibre. The latter will be referred to as a 'myocyte'.

The first fibre family consists of the large coiled perimysial fibres that are closely associated with the myocytes (Robinson, Geraci, Sonnenblick & Factor 1988*b*, MacKenna et al. 1996). The mean direction of this family is coincident with the longitudinal axis of the local myocytes and individual collagen fibres are assumed to lie in the plane of the myocardial sheet. The second family has a mean orientation centred about the sheet axis (which also lies in the sheet plane, but is perpendicular to the myocyte axis) and consists of tightly bound endomysial collagen (Caulfield & Borg 1979). The third family of fibres is assumed to have an axisymmetric distribution about a mean direction aligned with the local sheet-normal axis. This family consists of the sparse array of perimysial

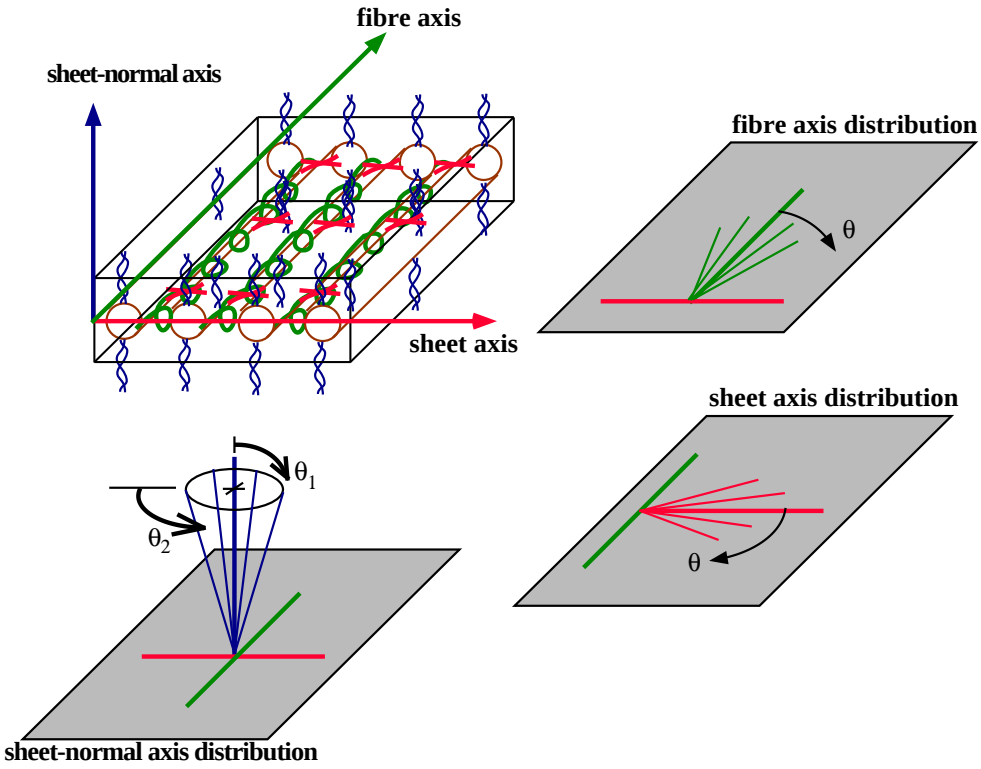

FIGURE A.1: The fibre distribution model: orientation of each fibre family about its mean orientation.

collagen struts that connect the myocardial sheets.

The variation of connective tissue fibre orientations about their mean directions is assumed to be different for each family of fibres. These variations are defined by standard deviations that describe the distribution of each family of fibres as illustrated in A.1. The first standard deviation defines the variation about the mean direction of the large coiled perimysial collagen fibres about the mean myocyte axis and is therefore relatively small. The second standard deviation defines the variation of the direction of in-sheet endomysial collagen about the local sheet axis and is greater than the first. Two further standard deviations define the axisymmetric variation of the inter-sheet collagen strut direction.

To evaluate the contribution that one particular fibre of a family makes to the total strain energy, consider a unit length fibre in the reference state at an angle of Θ to the Y_1-axis, as illustrated in Figure A.2. The Y_1 and Y_2 axes are not material axes (they do not change with material deformation), but rather are local *orthogonal* reference axes with the Y_1 coordinate defined to be aligned with one of the microstructural material axes. In the deformed state, the fibre has length λ and is oriented at an angle of θ to the Y_1-axis. In the undeformed state $X = \cos\Theta$ and $Y = \sin\Theta$, and in the deformed state $x = \lambda\cos\theta$ and $y = \lambda\sin\theta$.

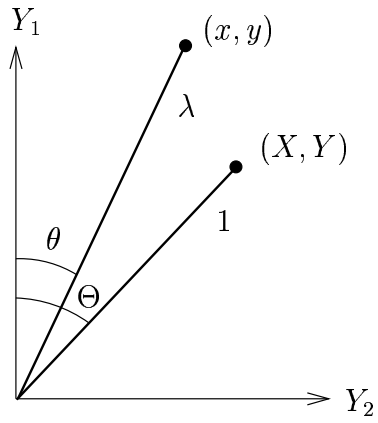

FIGURE A.2: Kinematic analysis of a typical deforming fibre.

Consider now a particular state of strain in the tissue, characterised by extension ratios λ_1 and λ_2 along the local reference axes, Y_1 and Y_2, respectively. These extension ratios can be expressed using Equation A.1.

$$\lambda_1 = \frac{x}{X} = \lambda \frac{\cos\theta}{\cos\Theta} \qquad \lambda_2 = \frac{y}{Y} = \lambda \frac{\sin\theta}{\sin\Theta} \tag{A.1}$$

By dividing the extension ratios, Equation A.1 may be used to determine an expression for the angle of the deformed fibre, θ, given in Equation A.2.

$$\frac{\lambda_2}{\lambda_1} = \frac{\tan\theta}{\tan\Theta} \qquad \text{or} \qquad \theta = \tan^{-1}\left(\frac{\lambda_2}{\lambda_1}\tan\Theta\right) \tag{A.2}$$

Thus, given λ_1 and λ_2, a fibre at initial position Θ is rotated to an angle θ and stretched by extension ratio λ in Equation A.3.

$$\lambda = \begin{cases} \lambda_1 \dfrac{\cos\Theta}{\cos\theta} & \text{when} \quad \theta < \dfrac{\pi}{2} \\ \lambda_2 \sin\Theta & \text{when} \quad \theta = \dfrac{\pi}{2} \end{cases} \tag{A.3}$$

The fibre strain is calculated from the extension ratio using Equation A.4.

$$E_f = \frac{1}{2}\left(\lambda^2 - 1\right) \tag{A.4}$$

The next step is to assume that the fibre orientations for each of the families are normally distributed about their mean directions. In this way, for example, the family of fibres associated with the myocyte axis may be approximated using the Gaussian probability distribution (with standard deviation σ_1) defined in Equation A.5. Note that the mean of this distribution is aligned with the local myocyte axis in the reference state and that Θ quantifies the *difference* between the direction of a particular fibre and the mean fibre direction.

$$p_1(\Theta) = \frac{1}{\sqrt{2\pi}\sigma_1} \exp\left[-\frac{1}{2}\frac{\Theta^2}{\sigma_1^2}\right] \tag{A.5}$$

The total strain energy (due to the deformation) stored in the family of fibres associated with the myocyte axis may be computed by summing up the individual strain energies of all fibres in the family. Equation A.6 expresses this sum as the integral over all possible fibres since the probability distribution function varies continuously with the undeformed position, Θ. In this expression, k_1, a_1 and b_1 are properties of the family of fibres associated with the myocyte axis. The dependence of the fibre strain, E_f, on Θ is defined using Equations A.2 and A.4.

$$W_1 = \int_{-\frac{\pi}{2}}^{\frac{\pi}{2}} p_1(\Theta) \frac{k_1 E_f^2}{(a_1 - E_f)^{b_1}} d\Theta \tag{A.6}$$

In a similar manner, the total strain energy stored in the family of fibres associated with the myocardial sheet axis may be calculated using Equation A.7.

$$W_2 = \int_{-\frac{\pi}{2}}^{\frac{\pi}{2}} p_2(\Theta) \frac{k_2 E_s^2}{(a_2 - E_s)^{b_2}} d\Theta \tag{A.7}$$

where $p_2(\Theta)$ is the Gaussian probability distribution function for the family of fibres associated with the sheet axis, k_2, a_2 and b_2 are properties of this family, and E_s is the material strain along the sheet axis. Note that E_s and $p_2(\Theta)$ may be evaluated using expressions similar to Equations A.4 and A.5, respectively.

The strain energy for the third family of sheet-normal fibres is calculated using Equation A.8, and the probability distribution function for this family is expressed in Equation A.9 in terms of the two standard deviations that describe an axisymmetric variation of inter-sheet collagen fibre orientations.

$$W_3 = \int_{\Theta_4=0}^{2\pi} \int_{\Theta_3=0}^{\frac{\pi}{2}} p_3(\Theta_3, \Theta_4) \frac{k_3 E_n^2}{(a_3 - E_n)^{b_3}} d\Theta_3 d\Theta_4 \tag{A.8}$$

with

$$p_3\left(\Theta_3,\Theta_4\right)=\frac{1}{2\pi\sigma_3\sigma_4}\exp\left[-\frac{1}{2}\left(\frac{\Theta_3^2}{\sigma_3^2}+\frac{\Theta_4^2}{\sigma_4^2}\right)\right] \tag{A.9}$$

where E_n is the material strain along the family of collagen fibres associated with the sheet-normal axis and k_3, a_3 and b_3 are properties of this family. Finally, it is assumed that the combined strain energy from each of the three families sums to yield the total strain energy in the tissue.

For present purposes, the fibre distribution model has been used to express the limiting strains for shear (namely a_{12}, a_{13}, and a_{23} in Equation 4.1) as a function of the axial poles, since it was assumed that the same underlying distributions of collagen connections determine both the tensile and shear characteristics of the tissue. This relationship is derived by considering the kinematics of a typical fibre during a simple shear deformation as shown in Figure A.3.

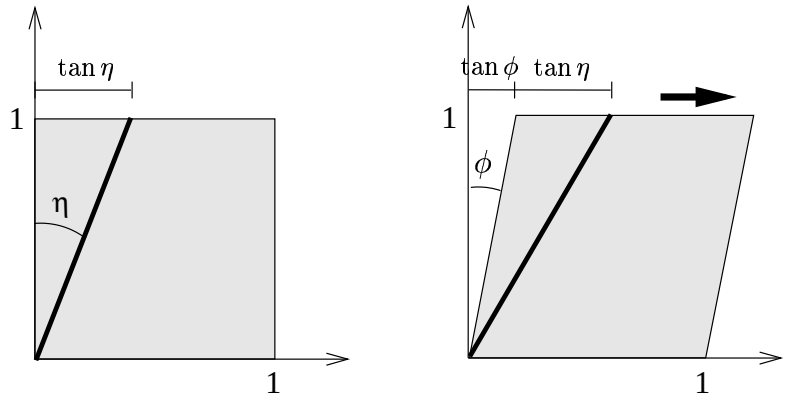

FIGURE A.3: Kinematic analysis of a fibre during simple shear.

The bold line segment in Figure A.3 represents a particular connective tissue fibre oriented at angle η to the mean direction for its family in the reference state. Using Pythagoras, this undeformed fibre has length $\sqrt{1+\tan^2\eta}\;=\;\sec\eta$. During the deformation the fibre moves through a shear angle of ϕ and due to the simple kinematics of the deformation, the deformed fibre length is $\sqrt{1+(\tan\eta+\tan\phi)^2}$. The extension ratio (deformed length divided by undeformed length) of the fibre is defined in Equation A.10 as a function of the undeformed fibre angle, η, and the shear angle, ϕ.

$$\lambda_\eta = \sqrt{1 + \tan^2\phi\cos^2\eta + \tan\phi\sin 2\eta} \tag{A.10}$$

For a given shear angle ϕ, the fibre angle η^* which produces maximum stretch is found from Equation A.10 by solving $\frac{\partial\lambda_\eta}{\partial\eta} = 0$ for η^*. The result is given in Equation A.11.

$$\eta^* = \frac{1}{2}\tan^{-1}(2\cot\phi) \tag{A.11}$$

As ϕ increases from $0°$ to $90°$, η^* decreases from $45°$ to $0°$. The extension ratio of the fibre with maximum stretch is determined by substituting Equation A.11 back into Equation A.10. Using some considerable manipulation (see (Nash 1998)) the maximum extension ratio for a given shear angle is written in Equation A.12.

$$\lambda_{\text{max}} = \frac{1}{2}\left(\kappa + \sqrt{4 + \kappa^2}\right) \tag{A.12}$$

where $\kappa = \tan\phi$. If this particular fibre yields when its Green's strain reaches the limit stop $a = \frac{1}{2}(\lambda^2_{\text{max}} - 1)$, then the maximum possible *elastic* shear strain is calculated using Equation A.13.

$$\kappa = \frac{2a}{\sqrt{1 + 2a}} \tag{A.13}$$

The key point here is that the shear poles of Equation 4.1 (namely a_{12}, a_{13} and a_{23}) may be directly determined from the limiting strains of the fibre families. For example, consider simple shearing deformations within the plane of the myocardial sheet, referred to here as the $(1,2)$-plane. The yield strain for a simple shear of the $(1,2)$-plane in the direction of the myocyte axis (a $2-1$ shear) is limited by the *sheet axis pole position*, a_{22}, since the collagen connections associated with the sheet axis family are put into tension. On the other hand, a $1-2$ shear is limited by the *fibre axis pole position*, a_{11}, since the collagen fibres aligned with the myocyte axis sustain the load. Thus for a

general shear of the $(1,2)$-plane, a reasonable approximation to the limiting shear strain, a_{12}, may be determined by substituting the minimum of a_{11} and a_{22} into Equation A.13, which monotonically increases with a. The pole position for the in-plane $(1,2)$ shear is defined in Equation A.14. Pole positions for the other shear terms may be determined in an analogous manner.

$$a_{12} = \begin{cases} \frac{2a_{22}}{\sqrt{1+2a_{22}}} & \text{if } a_{22} \leq a_{11}, \\ \frac{2a_{11}}{\sqrt{1+2a_{11}}} & \text{if } a_{22} > a_{11}. \end{cases} \tag{A.14}$$

Appendix B

The CMISS Command File for the Anatomical Porcine Ventricular Model

The CMISS (Section 1.3) command file for the anatomical porcine ventricular model. This file is presented to document the algorithms used within this thesis. The accompaning input files are prohibitively large to include here, but can be downloaded from `http://www.cmiss.org`.

```
$TRUE = 1; #  Initialise   logicals
$FALSE = 0;
#
use MySubs; # file manipulation & plotting  routines
#

#=============================================================================================================
print "\033[0;30;42m ========================================================== \033[0m\n";
print "\033[0;30;42m                          Execution Flow                          \033[0m\n";
print "\033[0;30;42m ========================================================== \033[0m\n";
#=============================================================================================================
#
set num_threads 1;
#
# Cell model
#
$CELL_MODEL="FM";
#$CELL_MODEL="HMT";
#
# LV free wall local refinement, only for inflation
$REFINE=$FALSE;
$REFINE_INFARCT=$FALSE;
#
# Output
#
if (! $REFINE || !$REFINE_INFARCT)
{
    $OUTPUT_DIR = "output_".$CELL_MODEL."/";
} else {
    $OUTPUT_DIR = "output_refined/";
}
if ( ! -d ${OUTPUT_DIR})
```

```
{
    mkdir ${OUTPUT_DIR};
}
#
# Solve phases
#
$SOLVE_INFLATION = $TRUE;
#
$SOLVE_ACTIVE_CONTRACTION = $TRUE;
#
$SOLVE_EJECTION = $TRUE;
#
if ( $SOLVE_ACTIVE_CONTRACTION )
{
    $CAVITY_REGIONS = $TRUE;
} else {
    $CAVITY_REGIONS = $FALSE;
}
#
$GRID_BASED_MECHANICS_PROPERTIES = $TRUE;

#=============================================================================================================
print "\033[0;30;42m ========================================================== \033[0m\n";
print "\033[0;30;42m                    Regions & Classes                       \033[0m\n";
print "\033[0;30;42m ========================================================== \033[0m\n";
#=============================================================================================================
#
# Regions
#
$WALL = 1;
$BASE = 2;
$LV_CAVITY = 3;
$RV_CAVITY = 4;
#
# Classes
#
$MECHANICS = 1;
$CELLULAR = 2;

#=============================================================================================================
print "\033[0;30;42m ================================================================ \033[0m\n";
print "\033[0;30;42m      Nodes, Elements, Fibres & Sheets for Pig heart Model       \033[0m\n";
print "\033[0;30;42m ================================================================ \033[0m\n";
#=============================================================================================================
#
fem define parameters;r;MRP01;
fem define coordinates;r;MRP01;
fem define region;r;MRP01;
#
fem define node;r;MRP01;
fem define nodes;r;MRP01_base region 2;
#
fem define base;r;MRP01;                                    # 1..8  Geometry and fibres
fem define;add bases;r;3Linear_2PressAuxXi3_4x4x4Gauss; # 9 Pressure
#
fem define elem;r;MRP01;
fem define elements;r;MRP01_base region 2;
#
fem define base;r;MRP01_readse;                             #redefine bases to read in  scale  factors
fem define;add bases;r;3Linear_2PressAuxXi3_4x4x4Gauss;
fem define  line ;r;MRP01;
fem define  line ;r;MRP01_base region 2;
#
fem update nodes hanging nodes 144,146 element 47 direction 1;
#
fem define  fibre ;r;MRP01;
fem define elem;r;MRP01 fibre;
#
# Node Groups
#
```

```
fem group nodes 3,4,7,8,18,20,32,34,89..94,105..106,115..120,121,122,123,134..136,109,110 as FIXED;
fem group nodes 9,13,21,23,35,37,41..42,45..46,49..50,53..54,81..82,95..96 as EQUATOR_LV_ENDO;
fem group nodes 22,24,36,38,83..84,11..12,15..16,97..98,101..102 as EQUATOR_LV_EPI;
fem group nodes 1..8,10,14,17..20,25..28,30..34,39..40,43..44,47..48,51..52,55..64,66,69,72,75,
85..94,99,100,103..110,120..133,135..142,65,67..68,70..71,73..74,76..80,111..119,134 as REMAINDER_INITIAL;
#
# Element Groups
#
fem group elements 14..21,32..34,37,43,51..52 as SEPTUM;
fem group elements 22,26,23..25,27,36,45..50,55 as RV_FREE_WALL;
#
fem group elements 8,13,31,39,53..54,59..63,76..80,22,23,71,72,1,36,75 as ISO;
fem group elements 2..7,9..12,14..21,24..30,32..35,37,38,40..52,55,57..58,64,68..70,73,74,65,66,67 as ANISO;
#
fem group elements 4..13,28,29,30,31,35,39,40,41,42,53,54,57,59,61..62,65..69 as LV_FREE_WALL_INITIAL;
#
fem group element all_elements as ALL_ELEMENTS;
#
if ($REFINE){
    fem refine Xi 1 element 4,5,6,7 at 0.7;
    fem refine Xi 3 element 10,11,29,28,30,12 at 0.5;
    fem refine Xi 3 element 5,6,7 at 0.5;
    #
    fem group nodes 158..161,166,167,168..183 as REMAINDER_REFINED;
    fem group nodes REMAINDER_INITIAL,REMAINDER_REFINED as REMAINDER;
    #
    fem group elements 89..92 as LV_FREE_WALL_REFINED;
    fem group elements LV_FREE_WALL_INITIAL,LV_FREE_WALL_REFINED as LV_FREE_WALL;
    #
    fem export nodes;${OUTPUT_DIR}."MRP01_refined" as MRP01 region all;
    fem export elements;${OUTPUT_DIR}."MRP01_refined" as MRP01 region $WALL;
    fem export elements;${OUTPUT_DIR}."MRP01_base_refined" as base_skel region $BASE;

} elsif ($REFINE_INFARCT) {
    fem refine Xi 1 element 4,5,6,7 at 0.7;
    fem refine Xi 3 element 10,11,29,28,30,12 at 0.5;
    fem refine Xi 3 element 5,6,7 at 0.5;
    fem refine Xi 1 element 10,11,12,93,94,98 at 0.5;
    fem refine Xi 1 element 10,11,12,93,94,98 at 0.5;
    fem refine Xi 1 element 102,103,104,105,106,107 at 0.5;
    #
    fem group nodes 1..8,10,14,17..20,25..28,30..34,39..40,43..44,47..48,51..52,55..80,85..94,99..100,103..142 as REMAINDER_REFINED1;
    fem group nodes 158,160,166..183,185..187,189..191,193,195,197..199,201..203,205,207,209..211,213..215,217,219 as REMAINDER_REFINED2;
    fem group nodes REMAINDER_REFINED1,REMAINDER_REFINED2 as REMAINDER;
    #
    fem group elements LV_FREE_WALL_INITIAL,LV_FREE_WALL_REFINED as LV_FREE_WALL;
    fem group elements 102..104,108..110,114..116 as LV_FREE_WALL_REFINED;
    fem group elements 103,106 as INFARCT_ELEMENTS;
    #
    fem export nodes;${OUTPUT_DIR}."MRP01_refined" as MRP01 region all;
    fem export elements;${OUTPUT_DIR}."MRP01_refined" as MRP01 region $WALL;
    fem export elements;${OUTPUT_DIR}."MRP01_base_refined" as base_skel region $BASE;
    #
    fem define fibre ; r ; MRP01_refined;

} else {
    fem group nodes REMAINDER_INITIAL as REMAINDER;
    fem group elements LV_FREE_WALL_INITIAL as LV_FREE_WALL;
}

if ($GRID_BASED_MECHANICS_PROPERTIES) {
    #=============================================================================================================
    print "\033[0;30;42m ========================================================= \033[0m\n";
    print "\033[0;30;42m                          Grid                             \033[0m\n";
    print "\033[0;30;42m ========================================================= \033[0m\n";
    #=============================================================================================================
    #
    fem define grid ; r ; MRP01_refined class $MECHANICS region $WALL;
    fem update grid geometry class $CELLULAR region $WALL;
    fem export element;${OUTPUT_DIR}."MRP01_grid" grid_numbers as grid class $CELLULAR;
```

```
    fem group grid;r;MRP01_refined region $WALL;
}

#=============================================================================================================
print "\033[0;30;42m ========================================================== \033[0m\n";
print "\033[0;30;42m                          Equations                         \033[0m\n";
print "\033[0;30;42m ========================================================== \033[0m\n";
#=============================================================================================================
#
fem define equation;r;finelas_tch_incomp lockregion $WALL;
fem define mapping;r;MRP01;
#
if ($GRID_BASED_MECHANICS_PROPERTIES) {
    fem define equation;r; cellular class $CELLULAR region $WALL; # Cellular equations (set, not used)
}

#=============================================================================================================
print "\033[0;30;42m ========================================================== \033[0m\n";
print "\033[0;30;42m                       Material Properties                  \033[0m\n";
print "\033[0;30;42m ========================================================== \033[0m\n";
#=============================================================================================================
#
if (!$GRID_BASED_MECHANICS_PROPERTIES) {
    fem define material;r;polezero region $WALL;
} else {
    fem define cell;r;polezero class $CELLULAR region $WALL;# Cell variant definitions
    fem define material;r;polezero_infarct_edited cell class $CELLULAR region $WALL;
    fem define material;r;polezero_grid region $WALL;       # Mechanics materials set from cells
}

#=============================================================================================================
print "\033[0;30;42m ========================================================== \033[0m\n";
print "\033[0;30;42m                       Initial Conditions                   \033[0m\n";
print "\033[0;30;42m ========================================================== \033[0m\n";
#=============================================================================================================
#
fem define initial;r;MRP01 region $WALL;

#=============================================================================================================
print "\033[0;30;42m ========================================================== \033[0m\n";
print "\033[0;30;42m                       Solution Method                      \033[0m\n";
print "\033[0;30;42m ========================================================== \033[0m\n";
#=============================================================================================================
#
fem define solve;r;lu region $WALL;


$ITERS = 15;
$TOL = 0.001;
if ( $SOLVE_INFLATION ) {
    #=========================================================================================================
    print "\033[0;30;42m ========================================================== \033[0m\n";
    print "\033[0;30;42m                       Solve Inflation                      \033[0m\n";
    print "\033[0;30;42m ========================================================== \033[0m\n";
    #=========================================================================================================
    print "\033[0;30;43m Increase cavity pressures incrementally to simulate diastole \033[0m\n";
    #
    set out;${OUTPUT_DIR}steps_inflate on;
    $NAME1 = "full_heart_press_";
    $MAXIMUM_INCREM = 1;
    $PRESS = 0.0;
    for $i ( 0.. $MAXIMUM_INCREM )
    {
        if ($i < 1)
        {
            $INCREM = 0.0;
        } else {
            $INCREM = 0.1;
        }
        #
```

```
$PRESS = $PRESS + $INCREM;
if ($PRESS < 1.3)
{
    $PRESS_mmHg = sprintf "%1.1f",${PRESS}*7.500637554192106;
} else {
    $PRESS_mmHg = sprintf "%2.1f",${PRESS}*7.500637554192106;
}
$FILE = ${NAME1}.${PRESS};
fem solve increment $INCREM iter $ITERS error $TOL class $MECHANICS;
fem define initial ;w;${OUTPUT_DIR}.${FILE};
fem export nodes;${OUTPUT_DIR}.${FILE} as heart;
fem export nodes;${OUTPUT_DIR}${FILE}_def field as heart;
fem export elements;${OUTPUT_DIR}.${FILE} as heart;
fem export elements;${OUTPUT_DIR}${FILE}_def field as wall;
#
fem update gauss strain fibre components region $WALL;
fem export gauss;${OUTPUT_DIR}.${FILE}."_gauss_strain" yg as gauss_strain;
fem update gauss stress fibre components region $WALL;
fem export gauss;${OUTPUT_DIR}.${FILE}."_gauss_stress" yg as gauss_stress;
if ($GRID_BASED_MECHANICS_PROPERTIES) {
    fem export element;${OUTPUT_DIR}.${FILE}."_grid_fields" field cell grid_numbers as grid class $CELLULAR;
    fem export gauss;${OUTPUT_DIR}.${FILE}."_gauss_material" parameters class $MECHANICS region $WALL;
}
#
for $ne ( 1..79 )
{
    $xi1 = 0.5;
    $xi2 = 0.5;
    MySubs::Create_File_strain_gauss("fibre",${OUTPUT_DIR}.${FILE}."_ne_".$ne."_fibre_strain_gauss",$ne);
    MySubs::Create_File_strain_gauss("wall",${OUTPUT_DIR}.${FILE}."_ne_".$ne."_wall_strain_gauss",$ne);
    MySubs::Create_File_stress_gauss("fibre",${OUTPUT_DIR}.${FILE}."_ne_".$ne."_fibre_stress_gauss",$ne);
    #
    MySubs::Create_File_strain_xi("fibre",${OUTPUT_DIR}.${FILE}."_ne_".$ne."_fibre_strain_xi",$ne,$xi1,$xi2);
    MySubs::Create_File_strain_xi("wall",${OUTPUT_DIR}.${FILE}."_ne_".$ne."_wall_strain_xi",$ne,$xi1,$xi2);
    MySubs::Create_File_stress_xi("fibre",${OUTPUT_DIR}.${FILE}."_ne_".$ne."_fibre_stress_xi",$ne,$xi1,$xi2);
}
#
if ($REFINE)
{
    for $ne ( 89..101 )
    {
        $xi1 = 0.5;
        $xi2 = 0.5;
        MySubs::Create_File_strain_gauss("fibre",${OUTPUT_DIR}.${FILE}."_ne_".$ne."_fibre_strain_gauss",$ne);
        MySubs::Create_File_strain_gauss("wall",${OUTPUT_DIR}.${FILE}."_ne_".$ne."_wall_strain_gauss",$ne);
        MySubs::Create_File_stress_gauss("fibre",${OUTPUT_DIR}.${FILE}."_ne_".$ne."_fibre_stress_gauss",$ne);
        #
        MySubs::Create_File_strain_xi("fibre",${OUTPUT_DIR}.${FILE}."_ne_".$ne."_fibre_strain_xi",$ne,$xi1,$xi2);
        MySubs::Create_File_strain_xi("wall",${OUTPUT_DIR}.${FILE}."_ne_".$ne."_wall_strain_xi",$ne,$xi1,$xi2);
        MySubs::Create_File_stress_xi("fibre",${OUTPUT_DIR}.${FILE}."_ne_".$ne."_fibre_stress_xi",$ne,$xi1,$xi2);
    }
    MySubs::Combine_Element_Files(${OUTPUT_DIR}.${FILE}."_ne_11_fibre_strain_gauss",${OUTPUT_DIR}.${FILE}
      ."_ne_94_fibre_strain_gauss",${OUTPUT_DIR}.${FILE}."_ne_11.94_fibre_strain_gauss")
    #
    MySubs::Combine_Element_Files(${OUTPUT_DIR}.${FILE}."_ne_11_fibre_strain_xi",${OUTPUT_DIR}.${FILE}
      ."_ne_94_fibre_strain_xi",${OUTPUT_DIR}.${FILE}."_ne_11.94_fibre_strain_xi")
}
if ($REFINE_INFARCT)
{
    for $ne ( 89..119 )
    {
        $xi1 = 0.5;
        $xi2 = 0.5;
        MySubs::Create_File_strain_gauss("fibre",${OUTPUT_DIR}.${FILE}."_ne_".$ne."_fibre_strain_gauss",$ne);
        MySubs::Create_File_strain_gauss("wall",${OUTPUT_DIR}.${FILE}."_ne_".$ne."_wall_strain_gauss",$ne);
        MySubs::Create_File_stress_gauss("fibre",${OUTPUT_DIR}.${FILE}."_ne_".$ne."_fibre_stress_gauss",$ne);
        #
        MySubs::Create_File_strain_xi("fibre",${OUTPUT_DIR}.${FILE}."_ne_".$ne."_fibre_strain_xi",$ne,$xi1,$xi2);
        MySubs::Create_File_strain_xi("wall",${OUTPUT_DIR}.${FILE}."_ne_".$ne."_wall_strain_xi",$ne,$xi1,$xi2);
        MySubs::Create_File_stress_xi("fibre",${OUTPUT_DIR}.${FILE}."_ne_".$ne."_fibre_stress_xi",$ne,$xi1,$xi2);
```

```
        }
            MySubs::Combine_Element_Files(${OUTPUT_DIR}.${FILE}."_ne_11_fibre_strain_gauss",${OUTPUT_DIR}.${FILE}
              ."_ne_94_fibre_strain_gauss",${OUTPUT_DIR}.${FILE}."_ne_11.94_fibre_strain_gauss")
            #
            MySubs::Combine_Element_Files(${OUTPUT_DIR}.${FILE}."_ne_11_fibre_strain_xi",${OUTPUT_DIR}
              .${FILE}."_ne_94_fibre_strain_xi",${OUTPUT_DIR}.${FILE}."_ne_11.94_fibre_strain_xi")
        }
    }
    #
    if (! $REFINE)
    {
        MySubs::Create_Slice_EXR_FILE();
        MySubs::Create_Section_EXR_FILE();
    }
    if (! $REFINE_INFARCT)
    {
        MySubs::Create_Slice_EXR_FILE();
        MySubs::Create_Section_EXR_FILE();
    }

} else {
    #=============================================================================================================
    print "\033[0;30;42m ========================================================== \033[0m\n";
    print "\033[0;30;42m                    End-Diastolic State                     \033[0m\n";
    print "\033[0;30;42m ========================================================== \033[0m\n";
    #=============================================================================================================
    #
    print "\033[0;30;43m              Reading in end-diastolic state                \033[0m\n";
    $FILE = "full_heart_press_1";
    $PRESS = 1;
    fem define initial ;r;${OUTPUT_DIR}.${FILE} region $WALL;
    fem define solve;r;lu region $WALL;
    fem solve increment 0.0 iter 20 error $TOL ;
}



if ( $CAVITY_REGIONS ) {
    #=============================================================================================================
    print "\033[0;30;42m ========================================================== \033[0m\n";
    print "\033[0;30;42m                    Set up Cavity Regions                   \033[0m\n";
    print "\033[0;30;42m ========================================================== \033[0m\n";
    #=============================================================================================================
    #
    fem define base;r;MRP01;                                # Redefine bases to calculate scale factors
    fem define;add bases;r;3Linear-2PressAuxXi3_4x4x4Gauss;
    #
    # Define geometry for LV and RV cavities
    #
    fem define region;r ; cavities ;
    #
    fem define coord;r;lv_cavity region $LV_CAVITY;
    fem define node;r;lv_cavity region $LV_CAVITY;
    fem define element;r;lv_cavity region $LV_CAVITY;
    #
    fem define coord;r;rv_cavity region $RV_CAVITY;
    fem define node;r;rv_cavity region $RV_CAVITY;
    fem define element;r;rv_cavity region $RV_CAVITY;
    #
    # Calculate the cavity volumes
    #
    fem list elements deformed total cavity_volume region $LV_CAVITY; # Defines and sets the var $LV_CAVITY_VOLUME
    fem list elements deformed total cavity_volume region $RV_CAVITY; # Defines and sets the var $RV_CAVITY_VOLUME
    print "\nLV cavity volume = ${LV_CAVITY_VOLUME}\n";
    print "RV cavity volume = ${RV_CAVITY_VOLUME}\n\n";
    $DIASTOLIC_LV_CAVITY_VOLUME = $LV_CAVITY_VOLUME;
    $DIASTOLIC_RV_CAVITY_VOLUME = $RV_CAVITY_VOLUME;
    #
    # Read back in scale factors for the ventricular wall elements
    #
```

```
    fem define base;r;MRP01_readse;                    # Redefine bases to read in scale factors
    fem define;add bases;r;3Linear-2PressAuxXi3_4x4x4Gauss;
    fem define line ; r ; MRP01;
    $LV_PRESS = $PRESS;
    $RV_PRESS = $PRESS*0.2;
}

if ( $SOLVE_ACTIVE_CONTRACTION ) {
    #=============================================================================================================
    print "\033[0;30;42m ========================================================= \033[0m\n";
    print "\033[0;30;42m                  Solving Active Contraction                \033[0m\n";
    print "\033[0;30;42m ========================================================= \033[0m\n";
    #=============================================================================================================
    #

    fem define material ; r ; polezero_active region $WALL;
    fem define active ; r ; $CELL_MODEL
    #
    # Set up the HMT cellular model -- used to calculate the active tension
    # Define a 3x3x3 grid scheme for use in all elements and calculate
    # their spatial location and metrics
    #
    fem define grid ; r ; cell - 3x3x3 gauss class $CELLULAR;
    fem update grid geometry;
    fem update grid metric;
    #
    fem group grid element ALL_ELEMENTS as ALL_GRID_POINTS;
    #
    # Define the cardiac cell mechanics model
    #
    fem define equation;r ; cell - $CELL_MODEL class $CELLULAR;
    fem define material ; r ; cell - FM class $CELLULAR; # unused
    #
    # Define the model parameters, there are no spatially varying cellular parameters
    #
    fem define cell ; r ; cell - $CELL_MODEL class $CELLULAR;
    fem define material ; r ; cell - $CELL_MODEL cell class $CELLULAR;
    fem update grid material class $CELLULAR;
    #
    # Define the [Ca]i transient
    #
    $cai = "cai";
    fem define time ; r ; cai - $CELL_MODEL;
    #
    # Define the initial condition for the cellular model -- setting the
    # [Ca]i variable in the cell model to be defined via the above time
    # variable
    #
    fem define initial ; r ; cell - $CELL_MODEL class $CELLULAR;
    #
    # Define a simple Euler interagtion for the cellular ODE's
    #
    fem define solve ; r ; cell - $CELL_MODEL class $CELLULAR;
    #
    # Cai index for grid (YQS) variables
    #
    fem inquire cell_variable Cai return_variables CAI_GRIDARRAY,CAI_GRIDIDX;
    #
    # Fibre extension ratio index for grid (YQS) and mechanics variables
    #
    fem inquire cell_variable ExtensionRatio return_variables L_GRIDARRAY,L_GRIDIDX;
    $L_MECHIDX = 1;
    #
    # Tension index for grid (YQS) and Gauss (YG) variables
    #
    fem inquire cell_variable IsometricTension return_variables T_GRIDARRAY,T_GRIDIDX;
    $T_GAUSSARRAY = "YG";
    $T_GAUSSIDX = 1;
    #
```

```
# Open a history file to store the cellular extension ratios
#
fem open history;${OUTPUT_DIR}."cell_ext" write variables yqs niqslist $L_GRIDIDX,$T_GRIDIDX,$CAI_GRIDIDX binary class $CELLULAR unit 21;
#
fem update gauss strain fibre components;
fem update grid extension_ratio component $L_MECHIDX $L_GRIDARRAY $L_GRIDIDX class $MECHANICS;
fem solve class $CELLULAR to 0;
fem update gauss gridvars $T_GRIDARRAY $T_GRIDIDX $T_GAUSSARRAY $T_GAUSSIDX;
fem solve class $MECHANICS increment 0.0 iterate 10 error 0.001;
#
#
# Loop through time, solving the coupled active dynamic HTM with coupled mecahnics
#
$RESOLVE=$FALSE;
$PRESSURE_INCREMENT=$FALSE;
$TIME = 0.0;
if ($CELL_MODEL eq "HMT") {
   $TIME_MAX=120;
} elsif ($CELL_MODEL eq "FM") {
  $TIME_MAX=30; # Time is actually activation level
}

$dt=1;
while ($TIME <= $TIME_MAX) {
     $iter = 0;
     $CONVERGED = 0;
     while ( $iter < 1) {
          $iter++;
  print "\ nIteration : $iter \n\n";
          if (!$PRESSURE_INCREMENT){
     fem update gauss strain fibre components;
     fem update grid extension_ratio component $L_MECHIDX $L_GRIDARRAY $L_GRIDIDX class $MECHANICS;
          }
          $local_time = $TIME;
          $local_tend = $TIME+$dt;
          $FILE = "fullheart_def_active_".${TIME};
          #
          if ($RESOLVE){
               $TIME_last=$TIME-$dt;
               $FILE_LAST="fullheart_def_active_".${TIME_last};
       fem read matrix;${OUTPUT_DIR}.${FILE_LAST}."_YQ_YQS" matrices YQ,YQS binary;
  }
          #
  fem solve class $CELLULAR from $local_time to $local_tend;
  fem update gauss gridvars $T_GRIDARRAY $T_GRIDIDX $T_GAUSSARRAY $T_GAUSSIDX ;
  fem solve increment 0.0 iterate 10 error 0.001;
          print "\n\n\n convergence iterations $CONVERGENCE_ITERATIONS \n\n\n";
          #
          fem list elements deformed total cavity_volume region $LV_CAVITY;
          fem list elements deformed total cavity_volume region $RV_CAVITY;
          print "\nLV cavity volume = ${LV_CAVITY_VOLUME}\n";
          print "RV cavity volume = ${RV_CAVITY_VOLUME}\n\n";
          #
          # Increase cavity pressures to maintain constant volume
          #
  if ($CONVERGED) {
               $PRESSURE_INCREMENT=$FALSE;
               if ($LV_CAVITY_VOLUME < ($DIASTOLIC_LV_CAVITY_VOLUME-$DIASTOLIC_LV_CAVITY_VOLUME*0.01) )
               {
                    $INCREM = 0.1;
                    fem update pressure boundary elements LV_FREE_WALL auxillary 1 increment $INCREM;
            fem update pressure boundary elements SEPTUM auxillary 1 increment $INCREM;
                    $LV_PRESS = $LV_PRESS+$INCREM;
                    print "\nIncreasing LV cavity pressure by $INCREM to $LV_PRESS kPa\n\n";
                    $RESOLVE=$TRUE;
                    $PRESSURE_INCREMENT=$TRUE;
            last ;
               }
               if ($RV_CAVITY_VOLUME < ($DIASTOLIC_RV_CAVITY_VOLUME-$DIASTOLIC_RV_CAVITY_VOLUME*0.01) )
               {
```

```
            $INCREM = 0.1;
          fem update pressure boundary elements SEPTUM auxillary 2 increment $INCREM;
          fem update pressure boundary elements RV_FREE_WALL auxillary 1 increment $INCREM;
            $RV_PRESS = $RV_PRESS+$INCREM*0.2;
            print " \nIncreasing RV cavity pressure by $INCREM to $RV_PRESS kPa\n\n";
            $RESOLVE=$TRUE;
            $PRESSURE_INCREMENT=$TRUE;
          last ;
            }
        }
        #
        # Increase time if all has gone well, otherwise try again
        #
  if ($CONVERGED) {
          if (( $CONVERGENCE_ITERATIONS == 1) || ($CELL_MODEL eq "FM" )) {
            $LAST_CONVERGED_TIME=$TIME;
            $TIME += $dt;
            $RESOLVE=$FALSE
          last ;
          } else {
            $RESOLVE=$TRUE
          last ;
          }
  }
    }
    if ($CONVERGED == 0) {
      print " \n\nCouldn't Converge, Exiting.\n\n\n";
      fem export nodes;${OUTPUT_DIR}.${FILE} field as heart region $WALL;
      fem export elements;${OUTPUT_DIR}.${FILE} field as wall region $WALL;
      fem export nodes;${OUTPUT_DIR}."lv_cavity_ref_".${TIME} as lv_cavity region all;
      fem export elements;${OUTPUT_DIR}."lv_cavity_ref_".${TIME} as lv_cavity region $LV_CAVITY;
      last ;
    }
    #
    fem export nodes;${OUTPUT_DIR}.${FILE} field as heart region $WALL;
    fem export elements;${OUTPUT_DIR}.${FILE} field as wall region $WALL;
    fem export nodes;${OUTPUT_DIR}."lv_cavity_ref_".${TIME} as lv_cavity region all;
    fem export elements;${OUTPUT_DIR}."lv_cavity_ref_".${TIME} as lv_cavity region $LV_CAVITY;
    #
    # Update grid and get new extension ratio values
    #
    fem update grid geometry deformed class $CELLULAR from_class $MECHANICS;
    fem update grid metric deformed class $CELLULAR from_class $MECHANICS;
    fem update grid material class $CELLULAR;
    #
    if (! $RESOLVE) {
      # A converged solution was obtained, so we are done for this time step..
      # Store the current cell state for the next set of iterations
      fem write matrix;${OUTPUT_DIR}.${FILE}."_YQ_YQS" matrices YQ,YQS binary;
      fem write history time $TIME variables yqs binary class $CELLULAR unit 21;
    }
}
#
fem close history binary class $CELLULAR unit 21;
#
# Export the history file to signal files
#
fem evaluate electrode;${OUTPUT_DIR}."/cell_ext" history ${OUTPUT_DIR}."/cell_ext" from grid yqs iy $L_GRIDIDX binary class $CELLULAR;
fem evaluate electrode;${OUTPUT_DIR}."/cell_tension" history ${OUTPUT_DIR}."/cell_ext" from grid yqs iy $T_GRIDIDX binary class $CELLULAR;
fem evaluate electrode;${OUTPUT_DIR}."/cell_cai" history ${OUTPUT_DIR}."/cell_ext" from grid yqs iy $CAI_GRIDIDX binary class $CELLULAR;
#
fem define export;r ; cell_3x3x3;
#
fem export signal;${OUTPUT_DIR}."/cell_ext" electrode signal ${OUTPUT_DIR}."/cell_ext";
fem export signal;${OUTPUT_DIR}."/cell_tension" electrode signal ${OUTPUT_DIR}."/cell_tension";
fem export signal;${OUTPUT_DIR}."/cell_cai" electrode signal ${OUTPUT_DIR}."/cell_cai";
#
print " Total LV cavity pressure = $LV_PRESS\n";
print " Total RV cavity pressure = $RV_PRESS\n";
print "End_diastolic LV cavity volume = ${DIASTOLIC_LV_CAVITY_VOLUME}\n";
```

```
    print "End-isovolumic contraction LV cavity volume = ${LV_CAVITY_VOLUME}\n\n";
    print "End-diastolic RV cavity volume = ${DIASTOLIC_RV_CAVITY_VOLUME}\n";
    print "End-isovolumic contraction RV cavity volume = ${RV_CAVITY_VOLUME}\n\n";
}


if ( $SOLVE_EJECTION ) {
    #=============================================================================================================
    print "\033[0;30;42m ============================================================ \033[0m\n";
    print "\033[0;30;42m                    Solving Ejection                          \033[0m\n";
    print "\033[0;30;42m ============================================================ \033[0m\n";
    #=============================================================================================================
    #
    # Decrement the cavity pressures to simulate ejection
    #
    set output;${OUTPUT_DIR}steps_ejection on;
    #
    $FILE = "fullheart_def_active_30_press_";
    $INCREM = -0.1;
    $ITER = 20;
    $ERROR_TOLERANCE = 0.001;
    $PRESS=$LV_PRESS*10;
    while ($PRESS > 0.0 )
    {
        fem solve increment $INCREM iter $ITER error $ERROR_TOLERANCE;
        fem define initial ;w;${OUTPUT_DIR}.${FILE}.${PRESS} region $WALL
        #
        fem list elements deformed total cavity_volume region $LV_CAVITY;
        print "\nLV cavity volume = ${LV_CAVITY_VOLUME}\n\n";
        #
        #
        fem export nodes;${OUTPUT_DIR}.${FILE}.${PRESS} field as heart region $WALL;
        fem export elements;${OUTPUT_DIR}.${FILE}.${PRESS} field as wall region $WALL;
        for $ne ( 1..79 )
      {
            $xi1 = 0.5;
            $xi2 = 0.5;
            MySubs::Create_File_strain_gauss("fibre",${OUTPUT_DIR}.${FILE}."_ne_".$ne."_fibre_strain_gauss",$ne);
            MySubs::Create_File_strain_gauss("wall",${OUTPUT_DIR}.${FILE}."_ne_".$ne."_wall_strain_gauss",$ne);
            MySubs::Create_File_stress_gauss("fibre",${OUTPUT_DIR}.${FILE}."_ne_".$ne."_fibre_stress_gauss",$ne);
            #
            MySubs::Create_File_strain_xi("fibre",${OUTPUT_DIR}.${FILE}."_ne_".$ne."_fibre_strain_xi",$ne,$xi1,$xi2);
            MySubs::Create_File_strain_xi("wall",${OUTPUT_DIR}.${FILE}."_ne_".$ne."_wall_strain_xi",$ne,$xi1,$xi2);
            MySubs::Create_File_stress_xi("fibre",${OUTPUT_DIR}.${FILE}."_ne_".$ne."_fibre_stress_xi",$ne,$xi1,$xi2);
  }
        $PRESS--;
    }
    set out off;
}

quit
```

Appendix C

The CMISS Command File for the Infarction Models

The CMISS (Section 1.3) command file for the myocardial infarction models based upon the Holmes data set. This file is presented to document the algorithms used within this thesis. The accompaning input files are prohibitively large to include here, but can be downloaded from `http://www.cmiss.org`.

```
#
# This is a reccursive command file! It invokes itself to
# solve the mechanics problem to evaluate the objective for
# the optimisation problem.
#

$SPECIMEN="scp04"
#
$TRUE = 1; # Initialise logicals
$FALSE = 0;
#
$pressure = "time"; # To use time variables to represent experimental pressure-strain data
#
use MyPlot; # Necessary for plotting commands

#=============================================================================================================
print "\033[0;30;42m ============================================================ \033[0m\n";
print "\033[0;30;42m                        Execution Flow                        \033[0m\n";
print "\033[0;30;42m ============================================================ \033[0m\n";
#=============================================================================================================
#
set num_threads 1;
#
# Output
#
$OUTPUT_DIR = "output/".${SPECIMEN}."/";
if ( ! -d ${OUTPUT_DIR})
{
    mkdir ${OUTPUT_DIR};
}
#
# Optmising
```

```
#
$OPTIMISE = $TRUE;

#
# Local Refinement
#
$LOCAL_REFINEMENT = $TRUE;
#
# Grids
#
$CALCULATE_INFARCT_CELLS = $TRUE;
#
# Constitutive law
#
#$CONSTITUTIVE_LAW = "POLE_ZERO";
$CONSTITUTIVE_LAW = "HOLMES";

#=============================================================================================================
 print "\033[0;30;42m ========================================================== \033[0m\n";
 print "\033[0;30;42m                    Regions & Classes                       \033[0m\n";
 print "\033[0;30;42m ========================================================== \033[0m\n";
#=============================================================================================================
#
# Regions
#
$WALL = 1;
$INFARCT = 2;
$CAVITY = 3;
#
# Classes
#
$MECHANICS = 1;
$CELLULAR = 2;


 if ($RESOLVE ne "TRUE") {   # Don't need to redo these commands when resolving during optimisation
   #=============================================================================================================
   print "\033[0;30;42m ========================================================== \033[0m\n";
   print "\033[0;30;42m                      Environment                         \033[0m\n";
   print "\033[0;30;42m ========================================================== \033[0m\n";
   #=============================================================================================================
   #
   fem define parameters;r;large;          # Large set for local refinement and hi-res grid
   fem define coordinates;r;rc3d;
   fem define regions;r;5_regions;

   #=============================================================================================================
   print "\033[0;30;42m ========================================================== \033[0m\n";
   print "\033[0;30;42m                        Bases                             \033[0m\n";
   print "\033[0;30;42m ========================================================== \033[0m\n";
   #=============================================================================================================
   #
   fem define bases;r;geom_fibres region $WALL;   # 1..8 Geometry and fibres
   fem define;add bases;r;pressure region $WALL;  # 9 Pressure

   #=============================================================================================================
   print "\033[0;30;42m ========================================================== \033[0m\n";
   print "\033[0;30;42m     Nodes, Elements & Fibre Fields for Ventricular Wall    \033[0m\n";
   print "\033[0;30;42m ========================================================== \033[0m\n";
   #=============================================================================================================
   #
   fem define nodes;r;"models/".${SPECIMEN}."/".${SPECIMEN} region $WALL;
   fem define elements;r;"models/".${SPECIMEN}."/".${SPECIMEN} region $WALL;
   #
   fem define fibres;r;60-60 region $WALL;          # zero sheets
   fem define elements;r;60-60 fibre region $WALL;
   #
   # Node Groups
   #
   fem group nodes 1..8,34..41 as fixed_positions region $WALL;
```

```
fem group nodes 1..33 as endo region $WALL;
fem group nodes 34..66 as epi region $WALL;

#=============================================================================================================
print "\033[0;30;42m ========================================================== \033[0m\n";
print "\033[0;30;42m                          Infarct                           \033[0m\n";
print "\033[0;30;42m ========================================================== \033[0m\n";
#=============================================================================================================
#
fem define node;r;"models/".${SPECIMEN}."/".${SPECIMEN}."_infarct" region $INFARCT;
fem define element;r;"models/".${SPECIMEN}."/".${SPECIMEN}."_infarct" region $INFARCT;
fem group elements 101..110 region $INFARCT as INFARCT_ELEMENTS;
fem export nodes;${OUTPUT_DIR}.${SPECIMEN}."_infarct" as infarct region $INFARCT offset 1000;
fem export elements;${OUTPUT_DIR}.${SPECIMEN}."_infarct" as infarct region $INFARCT offset_elem 1000;
#
fem export nodes;${OUTPUT_DIR}.${SPECIMEN}."_fitted" as ${SPECIMEN}."_fitted";
fem export elements;${OUTPUT_DIR}.${SPECIMEN}."_fitted" as ${SPECIMEN}."_fitted";

#=============================================================================================================
print "\033[0;30;42m ========================================================== \033[0m\n";
print "\033[0;30;42m                     Local Refinement                       \033[0m\n";
print "\033[0;30;42m ========================================================== \033[0m\n";
#=============================================================================================================
#
if ( $LOCAL_REFINEMENT) {
  fem refine Xi 2 at 0.6 element 19,20 region $WALL;
  #
  fem refine Xi 3 at 0.333 element 19,20 region $WALL;
  fem refine Xi 3 at 0.333 element 111,112 region $WALL;
  #
  fem refine Xi 3 at 0.5 element 113,114 region $WALL;
  fem refine Xi 3 at 0.5 element 115,116 region $WALL;
  #
  fem refine Xi 3 at 0.333 element 11,12 region $WALL;
  fem refine Xi 3 at 0.5 element 121,122 region $WALL;
  #
  fem refine Xi 2 at 0.5 element 11,121,123 region $WALL;
  fem refine Xi 2 at 0.5 element 12,122,124 region $WALL;
  #
  fem refine Xi 1 at 0.5 element 19,113,117,111,115,119,11,121,123,125,126,127;
  fem refine Xi 1 at 0.5 element 20,114,118,112,116,120,12,122,124,128,129,130;
  #
  fem group elements 1..32,111,112,125,128,131,134,137,140,143,146,149,152 as PLV region $WALL;
  #
  $GRID="refined_scheme_6";
  if ( $CONSTITUTIVE_LAW EQ 'POLE_ZERO' ) {
    fem define fibre ; r ; ${GRID}."_polezero" region $WALL;     # 30 degree infarct endo
  } else {
    fem define fibre ; r ; ${GRID} region $WALL;     # 30 degree infarct endo
  }
  #
  fem export nodes;${OUTPUT_DIR}.${SPECIMEN}."_refined" as ${SPECIMEN}."_refined";
  fem export elements;${OUTPUT_DIR}.${SPECIMEN}."_refined" as ${SPECIMEN}."_refined";

} else {
  $GRID="3x3";
  fem group elements 1..32 as PLV region $WALL;
  fem group elements all_elements as all region $WALL;
}

#=============================================================================================================
print "\033[0;30;42m ========================================================== \033[0m\n";
print "\033[0;30;42m                          Grid                              \033[0m\n";
print "\033[0;30;42m ========================================================== \033[0m\n";
#=============================================================================================================
#
fem define grid ; r ; $GRID class $MECHANICS region $WALL;
fem update grid geometry class $CELLULAR region $WALL;
#
fem export element;${OUTPUT_DIR}.${SPECIMEN}."_grid" grid_numbers as grid class $CELLULAR;
```

```
#
 if ( $CONSTITUTIVE_LAW EQ 'POLE_ZERO' )
 {
      if ( $CALCULATE_INFARCT_CELLS ) {
   fem group grid grid 1 as NORMAL_CELLS;
       fem group grid within elements INFARCT_ELEMENTS as INFARCT_CELLS region $INFARCT;
   fem group grid;w;$GRID."_polezero" region $WALL;
     } else {
   fem group grid;r;$GRID."_polezero" region $WALL;
      }
 } elsif ( $CONSTITUTIVE_LAW EQ 'HOLMES' ) {
      if ( $CALCULATE_INFARCT_CELLS ) {
   fem group grid grid 1 as NORMAL_CELLS;
       fem group grid within elements INFARCT_ELEMENTS as INFARCT_CELLS region $INFARCT;
   fem group grid;w;$GRID."_holmes" region $WALL;
     } else {
       fem group grid;r;$GRID."_holmes" region $WALL;
      }
 }

 #=============================================================================================================
 print "\033[0;30;42m ========================================================= \033[0m\n";
 print "\033[0;30;42m                    Equations                              \033[0m\n";
 print "\033[0;30;42m ========================================================= \033[0m\n";
 #=============================================================================================================
 #
 fem define equation;r;finelas_tch_incomp region $WALL lock;
 fem define equation;r; cellular class $CELLULAR region $WALL; # Cellular equations (set, not used)

 #=============================================================================================================
 print "\033[0;30;42m ========================================================= \033[0m\n";
 print "\033[0;30;42m                    Material Properties                    \033[0m\n";
 print "\033[0;30;42m ========================================================= \033[0m\n";
 #=============================================================================================================
 #
 if ( $CONSTITUTIVE_LAW EQ 'POLE_ZERO' )
 {
   fem define cell ;r;polezero class $CELLULAR region $WALL;# Cell variant definitions
   fem define material;r;polezero_infarct cell class $CELLULAR region $WALL;
   fem define material;r;polezero_grid region $WALL;      # Mechanics materials set from cells

 } elsif ( $CONSTITUTIVE_LAW EQ 'HOLMES' ) {
   fem define cell ;r;holmes class $CELLULAR region $WALL; # Cell variant definitions
   fem define material;r;"models/".${SPECIMEN}."/".${SPECIMEN} cell class $CELLULAR region $WALL;
   fem define material;r;holmes_grid region $WALL; # Mechanics materials set from cells
 }
 #
 fem export element;${OUTPUT_DIR}.${SPECIMEN}."_grid_numbers" grid_numbers as grid class $CELLULAR;
 fem export element;${OUTPUT_DIR}.${SPECIMEN}."_grid_fields" field cell grid_numbers as grid class $CELLULAR;
 fem export gauss;${OUTPUT_DIR}.${SPECIMEN}."_gauss_material" parameters class $MECHANICS region $WALL;
 #
 fem define active;r;active0_00

} # !resolve

 if ($RESOLVE eq "TRUE") { # Need to update the material parameters to those being evaluated by the optimiser
   fem update material optimise cell variant 2 parameter 3 optimisation_variable 1;
   fem update material optimise cell variant 2 parameter 4 optimisation_variable 2;
   fem update material optimise cell variant 2 parameter 5 optimisation_variable 3;
   fem define material;r;holmes_grid region $WALL;      # Mechanics materials set from cells
}

#=============================================================================================================
print "\033[0;30;42m ========================================================= \033[0m\n";
print "\033[0;30;42m                    Initial Conditions                     \033[0m\n";
print "\033[0;30;42m ========================================================= \033[0m\n";
#=============================================================================================================
#
fem define initial ;r;bcs region $WALL;
```

```
#=============================================================================================================
print "\033[0;30;42m ========================================================== \033[0m\n";
print "\033[0;30;42m                          Solution Method                   \033[0m\n";
print "\033[0;30;42m ========================================================== \033[0m\n";
#=============================================================================================================
#
fem define solve;r;lu region $WALL;

#=============================================================================================================
print "\033[0;30;42m ========================================================== \033[0m\n";
print "\033[0;30;42m                          Solve Inflation                   \033[0m\n";
print "\033[0;30;42m ========================================================== \033[0m\n";
#=============================================================================================================
#
print "\033[0;30;43m Increase cavity pressures incrementally to simulate diastole \033[0m\n";
#
set out;steps_inflate on;
$residual_index = 0;
$NAME1 = ${SPECIMEN}."_press_";
$TOL = 0.001;
$MAXIMUM_INCREM = 8;
$PRESS = 0.0;

for $i ( 0.. $MAXIMUM_INCREM ) # kPa increments
{
  if ($i < 1)
  {
    $INCREM = 0.0;
    $ITERS = 10;
  } else {
    $INCREM = 0.3333;          # nice mmHg unit increment
    $ITERS = 12;
  }
  $PRESS = $PRESS + $INCREM;
  if ($PRESS < 1.3)
  {
    $PRESS_mmHg = sprintf "%1.0f",${PRESS}*7.500637554192106;
  } else {
    $PRESS_mmHg = sprintf "%2.0f",${PRESS}*7.500637554192106;
  }
  $FILENAME = ${NAME1}.${PRESS_mmHg};
  fem solve increment $INCREM iter $ITERS error $TOL ;
  #
  if ($RESOLVE eq "TRUE") {
    if (( $PRESS_mmHg == 5 ) || ( $PRESS_mmHg == 10 ) || ( $PRESS_mmHg == 15 ) || ( $PRESS_mmHg == 20 )) {
      $depth__5_ne = 123;
      $depth_35_ne = 121;
      $depth_65_ne = 121;
      $xi1 = 0.5;
      $xi2 = 0.5;
      $depth__5_xi3 = 0.15;
      $depth_35_xi3 = 0.05;
      $depth_65_xi3 = 0.95;
      @transmural_elements = [123,121,11];
      #
      # average
      fem li strain e11 xi_point xi_1 $xi1 xi_2 $xi2 xi_3 $depth__5_xi3 element $depth__5_ne wall to YP $residual_index+1;
      fem li strain e11 xi_point xi_1 $xi1 xi_2 $xi2 xi_3 $depth_35_xi3 element $depth_35_ne wall to YP $residual_index+2;
      fem li strain e11 xi_point xi_1 $xi1 xi_2 $xi2 xi_3 $depth_65_xi3 element $depth_65_ne wall to YP $residual_index+3;
      fem evaluate $pressure variable circ_e11_infarct_depth_5 $pressure $PRESS_mmHg to YP $residual_index+1;
      fem evaluate $pressure variable circ_e11_infarct_depth_35 $pressure $PRESS_mmHg to YP $residual_index+2;
      fem evaluate $pressure variable circ_e11_infarct_depth_65 $pressure $PRESS_mmHg to YP $residual_index+3;
      $residual_index = $residual_index + 3;
      #
      #scpecimen specific
      #fem li strain e11 xi_point xi_1 $xi1 xi_2 $xi2 xi_3 $depth__5_xi3 element $depth__5_ne wall to YP $residual_index+1;
      #fem li strain e11 xi_point xi_1 $xi1 xi_2 $xi2 xi_3 $depth_35_xi3 element $depth_35_ne wall to YP $residual_index+2;
      #fem li strain e11 xi_point xi_1 $xi1 xi_2 $xi2 xi_3 $depth_65_xi3 element $depth_65_ne wall to YP $residual_index+3;
      #fem evaluate $pressure variable ${SPECIMEN}."_wall_e11_infarct_depth_5" $pressure $PRESS_mmHg to YP $residual_index+1;
      #fem evaluate $pressure variable ${SPECIMEN}."_wall_e11_infarct_depth_35" $pressure $PRESS_mmHg to YP $residual_index+2;
```

```
      #fem evaluate $pressure variable  ${SPECIMEN}."_wall_e11_infarct_depth_65" $pressure $PRESS_mmHg to YP $residual_index+3;
      #$residual_index = $residual_index + 3;
    }
  }
  #
  fem define  initial ;w;${OUTPUT_DIR}.${FILENAME};
  @transmural_ne = (123,121,11);
  $xi1 = 0.5;
  $xi2 = 0.5;
  MyPlot::Create_Transmural_Data_File(${OUTPUT_DIR}.${FILENAME}."_ne_".$transmural_ne[0]."_infarct",$transmural_ne[0],$xi1,$xi2);
  MyPlot::Create_Transmural_Data_File(${OUTPUT_DIR}.${FILENAME}."_ne_".$transmural_ne[1]."_infarct",$transmural_ne[1],$xi1,$xi2);
  MyPlot::Create_Transmural_Data_File(${OUTPUT_DIR}.${FILENAME}."_ne_".$transmural_ne[2]."_infarct",$transmural_ne[2],$xi1,$xi2);
  MyPlot::Combine_Transmural_Element_Files(\@transmural_ne,$PRESS_mmHg,$SPECIMEN);
  #
  fem export nodes;${OUTPUT_DIR}.${FILENAME} as heart;
  fem export nodes;${OUTPUT_DIR}${FILENAME}_def field as heart;
  fem export elements;${OUTPUT_DIR}.${FILENAME} as heart;
  fem export elements;${OUTPUT_DIR}${FILENAME}_def field as wall;
  fem export element;${OUTPUT_DIR}.${FILENAME}."_grid_fields" field cell grid_numbers as grid class $CELLULAR;
  fem export gauss;${OUTPUT_DIR}.${FILENAME}."_gauss_material" parameters class $MECHANICS region $WALL;
}

if ($RESOLVE eq "TRUE") {
  $ITERATION=$ITERATION + 1;
  print  "\033[0;30;43m                    Iteration  = ${ITERATION}                    \033[0m\n";
}

if  ( $OPTIMISE && ($RESOLVE ne "TRUE")) {
  #=============================================================================================================
  print  "\033[0;30;42m ========================================================== \033[0m\n";
  print  "\033[0;30;42m              Material  Paramter Optimisation               \033[0m\n";
  print  "\033[0;30;42m ========================================================== \033[0m\n";
  #=============================================================================================================
  #
  fem define $pressure;r;wall_e11_normal;      # Curves defining the _average_ experimental pressure-strain
  fem define $pressure;r;wall_e22_normal;      # data at various depths for normal & infarct tissue
  fem define $pressure;r;wall_e33_normal;
  fem define $pressure;r;wall_e12_normal;
  fem define $pressure;r;wall_e13_normal;
  fem define $pressure;r;wall_e23_normal;
  #
  fem define $pressure;r;wall_e11_infarct;
  fem define $pressure;r;"models/".${SPECIMEN}."/".${SPECIMEN}."_wall_e11_infarct";
  #
  fem define $pressure;r;"models/".${SPECIMEN}."/scp04_wall_e22_infarct"; # at various depths for infarct tissue in scp04
  fem define $pressure;r;"models/".${SPECIMEN}."/scp04_wall_e33_infarct";
  #
  $ITERATION = 1;
  $RESOLVE = "TRUE";
  #
  fem define optimise;r;C1_C2_C3_e11;
  #
  optimise;

}

quit
```

Appendix D

Ventricular Mechanics: Material Parameter Sensitivity

The following article, stemming from work completed in this thesis, has been accepted for publication in the Journal of Biomechanics.

Bibliography

Acton, F. S. (1970), *Numerical Methods That Work*, first edn, Harper & Row, 49 East 33rd Street, New York, N.Y.10016.

Akaishi, M., Weintraub, W. S., Schneider, R. M., Klein, L. W., Agarwal, J. B. & Helfant, R. H. (1986), 'Analysis of systolic bulging: mechanical characteristics of acutely ischemic myocardium', **58**, 209–217.

American Heart Association (2002), '2002 heart and stroke statistical update'.

Armour, J. A. & Randall, W. C. (1970), 'Structural basis for cardiac function', *Am. J. Physiol.* **218**(6), 1517–1523.

Atkin, R. J. & Fox, N. (1980), *An Introduction to the Theory of Elasticity*, Longman Group Limited, London.

Augenstein, K. F., McVeigh, E. R. & Young, A. A. (2001), 'Magnetic resonance imaging and ventricle mechanics', *Phil. Trans. R. Soc. Lond.* **359**, 1263–1275.

Azhari, H., Weiss, J. L., Rogers, W. J., Siu, C. O., Zerhouni, E. A. & Shapiro, E. P. (1993), 'Non-invasive quantification of principal strains in normal canine hearts using tagged MRI images in 3-D', *Am. J. Physiol.* **264**, H205–H216.

Bache, R. J. & Cobb, F. R. (1977), 'Effect of maximal coronary vasodilation on transmural myocardial perfusion during tachycardia in the awake dog', *Circ. Res.* **41**(5), 648–653.

Bergel, D. A. & Hunter, P. J. (1979), The mechanics of the heart, *in* N. H. C. Hwang, D. R. Gross & D. J. Patel, eds, 'Quantitative Cardiovascular Studies, Clinical and Research Applications of Engineering Principles', University Park Press, Baltimore, chapter 4, pp. 151–213.

Beyar, R., Yin, F. C. P., Hausknecht, M., Weisfeldt, M. L. & Kass, D. A. (1989), 'Dependence of left ventricular twist-radial shortening relations on cardiac cycle phase', *Am. J. Physiol.* **257**(26), H1119–H1126.

Bloor, C. M., White, F. C. & Lammers, R. J. (1986), *Cardiac ischemia and coronary blood flow in swine*, CRC Press, Boca Raton, chapter 5.

Bogen, D. K., Needleman, A. & McMahon, T. A. (1984), 'An analysis of myocardial infarction: the effect of regional changes in contractility', *Circ. Res.* **55**, 805–815.

Bogen, D. K., Rabinowitz, S. A., Needleman, A., McMahon, T. A. & Abelmann, W. H. (1980), 'An analysis of the mechanical disadvantage of myocardial infarction in the canine left ventricle', *Circ. Res.* **47**, 728–741.

Bradley, C. P., Pullan, A. J. & Hunter, P. J. (1997), 'Geometric modelling of the human torso using cubic Hermite elements', *Ann. Biomed. Eng.* **25**, 96–111.

Caulfield, J. B. & Borg, T. K. (1979), 'The collagen network of the heart', *Lab. Invest.* **40**(3), 364–372.

Choong, C. Y., Gibbons, E. F., Hogan, R. D., Franklin, T. D., Nolting, M., Mann, D. L. & Weyman, A. E. (1989), 'Relationship of functional recovery to scar contraction after myocardial infarction in the canine left ventricle', *Am. Heart J.* **117**, 819–829.

Choung, C. J. & Fung, Y. C. (1986), Residual stress in arteries, *in* G. W. Schmid-Schonbein, S. L. Y. Woo & B. W. Zweifach, eds, 'Frontiers in Biomechanics', Springer-Verlag, New York, pp. 117–129.

Costa, K. D., Hunter, P. J., Rogers, J. M., Guccione, J. M., Waldman, L. K. & McCulloch, A. D. (1996*a*), 'A Three-Dimensional Finite Element Method for Large Elastic Deformations of Ventricular Myocardium: Part I – Cylindrical and Spherical Polar Coordinates', *ASME J. Biomech. Eng.* **118**(4), 452–463.

Costa, K. D., Hunter, P. J., Rogers, J. M., Guccione, J. M., Waldman, L. K. & McCulloch, A. D. (1996*b*), 'A Three-Dimensional Finite Element Method for Large Elastic Deformations of Ventricular Myocardium: Part II – Prolate Spherical Coordinates', *ASME J. Biomech. Eng.* **118**(4), 464–472.

Costa, K. D., May-Newman, K., Farr, D., O'Dell, W. G., McCulloch, A. D. & Omens, J. H. (1997), 'Three-dimensional residual strain in midanterior canine left ventricle', *Am. J. Physiol.* **273**, H1968–H1976.

Dokos, S., Smaill, B. H., Young, A. A. & LeGrice, I. J. (2002), 'Shear properties of passive ventricular myocardium', *Am. J. Physiol.* (submitted).

Douglas, A. S., Rodriguez, E. K., O'Dell, W. & Hunter, W. C. (1991), 'Unique strain history during ejection in canine left ventricle', *Am. J. Physiol.* **260**, H1596–H1611.

Eason, J. C., Schmidt, J., Dabasinskas, A., Siekas, G., Aguel, F. & Trayanova, N. A. (1998), 'Influence of anisotropy on local and global measures of potential gradient in computer models of defibrillation', **26**, 840–849.

Eringen, A. C. (1980), *Mechanics of Continua*, Krieger, New York.

Fann, J. I., Sarris, G. E., Ingels, Jr., N. B., Niczyporuk, M. A., Yun, K. L., Daughters, G. T., Derby, G. C. & Miller, D. C. (1991), 'Regional epicardial and endocardial two-dimensional finite deformations in canine left ventricle', *Am. J. Physiol.* **261**(30), H1402–H1410.

Fishbein, M. C., Maclean, D. & Maroko, P. R. (1978), 'The histopathologic evolution of myocardial infarction', *Chest* **73**, 843–849.

Fox, C. C. & Hutchins, G. M. (1972), 'The architecture of the human ventricular myocardium', *Johns Hopkins Med. J.* **130**, 289–299.

Fox, L. (1967), *An Introduction to Numerical Linear Algebra*, London.

Fung, Y. C. (1965), *Foundations of Solid Mechanics*, Prentice-Hall, Inc., Englewood Cliffs, New Jersey.

Fung, Y. C. (1981), *Biomechanics: Mechanical Properties of Living Tissues*, Springer-Verlag, New York.

Green, A. E. & Adkins, J. E. (1970), *Large Elastic Deformations*, second edn, Clarendon Press, Oxford.

Greenbaum, R. A., Ho, S. Y., Gibson, D. G., Becker, A. E. & Anderson, R. H. (1981), 'Left ventricular fibre architecture in man', *Br. Heart J.* **45**, 248–263.

Guccione, J. M., Costa, K. D. & McCulloch, A. D. (1995), 'Finite element stress analysis of left ventricular mechanics in the beating dog heart', *J. Biomech.* **28**(10), 1167–1177.

Guccione, J. M., Le Prell, G. S., de Tombe, P. P. & Hunter, W. C. (1997), 'Measurements of active myocardial tension under a wide range of physiological loading conditions', *J. Biomech.* **30**(2), 189–192.

Guccione, J. M., McCulloch, A. D. & Waldman, L. K. (1991), 'Passive material properties of intact ventricular myocardium determined from a cylindrical model', *ASME J. Biomech. Eng.* **113**, 42–55.

Guccione, J. M., Moonly, S. M., Moustakidis, P., Costa, K. D., Moulton, M. J., Ratcliffe, M. B. & Pasque, M. K. (2001), 'Mechanism underlying mechanical dysfunction in the border zone of left ventricular aneurysm: a finite element study', *The Annals of Thoracic Surgery* **71**, 654–662.

Hamilton, D. R., Dani, R. S., Semlacher, R. A., Smith, E. R., Kieser, T. M. & Tyberg, J. V. (1994), 'Right atrial and right ventricular transmural pressures in dogs and humans: Effects of the pericardium', **90**(5), 2492–2500.

Holmes, J. W. (1995), Remodelling, Deformation, and Tissue Structure in Healing Myocardial Infarcts, PhD thesis, The University of California, San Diego.

Hort, W. (1957), 'Mikrometrische Untersuchungen an verschieden weiten Meerschweinchenherzen', *Verhandl. Deut. Ges. Kreislaufforsch* **23**, 343–346.

Huiskamp, G. (1998), 'Simulation of depolarization in a membrane-equations-based model of the anisotropic ventricle', *IEEE Trans. Biomed. Eng.* **45**, 847–855.

Hunter, P. J. (1975), Finite element analysis of cardiac muscle mechanics., PhD thesis, University of Oxford.

Hunter, P. J. (1995), Myocardial constitutive laws for continuum mechanics models of the heart, *in* S. Sideman & R. Beyar, eds, 'Molecular and Subcellular Cardiology: Effects of Structure and Function', Plenum Press, chapter 30, pp. 303–318.

Hunter, P. J., McCulloch, A. D. & ter Keurs, H. E. D. J. (1998), 'Modelling the mechanical properties of cardiac muscle', *Prog. Biophys. Molec. Biol.* **69**, 289–331.

Hunter, P. J., Nash, M. P. & Sands, G. B. (1997), Computational electromechanics of the heart, *in* A. V. Panfilov & A. V. Holden, eds, 'Computational Biology of the Heart', John Wiley & Sons Ltd, West Sussex, England, chapter 12, pp. 345–407.

Huyghe, J. M., Arts, T., van Campen, D. H. & Reneman, R. S. (1992), 'Porous medium finite element model of the beating left ventricle', *Am. J. Physiol.* **262**(Heart Circ. Physiol. 31), H1256–H1267.

Janz, R. F. & Grimm, A. F. (1973), 'Deformation of the diastolic left ventricle. i. nonlinear elastic effects', *Biophys. J.* **13**, 689–704.

Janz, R. F. & Waldron, R. J. (1977), 'Predicted effect of chronic apical aneurysms on the passive stiffness of the human left ventricle', *Circ. Res.* **42**, 255–263.

Katz, A. M. (1992), *Physiology of the Heart*, second edn, Raven Press, Ltd., 1185 Avenue of the Americas, New York 10036.

Krams, R., Sipkema, P. & Westerhof, N. (1989), 'Varying elastance concept may explain coronary systolic flow impediment.', *Am. J. Physiol.* **257**, H1471–H1479.

LeGrice, I. J. (1992), A Finite Element Model of Myocardial Structure: Implications for Electrical Activation in the Heart, PhD thesis, The University of Auckland, New Zealand.

LeGrice, I. J., Smaill, B. G. & Hunter, P. J. (1992), The laminar myocardium: Implications for ventricular function, *in* 'Biomechanics Conf. UCSD, San Diego'.

LeGrice, I. J., Smaill, B. H., Chai, L. Z., Edgar, S. G., Gavin, J. B. & Hunter, P. J. (1995), 'Laminar structure of the heart: Ventricular myocyte arrangement and connective tissue architecture in the dog', *Am. J. Physiol.* **269**(38), H571–H582.

LeGrice, I. J., Takayama, Y. & Covell, J. W. (1995), 'Transverse shear along myocardial cleavage planes provides a mechanism for normal systolic wall thickening', *Circ. Res.* **77**, 182–193.

Lessick, J., Sideman, S., Azhari, H., Marcus, M., Grenadier, E. & Beyar, R. (1991), 'Regional three-dimensional geometry and function of left ventricles with fibrous aneurysms: a cine-computed tomography study', *Circulation* **84**, 1072–1086.

MacCallum, J. B. (1900), 'On the muscular architecture and growth of the ventricles of the heart', *Johns Hopkins Hosp. Rep.* **9**, 307–335.

MacKenna, D. A., Omens, J. H. & Covell, J. W. (1996), 'Left ventricular perimysial collagen fibers uncoil rather than stretch during diastolic filling', *Basic Res. Cardiol.* **91**(2), 111–122.

MacKenna, D. A., Omens, J. H., McCulloch, A. D. & Covell, J. W. (1994), 'Contributions of collagen matrix to passive left ventricular mechanics in isolated rat hearts', *Am. J. Physiol.* **266**, H1007–H1018.

Mall, F. P. (1911), 'On the muscular architecture of the ventricles of the human heart', *Am. J. Anat.* **11**(3), 211–266.

Malvern, L. E. (1969), *Introduction to the Mechanics of a Continuous Medium*, Prentice-Hall, Inc., Englewood Cliffs, New Jersey.

Marsden, J. E. & Hughes, T. J. R. (1983), *Mathematical Foundations of Elasticity*, Prentice-Hall, Inc., New Jersey.

McCulloch, A. D. (1986), Deformation and Stress in the Passive Heart, PhD thesis, The University of Auckland.

McCulloch, A. D. (1995), Cardiac biomechanics, *in* J. D. Bronzino, ed., 'The Biomedical Engineering Handbook', CRC Press Inc., Boca Raton, Florida, chapter 31, pp. 418–439.

McCulloch, A. D. & Omens, J. H. (1991), 'Non-homogeneous analysis of three-dimensional transmural finite deformation in canine ventricular myocardium', *J. Biomech.* **24**(7), 539–548.

Menotti, A. & Lanti, M. (2003), 'Coronary risk factors predicting early and late coronary deaths', *Heart* **89**, 19–24.

Nash, M. P. (1998), Mechanics and Material Properties of the Heart using an Anatomically Accurate Mathematical Model, PhD thesis, The University of Auckland, New Zealand.

Nash, M. P. & Hunter, P. J. (2001), 'Computational mechanics of the heart: From tissue structure to ventricular function', *J. Elasticity*. (in press).

Nevo, E. & Lanir, Y. (1994), 'The effect of residual strain on the diastolic function of the left ventricle as predicted by a structural model', *J. Biomech.* **27**(12), 1433–1446.

Nielsen, P. M. F. (1987), The Anatomy of the Heart: A Finite Element Model, PhD thesis, The University of Auckland, New Zealand.

Nielsen, P. M. F., Le Grice, I. J., Smaill, B. H. & Hunter, P. J. (1991), 'Mathematical model of geometry and fibrous structure of the heart', *Am. J. Physiol.* **260**(Heart Circ. Physiol. 29), H1365–H1378.

Oden, J. T. (1972), *Finite Elements of Nonlinear Continua*, McGraw-Hill Book Company Inc., New York.

Omens, J. H. & Fung, Y. C. (1990), 'Residual strain in the rat left ventricle', *Circ. Res.* **66**(1), 37–45.

Omens, J. H., May, K. D. & McCulloch, A. D. (1991), 'Transmural distribution of three-dimensional strain in the isolated arrested canine left ventricle', *Am. J. Physiol.* **261**(Heart Circ. Physiol. 30), H918–H928.

Parmley, W. W., Chuck, L., Kivowitz, C., Matloff, J. M. & Swan, H. (1973), 'In vitro length-tension relations of human ventricular aneurysms', *Am. J. Cardiol.* **32**, 889–894.

Pfeffer, M. A., Pfeffer, J. M., Fishbein, M. C., Fletcher, P. J., Spadaro, J., Kloner, R. A. & Braunwald, E. (1979), 'Myocardial infarct size and ventricular function in rats', *Circ. Res.* **44**, 503–512.

Press, W. H., Flannery, B. P., Teukolsky, S. A. & Vetterling, W. T. (1989), *Numerical Recipes: The Art of Scientific Computing (FORTRAN version)*, Cambridge University Press.

Rademakers, F. E., Rogers, W. J. & Guier, W. H. (1994), 'Relation of regional cross-fiber shortening to wall thickening in the intact heart: Three-dimensional strain analysis by NMR tagging', *Circulation* **89**(3), 1174–1182.

Rankin, J. S., McHale, P. A., Arentzen, C. E., Ling, D., Greenfield, Jr., J. C. & Anderson, R. W. (1976), 'The three-dimensional dynamic geometry of the left ventricle in the conscious dog', *Circ. Res.* **39**(3), 304–313.

Rivlin, R. S. (1950), 'Large elastic deformations of isotropic materials VI. Further results in the theory of torsion,shear and flexure', *Phil. Trans.* **A242**, 173–195.

Robinson, T. F., Geraci, M. A., Sonnenblick, E. H. & Factor, S. M. (1988*a*), 'Coiled perimysial fibers of papillary muscle in rat heart: Morphology, distribution and changes in configuration', *Circ. Res.* **63**, 577–592.

Robinson, T. F., Geraci, M. A., Sonnenblick, E. H. & Factor, S. M. (1988*b*), 'Coiled perimysial fibers of papillary muscle in rat heart: Morphology, distribution and changes in configuration', *Circ. Res.* **63**, 577–592.

Rodriguez, E. K., Hoger, A. & McCulloch, A. D. (1994), 'Stress-dependent finite growth in soft elastic tissues', *J. Biomech.* **27**(4), 455–467.

Rodriguez, E. K., Hunter, W. C., Royce, M. J., Leppo, M. K., Douglas, A. S. & Weisman, H. F. (1992), 'A method to reconstruct myocardial sarcomere lengths and orientations at transmural sites in beating canine hearts', *Am. J. Physiol.* **263**(Heart Circ. Physiol.), H293–H306.

Rodriguez, E. K., Omens, J. H., Waldman, L. K. & McCulloch, A. D. (1993), 'Effect of residual stress on transmural sarcomere length distributions in rat left ventricle', *Am. J. Physiol.* **264**(4), H1048–H1096.

Saad, Y. & Schultz, M. (1986), 'GMRES: A generalised minimum residual algorithm for solving nonsymmetric linear systems', *SIAM J. Sci. Statist. Comput.* **7**, 856–869.

Sandler, H. & Dodge, H. T. (1963), 'Left ventricular tension and stress in man', *Circ. Res.* **13**(2), 91–104.

Smaill, B. H. & Hunter, P. J. (1991), Structure and function of the diastolic heart: Material properties of passive myocardium, *in* L. Glass, P. J. Hunter & A. D. McCulloch, eds, 'Theory of Heart: Biomechanics, Biophysics, and Nonlinear Dynamics of Cardiac Function', Springer-Verlag, New York, pp. 1–29.

Smith, R. M., Feild, B. J. & Rackley, C. E. (1974), 'Left ventricular compliance and abnormally contracting segments in postmyocardial infarction patients', *Chest* **65**, 368–378.

Sokolnikoff, I. S. (1964), *Tensor Analysis Theory and Applications to Geometry and Mechanics of Continua*, second edn, John Wiley & Sons, Inc., New York.

Spencer, A. J. M. (1980), *Continuum Mechanics*, Longman Group Limited, London.

Starling, E. H. (1915), The linacre lecture on the law of the heart, *in* C. B. Chapman & J. H. Mitchell, eds, 'Starling on the Heart', Dawsons Ltd.

Streeter, Jr., D. D. & Bassett, D. L. (1966), 'An engineering analysis of myocardial fiber orientation in pig's left ventricle in systole', *Anat. Rec.* **155**, 503–511.

Streeter, Jr., D. D., Spotnitz, H. M., Patel, D. P., Ross, Jr., J. & Sonnenblick, E. H. (1969), 'Fibre orientation in the canine left ventricle during diastole and systole', *Circ. Res.* **24**, 339–347.

Swan, H. J. C., Forrester, J. S., Diamond, G., Chaterjee, K. & Parmley, W. W. (1972), 'Hemodynamic spectrum of myocardial infarction and cardiogenic shock: a conceptual model', *Circulation* **45**, 1097–1110.

ter Keurs, H. E. D. J., Rijnsburger, W. H., van Heuningen, R. & Nagelsmit, M. J. (1980), 'Tension development and sarcomere length in rat cardiac trabeculae', *Circ. Res.* **46**(5), 703–714.

Terzopoulos, D. (1986), 'Regularization of inverse visual problems involving discontinuities', *IEEE Trans. Pattern Anal. Machine Intell.* **PAMI-8**(4), 413–424.

Tyberg, J. V. & Smith, E. R. (1990), 'Ventricular diastole and the role of the pericardium', *Herz* **15**(6), 354–361.

Tyson, Jr., G. S., Maier, G. W., Olsen, C. O., Davis, J. W. & Rankin, J. S. (1984), 'Pericardial influences on ventricular filling in the conscious dog: An analysis based on pericardial pressure', *Circ. Res.* **54**, 173–184.

Villarreal, F. J., Lew, W. Y. W., Waldman, L. K. & Covell, J. W. (1991), 'Transmural myocardial deformation in the ischemic canine left ventricle', *Circ. Res.* **68**(2), 368–381.

Waldman, L. K., Fung, Y. C. & Covell, J. W. (1985), 'Transmural myocardial deformation in the canine left ventricle: Normal *In Vivo* three-dimensional finite strains', *Circ. Res.* **57**(1), 152–163.

West, B. J. (1985), *Best and Taylor's physiological basis of medical practice*, Williams and Wilkins, Baltimore.

Wong, A. Y. K. & Rautaharju, P. M. (1968), 'Stress distribution within the left ventricular wall approximated as a thick ellipsoidal shell', *Am. Heart J.* **75**(5), 649–662.

Woods, R. H. (1892), 'A few applications of a physical theorem to membranes in the human body in a state of tension', *J. Appl. Physiol.* **26**, 362–370.

Yang, M. & Taber, L. A. (1991), 'The possible role of poroelasticity in the apparent viscoelastic behaviour of passive cardiac muscle', *J. Biomech.* **24**(7), 587–597.

Yin, F. C. P. (1981), 'Ventricular wall stress', *Circ. Res.* **49**(4), 829–842.

Yin, F. C. P. (1985), 'Applications of the finite-element method to ventricular mechanics', *Crit. Rev. Biomed. Eng.* **12**(4), 311–342.

Young, A. A., Hunter, P. J. & Smaill, B. H. (1989), 'Epicardial surface estimation from coronary angiograms', *Comput. Vision Graphics Image Process.* **47**, 111–127.

Zienkiewicz, O. C. & Taylor, R. L. (1994), *The Finite Element Method. I. Basic Formulation and Linear Problems*, fourth edn, McGraw-Hill Book Company Inc., Berkshire, UK.